Universitat Autònoma de Barcelona

Organic vapour-deposited stable glasses: from fundamental thermal properties to high-performance organic light-emitting diodes

Joan Ràfols Ribé

Universitat Autònoma de Barcelona

Organic vapour-deposited stable glasses: from fundamental thermal properties to high-performance organic light-emitting diodes

Doctoral Thesis submitted by
Joan Ràfols Ribé
to apply for the degree of Doctor in Physics

Supervised by
Prof. Javier Rodríguez Viejo
and
Dr. Marta Gonzàlez Silveira

Nanomaterials and Microsystems Group
Physics Department
September 2017

El Prof. Javier Rodríguez Viejo, catedràtic d'universitat numerari del Departament de Física de la Facultat de Ciències de la Universitat Autònoma de Barcelona i la Dra. Marta Gonzàlez Silveira, professora agregada interina del Departament de Física de la Facultat de Ciències de la Universitat Autònoma de Barcelona,

CERTIFIQUEN que en Joan Ràfols Ribé, Llicenciat en Física per la Universitat de Barcelona, i en possessió del Màster oficial en Radiació Sincrotró i Acceleradors de Partícules, ha realitzat sota la direcció d'ambdós el treball que porta com a títol *Organic vapour-deposited stable glasses: from fundamental thermal properties to high-performance organic light-emitting diodes* el qual es recull en aquesta memòria per tal d'optar al Títol de Doctor en Física per la Universitat Autònoma de Barcelona.

Prof. Javier Rodríguez Viejo
Bellaterra, Setembre 2017

Dra. Marta Gonzàlez Silveira
Bellaterra, Setembre 2017

“42”

Deep Thought

Abstract

Physical vapour deposition has recently emerged as an alternative route to prepare glasses that span a broad range of stabilities, together with other features. Particularly, it is possible to achieve glasses with properties that outperform conventional glasses, and that would otherwise require times from tenths to several thousands of years of slowly-cooling or ageing. For this reason, these glasses are referred as highly stable glasses or ultrastable glasses. In particular, it has been shown that for many molecular organic glass-formers, the deposition temperature plays a crucial role in determining glass properties, such as thermal stability, density or molecular orientation among others, giving the possibility to enhance the inherent instability of glasses. Vapour-deposited glasses offer new insights into the glass transition phenomenon but also potential applications in many technological processes such as in organic electronics. This work is committed to further deepen the knowledge on vapour-deposited glasses using organic semiconductor materials. We use two silicon nitride membrane-based techniques—fast-scanning quasi-adiabatic nanocalorimetry and the 3ω–Völklein method—to characterise several facets of these glasses. Firstly, we show that the most stable amorphous films are obtained when evaporated at 85 % of its corresponding glass transition temperature (T_g). Secondly, we show how vapour-deposited films transform into the supercooled liquid via a propagating growth front that starts at the highly-mobile regions (surface and interfaces). The characteristics of this mechanism are examined and rationalised regarding the different glass properties. Thirdly, we demonstrate how this heterogeneous transformation can be effectively suppressed when the high-mobility interface is capped with a lower mobility layer, gaining access to the bulk transformation. We see how the kinetic stability of the capped layers is improved using this strategy. After characterising the glass transition, we look at the thermal conductivity of these glasses. We observe how the in-plane thermal conductivity changes with the deposition temperature and we attribute this behaviour to variations in the molecular alignment. Finally, we present a simple phosphorescent organic light-emitting diode device (OLED), consisting only of two organic layers, to check the influence of the deposition temperature on the device performance. We demonstrate how its efficiency and lifetime are enhanced when its functional layers are evaporated at the $0.85T_g$. These results are achieved considering only the glass transition temperature and, therefore, they could be generalised to any OLED device. This work contributes to the existing knowledge of vapour-deposited glasses by providing new insights into their thermal properties and devitrification mechanisms and by exploring their potential application in the state-of-the-art OLED devices.

Agraïments

Són unes quantes les persones amb les quals, al llarg d'aquests quatre anys de doctorat, m'he creuat i que han contribuït, en major i menor mesura, al fet que pogués acabar aquesta etapa personal i professional. No només que pogués acabar, sinó que pogués aprendre tant i tant, a formar-me com a científic però també a ampliar coneixements i acumular experiències increïbles. Més enllà d'aquests quatre últims anys també hi ha hagut gent magnífica que ha deixat el seu granet de sorra al fet que avui sigui aquí. A tots, moltes gràcies.

Primer de tot gràcies a tota la gent del meu grup de recerca, el GNaM. Gràcies per totes les tardes de birres, les calçotades, els sopars i les barbacoes al llarg d'aquests anys. Vull agrair abans que res als meus directors de tesis, el Prof. Javier Rodríguez i a la Dra. Marta Gonzàlez. Al Javier, per oferir-me aquesta gran oportunitat i confiar en mi. Gràcies per totes les grans oportunitats, ben aprofitades, d'aprendre i ampliar coneixement que he tingut al llarg d'aquests anys. A la Marta, per la teva constant dedicació a la supervisió del treball, pels seus consells i per fer-me créixer (encara més) l'esperit científic. Però sobretot, gràcies també per esdevenir una gran amiga. Gràcies a la Gemma Garcia per la seva ajuda quan l'he necessitat i per als seus consells, tant els científics com els cervesers! Gràcies a l'Aitor Lopeandía, per iniciar-me al fascinant món de l'electrònica i nanocalorimetria del qual he après tant. Gràcies al Manel Molina, per ensenyar-me tant en els meus inicis, però també pels teus acudits... dolents! Gràcies a l'Antonio Pablo Pérez, per la seva simpatia, per no callar mai i per regalar-me una gran antologia de "grans" frases. Gràcies a en Pablo Ferrando, per ser tan simpàtic, per ser tan científicament motivat, per ajudar-me tant i per tots els Catans i cerveses fetes. La ciència compta amb tu, torna! Al Gustavo Dalkiranis, per tenir tanta son i a la vegada encomanar tanta energia i motivació. Als estudiants del grup presents i passats; a l'Ivan Álvarez, pels viatges amb el cotxe i per les tertúlies post-capítol, a l'Ana Vila, per ser tan divertida, al Pere i a la Clàudia. Finalment i no per això menys, moltes gràcies tu, Cristian Rodríguez, per tot i per tant, pel que ha estat i pel que vindrà.

M'agradaria agrair també a la gent del Departament de Física que m'ha ajudat. Gràcies al Manel Garcia, per la seva inestimable ajuda tècnica. Moltes gràcies també a la Dori Pacho per a la seva simpatia, el seu temps i la seva paciència amb mi i els meus oblits administratius, així com a la resta de la secretaria de Física. Gràcies a en Francesc Pi per a les seves evaporacions. Vull agrair també a la Raquel Palencia del Laboratori d'Ambient Controlat, per la seva ajuda desinteressada. Gràcies a la Camilla Maggio, per les hores i preparacions de classe compartides.

Enormous thanks also to Theo Bijvoets. My vacuum knowledge, our lab, my experimental setups and, of course, my research, wouldn't have been the same without your invaluable advice. Thanks also for your 'magnetic' advice and help!

I would like to thank also Prof. Dr Sebastian Reineke from the Dresden Integrated Center for Applied Physics and Photonic Materials (IAPP) and Institute for Applied Physics for giving me the opportunity to carry out part of this work at his group and to all the people I met in Dresden. Thanks also to Simone Lenk for taking care and showing me all the insights of the IAPP and the OLED world. Big thanks also to Christian Hänisch and Paul-Anton for teaching me so much of OLEDs, for the fruitful discussions and your participation in our ultrastable OLED adventure.

Vull agrair també a la gent de sempre. Hi han hagut professors i mestres, tant de primària com secundària, que m'han deixat un bon record i que, per més o per menys, han contribuït a fer que acabi presentant aquest treball. De tots aquests, en guardo un especial record tant de la Montse Magem com del Joan Andreu. A tots ells, moltes gràcies. Gràcies també als meus companys de pis: Pol Pallàs i Anna Font, per aguantar-me els dies bons i els dolents, per als múltiples vespres de birres, Carcassones, Pandemics i aventures varies. Gràcies també a la Merche, Anna, Dani per les agradables i divertides tardes i vespres a Vilafranca. A la resta de la colla també! Aida, Albert, Aina, Òscar, Jordi, Laia, Ferran, Heura, Salva, Ivan, Alba, Gerard, Natàlia, Neus, Xavi... a tots! A la gent d'aquí i d'allà amb la que m'he anat creuant a la carrera, màster, vida... Xavi, Cristina, Carlos, Elisenda, Marc, Andrea, Pau, Mireia, Julián i d'altres que segurament em deixo. A tots, moltes gràcies!

Finalment, moltes gràcies als meus pares, Elisabet i Lluís, per educar-me en qui sóc avui, inocular l'esperit crític i per tot, per tot. Evidentment, gràcies també als meus germans Jordi i Júlia! A la resta de la meva família avis, tiets i cosins. Gràcies Sara, Amir, Maria i Ibai per acollir-me en les meves visites a casa vostra!

Des d'una plana més institucional agraeixo al Ministerio de Educación, Cultura y Deporte per a la beca del Programa de Formación de Profesorado Universitario (FPU) de la que he gaudit els últims tres anys.

A tothom que d'una manera o altra m'ha ajudat i contribuït en aquesta etapa,

moltes gràcies!

Contents

List of Figures

List of Abbreviations

AC	Alternated Current
AD	As Deposited
AFM	Atomic Force Microscopy
α-NPD	N,N′-Di-1-naphthyl-N,N′-diphenylbenzidine (hole transport material)
CC	Calorimetric Cell
CG	Conventional Glass
DAQ	Data Acquisition
DC	Direct Current
DSC	Differential Scanning Calorimetry
EL	Electroluminescence
EML	Emission Layer
ETL	Electron Transport Layer
EQE	External Quantum Efficiency
FC	Fast-Cooled
FEM	Finite Element Modelling
GNaM	Group of Nanomaterials and Microsystems
HTL	Hole Transport Layer
HV	High Vacuum
HOMO	Highest Occupied Molecular Orbital
IAPP	Dresden Integrated Center for Applied Physics and Photonic Materials and Institute for Applied Physics
IMC	Indomethacin
LE	Luminous Efficacy
LUMO	Lowest Unoccupied Molecular Orbital
OLED	Organic Light-Emitting Diode
OSG	Organic Semiconductor Glass-former
PVD	Physical Vapour Deposition
PID	Proportional-Integral-Derivative controller
PL	Photoluminescence
QCM	Quartz Crystal Monitor
SCL	Supercooled Liquid
SEM	Scanning Electron Microscopy

SI	International System of Units
SIMS	Second Ion Mass Spectrometry
TCTA	4,4′,4″-Tri-9-carbazolyltriphenylamine (hole transport material)
TCR	Temperature Coefficient of Resistance
TPBi	2,2′,2"-(1,3,5-benzinetriyl)-tris(1-phenyl-1-H-benzimidazolee (electron transport material)
TPD	N,N′-Diphenyl-N,N′-di(m-tolyl)benzidine (hole transport material)
TNB	α,α,β-tris-naphthylbenzene
UHV	Ultra-High Vacuum
UG	Ultrastable Glass
VD	Vapour Deposited
VFT	Vogel-Fulcher-Tammann

List of Symbols

c_p	specific heat at constant pressure	$\mathrm{J\,K^{-1}\,g^{-1}}$
C_p	heat capacity at constant pressure	$\mathrm{J\,K^{-1}}$
G	thermal conductance	$\mathrm{W\,K^{-1}}$
f	frequency	Hz
I	intensity	A
I_e	radiant intensity	$\mathrm{W\,m^{-2}\,sr^{-1}}$
j	current density	$\mathrm{mA\,cm^{-2}}$
k	thermal conductivity	$\mathrm{W\,m^{-1}\,K^{-1}}$
$k \parallel$	in-plane thermal conductivity	$\mathrm{W\,m^{-1}\,K^{-1}}$
$k\perp$	out-of-plane thermal conductivity	$\mathrm{W\,m^{-1}\,K^{-1}}$
L	luminance, brightness	$\mathrm{cd\,m^{-2}}$
P, Q	power	W
R	electrical resistance	Ω
T_f'	limiting fictive temperature	K
T_f	fictive temperature	K
T_g	glass transition temperature	K
T_m	melting temperature	K
T_{on}	onset temperature	K
V, U	voltage	V
v_{gr}	growth front velocity	$\mathrm{nm\,s^{-1}}$
β	heating rate	$\mathrm{K\,s^{-1}}$
β	stretched exponent	
η	various efficiencies	
γ	charge balance factor	
ω	angular frequency	rad
ρ	density	$\mathrm{kg\,m^{-3}}$ or $\mathrm{g\,cm^{-3}}$
τ	relaxation time (generic)	s
ξ	liquid layer thickness, crossover length	nm

Als meus pares

Motivation and objectives

Glasses have the disordered molecular structure of liquids but behave mechanically like solids. The easiest and most common way to prepare a glass is by cooling the liquid fast enough, so the crystallisation is avoided. Although humankind has known this route of preparing glasses for some millennia, a complete understanding of the glassy physics is still missing. The first records of humans using glasses can be traced back to the Stone Age, where objects made of obsidian—a naturally occurring volcanic glass—were used both as tools and as decorative objects. The origins of the glass-making technology have been traced as far back as 1500 BC in regions such as Egypt or Mesopotamia, where most glasses are found in the form of beads. It was not until the 1st century BC that the glassblowing technique was invented, somewhere along the Syrio-Palestinian Coast, and it subsequently spread through the Roman Empire. Throughout history, the term "glass" has been directly associated with the "silicate glasses" based on the chemical compound silica (SiO_2 or quartz), which is the primary constituent of sand. Nowadays, the term is understood in a broader sense, and we can find a wide variety of glasses besides the canonical silicate glasses.

In fact, glasses are present in our daily life both in nature and in a wide diversity of technological processes. The most emblematic example of an engineered glass today is probably window glass, composed mostly of sand, lime and soda (sodium carbonate). Optical fibres, essential in the communication era we live today, are made of pure amorphous silica. Glasses are also of vital importance in the processing of food [1] or in the plastic manufacturing, where most products are usually in their amorphous form. Metallic glasses have also been a field of interest in the past decades due to their excellent properties, such as corrosion resistance, high strengths or soft magnetism, evolving from laboratory curiosities into materials for industrial applications [2]. Vitrification is the universal method to treat most dangerous nuclear waste [3]. In cryopreservation, vitrification is also a common method to preserve human egg cells and embryos [4]. The multidisciplinary nature of glasses is extraordinary, even having a special role in cinema and literature. While a naturally aged amber glass containing a mosquito with dinosaur's blood is the starting point of the Jurassic Park film (based on the former novel of the same name by Michael Crichton), a glass of a more fantastic nature—the so-called dragonglass or obsidian—has revealed of key importance for the future of the seven kingdoms of Westeros in the epic fantasy drama television series Game of Thrones (based on the series of novels by George R. R. Martin). Although amber glasses

can be millions of years old (from the Cretaceous or younger), the oldest glasses found on Earth, currently, correspond to 3.6 billion years old and are glass beads that astronauts from the Apollo missions brought back from the Moon in the 70s [5]. Despite many years of intense research in glassy physics, both theoretical and experimental, the interest in glasses is far from decreasing, as they have revealed their importance for multiple industrial potential applications.

A good example of an interesting application of glasses can be found in the pharmaceutical industry. Drugs that are typically taken in the form of a pill are in the crystalline state, which generally shows poor-water solubility that leads to limited bioavailability—most of the drug is excreted without reaching the site of action. Bioavailability can be directly increased if the drug is delivered in its amorphous form [6]. However, the major drawback preventing the commercialisation of amorphous-based drugs is their limited stability. Pharmaceutical glasses tend to crystallise easily, something that could happen during the production, storage or usage of the product. That would change the effective doses that should be taken, making the commercialisation unviable. The amorphous pharmaceutical drugs field could benefit from the breakthroughs in glass science and eventually overcome the current drawbacks and make a step forward in solving the low glass stability of these drugs.

Another important field that might benefit from the new developments in glass physics is the organic electronics industry. For instance, in recent years, several commercial TV and smartphone displays based on organic light-emitting diodes (OLEDs) are being sold worldwide. OLEDs consist of amorphous thin films, typically $<$100 nm, of organic (carbon-based) semiconductor materials sandwiched between two electrodes. One of the advantages of OLEDs compared to their counterparts, inorganic LEDs, is that their amorphous nature allows them to be prepared homogeneously over large areas or even on flexible substrates due to their softness [7]. OLEDs also offer many other advantages in contrast to the inorganic LEDs, such as excellent wide viewing angles, vivid colours, possible fabrication of transparent devices and cost-effective production [7]. However, it is not yet a mature technology, and there are still some drawbacks to work out. One of them is their lack of stability over time and their temperature degradation [8] that prevents their use for lighting applications. Again, glass science can provide a better understanding and even a solution to some of the problems found in this field.

Despite glasses being found both in nature and in a handful of technological applications, there is not yet a satisfactory explanation of the physics behind the transition from the supercooled liquid into a glass. This phenomenon occurs at the glass transition temperature (T_g), approximately when the temperature of the supercooled liquid is two-thirds of its melting point. Starting frm the liquid and as the temperature goes down, the motion of the molecules is continually reduced—it becomes a viscous

liquid—until it suffers a dramatic slowdown that leaves the system completely arrested. Thus, the system has a molecular structure that completely resembles that of the liquid but it behaves, for all practical purposes, as a solid. Actually, it is a common view—although imperfect and incomplete—to think of a structural glass as a frozen snapshot of the liquid state. In the scientific community, it is still not clear whether the glass transition involves an underlying thermodynamic (static) or kinetic (dynamic) phase transition [9]. The mechanisms governing the drastic slowdown of the molecular motion are still in an ongoing discussion since the large timescales involved preclude having experimental access to them. It is evident, therefore, that a complete understanding of the glass transition phenomenon would be beneficial both from the theoretical and practical point of view.

Since 2007, physical vapour deposition (PVD) has emerged as an alternative route to prepare glasses [10]. The advantage of this methodology is that glasses spanning a broad range of stabilities (among other features) can be prepared by just controlling few processing factors—essentially the deposition temperature and the growth rate. More interestingly, by using this route, it is possible to achieve glasses with properties that outperform conventional glasses prepared by quenching the liquid. Rather than the methodology to prepare glasses from the vapour phase, the breakthrough came from the prominent evidence that these glasses can indeed be far more stable than the liquid cooled ones when the necessary conditions are met. With physical vapour deposition, it is possible to achieve low-energy glasses that would otherwise require times from tenths to several thousands of years of slowly-cooling or ageing a liquid. For this reason, they are referred as highly stable glasses or ultrastable glasses (UG). Moreover, vapour-deposited (VD) glasses offer new insights into the glass transition phenomena by gaining access to—until recent times—inaccessible regions of the energy landscape.

Thesis structure

This work is committed to further deepen the knowledge on organic vapour-deposited glasses by using different techniques and approaches. From a more fundamental approach, we aim to study various facets of VD glasses which depend on its deposition temperature, the parameter that ultimately determines the glass properties. The kinetic and thermodynamic stability, the mechanisms by which they transform into the supercooled liquid or the thermal transport are some of the features addressed. From a more practical point of view, this thesis intends to determine the extent to which modifying the preparation conditions of VD glasses can be advantageous in the organic electronics technology. More specifically, how the inclusion of ultrastable glass layers influences the performance of organic light-emitting diodes (or OLEDs).

The manuscript is divided into eight chapters:

- In Chapter 1 the theoretical framework for this work is given. Since the field of glass science is very broad, only the most significant aspects relevant to this work regarding the phenomenology of the glass transition are presented. The signature of the glass transition on a heat capacity scan is thoroughly discussed, as calorimetry has been a fundamental technique to characterise the glasses prepared in this work. Moreover, an introduction to vapour-deposited glasses is also offered to provide the reader with a complete, up-to-date, overview of the research being done in this specific area.

- Chapter 2 is concerned with the methodology used in this study. All the samples (glasses) used and characterised here have been prepared by physical vapour deposition, more specifically, vacuum evaporation, which is briefly detailed. The details regarding the specific experimental setups used throughout this thesis are also described in this chapter as well as the materials used. Along with sample preparation, home-made characterisation tools are of fundamental importance in this work. We introduce two membrane-based techniques for thermal characterisation that rely on microfabricated devices, which can both be used for in situ characterisation of the VD glasses. First, the fast-scanning quasi-adiabatic nanocalorimetry is presented and its working principle described. Secondly, a new technique recently implemented at GNaM's group is also presented: the 3ω-Völklein. This method allows measuring the in-plane thermal conductivity of any layer deposited on top of the sensor.

- Chapters 3, 4 and 5 describe the calorimetric characterisation of vapour deposited glasses as a function of the deposition temperature (T_{dep}). A thorough analysis of the calorimetric trace obtained using fast-scanning quasi-adiabatic nanocalorimetry allows us to get valuable data regarding different aspects and properties of these glasses. In Chapter 3, the kinetic and thermodynamic stability of three different glass-formers—toluene and two organic semiconductor molecules—as a function of T_{dep} is obtained from the specific heat curves and discussed. The calorimetric trace during the devitrification also allows identifying a heterogeneous transformation mechanism characteristic of these VD glasses. In 4, the heterogeneous mechanism—consisting of a devitrification transformation front that starts at the free surface—is further explored for the same three materials. Finally, in Chapter 5, the transformation front is blocked using a capping layer of a material with higher T_g gaining access to the bulk transformation.

- Chapter 6 deals with thermal transport data obtained using the 3ω–Völklein technique. The in-plane thermal conductivity of two organic semiconductors (TPD and α-NPD) is measured as a function of the deposition temperature of the glass. We report, for the first time, how the thermal conductivity of organic amorphous

can be effectively tuned in a significant percentage by playing only with the deposition conditions. Moreover, due to the high resolution and sensitivity of the 3ω–Völklein technique, we can monitor the early stages of the organic layer formation by tracking conductance during the evaporation. Although preliminary, the possibility to obtain valuable data on the stable glass formation is discussed.

- The main goal of Chapter 7 is to prove the impact that ultrastable glasses have on a fully functional organic light-emitting diode. The results presented here were done in collaboration with the group of Prof. Sebastian Reineke at the Dresden Integrated Center for Applied Physics and Photonic Materials (IAPP) and Institute for Applied Physics from the Technische Universität Dresden. We use a simplified OLED stack and measure its performance—both lifetime and efficiency—as a function of the deposition temperature at which the device is prepared. Although we address the discussion from a "glass physics" perspective, there are some fundamental notions of organic electronics and OLEDs that need to be introduced. Therefore, and since this chapter is meant to be alomst self-contained, a short introduction to organic semiconductors and organic light-emitting diodes physics is provided, as well as a brief description of the techniques used to characterise the performance of these devices. After this introduction, the results for the device under study are presented and discussed.
- The last chapter is devoted to the conclusions of the entire work presented here.

Chapter 1

Introduction

1.1 Phenomenology of the glass transition

To better understand how a glass is formed, we can look at the schematic representation of volume, enthalpy or entropy versus temperature (Figure 1.1). Consider we heat a solid above its melting point: we have, therefore, a liquid. We now start decreasing the temperature down to the melting temperature again. We see at the same time that the volume, the enthalpy and entropy decrease too. Around the melting temperature, the liquid might suffer a sudden drop in the volume, experimenting a first-order transition into the crystalline state. After this drop, the volume will continue to decrease with the temperature but at a slower pace. However, if the cooling is fast enough to avoid the crystallisation, we enter the supercooled liquid regime. In this case, the volume will continue decreasing with the temperature at the same pace as the liquid, although the system will start becoming more and more viscous. At a low enough temperature, the rate of the variation of volume with temperature will change, and the viscous liquid will solidify according to our experimental timescale. The variation of the volume with temperature per unit volume at a constant pressure is known as the thermal expansion coefficient,

$$\alpha_V(T) = \frac{1}{V}\left(\frac{\partial V}{\partial T}\right)_p \tag{1.1}$$

The temperature at which this change of slope occurs is referred as the *glass transition temperature*, T_g, and it is material dependent. However, even for the same material, this temperature is not unique and it depends on the cooling rate. If the supercooled liquid is cooled slowly, the system will have more time to properly explore the configurational phase space before falling out of the equilibrium at a lower temperature. At T_g, the number of degrees of freedom which are accessible to the system is suddenly reduced. This drop is translated into a reduction (up to a factor of 2) of the specific heat at constant pressure [11], c_p, which is defined as:

$$c_p(T) = \left(\frac{\partial H}{\partial T}\right)_p \tag{1.2}$$

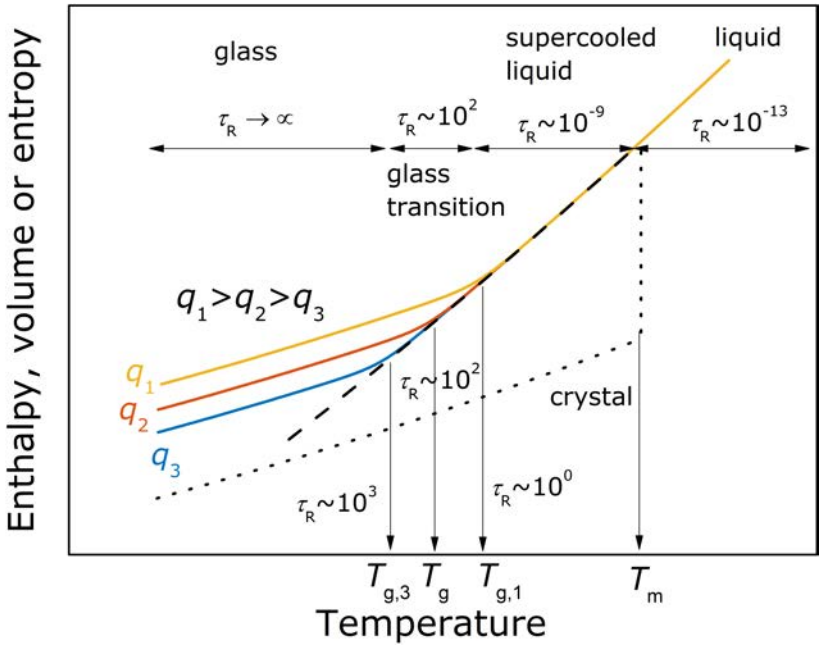

Figure 1.1: Schematic of the enthalpy evolution with temperature (equivalent also for entropy or volume) of a liquid when cooling it from the high-temperature region down to the supercooled liquid region and glass region. The different coloured curves correspond to different cooling rates paths, indicated by q. The different regions are described by their characteristic relaxation times (see Section 1.1.1)

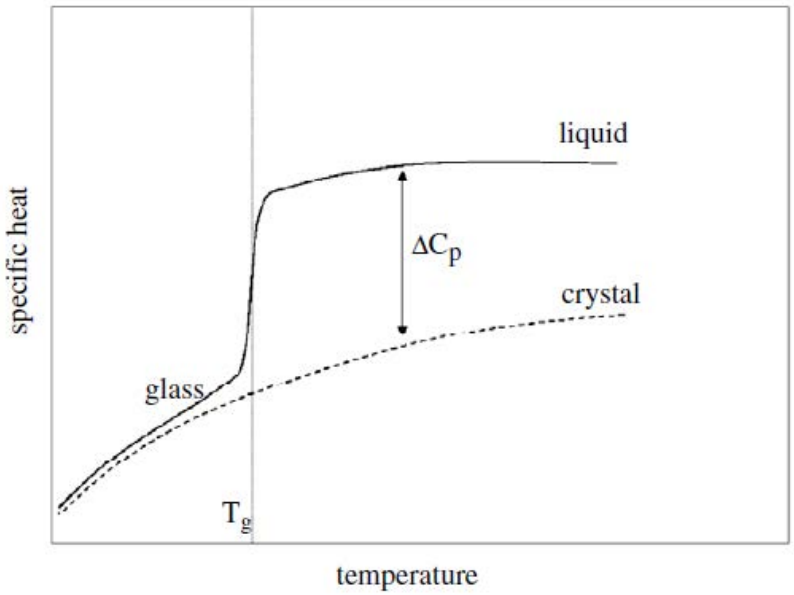

Figure 1.2: Specific heat of the glass and liquid regions showing the jump during the glass transition. The dashed line is the specific heat of the crystal. Figure reprinted from [11]

The change in the slope of the enthalpy versus temperature in Figure 1.1 is translated into the c_p step at T_g in Figure 1.2. At T_g, the experimental time needed for the system to explore a representative fraction of the phase space is much smaller that the time

needed in the supercooled liquid or liquid region. The capacity of a system to explore its phase space of microstates within a given time is called ergodicity. From a dynamic point of view, one can say that a system that has become a glass is no longer ergodic since it cannot sample its phase space within laboratory timescales.

It is interesting to note, as can be seen in Figure 1.2, that the specific heat of the glass below T_g has a temperature behaviour similar to that of the crystal [11]. In the latter, the ergodicity is broken and the system is confined in an absolute energy minimum in the phase space. There, the motion of the particles/molecules consists in vibrations around their equilibrium positions. The similar behaviour of the glass specific heat at lower temperatures indicates that the particles (or molecules) vibrate around their "equilibrium" positions, completely disordered in this case and with practically no structural rearrangements. In that sense, the ergodicity of a glass is dynamically broken, only capable of exploring a small region of local minimums in its phase space. Therefore, contrary to the crystal, a glass is an out-of-equilibrium system. The properties of the glass will continuously evolve over time from the moment it is cooled below T_g, until reaching the corresponding supercooled liquid equilibrium. This is a crucial difference between a crystal and a glass: in a crystal, the broken ergodicity is the result of a true thermodynamic phenomenon (a first-order transition), whereas the ergodicity breaking in a glass is purely a dynamic phenomenon.

1.1.1 Relaxation time

The concept of relaxation time is fundamental and extremely useful in glass science. It can be defined as the time that a system needs to restore its equilibrium configuration after being externally excited. For instance, in mechanical measurements, after a certain strain is applied to a material, we will observe a stress decrease over time allowing to define a relaxation time for the system. In dielectric spectroscopy, the relaxation time is obtained from the response of the dipole de-excitation to an applied external oscillating electric field. Figure 1.1 shows that, at each temperature, the supercooled liquid needs a certain amount of time to relax to its corresponding equilibrium volume or enthalpic state. By decreasing T, the relaxation time increases and the system will eventually reach a temperature at which this time will be larger than the experimental time available for the observer. A typical definition of the glass transition temperature is that at which the relaxation time (often referred as the α-relaxation time, see Section 1.1.5) of the system is

$$\tau_R(T_g) \simeq 100\,\mathrm{s} \tag{1.3}$$

Dielectric spectroscopy is a useful technique to measure the relaxation time (or times, see Section 1.1.5) of the liquids, and it is widely used to characterise the relaxation processes in the supercooled liquid state.

1.1.2 Viscosity

Along with the relaxation time, the viscosity is another frequently measured property in these systems. Viscosity (η), relaxation time and shear modulus (G_∞, at infinite frequency) are related through the expression

$$\eta = G_\infty \tau_R \tag{1.4}$$

Although this equation is strictly valid only for Maxwell liquids, for which the shear stress depends only on one exponential relaxation time, the proportionality between viscosity and relaxation time, $\eta \propto \tau_R$, is generally assumed for glass-forming liquids [11], in which the largest relaxation time of the system is used.

The rate at which viscosity changes with temperature as we approach the T_g from the liquid serves as a criterion to classify the glass-forming liquids. For instance, in silica, the dependence of viscosity on temperature follows an Arrhenius type equation

$$\eta = A \exp\left(\frac{E}{k_B T}\right) \tag{1.5}$$

where E is the activation energy and A a prefactor, both temperature independent, and k_B is the Boltzmann's constant. In these systems, the logarithm of the viscosity scales linearly with $1/T$, and the only "special" feature occurring at T_g is that η is so high that at all practical purposes, the system behaves as a solid. However, other liquids exhibit more drastic changes in viscosity as they approach the T_g. In these systems, the viscosity (or relaxation time) varies in a super-Arrhenius fashion between temperatures much above T_g and close to it. This behaviour is well-represented by the phenomenological Vogel-Fulcher-Tammann (VFT) expression [12]

$$\eta = A \exp\left(\frac{B}{T - T_0}\right) \tag{1.6}$$

where A and B are temperature independent. Here, the viscosity rapidly arises as the temperature approaches T_0, eventually diverging when $T = T_0$.

These two types of temperature behaviours for the viscosity define the limits between *strong* and *fragile* liquids, a classification first suggested by Angell [13]. A natural plot to visualise the viscosity data as a function of temperature for a wide variety of systems is the representation of η (or τ_R) versus the rescaled reciprocal temperature, T_g/T, often referred as Angell's plot in the literature. The systems in which the viscosity or relaxation time change in a nearly Arrhenius fashion are called *strong* liquids, represented as straight lines in the Angell's plot (Figure 1.3). Therefore nothing particular occurs at T_g except that the viscosity reaches $\eta = 10 \times 10^{13}\,\mathrm{Pa\,s}$, the typical value assumed at T_g and equivalent to the definition of $\tau(T_g) = 100\,\mathrm{s}$ [11]. These liquids tend to have

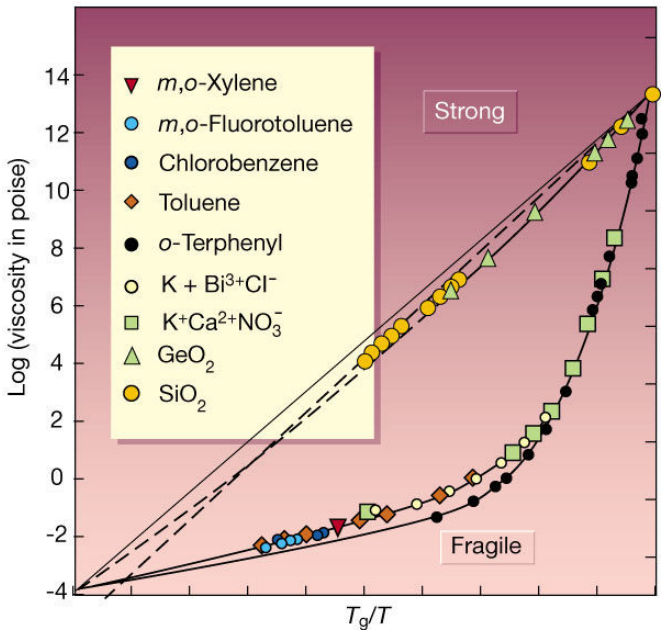

Figure 1.3: Angell's plot. The logarithm of viscosity is represented versus the inverse of temperature, rescaled to the glass transition temperature of each material, labelled in the plot. Figure reprinted from [1]

tetrahedrally coordinated structures with strong directional covalent bonds such as silica (SiO_2)—the canonical strong glass-former—or germanium oxide (GeO_2) [13].

On the other hand, fragile liquids are those that show super-Arrhenius behaviour such as the one represented by the VFT equation 1.6, like the prototypical fragile glass-formers o-terphenyl or toluene. On these systems, the viscosity shows a moderate growth at high temperatures whereas it becomes steeper and steeper as we approach T_g. Fragile liquids are characterised by simple non-directional coulomb attraction—or by Van der Waals interactions in the subgroup of molecular organic glass-formers. Strong liquids show an inherent resistance to structural changes over a wide temperature interval. In fragile liquids, in contrast, small thermal fluctuations around the T_g provoke glassy state configurations that bounce over a wide variety of orientation and coordination states. For that reason, fragile liquids tend to exhibit a much higher c_p jump at T_g than strong liquids.

The fragility of a liquid can be quantified by how the viscosity—or relaxation time—change over temperature as we approach T_g. Therefore, a *kinetic fragility index* can be readily calculated from:

$$m = \left[\frac{\partial \log \eta}{\partial \left(\frac{T_g}{T} \right)} \right]_{T_g} \tag{1.7}$$

From this equation and from Figure 1.3 we can see that the larger the fragility index, the more fragile is the liquid.

1.1.3 Dynamic heterogeneity

The concept of dynamic heterogeneity is also a key feature which is characteristic of amorphous materials and that has emerged from the experimental studies looking at the response functions of a liquid near its T_g. The temporal behaviour response of a system that has been excited, for example, via an applied electric field or through a mechanical deformation, is highly non-exponential in deeply supercooled liquids. This response, also called relaxation spectra, can often be described by the stretched exponential, or Kohlrausch-Williams-Watts (KWW) function [11]

$$C(t) = \exp\left[-\left(\frac{t}{\tau_R}\right)^{\beta}\right] \quad \beta < 1 \tag{1.8}$$

where $C(t)$ can be any correlation or relaxation function, such as those observed in dielectric loss relaxation or nuclear magnetic resonance spectroscopy [11] and τ_R is the characteristic relaxation time that depends on T, often following the VFT equation for fragile liquids. Far above T_g, the exponent β has a value of one. This essentially means that the system can be described by one intrinsic timescale. However, for a typical fragile glass-former, β decreases with temperature as it approaches to T_g, reaching values about 0.5. This nonexponential behaviour suggests the existence of a broad distribution of relaxation times.

In the literature, one can find two approaches explaining this broad distribution of times. From the dynamic heterogeneity point of view, there is a set of different environments in the supercooled liquid, each one relaxing in a different manner and at a different rate. That fact produces the broad spectra seen in relaxation times. In this picture, above the glass transition temperature, the particles are constantly rearranging, so the different spatiotemporal environments only have one finite and experimentally short timescale. According to the second approach, the supercooled liquids are homogeneous, and each molecule is equally relaxing towards the equilibrium in a nonexponential manner. It is argued that while the first heterogeneous explanation is caused by a spatial distribution of relaxation times, the second homogeneous view has no direct physical interpretation [14]. Moreover, a growing body of literature in the past two decades has well established the spatiotemporal heterogeneity close to the glass transition both experimentally [15] and theoretically [16, 17]. This heterogeneity can lead to molecules or regions that, being only separated a few nanometers from each other, might exhibit relaxation times that differ by orders of magnitude [14].

1.1.4 Stokes-Einstein violation

Dynamic heterogeneity is also thought to be the cause of another interesting phenomenon occurring in deeply cooled liquids. At high temperatures, in a liquid which is above $1.2T_g$, the Stokes-Einstein (SE) relationship links the diffusion coefficient, D, with temperature and the inverse of viscosity [11]

$$D \sim \frac{T}{\eta} \tag{1.9}$$

However, at approximately $1.2T_g$ and below a decoupling between the translational diffusion coefficient, D_t, and the viscosity occurs. The same happens between the rotational diffusion, D_r, and the translational diffusion [14, 18]. Close to the glass transition, the coefficient D_t can be orders of magnitude higher than the T/η ratio, a difference that is far more accentuated as the temperature is lowered [19]. Among the several authors linking the violation of the SE relationship with the dynamic heterogeneity, Cicerone and Ediger [18] provide a simple and convincing argument. It basically states, providing that there is dynamic heterogeneity, that the diffusion dominates in the faster clusters while the relaxation time does in the slower ones. The conclusion one arrives is that $D >> 1/\tau_R$, being the diffusion a much faster process and completely decoupled from the relaxation times.

1.1.5 Two-step relaxation

There is yet another decoupling that occurs in the moderately supercooled range, as we approach to T_g from the SCL. At high temperatures, the correlation function $C(t)$ exhibits a single nonexponential behaviour as described by equation 1.8 (see Figure 1.4). However, as the temperature is lowered, a plateau emerges and the relaxation can no longer be explained by a single relaxation process. This kind of relaxation is called *two-step relaxation*.

The two-step relaxation mechanism is also a characteristic fingerprint telling us that we are approaching the glass transition. Experimentally, this mechanism is often measured and quantified using dielectric relaxation spectroscopy. The first and rapid relaxation corresponds to the β-relaxation and is related to the vibration of the molecules around a more or less fixed position in the *frozen matrix* and exhibits and Arrhenius behaviour with temperature. The slower relaxation that appears after the plateau (Figure 1.4) is the so-called α-relaxation. This process accounts for the particles seeking the thermodynamic equilibrium and moving across the *frozen matrix*. Since the relaxation in supercooled liquid has two characteristic timescales, it should be specified which one

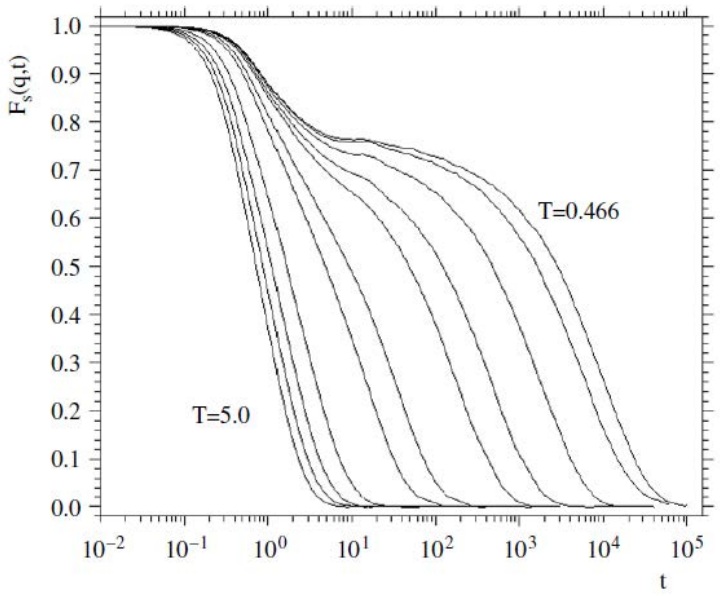

Figure 1.4: Two-step relaxation. The dynamical correlation function (arbitrary) as a function of time. In this case, the temperature is given in computational units. At high temperatures ($T = 5$) there is a single nonexponential function. As the temperature increases, the relaxation takes place via two relaxation processes. Reprinted from [11].

we are referring to when talking about relaxation time. It is generally assumed that τ_R of a liquid is the α-relaxation time, τ_α, since it is the largest.

1.1.6 The Kauzmann entropy crisis

In 1948, Kauzmann showed how the extrapolation of the supercooled liquid entropy to lower temperatures would reach a point at which its entropy would become equal to that of the crystal and eventually negative upon further cooling, at a non-zero temperature. This paradox is named the Kauzmann entropy crisis. The Kauzmann temperature, T_K, is defined as the temperature at which the difference in specific heat between the crystal and the liquid vanishes. Going back to Figure 1.1, and considering now the y-axis as the entropy, the rate at which entropy changes with temperature is given by

$$\left(\frac{\partial s}{\partial T}\right)_p = \frac{c_p}{T} \tag{1.10}$$

Therefore, the entropy crisis starts because the specific heat of the liquid is larger than that of the crystal. The Kauzmann paradox is far more accentuated for fragile glass-forming liquids rather than for strong ones, due to their higher specific heat of the supercooled liquid with respect to the glass. The T_K in fragile systems often falls not far from the glass transition. On the contrary, in strong liquids, the extrapolation of the entropy of the liquid yields T_K's already close to absolute zero.

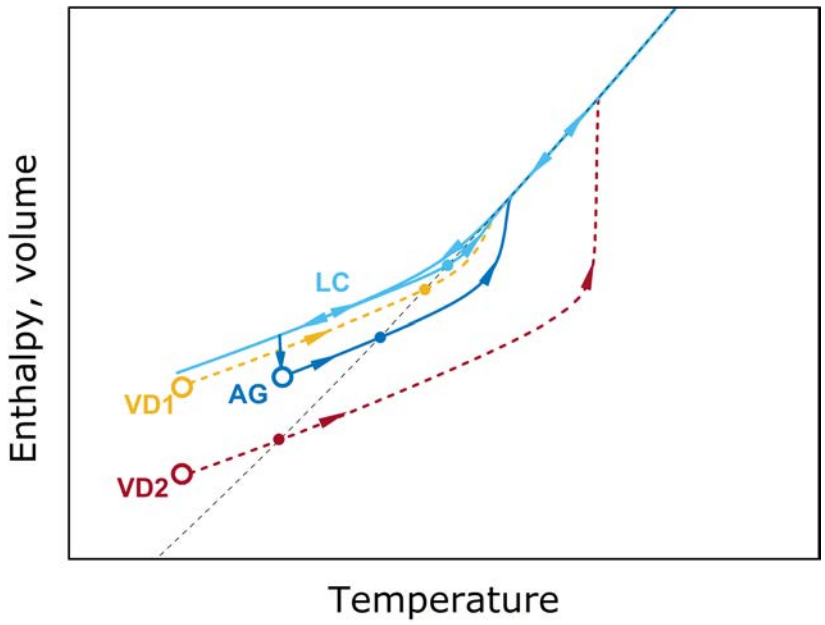

Figure 1.5: Sketch of the possible routes to obtain higher stability glasses. The light blue curve represents the enthalpy evolution during the cooling and subsequent heating of liquid-cooled (LC) glass, the arrows represent the path followed. The dark blue curve (AG) accounts for the ageing for a given time of a glass and subsequent heating. The dashed lines correspond to vapour-deposited glasses (VD1 and VD2), starting from their initial enthalpic state (see Section 1.2). Since they are not created from the liquid, there is no "cooling" path. The dashed black line is the extrapolated supercooled liquid enthalpy which defines the limiting fictive temperature when crossing the enthalpic paths of the different prepared glasses.

1.1.7 Glass stability and limiting fictive temperature

As we have already discussed, the experimentally observed glass transition is a purely dynamic event that leaves the system in an out-of-equilibrium state. Therefore, once the glass is formed, it will continuously evolve towards its *equilibrium state*, in this case, the supercooled liquid phase. The process by which a glass relaxes towards a more stable configuration due to an isothermal treatment below T_g is called physical ageing. This process is of vital importance for many "high performance" applications, in which materials' properties in their glassy form can evolve over time, especially when used at temperatures which correspond to large fractions of their glass transition temperature [20].

Figure 1.5 shows, schematically, the route towards equilibrium for a physical ageing at a given temperature T. During the ageing, the enthalpy of the system will decrease with time following a nonexponential increasing timescale. The initial enthalpic state of the system before the ageing strongly depends on how we have created the glass. Glasses prepared by cooling the liquid will be trapped in different locations in the energy landscape depending on the cooling path followed.

For instance, let's consider the three cooling routes shown in Figure 1.1; in a first and fast cooling (yellow line) the system falls out of the equilibrium at $T_{g,1}$. On the other hand, by using slower cooling rates (orange and blue lines), the system will have more time to equilibrate at a given temperature and will fall out of equilibrium at lower temperatures, $T_{g,2}$ and $T_{g,3}$, respectively. Therefore, the lower the cooling rate, the lower the glass transition. However, the sharp increase in the relaxation times of the supercooled liquids—especially on fragile liquids—will confine the measured T_g in a narrow range of temperatures, e.g. the T_g changes between 3-5 K for an order of magnitude change in the cooling rate [18]. This fact precludes the formation of highly stable glasses—and crystallisation—within human timescales by cooling or ageing processes.

The fictive temperature, T_f, is a useful parameter to describe the progress of the glass to lower energy states. This temperature is defined as the temperature at which a property of the glass (enthalpy, volume) is equal to that of the supercooled liquid. At temperatures above the glass transition, the T_f is equal to the physical temperature, as we are in equilibrium. As the system is cooled, the fictive temperature starts departing from equilibrium being $T_f > T$. At lower temperatures, the system will be completely arrested reaching a final value of T_f well above the physical temperature. This value is called the limiting fictive temperature (T'_f) [21]. In the cooling scheme shown in Figure 1.1, the T'_f coincides typically with the glass transition, obtained from the crossover between the glass enthalpy and the liquid enthalpy. On the other hand, Figure 1.5 represents the enthalpy path followed during a heating scan for glasses prepared using different routes together with the limiting fictive temperature of each one of them. For instance, the aged glass prepared at the same cooling rate as the liquid cooled (LC) glass (light-blue curve at Figure 1.5) but physically aged at a temperature T_a will have a lower value of T'_f. The fictive temperature of the glass depends on its thermal history and the physical temperature of the system as sketched in Figure 1.5. The vapour-deposited glasses sketched in this same figure will be discussed in Section 1.2.

1.1.8 Measuring the glass transition temperature: the heat capacity

The glass transition temperature can be studied using a wide variety of techniques [22] by measuring properties such as the thermal expansion coefficient, the density, the viscosity or the heat capacity. The latter is probably one of the most broadly used magnitudes to measure the T_g. The heat capacity measures the amount of heat needed to raise the system's temperature by one Kelvin. The heat refers to the amount of energy transferred into a system other than work and matter. The heat capacity, as an extensive property, depends on the size of the system. The magnitude usually used is the specific heat capacity or, simply, the specific heat, which is the heat capacity per unit mass. The specific heat depends on the number of degrees of freedom available in a

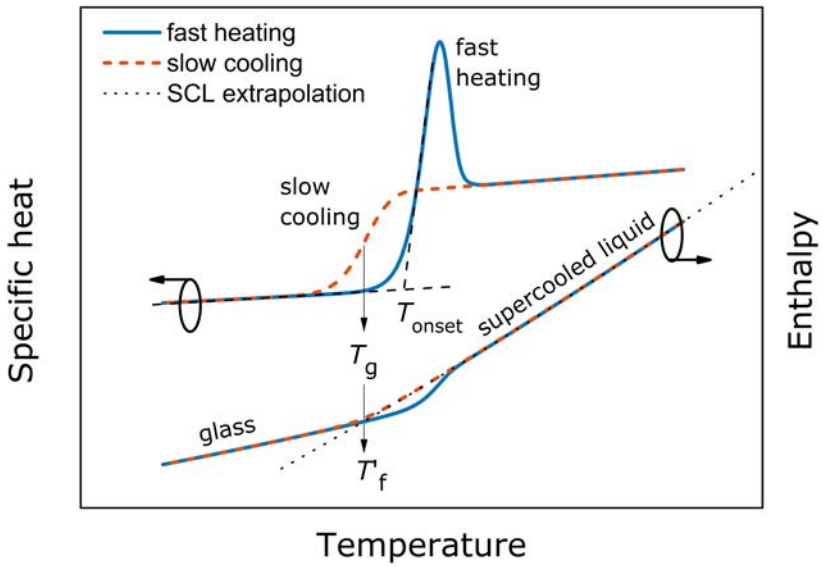

Figure 1.6: Schematic representation of the specific heat during a slow cooling (upper dashed line) and a faster heating scan (continuous upper line). The lower curves represent the corresponding enthalpy during the same cooling and heating procedure. The dashed curve corresponds to the SCL extrapolation line in the enthalpy representation. The different relevant temperatures are indicated in the sketch.

system. Whereas a gas has translational, rotational and vibrational degrees of freedom, a solid typically only has the vibrational ones, although some other contributions might be present in this case—such as magnetic or electronic ones.

Calorimetry is the science or act of measuring the amount of heat exchanged between a sample during a thermal process, giving access to kinetic and thermodynamic information of the materials' state. Information such as heat capacity, enthalpy, entropy or phase transition temperatures can be obtained. As we have already seen, during the glass transition there is a jump in the specific heat due to a sudden reduction in the number of available states. Typically, the heat capacity (at constant pressure) measurements in glasses are performed during heating temperature ramps. What is usually measured, then, is the devitrification of the glass rather than its formation.

From the heat capacity signature during the devitrification of a glass, several kinetic and thermodynamic properties can be readily obtained. Figure 1.6 summarises some of the key features from a specific heat scan. The temperature at which the devitrification takes place is the onset temperature (T_{on}) of devitrification. This temperature depends on the kinetics of the experiment. When the heating rate is low, the system has more time to relax towards the equilibrium at each *temperature step* so the onset temperature will finally be lower than during a faster heating rate scan. When the heating rate and cooling rate are the same, then the glass transition and the onset temperature typically coincide (assuming the ageing effects below T_g are negligible, otherwise there would be hysteresis effects). That is because the same relaxation path is followed both in cooling

and heating. On the other hand, when the heating rate is higher than the cooling, the onset temperature will be shifted to higher temperatures as the system will not have the same amount of time to relax towards the SCL equilibrium.

Now, for the same heating rate, the onset temperature will scale with the kinetic stability of the glass. In a more stable glass, higher temperatures (or times) are needed to dislodge the molecules from their glassy configurations. Besides the jump in specific heat, the heating scan can also be characterised by a peak overshoot, as seen in Figure 1.6. The area of this peak is the excess of enthalpy that the system needs to return to the SCL equilibrium state and it is related to the thermodynamic stability of the glass. The parameter to quantify the thermodynamic stability is the (enthalpic) limiting fictive temperature. In that case the lower the T_f', the higher the thermodynamic stability of the glass.

In practice, the enthalpic limiting fictive temperature can be obtained from the specific heat data in a heating scan. First, the specific heat is integrated with respect to temperature obtaining the enthalpy (see equation 1.2). Then, the enthalpy line for the supercooled liquid is extrapolated until it intersects with the integrated enthalpic curve at T_f'. Figure 1.6 schematically describes the obtaining of the T_f' in a heating scan, equivalently as it is done for a cooling measurement.

1.2 Physical vapour-deposited glasses

Up to now, we have only considered the possibility of creating a glass upon a cooling process from the liquid phase. There are, however, other routes to obtain amorphous solids, such as milling —widely used for pharmaceutical drugs [6]— or physical vapour deposition. Different techniques such as sputtering deposition, electron beam deposition or thermal evaporation allow to vapour-depositing glasses. Thermal evaporation was the technique employed by Hikawa et al. [23] in one of the first works on vapour-deposited glasses. In this work, they prepared VD glasses at substrate temperatures corresponding to the 41 % and 69 % of the glass transition of the material, the organic liquid butyronitrile with $T_g = 97\,\mathrm{K}$, and compared their thermal response with a conventional glass prepared from the liquid. They found that the devitrification temperature of the VD glasses was the same for both vapour-deposited glasses and the glass cooled from the liquid. However, they also discovered that the sample deposited at $0.41T_g$ showed a much higher configurational enthalpy than the sample cooled from the liquid while the sample deposited at $0.69T_g$ lied in-between. They also traced the spontaneous heat evolution during a heating experiment, which is related to the enthalpy relaxation in an ageing process. The VD samples were unstable and released large amounts of enthalpy compared to the liquid cooled sample, even well below the T_g. They concluded that the molecules deposited on the cold substrate were arrested as

they arrived, so the glass got trapped in an entirely different and less stable configuration than the LC sample. Later on, similar results were obtained in other systems, such as 1-pentacene, where the authors concluded, and quoting: "*This [higher configuration enthalpy and entropy] indicates that the VQ [vapour-quenched] glass possesses much locally-strained and disordered structure compared with the LQ [liquid-quenched] glass*"[24]. The idea of vapour-deposited glasses (at low temperatures) being less stable than the ones cooled from the liquid was extended as a general behaviour to all simple glass-forming molecules and all deposition temperatures.

In stark contrast to that view, in 2007, physical vapour deposition settled in as an alternative way to effectively prepare glasses with significantly enhanced properties compared to the liquid cooled ones. Swallen et al. [10] reported how the kinetic restrictions of the drastic slowdown suffered when cooling a liquid could be bypassed by vapour-depositing the material at the optimal conditions achieving, thus, glasses which were much deeper in the potential energy landscape. They used differential scanning calorimetry to examine the kinetics and thermodynamics of PVD glasses of the molecular organic glass-formers 1,3-bis-(1-naphthyl)-5-(2-naphthyl)benzene (TNB) and indomethacin (IMC). When the substrate temperature during the deposition (T_{dep}) was held at $\sim 0.85 T_g$ and using low growth rates of $5\,\mathrm{nm\,s^{-1}}$, glasses with surprisingly low limiting fictive temperatures (high thermodynamic stability) and high devitrification onsets (high kinetic stability) were achieved. In Figure 1.5, the enthalpy of vapour-deposited glass versus temperature is sketched for a heating scan together with the enthalpy paths for LC glasses.

As an example, Figure 1.7 shows the calorimetric trace of the devitrification for three differently prepared glasses of an organic molecule—TPD— measured by differential scanning calorimetry. The glass exhibiting the lowest onset for the glass transition and the smallest overshoot is the glass prepared from the liquid by cooling it at $10\,\mathrm{K\,min^{-1}}$. On the other hand, the two glasses prepared from the vapour phase at deposition temperatures of $0.86 T_g$ and $0.90 T_g$ and growth rates of $0.2\,\mathrm{nm\,s^{-1}}$, exhibit much higher onset temperatures and overshoot, indicating a substantial increase of the kinetic and thermodynamic stabilities.

1.2.1 Stable glass formation mechanism

The mechanism initially proposed by Swallen et al. [10] for the formation of these stable glasses is based on the higher molecular mobility at the surface compared to the bulk. The existence of enhanced surface dynamics—in the form of a highly-mobile layer—has been proven in many systems, from polymers [25] to these same molecular glass-formers systems [26, 27]. For instance, Zhu et al. [27] found that the surface self-diffusion can be up to 10^6 times greater than the self-diffusion in the bulk.

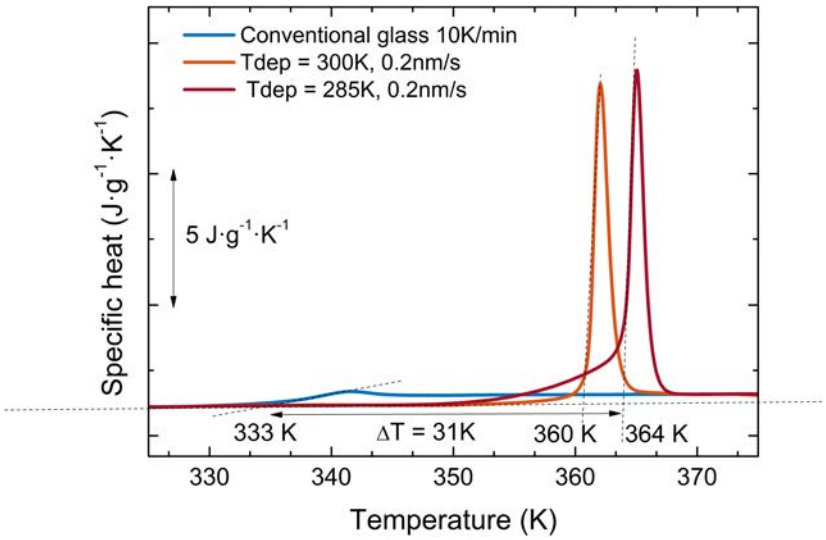

Figure 1.7: Calorimetric trace of the devitrification of three differently prepared glasses of TPD ($T_g = 333\,\mathrm{K}$), an organic semiconductor hole transport molecule. CG stands for conventional glass, which is the glass prepared from the liquid. T_{dep} stands for deposition temperature of the vapour-deposited glasses at the indicated growth rate. The dashed lines indicate the determination of the onset temperatures.

When the vapour-deposited molecules arrive at the substrate—at a given T below T_g—they get into this high-mobility surface layer. This mobility allows them to sample their best configurations in their potential energy landscape according to the temperature of the substrate during the deposition. If the deposition rate is low enough, these molecules can find a favourable configuration before being buried into the bulk by the subsequent incoming molecules. If the deposition rate is too fast, the molecules get trapped into the slow dynamics of the bulk before having time to explore a significant fraction of the configurational space and, therefore, a less stable glass is produced. Typically, when the deposition rate is below $0.5\,\mathrm{nm\,s^{-1}}$, the stability is no longer improved since molecules have "time enough" for the configurational sampling, as seen by different molecular glass-formers [28–30].

The other factor controlling the formation of these glasses is the substrate temperature. Close to T_g, the mobility is high enough so the molecules can find the equilibrium at the corresponding temperature. When the temperature is lowered, the mobility is reduced but also the configurational phase space. Therefore, the stability will increase as the substrate temperature is decreased until the molecules can no longer equilibrate: the mobility will be too low and the equilibration times will exceed the laboratory timescale. Experimentally, this temperature is found to be $\sim 0.85 T_g$ for most vapour-deposited glass-formers, as an indication of a universal behaviour. The glasses deposited below this temperature will be less stable; the molecules will get trapped as they arrive at the surface, being able to explore fewer and fewer fractions of the phase space as temperature decreases.

Very recently, Ngai et al. [31] have linked the stable glass formation with the β-relaxation (particularly a subtype of β-relaxation called Johari-Goldstein relaxation). They rationalise it in terms of a secondary glass transition, $T_{g,\beta}$, which they define as the temperature at which the β-relaxation time is equal to 1000 s—equivalently yo the standard T_g and the α-relaxation[1]. They found this temperature to be a good indicator of the enhancement of the surface diffusion and, therefore, the capability to form a stable glass. This is still a hot topic since recent data seem to suggest that stable glasses can also be formed even in molecular systems with very low-surface mobilities [32].

1.2.2 Highly stable glass properties

Originally, in reference [10] from 2007, higher thermal and kinetic stability were reported for glasses of IMC and TNB when deposited at $0.85T_g$. Since then, highly stable glasses of many other systems (mostly organic) have been produced and their different properties measured using a broad variety of techniques. Here we list the most outstanding characteristics that vapour-deposited glasses exhibit, which have been measured for various materials:

- *Higher kinetic stability and lower enthalpies* have been seen by differential scanning calorimetry [28, 33, 34], fast-scanning nanocalorimetry [29, 34], alternating current nanocalorimetry [35, 36], dielectric relaxation spectroscopy [37, 38], ellipsometry [39, 40], second ion mass spectrometry (SIMS) [41, 42] or inert gas permeation [43] among other techniques. Related to the kinetic stability, highly stable glasses require up to 10^5 times the structural relaxation time of the supercooled liquid to fully transform [41].
- *Higher densities*: glasses prepared at $0.85T_g$ can be up to 1.5 % denser than the conventional glass, density variations scale with stability [39, 40, 44, 45]. This variation as a function of T_{dep} have been reported using mainly ellipsometry, but also other light interference techniques [46] and X-ray reflectivity measurements [10].
- *Enhanced mechanical properties*, such as higher mechanical moduli and higher longitudinal sound velocities can also be achieved by properly setting the deposition conditions [39, 47, 48].
- *Lower heat capacities*, lower expansion coefficient and increased resistance to water uptake have also been reported for different systems [36, 44, 49].

[1] We have defined before this time to be 100 s. Since it is a convention, there is no exact definition and some authors prefer to use 1000 s instead. Anyhow, the accepted range lie between these two values.

- *Suppression of β-relaxation*, it has only been reported on toluene, n-propanol and 2-picoline using dielectric relaxation spectroscopy[50]. More recently, it has been also shown for the pharmaceutical drug etoricoxib[51].
- *Different anisotropic packing* that depends on the ratio T_{dep}/T_g at which the glass is deposited. The degree of molecular orientation and its direction (horizontal or vertical) strongly depends also on the molecular shape. Techniques such as X-ray diffraction [52], ellipsometry using birefringence modelling [44, 45] or dichroism measurements [45] have been used to quantify the anisotropy of these glasses.
- *Heterogeneous transformation mechanism*, which is maybe one of the most exceptional features of vapour-deposited glasses. While conventional glasses transform via a homogenous process, taking place at the whole volume, in VD stable glasses the transformation takes place via a surface-initiated growth front that propagates into the bulk. This mechanism has been directly and indirectly observed or inferred using several techniques [34, 40–42, 53, 54].
- *Suppression of the two-level systems*, a feature that was considered to be universal among all glasses at very low temperatures but that has not been observed in indomethacin ultrastable glasses [55].

Most of the systems that have been reported to form ultrastable glasses are organic molecules: from simple aromatic hydrocarbons (toluene [29, 30, 35, 43, 46, 53], ethylbenzene [29, 30, 35, 43, 46, 56], propylbenzene [46] or isopropylbenzene [46] among others), pharmaceutical drugs (indomethacin [10, 34], celecoxib [33] and others [57]), general well-known molecular glass-formers (TNB [44], cis/trans-decalin mixtures [58], o-terphenyl [59], tetrachloromethane [60]) to organic semiconductor molecules (TPD, α-NPD or DSA-Ph [45]). More recently some studies on ultrastable metallic glasses [61] and polymers can also be found [62].

Ultrastable glasses have also been produced by computer simulations. In 2010, Léonard and Harrowell [63] used a minimalist model of cooperative dynamics, the facilitated kinetic Ising model, to reproduce the ultrastable glasses produced by PVD. Using this simple spin model, they could produce ultrastable glass films that exhibit a front-like transformation to the supercooled liquid, just as seen experimentally. The melting of ultrastable glasses using this dynamic facilitation point of view have also been addressed by Gutiérrez and Garrahan [64], who specifically addressed the competition between the bulk and surface transformation mechanisms. Other different approaches to mimic ultrastable glasses have also been proposed in molecular dynamics simulations, such as vapour-depositing Lennard-Jones particles one by one [65], random pinning [66] and particle swapping [67], overcoming in different ways the difficulty of producing in silico VD stable glasses because of the large computational times involved.

Vapour-deposited ultrastable glasses have opened a new route to gain access to glasses with properties equivalent to liquid cooled glasses aged for millions of years [10]. They are good candidates to explore the possibility of experimentally determining how the Kauzmann entropy crisis can be avoided [28].

The role of fragility in the ability to form highly stable glasses has also been considerably discussed. A common feature of the most stable glasses is their fragile nature, and some authors have attempted to establish a straight correlation between these two characteristics [61, 68]. This interpretation contrasts with recent results with two less fragile organic glass-formers (methyl-m-toluate and ethylcyclohexane), which can also be prepared in a stable form [38, 69]. The anisotropic packing, which is also a common feature in many organic PVD glasses, leads to the discussion of the role that the asymmetry in the molecular structure has in the formation of ultrastable glasses. However, recently Chua et al. [60] have been able to produce stable glasses of tetrachloromethane, which has a nearly spherical structure. Therefore, they ruled out the anisotropy as a prerequisite for the ultrastable glass formation.

As we have seen, there is still an ongoing debate on the mechanisms and characteristics behind the vapour-deposited glasses that, at the same time, can provide further insights into the glass transition science. This work is committed to contribute to the understanding of the striking properties of these glasses and their possible applications in a specific area: the organic light-emitting diodes.

Chapter 2

Experimental methods

In this chapter, we describe the basic methodology followed in this study, covering from the samples' preparation to their characterisation. This work is based on vapour-deposited organic glasses. Hence, the experimental setup and the materials used in this work are firstly described. Secondly, the charaterisation techniques are presented. The deposited organic samples have been characterised in situ using membrane-based microfabricated sensors that have been developed at GNaM's group. Quasi-adiabatic fast-scanning nanocalorimetry and 3ω–Völklein technique working principles are addressed together with a brief description of the well-established 3ω method.

2.1 Experimental setup for physical vapour deposition

Physical vapour deposition is a process where a material, either liquid or solid, is vaporised and transported through a vacuum or low-pressure environment in its basic units—atoms or molecules—to a substrate, where it condensates. PVD processes are typically used to prepare thin films with thicknesses than can range from a few atoms to thousands of nanometers. There exist several PVD techniques that are used to prepare films of different natures, from various single elements such gold, zinc, aluminium or silicon (both in crystalline or amorphous forms), alloys such as indium tin oxide or organic molecules such as has been done in this work. These thin films are later used for several technological and research purposes such as single and multi-layered coatings, optical films, decorative coatings, corrosion-resistance films, electrically insulating layers in microfabrication processes, active layers in organic electronic devices among many others [70]. Among the different methods for PVD processing, the main ones are sputter deposition, arc vapour deposition, ion plating and vacuum deposition. The latter, also called vacuum evaporation, is the method used in this work to evaporate different organic materials. Vacuum evaporation is a PVD process in which the source material is thermally evaporated so that the molecules or atoms travel from the vaporisation source to the substrate without any (or few) collisions with the residual gas molecules

2.1.1 Vacuum evaporation

To achieve a long mean free path of the molecules or atoms, vacuum deposition normally requires vacuum levels better than 10^{-4} mbar. For example, at 10^{-6} mbar the mean free path of a molecule is already about 5 m and the time needed for the residual species to form a monolayer at room temperature is about one second. Therefore, when the film contamination is a problem (as it can be in organic films) higher vacuum conditions are needed. The high vacuum (HV) levels needed for thermal evaporation are achieved in this work by using a turbomolecular pump attached to a dry scroll pump. Using this configuration ultra-high vacuum (UHV) levels between 10^{-7} and 10^{-8} mbar are attained within a few hours. Moreover, we have used the concept of *cold trap* to further reduce the base pressure of the chambers. It consists on a specially designed copper recipient which can be filled with liquid nitrogen (LN2) from the outside and, therefore, be refrigerated to 77 K (LN2 boiling point at ambient pressure). In the inner part, the copper surface is maximised using copper disks. Due to the condensation on the cold trap surface of water (and possibly other atmospheric constituents), the pressure of the chamber can decrease up to an order of magnitude, reaching up to 10^{-8} and 10^{-9} mbar vacuum levels.

The vapour pressure of a given material strongly depends on the temperature, which is, therefore, a crucial parameter to set a given evaporation rate. It is generally assumed that the minimal value of vapour pressure necessary to achieve a useful deposition rate is around 10^{-2} mbar [71]. In that sense, materials that exhibit this value of vapour pressure at the solid phase are considered sublimating materials whereas materials that achieve this value at their liquid phase are described as evaporating materials.

The vaporisation sources used to create the material flux will depend on the characteristics of the materials at room temperature; essentially whether they are liquid or solid. For instance, the aromatic hydrocarbon toluene used in this work is liquid at room temperature, with a vapour pressure—35 mbar—high enough to be directly injected into a UHV chamber. If that is the case, the liquid is loaded in a high vacuum pre-chamber, and the deposition rate is controlled using a high precision valve. On the other hand, the other materials used in this work are solid at room temperature and normally found in their powder crystalline form. These materials need to be heated above—or near—their melting point to achieve the necessary vapour pressures to give useful deposition rates. To do so, we have used effusion cells that allow an accurate control of the temperature and, therefore, of the vapour pressure and the deposition rate of the heated materials. Those evaporators consist basically of a crucible (metallic or quartz) where the materials are loaded and subsequently heated radiatively throughout via a hot filament, achieving highly uniform temperature profiles across the cell.

Vacuum chambers can be equipped with multiple accessories that are needed either

for film deposition or in situ characterisation. Here, we briefly describe the essential elements that are used in our setups before presenting the specific setup employed in this work.

For instance, the deposition rate is an important variable in PVD processes and especially for vapour deposited glasses, since it is one of the key parameters to control the stability of the glassy deposited films, as seen in Chapter 1. A quartz crystal microbalance (QCM) monitor is used to measure the real-time in situ deposition rate. This technique relies on the piezoelectricity of the quartz single crystal and the change of its natural resonant frequency as mass is deposited on top of the crystal surface. By properly calibrating the QCM, it is possible to measure the deposition rate and the total amount of mass deposited on top of a given substrate. In this work, typical evaporation rates between $0.01\,\mathrm{nm\,s^{-1}}$ and $0.4\,\mathrm{nm\,s^{-1}}$ have been used.

Another indispensable element that a PVD chamber must have is a moveable shutter, which is used to intercept the particles on their way from the vapour source to the sample's substrate. Shutters are employed to protect the sample from contamination while degassing the source, to control the deposition time, to protect the sample while a uniform deposition rate is established or for preparing multilayers.

Sometimes it is necessary to control the temperature of the substrate during the evaporation of the films. For instance, as we have seen in Chapter 1, the deposition temperature plays a fundamental role in setting the properties of vapour deposited organic glass layers. In this work, a control of the substrate temperature is also necessary to calibrate and perform the in-situ measurements with the sensors placed on this same substrate, as it is thoroughly described in the following sections. Therefore, the chamber must also be equipped with liquid feedthroughs to act as a heating/cooling system or simply as a heat reservoir together with heating elements for a more precise temperature control.

Finally, besides the liquid feedthroughs, the vacuum chamber must be equipped with electrical feedthroughs that can be used either for power supply (e.g. the resistive heating) or for sensing purposes (e.g. signal measurement).

2.1.2 Evaporation chambers

Two different UHV evaporation chambers have been used during this work. Figure 2.1 shows a picture of the two used setups. Both chambers have been adapted to fulfil the requirements of each experiment. Chamber A is equipped with an effusion cell which allows evaporating materials that are solid at ambient temperature by heating and increasing their vapour pressure. On the other hand, Chamber B was initially equipped with a pre-chamber and a leak valve that allowed to evaporate materials that

are liquid at room temperature. This chamber was later equipped with two effusion cells so multilayers of different materials could be evaporated without breaking the vacuum.

Both UHV chambers have the same elements in common connected to their different ports:

(i) A dry scroll pump Varian SH-110 for generating the primary vacuum, down to 6×10^{-2} mbar.

(ii) A turbomolecular pump Varian Turbo-V 301 for generating the ultra-high vacuum, down to $\sim 2 \times 10^{-8}$ mbar. A smaller turbomolecular pump Varian Turbo-V 81-T is used in the pre-chamber of B.

(iii) A liquid nitrogen (LN2) cold trap is installed on top of both chambers. In chamber B, the cold trap is also used as a cold source and sample holder (later explained).

(iv) A hot cathode Bayard-Alpert gauge to measure the pressure.

(v) A commercial quartz crystal microbalance (QCM) monitor from Sycon Instruments. Although the head of the crystal is placed near the sample, a proper calibration needs to be performed to determine the ratio between the thickness read by the QCM and the real thickness evaporated at the sample's position. This is regularly done by measuring control samples using standard profilometry. The mass, when possible, is inferred from the heat capacity measurements.

(vi) A movement feedthrough, either with linear or rotatory motion. At the end of this feedthrough a shutter blade is placed to protect the sample from the incoming particle flux when necessary—i.e. while stabilising the rate, temperature or in-between different sample depositions.

(vii) An electrical feedthrough for sensing and controlling purposes.

2.1.3 Evaporators

As previously described, the requirement for physical vapour deposition is to have the corresponding material with sufficient vapour pressure.

Chamber B was initially used for materials that are liquid at room temperature, such as toluene. The liquid to be evaporated is placed in a Pyrex container and put in a pre-chamber. The liquid container is coupled with the UHV pre-chamber by opening the valve. If the liquid vapour pressure is high enough at ambient pressure (as it is for toluene), the vapour can be introduced to the UHV main chamber through a high-precision leak valve. Otherwise, the pre-chamber can be heated to increase the liquid vapour pressure of the corresponding material. The high-precision leak valve allows a

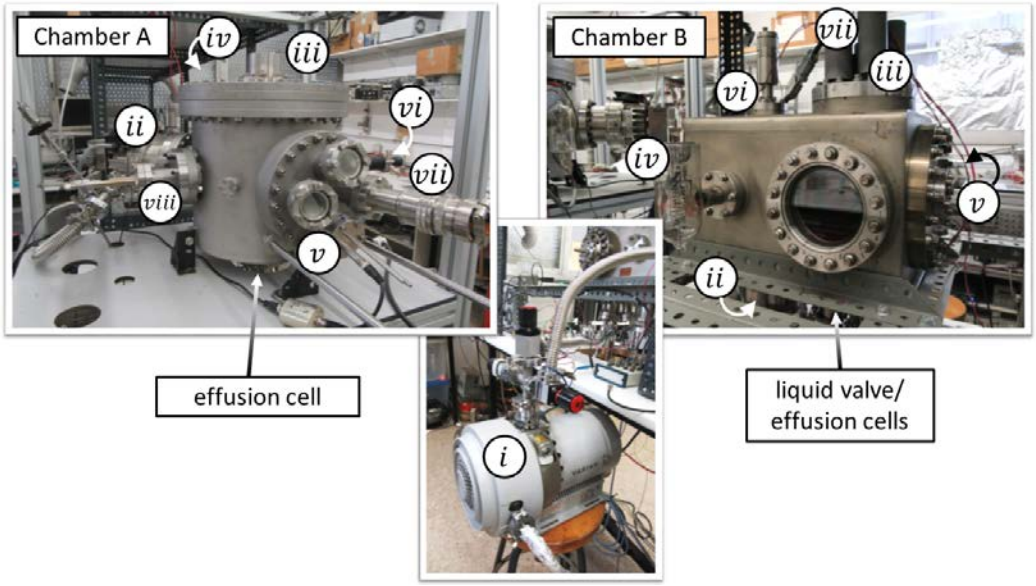

Figure 2.1: Photographs of the experimental vacuum chambers (A and B) used in this work. The major components are numbered. (i) Primary scroll-pump, (ii) turbomolecular pumps, (iii) cold trap, (iv) pressure sensor, (v) quartz crystal microbalance, (vi) movement feedthroughs and (vii) electrical feedthroughs.

fine tuning of the amount of vapour entering the main chamber and, therefore, the rate at which the material is arriving at the substrate. Connected to the leak valve, there is a copper pipe with an opening of 4 mm that leads the vapour directly to the sensor. The end of the pipe is placed 2 cm away from the substrate and centred to the position of the sensor device (the sample nanocalorimeter in this case). The distance and the wide opening of the pipe allow part of the material to arrive at the QCM for monitoring the rate. Figure 2.2 shows a sketch of part of the setup.

Both chambers are equipped with low-temperature effusion cells for the evaporation of materials that are solid at room temperature. These effusion cells consist basically of a crucible—stainless steel or quartz—where the raw material is loaded. The crucible is heated by radiation using hot tantalum filaments until the material starts evaporating or sublimating. A Createc low-temperature effusion cell with a stainless-steel crucible and an organic material effusion cell (OME) from MBE Komponenten with a quartz crucible were used in this work. The temperature of both cells was monitored through a K-type thermocouple and controlled with a power source and a PID system. Chamber B, was equipped with both effusion cells in a costume-designed flange to adapt the direction of each cell flux to the same focal point.

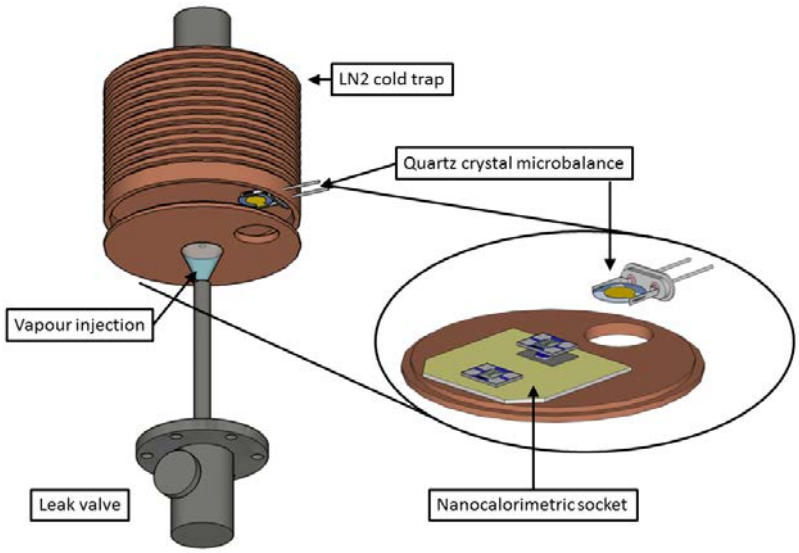

Figure 2.2: Sketch of the toluene evaporation setup showing the leak-valve and LN2 cold trap.

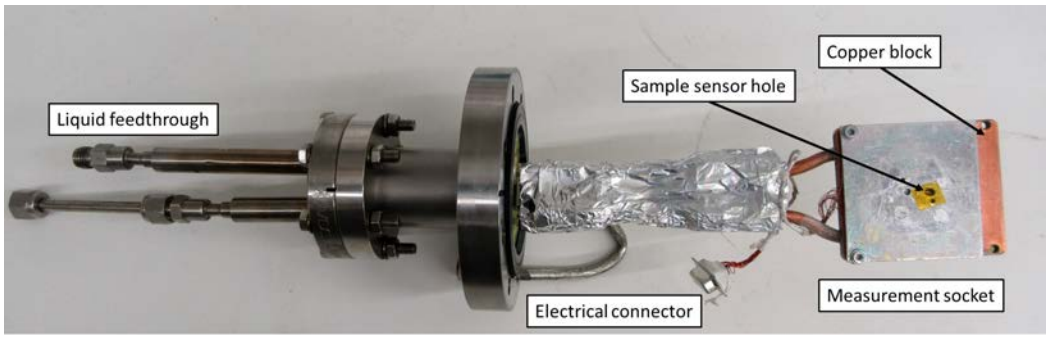

Figure 2.3: Photograph of the sample holder used in chamber A with the various elements labelled.

2.1.4 Sample holders

The sample holder is where the temperature controlled socket with the sensing devices is located. The sample holder must be refrigerated to act as a controlled bath (heat sink) temperature from which the sample's socket can be heated, or just cooled. This is achieved in two different ways in the two chambers.

Chamber A has a holder-arm (Figure 2.3) consisting of a liquid feedthrough in which a copper block is attached and welded to an extreme for a good thermal link. The copper block serves as a holder for the sample's socket while the liquid feedthrough provides the cooling to the system. Depending on the minimum temperature desired, a refrigerant liquid or liquid nitrogen can be circulated through this piece. In chamber B, the LN2 cold trap is also acting as a heat sink. At the bottom of the trap (as sketched in Figure 2.2) a copper cover can be attached with screws and, therefore, be at the same

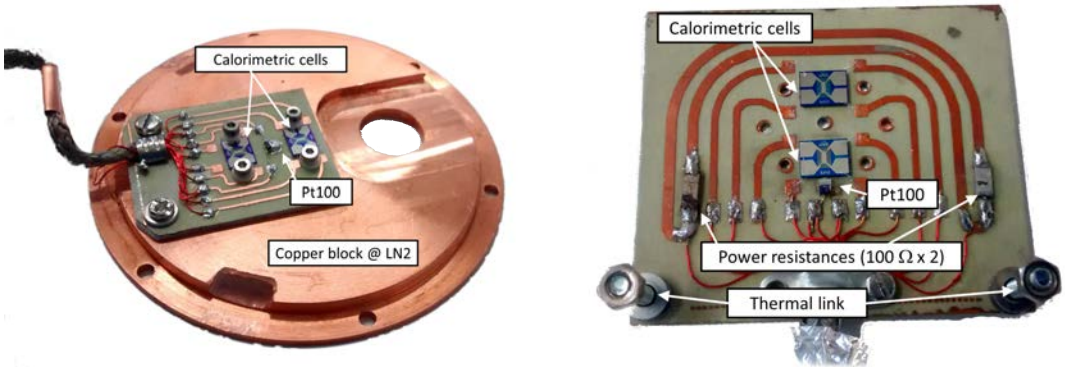

(a) The socket completely linked to the copper block at LN2. The sensors/chips placed on this socket must be previously calibrated in another setup.

(b) Socket with temperature control thanks to the two heaters added to the circuit.

Figure 2.4: Photograph of the measurement sockets used in this work.

temperature as the cold trap, i.e. ~ 77 K.

2.1.5 Sockets

The different microfabricated sensing devices—nanocalorimeters and the 3ω–Völklein sensors—are placed in different costume-built measuring sockets to control the temperature at which the samples are deposited and to extract the electrical signals from the measurement. The sockets are fabricated using a single sided photoresist board. The typical circuit used is shown in Figure 2.4, basically consisting of twelve tracks to connect in a 4-wire configuration the sample device, the reference device and the temperature sensor, which is a cryogenic Pt100.

The socket in Figure 2.4a, which is directly attached to the copper cover of the LN2 cold trap, was used in chamber B for the characterisation of toluene. Since the nanocalorimeters had been pre-calibrated in a cryostat, there was no need for heating elements. The sample was deposited directly on the sensing area of the nanocalorimeter which was fed with a suitable constant current that raised the temperature up to the desired value (see Section 2.3.4).

The socket in Figure 2.4b, which has two extra tracks used to fed the heater resistances, is used in chamber A. The two screws indicated in Figure 2.4b provide the thermal link to the copper block, which is set at a reference temperature. The temperature control is later performed by a home-made LabView PID software. A similar socket with a temperature control was also made for chamber B for the deposition of room-temperature solid materials.

2.1.6 Materials

Five different materials have been used in this work for thin film deposition and subsequent measurement of their thermal properties. The organic solvent toluene was first used as a model glass-former. Since it is liquid at room temperature and it has a high vapour pressure (38 mbar) its vapour can be directly injected into the UHV chamber with the previously described setup. Anhydrous toluene (purity 99.8 %) dried over molecular sieves and packaged under an argon atmosphere was purchased from Cymit Quimica and placed in a Pyrex container which was afterwards connected to a high vacuum pre-chamber. Extra purification of the source material was achieved by applying several sequences of freeze–pump–thaw cycles [29]. Figure 2.5a shows the chemical structure for toluene.

Most of the experiments have been performed with the two organic semiconductor molecules TPD (N,N'-Diphenyl-N,N'-di(m-tolyl)benzidine) and α-NPD (N,N'-Di-1-naphthyl-N,N'-diphenylbenzidine) which are both hole transport materials used in organic electronics. Two other organic semiconductor glass-formers have also been employed in this work: the hole transport material TCTA (4,4',4''-Tri-9-) and the electron transport material TPBi (2,2',2"-(1,3,5-benzinetriyl)-tris(1-phenyl-1-H-benzimidazole). All these materials were purchased in their crystalline powder phase (sublimated grade $>$99.8 %) from TCI Chemicals and used as received. The melting point of all these materials lies between 448 K and 573 K (see table 2.1). Therefore, it is necessary to use an effusion cell to get high enough temperatures and reach the desired deposition rates at the substrate position. Figure 2.5 shows the chemical structure of the molecules.

All five materials exhibit quite distinguishable glass transition temperatures, as listed in table 2.1. Toluene, as it has a unique nature compared to the other materials, has its glass transition at 117 K and a more simplified molecular structure. For TPD and α-NPD the calorimetric glass transition was measured with a standard differential scanning calorimetry (DSC7, Perkin Elmer) by cooling the glass at $10\,\mathrm{K\,min^{-1}}$ and measured during a heating scan at the same rate. For the latter two, the glass transition was directly taken from the literature.

Mass determination in nanocalorimetry measurements

With quasi-adiabatic fast-scanning nanocalorimetry, one obtains the heat capacity of the sample deposited on top of the sensor (further details are provided in Section 2.3). The mass of the sensed sample can be directly obtained from the quotient between the heat capacity and the specific heat, provided that the latter is known. In this work, for each calorimetric scan, the mass has been obtained by dividing the heat capacity of the sample in the temperature range after the glass transition—that is, in the supercooled

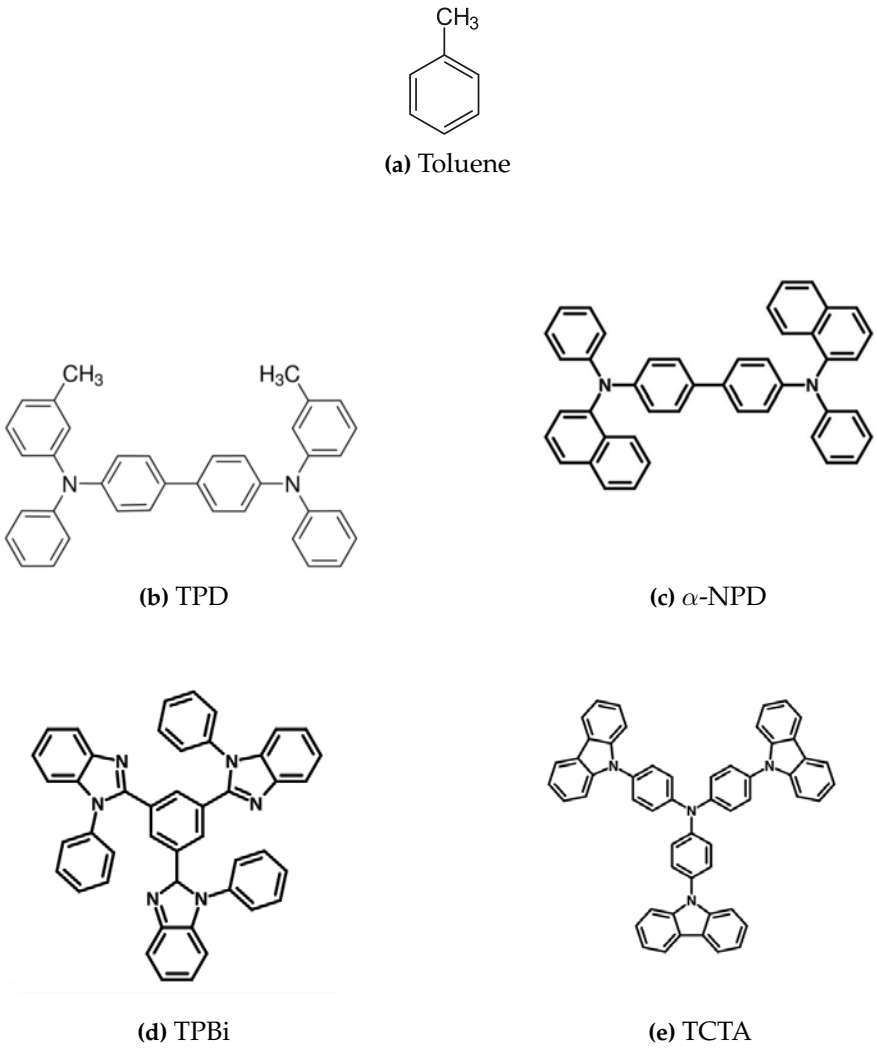

(a) Toluene

(b) TPD

(c) α-NPD

(d) TPBi

(e) TCTA

Figure 2.5: Chemical structure of the different molecules used in this work.

Material	$\mathbf{T_g}$ **[K]**	$\mathbf{T_m}$ **[K]**	ρ [g cm^{-3}]
Toluene	117 [72]	178	1.028 [46]
TPD	333†	448-450	1.08 [73]
α-NPD	368†	552-556	1.22 [73]
TPBi	395‡	546-550	1.25‡
TCTA	424‡	571-573	1.15‡

Table 2.1: Basic materials properties for this work: melting and glass transition temperature and density (at room temperature for the organic semiconductors and at 120 K for toluene). † Glass transition temperatures obtained from conventional DSC by cooling and heating the sample at 10 K min^{-1}. ‡ Data taken from the internal database of the Dresden Integrated Center for Applied Physics and Photonic Materials (IAPP). All the melting temperatures are the ones reported by the supplier.

liquid region—by the specific heat at this same temperature range. In doing so, we are always assuming that the supercooled liquid is always the same, regardless the

original glassy state.

For toluene, the specific heat is well reported by Yamamuro et al. [72] for the whole liquid and supercooled liquid range. On the other hand, the specific heats of the different organic semiconductors used in this work are barely reported in the literature, and no records of their value were found. In these cases, a previous calibration was performed to obtain the specific heat value of the evaporated samples. First, a sample of $\sim$100 nm was deposited simultaneously on the nanocalorimeter and a silicon wafer, close to each other during the evaporation. The calorimetric scan was performed as usual to get the heat capacity. The thickness of the sample was measured using standard profilometry. In this way, the mass deposited on the calorimeter could also be inferred by knowing the sensing area of the chip and the density of the material—more easily found in the literature. The densities are also reported in table 2.1. The specific heat obtained from the mass normalisation of the performed heat capacity scan was later used to get the mass of the subsequent samples as described in the previous passage.

The accuracy of this procedure to get the specific heat for the organic semiconductors is low, estimated to be $\sim$10 %, due to the multiple sources of uncertainties in determining such small masses. Errors might come from the thickness determination, density values found in the literature or the sensing area determination. However, the precision and reproducibility of the technique allow us to measure small differences between different samples through the calorimetric scans regardless of the possible lack of accuracy, which will affect all the samples equally without affecting the conclusions of the attained results. Probably, the larger consequences due to this lack of accuracy are found in the determination of the limiting fictive temperature. The main problem comes from the large extrapolation that must be done of the liquid's enthalpy curve, more precisely, from the specific heat integration over temperature. This fact is further and more extensively addressed in Chapter 3.

2.2 Thermal characterisation techniques

We have used two main characterisation techniques: quasi-adiabatic fast-scanning nanocalorimetry to obtain the heat capacity (C_p) and the 3ω–Völklein technique to measure the thermal conductance (G). We first provide some brief notes on the equations governing the heat transfer in a simplified system. In this way we pretend to illustrate the characteristics of our thermal sensors and how it is possible to obtain either C_p or G data.

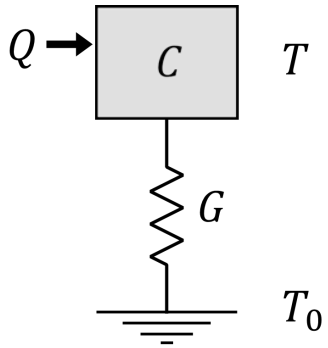

Figure 2.6: Sketch of a calorimeter system as a thermal circuit consisting of a thermal mass C at a temperature T and connected to a heat bath at T_0 through a thermal conductance G. Q represents the injected power.

From the energy conservation principle and Fourier's law for heat conduction, it is possible to derivate the parabolic differential equation that describes the heat distribution—and temperature T—inside a given spatial region over time [74]:

$$\rho c \frac{\partial T}{\partial t} - \nabla \cdot (k \nabla T) = q \tag{2.1}$$

where ρ is the density of the medium, c the specific heat, k the thermal conductivity and q the heat flux per unit volume. We need to solve this equation for our thermal sensors. We can simplify our system/sensor as a solid with a heat capacity C connected to a heat bath at T_0 by a thermal conductance G, as sketched in Figure 2.6. Integrating equation 2.1 over the volume V of a solid and using the Gauss' theorem in the second left-hand term (assuming the surface of the volume to be A and the gradient pointing towards this surface), it leads to:

$$C \frac{\partial T}{\partial t} + k \nabla T = Q \tag{2.2}$$

where C is the heat capacity ($C = \rho V c$), and $Q = qV$ the total power exchanged with the system. We can simplify even further equation 2.2 by linearizing the gradient as $\nabla T = \Delta T / L$, obtaining:

$$C \frac{\partial T}{\partial t} + G \Delta T = Q \tag{2.3}$$

where we have defined the thermal conductance from the solid to the thermal bath as $G = kA/L$.

Equation 2.3 reflects the conservation of energy of the system. The heat generated inside the solid is spent either in the dynamic heating (first term) or in heat conduction through the thermal link (second term). When there is no heat generation but an initial temperature mismatch between the two bodies (calorimeter and heat bath), equation 2.3 has the trivial solution

$$\Delta T = \Delta T_0 \exp\left(-t/\tau\right) \tag{2.4}$$

where we have defined $\tau = C/G$ as the characteristic time of the system. The evaluation of this parameter is of vital importance for any thermal sensor and for the thermal properties that need to be measured. Let's study two cases: (i) for $t >> \tau$ the system will have time to relax towards the equilibrium—i.e. the initial temperature gradient goes to zero—and therefore, reaches the steady state. If all the power is spent on heat dissipation, it is possible to directly extract the thermal conductance between the system and the heat bath. (ii) On the contrary, for $t << \tau$, the system will have no time to dissipate all the input power, which will be used to heat the system dynamically, increasing its temperature. In this case, the system behaves in an adiabatic mode (or in the so-called quasi-adiabatic mode if the heat losses are small), making it possible to extract the heat capacity of our system directly. Both strategies, (i) and (ii), will be the basis for the thermal characterisation techniques used in this work.

The demand in science and, specifically, in nanoscience, for measuring smaller and smaller systems, has forced the characterisation techniques to equally evolve to higher and higher sensitivities by reducing the size of the sensing element. Thanks to the advances in microfabrication techniques it is possible to fabricate devices with reduced mass and size capable of developing multiple functions. It is in that scenario where a new family of membrane-based calorimetry techniques have appeared. These techniques rely on the use of thin dielectric free-standing membranes ($\sim$150 nm), generally made of silicon nitride. These membranes serve as a substrate to hold the actuators on one side and transducers required for the calorimetric measurements on the other side, the sample under study. In the following sections, we describe two of these techniques: fast-scanning nanocalorimetry and the 3ω–Völklein technique. The former is used to measure the heat capacity while the latter is used to measure the in-plane thermal conductivity.

2.3 Fast-scanning quasi-adiabatic nanocalorimetry

Calorimetry is the science that measures the heat transfer in a body to follow its state variables, whose changes are associated to physical changes, phase transitions or chemical reactions. More particularly, nanocalorimetry is a characterisation technique that allows measuring the small amounts of energy that are involved in thermal processes of nano-sized systems. A complete calorimetric measurement requires the simultaneous monitoring of the temperature evolution, the injected power and the heat losses to the surroundings. The first two quantities can be readily measured by placing a single platinum thin film on top of the membrane ($\sim$180 nm), which acts both as a heater and as a sensor. The fact of having a two-in-one heater and sensor together with the ultrathin membrane yields a very low mass for the calorimetric cell (CC). The planar geometry of the membrane provides excellent vertical heat diffusion, ensuring vertical

temperature homogeneity between the metallic heater and the sample, even for high heating rates (up to $10^6\,\mathrm{K\,s^{-1}}$). Moreover, due to the reduced thickness of the membrane, the lateral heat diffusion is limited and—in high vacuum conditions—provides an efficient thermal insulation between the sensing area (the calorimetric cell) and the surroundings. Taking advantage of this fact, we can minimise the heat losses to the surroundings using fast-heating rates, which are easily achieved due to the low mass of the calorimetric cell. The working principle behind quasi-adiabatic fast-scanning nanocalorimetry relies, precisely, on the use of very high heating rates produced by the injection of short current pulses [75–77].

The use of a calorimeter with a calorimetric cell with low heat capacity permits achieving high sensitivities. By performing differential measurements, it is even possible to measure samples with much smaller masses than the calorimetric cell itself. Moreover, using high heating rates also provides several advantages when measuring the heat capacity. First, it minimises—making it almost negligible—any heat transfer to the surroundings, with the cell behaving quasi-adiabatically. Secondly, it reduces the noise of the calorimetric signal and, therefore, the heat capacity for smaller samples can be resolved. Third and last, it also ensures a good temperature profile in the sensor/heating element, necessary for accurate measurements of the heat capacity.

2.3.1 Nanocalorimeter description

Figure 2.7 shows a sketch of the nanocalorimeter device used in this work, consisting of a microfabricated silicon chip. A silicon frame holds a $3\times6\,\mathrm{mm^2}$ silicon nitride free-standing membrane with a thickness of 180 nm. On top of this membrane and at its centre, a 100 nm thick platinum film in the form of a serpentine circuit is deposited together with four contacts for the external connection. These four contacts, two for feeding with the current and two for sensing the voltage drop, permit the metallic element to act both as heating and sensing element. With this 4-wire configuration, see Figure 2.8a, it is possible to measure the amount of power released only in the central area—referred as the sensing area—which has a surface of $1.085\,\mathrm{mm^2}$.

2.3.2 Principle of operation

The principle of operation of the nanocalorimeters is the Joule effect. The power released to the sensing area is $P_{in}(t) = I(t)V(t)$. The temperature can be determined by the resistance of the heating element, $R(t) = V(t)/I(t)$. The resistance dependence of the platinum strip must be previously calibrated, a procedure that is described in Section 2.5.2.

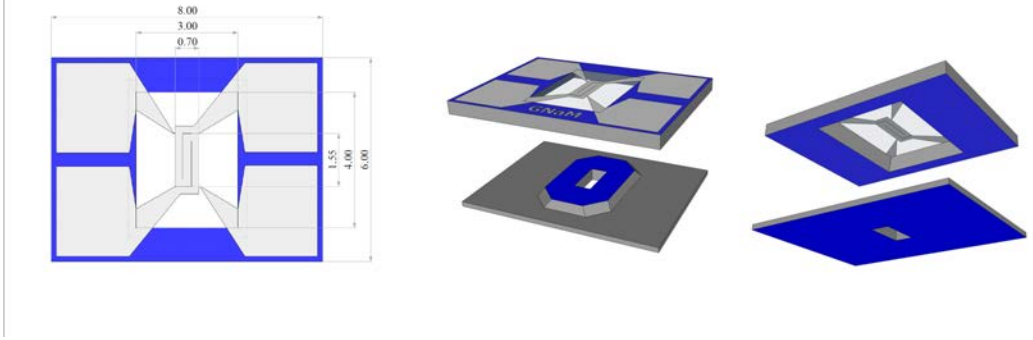

Figure 2.7: Scheme of the calorimeters. In the left, a top view of the nanocalorimeter with its dimensions given in millimetres. In the middle and the right-side, a 3D sketch of the nanocalorimeter and the shadow mask used in this work viewed from the top and the bottom.

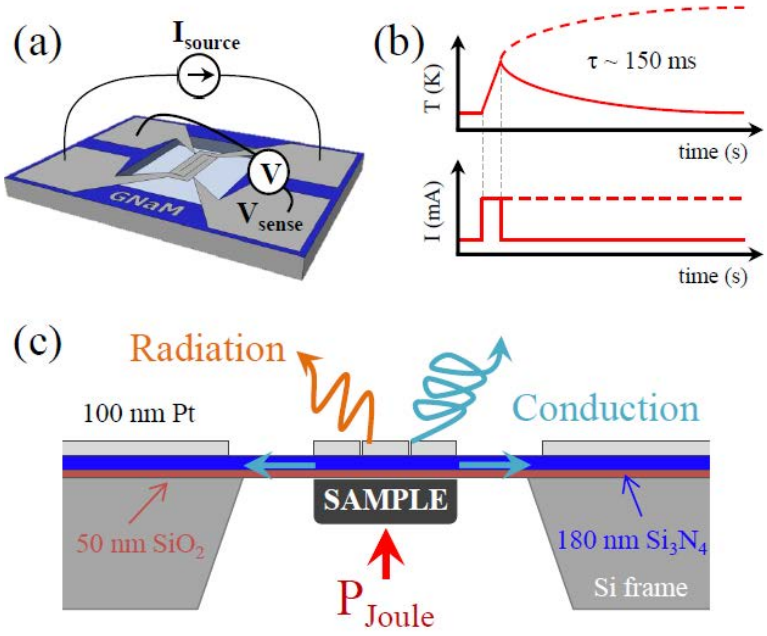

Figure 2.8: The principle of operation of the nanocalorimeter. (a) Schematics of the electrical connections: two for the current feeding and to for the voltage sensing. (b) Temperature dynamic response of the nanocalorimeter to short and intense current pulse (the continuous line) and the steady state (dashed line). τ represents the characteristic time of a typical nanocalorimeter. (c) Cross section scheme of a nanocalorimeter with the input power and the possible dissipation mechanisms. Figure reprinted from [78].

At room temperature, the characteristic resistance of the heater/sensing element is around $30\,\Omega$ with a total heat capacity of $\sim 0.6\,\mu J\,K^{-1}$. Figure 2.8c, shows a scheme of the heat losses of the nanocalorimeter; in UHV conditions, any conduction through the air is suppressed and heat losses can only go through conduction across the SiN_x membrane or through a radiative process. The latter is negligible at temperatures below 500 K, and as long as the sample thickness is kept small, the radiation losses can be cancelled out by a baseline subtraction [78]. The other path for the heat losses is

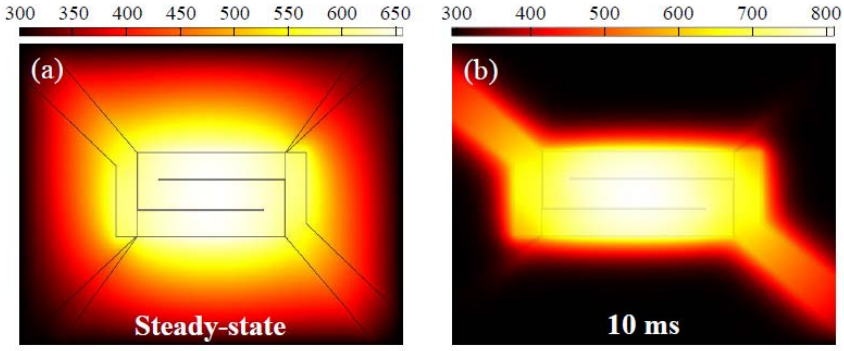

Figure 2.9: Finite Element Modelling using the platform COMSOL Multiphysics®. (a) The temperature profile of the membrane of a nanocalorimeter in the steady state. (b) Same membrane temperature profile after 10 ms of a short current pulse, which leads to a heating rate of $8 \times 10^4\,\mathrm{K\,s^{-1}}$. Reprinted from [78].

the conduction across the membrane, which has an effective thermal conductance of $\sim$4 µW $\mathrm{K^{-1}}$ at room temperature. Therefore, the thermal relaxation time of the nanocalorimeter (equation 2.4) is of $\tau\sim$150 ms. With such rapid dynamics, it is possible to obtain high-speed cooling rates during the thermal relaxation. For instance, for a temperature gradient between the silicon frame and the heater of 150 K, cooling rates of the order of $\sim$1000 $\mathrm{K\,s^{-1}}$ are easily achieved. On the other hand, if the heater is fed with short current pulses—let's say of 40 mA for a few milliseconds (see Figure 2.8)—the amount of power released by the Joule effect will be of 48 mW, promoting heating rates on the CC of the order $\beta\sim 8 \times 10^4\,\mathrm{K\,s^{-1}}$. Given that this heat is delivered in much shorter times than the τ of the system, the energy losses through conduction can be neglected, and the measurement can be considered quasi-adiabatic. Lower heating rates can also be achieved at the expense of resolution and the quasi-adiabaticity, what would require further analysis of the heat losses. However, all the calorimetric scans performed throughout this thesis are performed using high heating rates ($\sim 3.5 \times 10^4\,\mathrm{K\,s^{-1}}$) and therefore, under the quasi-adiabatic condition.

The planar geometry ensures an excellent thermal contact between the metallic element and the sample and, together with the out-of-plane reduced dimensionality, this geometry produces a negligible vertical temperature gradient. Therefore, the 2D temperature map of the sensing area follows the temperature profile described, precisely, by the heater. The in-plane temperature homogeneity of the sensing area is a general drawback of this type of thin film cells. Figure 2.9a shows the 2D temperature map in steady state conditions (constant current for times $t >> \tau$) and Figure 2.9b the same map just 10 ms after starting a heating ramp at $8 \times 10^4\,\mathrm{K\,s^{-1}}$, both obtained from finite element modelling (FEM) of heat transfer using the platform COMSOL Multiphysics®. Further details of the modelling can be found elsewhere [79]. In the steady state, the profile is parabolic whereas at very fast heating rates the profile gets flattened due to

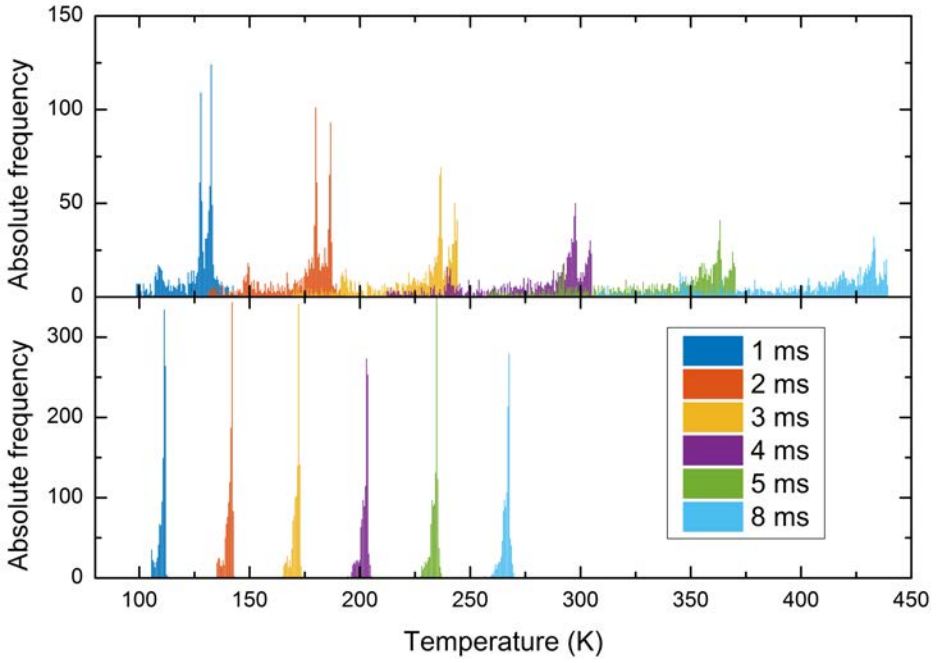

Figure 2.10: Histogram of the temperature profile of the sensing area of the nanocalorimeter over time for the same intensity current pulse. The legend indicates the time step. The histogram is built using the temperature of each element of the mesh used in the FEM. (a) The temperature profile of a nanocalorimeter without plate, used as it is. (b) Histogram of a nanocalorimeter with a 200 nm aluminium plate.

the limited lateral diffusion and the short times explored. Still, certain inhomogeneity in the profile is still present, and it increases over time (and temperature). Figure 2.10 shows how the temperature profile (as a histogram of the temperature distribution over a meshed sensing area) evolves and goes larger as the time and the average temperature increases. A thermal diffusive layer is deposited on top of the silicon nitride membrane to reduce the temperature inhomogeneity across the sensing area. Figure 2.10 shows how the temperature profile at different times of the current pulse does not degrade over time when we consider the inclusion of a thermal plate of 200 nm of aluminium on top of the sensing area. Of course, this is at the expense of increasing the heat capacity of the CC, which limits the heating rate achievable (for the same input power) and lowers the mass resolution . Since our samples are deposited in the steady state conditions, the deposition temperature also benefits from the improvement in the homogeneity of the temperature profile.

2.3.3 Heat capacity derivation

The heat capacity is obtained by performing a temperature scan of our sample and monitoring both the input power and the temperature of the sensor through the resistance. The temperature evolution of the CC is embedded in the voltage drop signal

due to the $R(T)$ dependence of the platinum sensor.

The highest sensitivity and resolution can be obtained when the measurement is performed in differential mode. Using a pair of twin calorimeters, that is, with similar heat capacity and temperature coefficient of resistance (TCR, see Section 2.5.2), the differential voltage between them in a heating temperature scan will be close to zero. Now, if one nanocalorimeter has a sample deposited, the differential voltage between the sample and the reference calorimeters will correspond solely to the calorimetric signal generated by the sample itself. This signal, generally small, can be heavily amplified using instrumental amplifiers to accommodate it to the typical ± 10 V range of a digital data acquisition (DAQ) system. This is the key point of differential nanocalorimetry that allows obtaining high sensitivities and resolutions.

Under the assumption of adiabatic conditions, the delivered energy is spent into promoting the temperature of the system. This temperature increase is proportional to the heat capacity of the system

$$C_p(T)dT = P_{in}dt \tag{2.5}$$

We can express the input power, P_{in} in terms of the measured variables, in that case, the heat capacity reads,

$$C_p(T) = \frac{V(t)I(t)}{\beta(t)} \tag{2.6}$$

where we have defined the temperature variation with time as the heating rate $\beta(t)$. It is important to note that all the magnitudes are a function of time. For simplicity, this dependence will not be shown explicitly from now on. Now, if using the differential configuration, the heat capacity of the measured samples will be the differential calorimetric signal of both sensors

$$\Delta C_p(T(t)) = \frac{V_S I_S}{\beta_S} - \frac{V_R I_R}{\beta_R} = \frac{I_R V_R}{\beta_R}\left(\frac{V_S I_S \beta_S}{V_R I_R \beta_R} - 1\right) \tag{2.7}$$

where subscripts S and R stand for sample and reference, respectively. We can consider some simplification of our analysis before continuing:

(i) In our case, the calorimeters are fed with a constant current pulse. Hence, the intensity is constant throughout time. In that case, since $V = IR$, voltage and resistance derivative are directly related by $dV = d(IR) = IdR$.

(ii) Both devices, the sample and the reference, are connected in series to ensure that they are fed with the same current. Therefore, we can write $I_S = I_R = I$.

(iii) The signal containing the sample's information is the differential voltage, ΔV, which can be heavily amplified compared to the single calorimeter signal. We can use the relation $V_S = V_R + \Delta V$ to include the measured signal.

Including all these considerations we can rewrite expression 2.7 as

$$\Delta C_p = \frac{I\Delta V}{\beta_S} + \frac{V_R I}{\beta_S}\left(1 - \frac{\beta_S}{\beta_R}\right) \tag{2.8}$$

In this last equation, the term β_S/β_R is the noisiest due to the β_S term in the numerator. To significantly decrease its noise, we can follow the development followed by Efremov et al. [75], which consists in using the derivative of the differential signal instead, that reads

$$\frac{d\Delta V}{dt} = \frac{dV_S}{dT_S}\beta_S - \frac{dV_R}{dT_R}\beta_R \longrightarrow \frac{\beta_S}{\beta_R} = \frac{(d\Delta V/dt)_t}{\beta_R\,(dV_S/dT_S)_t} + \frac{(dV_R/dT_R)_t}{(dV_S/dT_S)_t} \tag{2.9}$$

After all the previous considerations, a final derivation of the heat capacity of the sample can be obtained:

$$\Delta C_p(T_S(t)) = \frac{I\Delta V}{\beta_S} - \frac{V_R\,(d\Delta V/dt)_t}{\beta_S\beta_R\,(dR_S/dT_S)_t} + \frac{V_R I}{\beta_S}\left(1 - \frac{(dR_R/dT_R)_t}{(dR_S/dT_S)_t}\right) \tag{2.10}$$

where the voltage and resistance have been related considering the assumption (i). The temperature derivative of the resistance can be directly obtained from the $R(T)$ dependence of the metallic element, previously calibrated.

Ideally, if both nanocalorimeters were exactly equal, the differential signal would correspond solely to the calorimetric signal of the sample. The pair sample-reference are chosen to be as similar as possible, but there are always minor differences. For that purpose, previous measurements to determine the ΔC^0_{pS} with the empty calorimeters—denoted with the super-index 0—are performed. This is called the baseline correction. It is possible to reduce the noise of the baseline by performing multiple scans (typically from 100 to 200) and averaging the output data. The baseline correction makes necessary an additional—and final—correction to obtain the neat heat capacity of the sample. The heating rate of the loaded sample cell can diminish substantially due to the increment of heat capacity. Therefore, for a given temperature of the sample cell, the subtraction of the heat capacity will be larger in the scan with the loaded cell ($\Delta C^1_{p_S}$, where the super-index 1 stands for the loaded cell). Knowing the relative temperature evolution between both cells and between the baseline and the loaded sample measurements, it is possible to determine the excess of subtracted heat capacity ($\Delta C^1_{pR} - \Delta C^0_{p_R}$). Finally, the heat capacity of the sample can be expressed (in the T^1_S space) as

$$C_p^{sample}\,(T_S) = \Delta C^1_{pS}\,(T_S) - \Delta C^0_{pS}\,(T_S) + \Delta C^1_{pR}\,(T_S) - \Delta C^0_{pR}\,(T_S) \tag{2.11}$$

Finally, Figure 2.11 shows a comparison between using the differential and nondifferential (using only the V_S signal and directly equation 2.5) measurements of the calorimetric trace of two ultrathin films of vapour deposited toluene. The improvement in

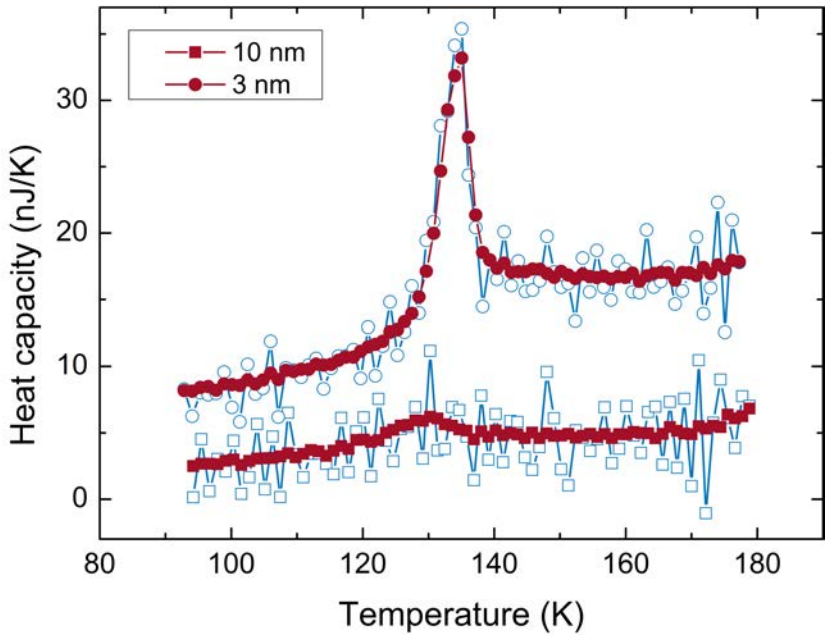

Figure 2.11: Heat capacity scan of two ultrahin layers, as indicated in the legend, of vapour deposited films of toluene. In red and filled symbols the differential measurement, in blue and open symbols, the nondifferential measurement.

the signal-to-noise is highly improved when using the differential measurement.

2.3.4 Measurement procedure

First, a couple of temperature-calibrated twin nanocalorimeters are placed on a temperature controlled socket at a given reference temperature. Then, several temperature scans are performed and subsequently averaged to obtain the baseline. The raw voltage data acquired with a DAQ system is box averaged to increase the signal-to-noise ratio. With the acquisition frequency (2.5 MHz) and the heating rates ($\sim$35 000 K s^{-1}) used, a typical box averaging with box sizes between N =100-200 is applied. This procedure leads to heat capacity curves with temperature steps between 0.5 K to 1.5 K.

Once the baseline is measured, we can place our sample at the sensing area of the nanocalorimeter. In this work, samples are prepared using physical vapour deposition (see Section 2.1) at different deposition temperatures, which are achieved by feeding the sensor with a constant DC. After the deposition, a new scan is performed with the same parameter and reference temperature as the baseline scan. The duration of the current pulse is chosen accordingly to the maximum temperature we need to achieve. In the case of organic glass-forming molecules, if the temperature reached is high enough, the material is re-evaporated from the sensor leaving it clean for a subsequent new evaporation. The cleanliness of the sensor is checked by comparing the base heat capacity of the cell. Otherwise, if the maximum temperature is not high enough to

evaporate the material again, a so-called fast-cooled (FC) glass is created on top of the sensing area of the nanocalorimeter. Due to the low mass of the calorimetric cell and once the input power is cut, the passive cooling rates achieved are on the order of 500 K s^{-1} to 1000 K s^{-1}. These fast rates produce very low stability glasses. Contrary to the VD glass, which needs to be evaporated each time, the creation of the FC glass is reversible and can be measured several times—tenths to hundreds—allowing to average all the curves and to obtain much better statistics of the calorimetric trace. For the VD glasses, especially the thinnest (<50 nm), the calorimetric traces shown are typically the result of averaging the data from 2-10 equally prepared samples (same thickness, same T_{dep}).

2.4 Thermal conductivity: the 3ω-Völklein method

The 3ω–Völklein is a combination of a widely used method—the 3ω—and the Völklein method for measuring the thermal conductivity of different insulating materials. The 3ω method was first described by Cahill in 1990 [80] and was primarily intended for measuring bulk materials. It consists in depositing a metal strip on top of the sample under test and feed it with an alternating-current (AC) at a given frequency ω. Due to the self-heating of the metallic strip, the voltage through the strip will exhibit a third harmonic component. This $V_{3\omega}$ can be directly related to the temperature gradient generated at the substrate which, in turn, is linked to the thermal conductivity. This method was later adapted for measuring thin film samples in the out-of-plane direction ($k_\perp$) [81, 82]. This latter modification is briefly detailed in Section 2.4.2. However, the Völklein method was introduced in 1997 by Völklein and Starz [83]. They presented a membrane-based sensor that operated in direct-current (DC) mode to measure the in-plane thermal conductance ($k_\parallel$) of thin films. However, the measurements of thermal conductance were limited to metallic samples and thicknesses lower than 1 µm. This limitation was later circumvented by Sikora et al. [84] in 2012, who presented a method to measure thermal conductivity of very thin suspended membranes based on a mix of the 3ω method and the Völklein method, achieving a high sensitivity, up to 10 nW K^{-1}, and a high resolution $\Delta G/G \simeq 10^{-3}$.

Figures 2.12a and 2.12b show a scheme of the 3ω method for thin films and the 3ω-Völklein method for the out and in-plane measurements. The arrows indicate the main direction of the heat flux for each method, further detailed in the following sections. The light grey represents the metallic element (e.g. platinum) needed for injecting the power, the dark-grey represents the thin film sample and/or free-standing membrane whereas the black corresponds to the substrate (e.g. silicon).

At GNaM's, we have developed a modification of the 3ω–Völklein technique that allows measuring in situ the thermal conductance of thin films, from either insulating

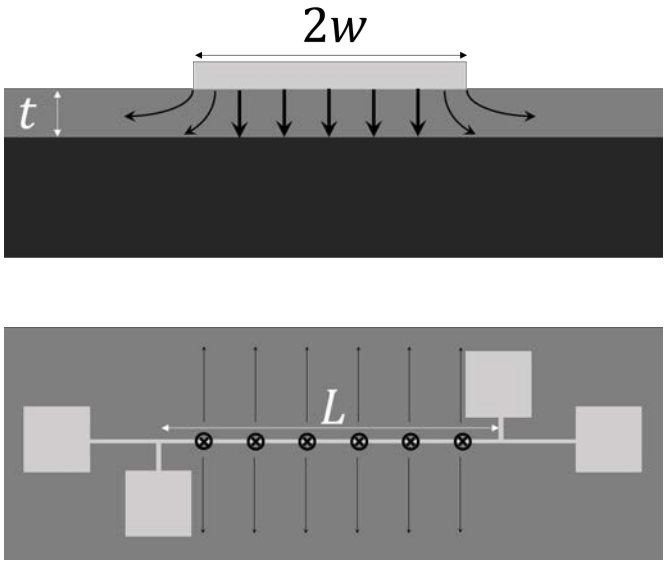

(a) Geometry for the 3ω to obtain the out-of-plane thermal conductivity of the film (dark-grey).

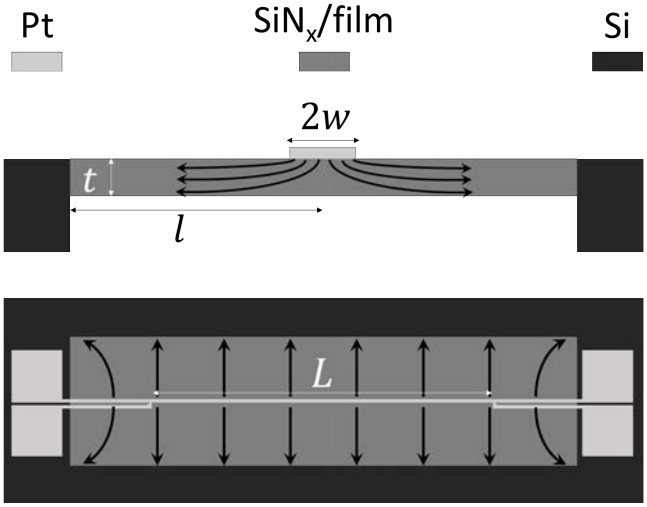

(b) Geometry for the Völklein and 3ω–Völklein to obtain the in-plane thermal conductivity of the membrane plus film system (dark-grey).

Figure 2.12: Schematic representation (top and side-view) of the heat flux for the 3ω and the 3ω–Völklein geometries. The light-grey describes the metallic elements, the dark grey the film under study (or membrane) and the black the substrate or frame. The arrows indicate the direction of the heat flux, the main direction is described by the arrows' thickness. The relevant lengths are also indicated: $2w$ is the width of the sensor, L the length of the strip, t the thickness of the membrane plus sample and l the width of the membrane for the 3ω–Völklein geometry.

or thermally and electrically conductive material. The high resolution achieved allows monitoring the thermal conductance during layer growth by PVD even from the very firsts stages (less than one nanometer thick).

(a) 3D sktech showing the top and bottom view.

(b) Optical image.

(c) Photograph of the sensor

Figure 2.13: Different images describing the 3ω–Völklein sensor.

2.4.1 Device description

The thermal sensor developed at GNaM is based—as the nanocalorimeters were—on a metallic sensor built on top of a free-standing SiN_x membrane. Two parallel platinum strips are deposited on top of the membrane, as can be seen from the different images in Figure 2.13, each one of the strips prepared to be connected in a 4-wire configuration. For the more standard DC operation (Völklein method), both platinum lines are used to measure the thermal conductance of the membrane (or membrane plus sample) beneath the two probes exclusively . The measurements performed in this thesis are done in the AC mode, for which we only use of the central strip, assuming the frame temperature to be the same as the temperature probe were the sensors are placed (see Section 2.1.5).

The geometry of the sensors was previously optimised [85] using finite element modelling with the platform COMSOL Multiphysics® to ensure the temperature homogeneity between the voltage probes. The fabricated sensor consists of a membrane with an area of 3 mm$\times$ 250 µm and 180 nm thick. The two platinum sensing strips are 3 mm$\times$ 5 µm and have a thickness of 100 nm. The voltage probes are separated by 2 mm. Further details on the sensor optimisation can be found elsewhere [85].

2.4.2 Principle of operation

The principle of operation of this type of sensor is the same as in the nanocalorimeter device: the self-heating of the metallic element due to the Joule effect together with its duality as heater and sensor. The main difference here is that we are using AC of a certain angular frequency ω to promote a temperature rise that will generate a voltage component in 3ω due to the self-heating of the metallic strip. This voltage is

used to quantify the amplitude of the temperature oscillations and later extract the conductance of the film/substrate beneath the sensor.

The generation of the $V_{3\omega}$ can be derived from the evolution of the dissipated power to the sensor. First, we feed the sensor with AC with an angular frequency $\omega = 2\pi f$,

$$I = I_0 \sin(\omega t) \tag{2.12}$$

which produces a dissipated power of

$$Q = I^2 R = I_0^2 R \sin^2(\omega t) = \frac{I_0^2 R}{2}(1 - \cos(2\omega t)) = Q_0(1 - \cos(2\omega t)) \tag{2.13}$$

where we have defined the quantity $Q_0 = I_0^2 R/2$. Therefore, the dissipated power has two components. The first, the DC component, will produce a transient self-heating that tends to a constant temperature value for times $t >> \tau$, where τ is the characteristic thermal constant of the system. The second term produces a temperature evolution that oscillates with time. We can define the temperature steps produced for each component as

$$\Delta T_{DC} \equiv \frac{Q_0}{G} \qquad \text{and} \qquad \Delta T_{2\omega} \equiv \frac{Q_0}{G_{2\omega}} \tag{2.14}$$

where we have introduced the apparent conductance $G_{2\omega}$. Due to the permanently transient state of the time-dependent term, part of the heat will be expended in dynamically heating the sensor. Therefore, the $G_{2\omega}$ will always be lower than the real conductance. In a more general framework, the temperature oscillation can also be out of phase with respect to the heating wave,

$$\lim_{t\to\infty} \Delta T = \Delta T_{DC} - |\Delta T_{2\omega}| \cos(2\omega t + \phi) \tag{2.15}$$

These temperature oscillations will be translated into resistance oscillations too,

$$R = R_0 + \frac{dR}{dT}\Delta T = R_0 + \frac{dR}{dT}(\Delta T_{DC} - \Delta T_{2\omega}\cos(2\omega t + \phi)) \tag{2.16}$$

which, in turn, will affect the voltage of the strip through the Ohm's law,

$$V = I_0\left(R_0 + \frac{dR}{dT}\Delta T_{DC}\right)\sin(\omega t) - I_0 \Delta T_{2\omega}\frac{dR}{dT}\sin(\omega t)\cos(2\omega t + \phi) \tag{2.17}$$

The last term can be rewritten using trigonometrical identities, leading to the following expression:

$$\begin{aligned} V = I_0\left(R_0 + \frac{dR}{dT}\Delta T_{DC}\right)\sin(\omega t) + I_0\frac{\Delta T_{2\omega}}{2}\frac{dR}{dT}\sin(\omega t + \phi) \\ -I_0\frac{\Delta T_{2\omega}}{2}\frac{dR}{dT}\sin(3\omega t + \phi) \end{aligned} \tag{2.18}$$

Here, a term oscillating at 3ω with a certain phase appears explicitly. By measuring this term selectively, we can infer the temperature oscillation $\Delta T_{2\omega}$ as

$$\Delta T_{2\omega} = \frac{2V_{3\omega}}{I_0 \frac{dR}{dT}} \tag{2.19}$$

which can be, later, related to the thermal conductance.

2.4.3 Thermal conductance derivation

Because of the geometry of the sensor—the free-standing membrane with a large central metallic strip—and the lack of a substrate, the heat will flow perpendicular to the long axis, from the central heater to the silicon frame (see Figure 2.12b). Therefore, the heat equations can be simplified to 1D geometry. In the normal DC operation, where a constant power is generated at the central strip, the conductance can be readily obtained from the 1D Fourier law, which yields

$$G = (k_{SiN_x} t_{SiN_x} + k_s t_s) \frac{2L}{l} \tag{2.20}$$

where k stands for the in-plane thermal conductivity and t for the thickness of the SiN_x membrane and sample, L is the length of the Pt strip between the voltage probes and l is the distance between the central strip and the frame.

However, when operating in AC mode, a more complex analysis is needed. Again, to derive how the thermal oscillations depend on the sensor geometry and properties (conductance, density, heat capacity) the 1D heat equation can be used. The exact solution for $\Delta T_{2\omega}$ has a complex dependence on the angular frequency ω and can be found elsewhere [84, 85]. In an excellent approximation, this solution can be developed in Taylor expansion series considering only the first-order terms in ω [84–86], yielding the much more simplified and still valid expression for low angular frequencies

$$\Delta T_{2\omega} = \frac{Q_0}{G\sqrt{1 + \omega^2 \left(4\tau^2 + \frac{4}{3}\frac{l^2}{D}\tau + \frac{2}{3}\frac{l^4}{D^2}\right)}} \tag{2.21}$$

where D is the effective thermal diffusivity of the membrane defined by $D = k/\rho c$, τ is the characteristic time of the system $\tau = C'/G$ and C' is the combined heat capacity of the sensor plus the membrane: $C' = c_{SiN_x}\rho_{SiN_x} t_{SiN_x} + c_{Pt}\rho_{Pt} t_{Pt}$. From equation 2.14, we can write now the apparent conductance as

$$G_{2\omega} = \frac{Q_0}{\Delta T_{2\omega}} = G\sqrt{1 + \omega^2 \left(4\tau^2 + \frac{4}{3}\frac{l^2}{D}\tau + \frac{2}{3}\frac{l^4}{D^2}\right)} \tag{2.22}$$

The $G_{2\omega}$ will strongly depend on the frequency, the characteristic time of the system and the relationship between the distance l and the penetration depth $d = \sqrt{D/\omega}$, which describes the spatial damping of the thermal wave that has produced the heater. When $d >> l$ or $\omega^2 << D/l^2$, all the power generated in the central strip will be dissipated via conduction across the membrane. If the frequency increases, the spatial penetration depth will decrease as the system will not have time to dissipate the heat through conduction and, therefore, part of it will be spent in the dynamic heating of the membrane.

If the frequency is low enough, the apparent thermal conductance can be well approximated by the real conductance, $G_{2\omega} \simeq G$. In that case, we can make the DC calculation of the thermal conductivity provided in equation 2.20. However, when a sample is grown on top of the membrane, the characteristic time and penetration depth of the system will change, and the $G_{2\omega}$ will start deviating again from the real conductance. An effective thermal diffusion coefficient can be rewritten in terms of the sample thickness, t_S,

$$D_{eff} = \frac{(k_{SiN_x} t_{SiN_x} + k_S t_S)(t_{SiN_x} + t_S)}{(\rho_{SiN_x} t_{SiN_x} + \rho_S t_S)(c_{SiN_x} t_{SiN_x} + c_S t_S)} \tag{2.23}$$

and the extensive values of G and C' can be updated to:

$$G(t_s) = (k_{SiN_x} t_{SiN_x} + k_S t_S)\frac{2L}{l} \tag{2.24}$$

$$C'(t_s) = (c_{Pt}\rho_{Pt} t_{Pt} + c_{SiN_x}\rho_{SiN_x} t_{SiN_x} + c_s \rho_S t_S) wL \tag{2.25}$$

with the consequent change in τ.

The measurement should be carried in the range of frequencies where the approximation $G_{2\omega} \approx G$ is still valid. Measuring at higher frequencies will increase the dependence of the apparent conductance with sample's properties such as ρ and c, complicating the evaluation of the real thermal conductance. Figure 2.14 shows a colourmap of the ratio $G_{2\omega}/G$, as a function of the frequency and the sample's thickness. The parameters used to build this plot are listed in table 2.2. For the sample, we have used the characteristic parameters of the organic semiconductor molecule TPD, which will be studied in Chapter 6. From the colourmap in Figure 2.14 we see how, by increasing either the frequency or the sample thickness, the apparent conductance values start deviating from the real conductance. For the measurements performed in this thesis, current waveform frequencies of 0.5 Hz and 1 Hz have been used. These frequencies allow measuring the conductance for thicknesses up to 1 µm with a total deviation of ∼1.5 % at most for a frequency of 1 Hz and less than 0.5 % for 0.5 Hz. This frequency range is a good compromise between reasonable acquisition times (about 3 s to 6 s) and the small deviation expected from the $G_{2\omega} \approx G$ approximation.

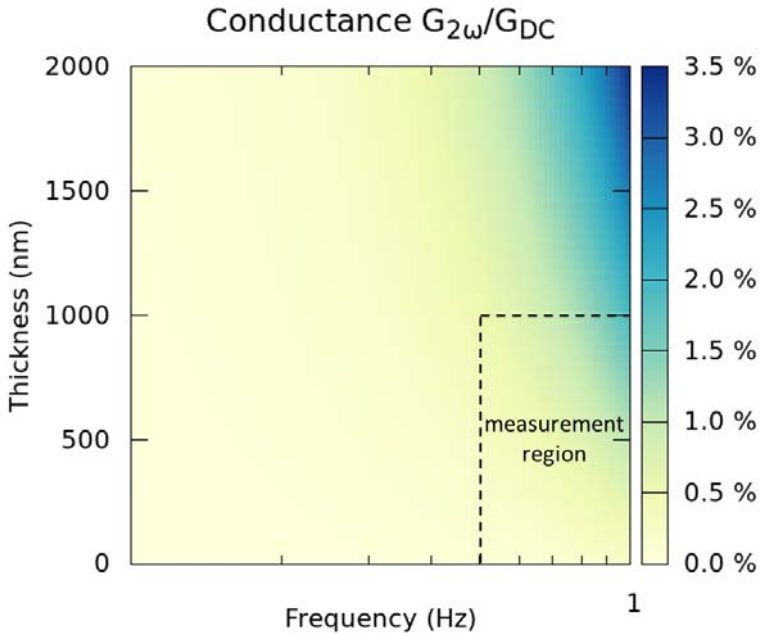

Figure 2.14: Colourmap of the ratio between the $G_{2\omega}$ and the G_{DC} as a function of the frequency and the thickness of an organic TPD sample, in this case. This Figure has been generated using equation 2.22 and the parameters listed in table 2.2.

Parameter/material	Pt	SiN_x	TPD layer
k [W m^{-1} K]	33	2.65	0.16
c_p [J kg^{-1} K^{-1}]	133	700	1000
ρ [kg m^{-3}]	21450	3180	1080

Table 2.2: Parameters used to calculate the $G_{2\omega}$ dependence on frequency and mass shown in Figure 2.14.

2.4.4 Measurement procedure

Samples are deposited using PVD directly on the membrane without the need of a shadow mask. The thermal conductance of the system membrane/sample at a given temperature is measured several times (50 to 100) and subsequently averaged to obtain enough statistics. Figure 2.15 shows an example of the $V_{1\omega}$ (both from the sample and the reference) and $V_{3\omega}$ signals, with the latter having, essentially, the 3ω contribution due to the good cancellation of the primary 1ω signal. Further details on the specific procedure to obtain the conductance of the sample films are given directly in Chapter 6.

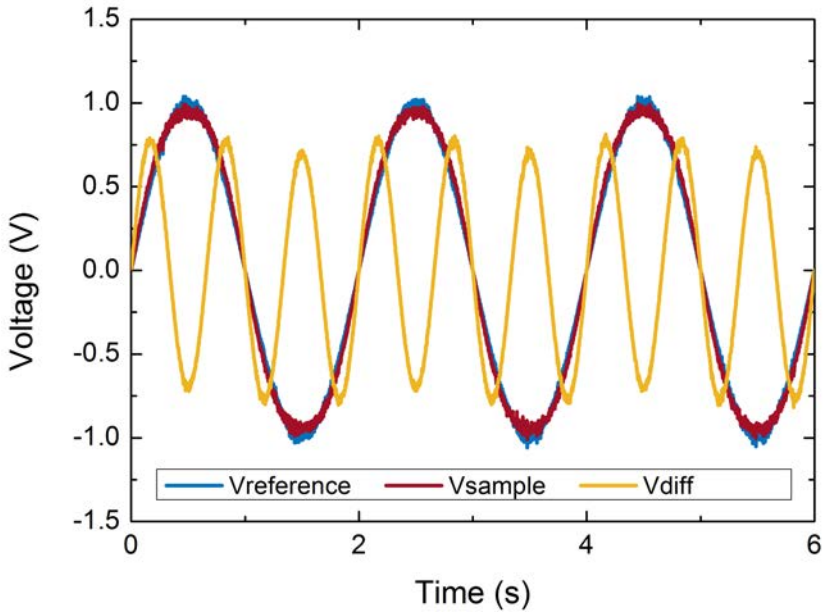

Figure 2.15: The different signals generated for the 3ω–Völklein measurements. The differential voltage contains basically the $V_{3\omega}$ signal due to almost total cancellation of the $V_{1\omega}$ signal. The data from the Figure is simulated and does not correspond to a real measurement.

2.4.5 3ω technique: out of plane measurements

In this work, we have also used the well-established 3ω technique to gain access to out-of-plane ($k_\perp$) of thin films and, in this way, complement the data of the $k_\parallel$ obtained with the 3ω–Völklein. We briefly present here the basic details of this specific technique.

As stated before, this technique is also based on the measurement of the $V_{3\omega}$ signal generated by the self-heating of the metallic element, which allows obtaining the temperature rise of the strip (ΔT). What differs this method from the 3ω–Völklein technique is the geometry. In this case, we have a long and narrow strip on top of the sample film we want to measure, as sketched in Figure 2.12a. As long as the half-width of the strip (w) is much larger than the thickness of the film (t_{film}), the heat flows from the heater to the substrate almost perpendicularly. Because of this approximation and simplified geometry, the contribution to the temperature rise of the strip of the film can be simply written as [74]

$$\Delta T_{film} = \frac{Q_0}{k_{film}} \frac{t_{film}}{2wL} \tag{2.26}$$

where L is the length of the strip (also much larger than its thickness). The film is placed, on top of a substrate—silicon in this case. In fact, this method was initially developed and used to measure the bulk thermal conductivity [80]. The contribution of the substrate, which also contributes to the temperature amplitude of the strip, can be cancelled out by measuring with and without the thin film using the same sensor

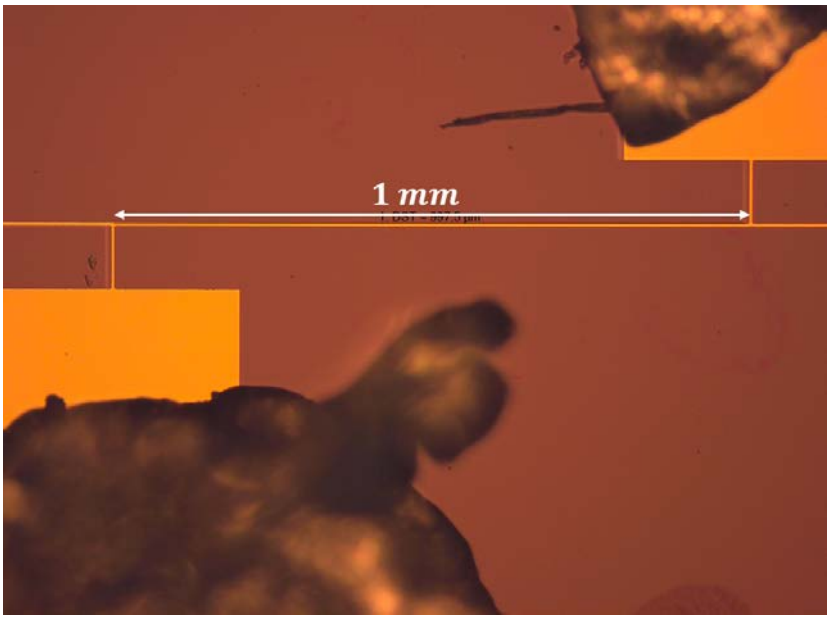

Figure 2.16: Optical image of the 3ω sensor deposited using a shadow mask on top of a 150 nm thick film of the organic semiconductor molecule TPD. The two big square pads are the voltage probes; the current pads are left out the picture.

and frequency.

Sensor deposition

Here we have used as substrate monocrystalline silicon with a 450 nm silicon nitride film on top of it to act as a dielectric insulating layer to prevent current leakage from the sensor to the substrate. TPD samples are evaporated on top of the SiN_x layer. Contrary to the 3ω–Völklein, the sample needs now to be removed from the chamber to evaporate the sensor on top of it in a different setup. A reference substrate (silicon plus SiN_x) is also prepared. The deposition of the sensor is performed using shadow masks to shape its geometry (Figure 2.7). The sensor is evaporated by e-beam deposition and consists of an adhesion layer of 10 nm Ti together with a 100 nm Au layer. Figure 2.16 shows an optical microscope image of the strip and the two pads for the voltage probes. This method produces sensors with subtle differences in both thickness and width of the strip which requires further corrections of the measured data, as explained in the following Section. The nominal dimensions of the evaporated sensor are $L = 1\,\mathrm{mm}$, $2w = 5\,\mu\mathrm{m}$ and a thickness of 100 nm.

Sensor correction

Since the sensors can be slightly different, a direct subtraction between the sample and reference temperature amplitudes cannot be performed. A different thickness and

width of the strip will affect the resistance of the strip and therefore, the injected power Q_0 if the measurements are performed at a fixed current. A different width of the sensor will also affect the Si bulk and the SiN_x layer contribution to the temperature amplitude. To obtain the equivalent ΔT_{ref}, its value has to be scaled to the geometry of the sample sensor. A more detailed procedure of this correction can be found elsewhere [85].

The 3ω measurements performed in this work (see Chapter 6) required high precision to resolve minor differences in $k_\perp$ of the samples. For this reason, the geometry of the sensors needs to be well-characterised. The width of the sensors was measured by AFM with a precision of ± 100 nm.

2.5 Microfabrication, data acquisition and calibration

2.5.1 Device microfabrication

The microfabrication process for the nanocalorimeter is schematically described in Figure 2.17. The fabrication starts with a double-sided polished p-type silicon wafer. First, a 50 nm silicon oxide film is grown by thermal oxidation (a). The second step consists in growing a 180 nm thick film of low-stressed silicon nitride layer by low-pressure chemical vapour deposition (b). Then, square windows at the backside of the chip are opened using combined standard photolithography and reactive etching techniques (c), leaving exposed the underlying silicon. Now, on the front side, the metallic elements—meander-shaped circuit and electrodes—are deposited (d). Finally, a window is opened in the backside by KOH anisotropic etching of the Si layer (e) with the bottom silicon nitride window defining its area. This last process will open a cavity with a trapezoidal cross-section and a free-standing silicon membrane layer. More details on the microfabrication process can be found elsewhere [78, 79].

The sample must be placed selectively only on the sensing area, so the temperature profile is not disturbed and an accurate measurement can be performed. This is achieved by using microfabricated silicon shadow masks (as shown in the sketched Figure 2.7). These masks self-align due to the same window geometry as the chip, guaranteeing the well-adjustment between the sensing area and the mask's window. In this way, the evaporation area is completely delimited when preparing the sample with a physical vapour deposition method.

The microfabrication process of the 3ω–Völklein devices is relatively similar to the nanocalorimeter devices. More details on the specific followed steps can be found elsewhere [85].

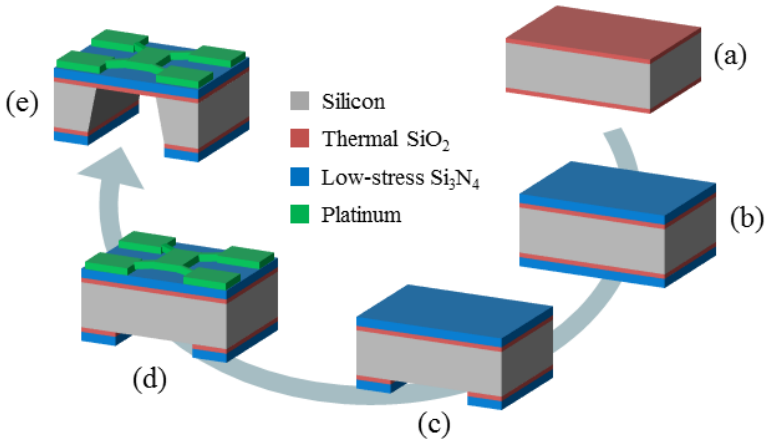

Figure 2.17: Microfabrication process schematics for the nanocalorimeters, briefly described in the text. The fabrication process for the 3-Völklein sensors can be also well described by this Figure. Figure adapted from [78].

2.5.2 Calibration of the sensors

The nanocalorimeters used in this thesis use the platinum thin film meander both as a heater and thermometer. It is, therefore, necessary to determine the relation between the resistance and the temperature, $R(T)$ of this Pt film. In this work, the studied samples lie in two different temperature ranges: the first going from 77 K (liquid nitrogen temperature) to $\sim$ 180 K and the second going typically from 200 K up to 500 K. The calibration for a given device is only done for the temperature range in which it will be used. This relation can be well approximated by a quadratic dependence of the resistance versus temperature:

$$R(T) = R_0(1 + AT + BT^2) \tag{2.27}$$

commonly known as the Calendar-Van Dusen equation.

The parameters of equation 2.27 are fitted using experimental data from the measurement of the resistance at several temperatures. Most of the measurements are performed in high vacuum conditions by placing the nanocalorimeter either in a thermostatic probe of a cryostat (for the lowest temperature range) or a temperature controlled socket using a standard power resistor and a home-made proportional-integral-derivative (PID) controller. Once the whole calorimeter is set at a given temperature, current/voltage curves are performed and the resistance is obtained by the extrapolation to zero current to eliminate the self-heating contribution. The resistance is measured at several temperatures, typically at steps of 10 to 20 K, to obtain enough data to ensure a proper fitting of equation 2.27. For temperatures higher than 400 K, a slightly different procedure is used. In this case, the calorimeters are placed on a temperature controlled hot plate (see Figure 2.18) and the resistance is measured under

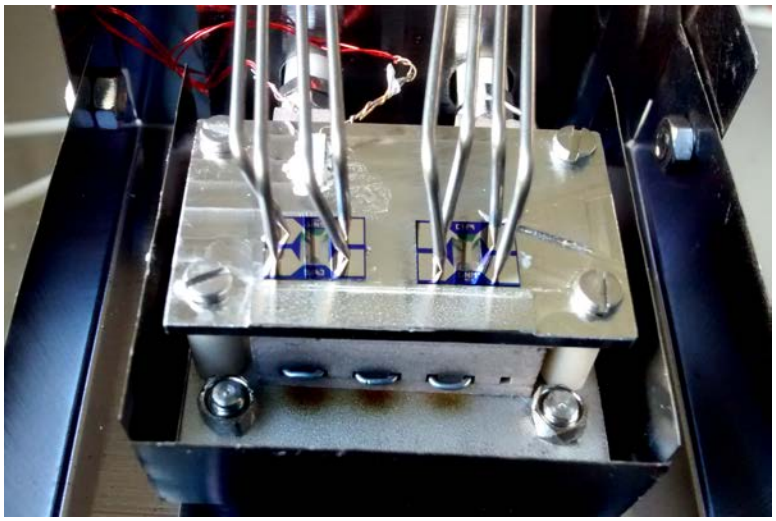

Figure 2.18: Setup for the high-temperature range calibration. The calorimeters are placed on a hot plate that is resistively heated.

argon at near-ambient pressure conditions to ensure temperature homogeneity. The advantage of this setup is that the connections are mechanical through the metallic rods (Figure 2.18) and the temperature of the hot plate can be raised higher than 400 K. In this case, the self-heating of the heater/sensor at low currents can be neglected due to the excellent heat conduction through the surrounding gas, which prevents the temperature rise. Figure 2.19 shows how the combined results of $R(T)$ using both approaches exhibit a perfect agreement in the common temperature range explored. The inset shows the melting of a 130 nm indium film used as a benchmark for the calibration. The onset of the peak is found at (429 $\pm$ 1) K, in agreement the 429.75 K melting temperature for this material.

The 3ω–Völklein microchips are calibrated following a similar proceeding as the nanocalorimeters. In this case, the important parameter to know is the dR/dT coefficient, needed to calculate the $\Delta T_{2\omega}$ (see equation 2.19) between the central platinum strip and the silicon frame. This coefficient is obtained from the polynomial fit of the $R(T)$ curve and subsequent derivative. The temperature of the whole device is set using the temperature socket (Figure 2.4).

2.5.3 Electronics and data acquisition

The same electronics (schematically shown in Figure 2.20) can be used for the fast-scanning nanocalorimetry setup, the 3ω–Völklein and the conventional 3ω. In , two twin calorimeters are. The voltage drop in both sensors (sample and reference) is pre-amplified using the low-noise instrumental amplifiers INA 114 to fit the DAQ system voltage range ($\pm$10 V). The gain of the instrumental amplifiers can be finely adjusted to offer an even higher cancellation of the differential signal. Then, this voltage can

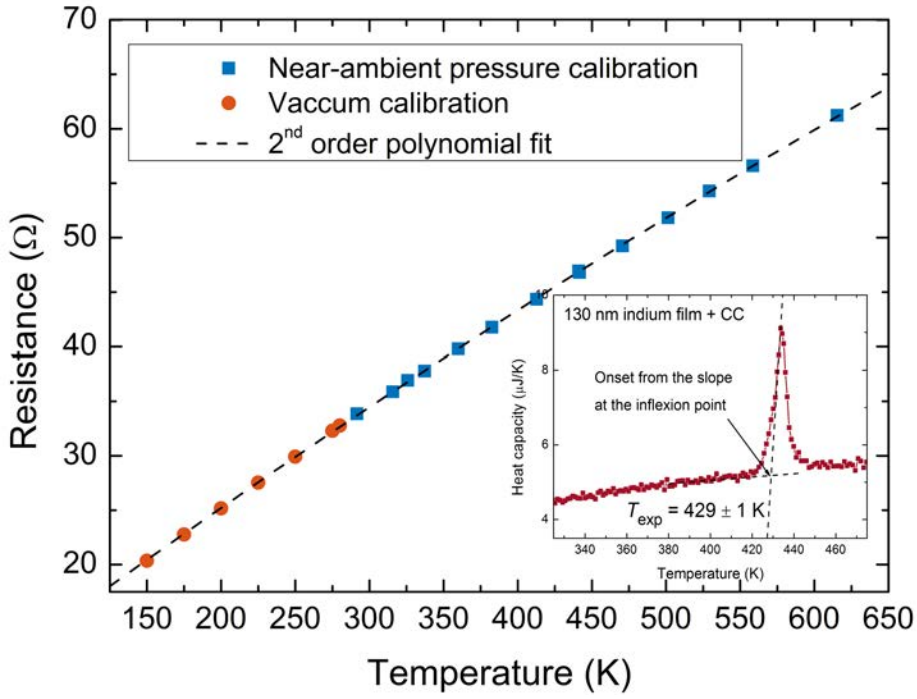

Figure 2.19: Resistance versus temperature data of a typical nanocalorimeter sensor. The points correspond the experimental data using the two setups explained in the text. The dashed line is a 2nd order polynomial fit of the whole dataset. Inset: melting of a 130 nm of indium to test the calibration procedure, with an onset temperature in agreement with the values found in the literature.

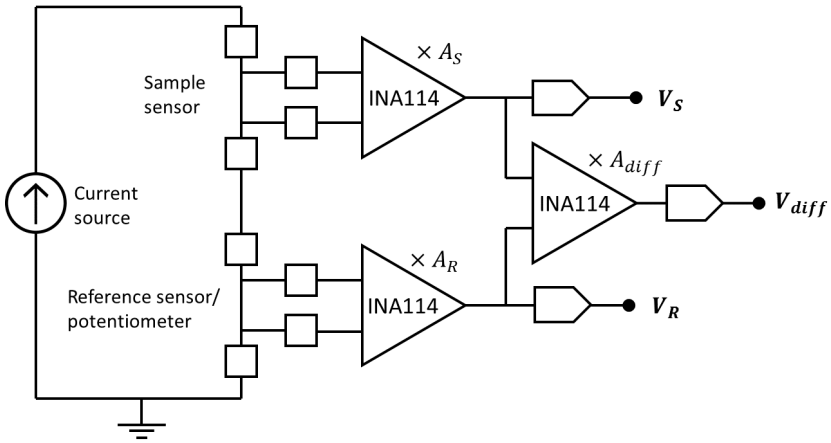

Figure 2.20: Scheme of the electronics employed in this work for both quasi-adiabatic fast-scanning nanocalorimetry and 3ω–Völklein techniques using, respectively, a DC or an AC source.

be heavily amplified accommodating the signal to the DAQ range. The calorimetric scans are performed by feeding both nanocalorimeters with a constant current pulse—typically ca. 35 mA for few milliseconds—with a software-controlled Keithley 2400 source-meter. The raw-voltage signals during the pulse are acquired using a National Instruments PCI-6221 DAQ (16-bits, 2.5 MS s^{-1}).

In a very similar way as we do in nanocalorimetry, one of the key points of the 3ω-based techniques is that a differential measurement permits to heavily amplify the 3ω voltage coming from the sample which is, generally, small. Two sensors are used again, a sample and a reference, fed in series with a current wave of known intensity by a Keithley 6221. To measure only the 3ω contribution from the sample sensor, the membrane from the reference sensor is not freed from the bulk silicon. Therefore, the self-heating is completely suppressed due to the excellent thermal link between the heater and the substrate and no $V_{3\omega}$ signal is generated. In such a way, the 1ω signal is cancelled out between both sensors and the $V_{3\omega}$ component is only produced in the sample sensor. The reference sensor can be substituted by a simple potentiometer to adjust the cancellation of the 1ω.

The same acquisition system used for the nanocalorimetry setup is also used for the 3ω–Völklein and 3ω, although at lower acquisition frequencies. The used time window corresponds to three current periods, which is translated into nine periods for the $V_{3\omega}$ component. Using LabView software, a discrete Fourier transform is performed, so the amplitude and phase of the signals in 1ω and 3ω are extracted. Once the sample device is calibrated, the $\Delta T_{2\omega}$ and, subsequently, G, can be obtained using equations 2.19 and 2.20.

Chapter 3

Stability of physical vapour-deposited glasses

3.1 Introduction

As we advanced in the Introduction chapter, one of the advantages of physical vapour deposition is the possibility to tailor the stability of the glass by tuning the deposition conditions. Briefly, when the substrate temperature is around 0.85 times the glass transition temperature, the vapour-deposited glasses, also dubbed ultrastable glasses (UG), exhibit enhanced properties, such as low enthalpy [28, 29, 56], high kinetic stability [29, 35], low heat capacities [35, 69] or high density [39, 45].

In this chapter, we use fast-scanning nanocalorimetry to obtain the specific heat signature of the glass transition in VD glasses grown at different deposition temperatures. Nanocalorimetry allows access to several properties of the evaporated organic amorphous layers. For instance, the thermodynamic stability of a glass can be quantified using the limiting fictive temperature, calculated by integration of the specific heat curve [21]. Here, three glass-formers of two different natures are used. The first studied material is the organic solvent toluene, which is taken as a model glass former. Ultrastable glasses of toluene have been prepared and characterized by several groups. At GNaM, we had previously characterized VD toluene glasses using the fast-scanning nanocalorimetry technique [29, 30]. Those studies already demonstrated the growth of glassy films with much higher onset temperatures and lower enthalpies than the liquid-cooled glasses. Ishii et al. [46, 87] used laser-light interference techniques to measure the specific volume of these glasses and showed its dependence on deposition temperature. Ahrenberg at al. [35] and Bhattacharya et al. [53] used, respectively AC chip-calorimetry and fast scanning calorimetry (using a filament as a heater/sensor) and measured the kinetic and thermodynamic stability of glasses deposited at different temperatures. Smith et al. [43] used inert gas permeation to proof also the stability of these glasses.

The nanocalorimetry technique and data analysis have been refined since the first studies performed at GNaM [29]. Therefore, the present study on toluene films aims to gain further insights into the main mechanisms governing the formation of VD glasses thanks to the improvement of the technique, a feature that will be further explored in Chapter 4.

The other two studied glass-formers are the organic semiconductor molecules TPD and α-NPD, both solid at room temperature, with their glass transition at 333 K and 368 K, respectively. In a recent work from Dalal et al. [45], both TPD and α-NPD were already shown to form denser glasses—and thus, more stable—when evaporated at the temperature window of 0.8-0.9T_g.

Regardless of the different nature between toluene and the two organic semiconductor molecules, their behaviour with respect to their glass-forming ability is fairly similar. Hence, the results concerning the three materials are displayed and discussed in parallel throughout this chapter. The thermodynamic and kinetic stabilities are studied as a function of the deposition conditions through the specific heat trace of the devitrification.

3.2 Stability of vapour-deposited glasses

The properties of VD glasses strongly depend on the deposition conditions. From the analysis of the specific heat curves corresponding to glasses deposited at different temperatures, information on both kinetic and thermodynamic stability is obtained for toluene, TPD and α-NPD. However, the deposition temperature is not the only factor controlling the stability of the evaporated glasses. The stability is always a compromise between the molecular mobility at the surface, provided by the substrate temperature that will also set the maximum stability attainable, and the time that the molecules have to explore their best configuration before being buried into the bulk, which will be determined by the deposition rate. When the deposition rates are as low as 0.5-1 nm s^{-1} or below, the stability is not largely affected by this factor. Hence, in this study, we focus only on the deposition temperature effect on the glass stability for a fixed deposition rate—generally, below 0.5 nm s^{-1}.

3.2.1 Toluene

Thin film glasses, between 20 and 250 nm thick, of toluene of different stabilities are prepared by changing the substrate temperature (T_{dep}) between 82 K (0.71T_g) and 135 K (1.15T_g) at a growth rate of 0.32 nm s^{-1}. Figure 3.1 shows the calorimetric trace for films of toluene of equal thickness but deposited at six substrate temperatures, together with

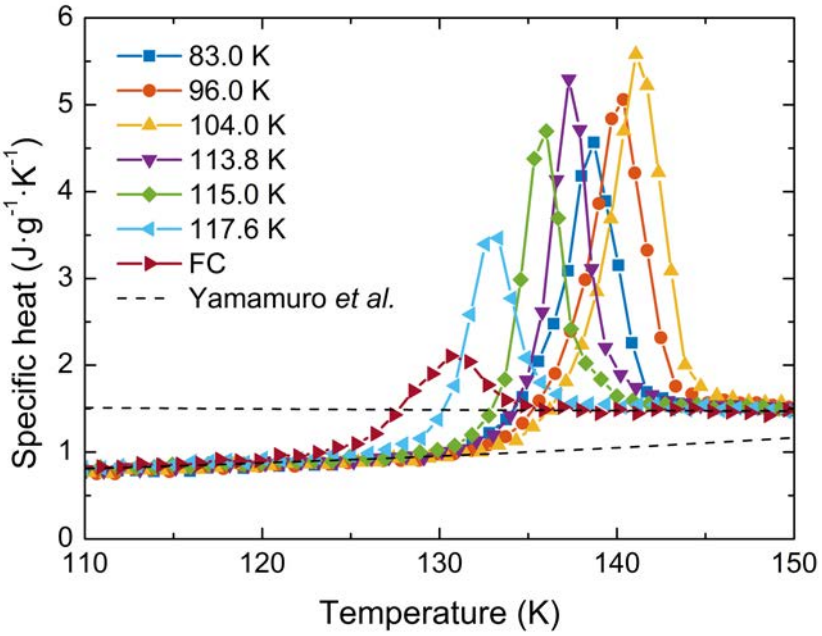

Figure 3.1: Specific heat curves of 74 nm thick toluene glasses, with a thickness dispersion of ±5 % , deposited at different temperatures (indicated by the legend) measured in-situ using quasi-adiabatic nanocalorimetry in differential mode at a heating rate of 35 000 K s^{-1}. FC stands for the fastcooled glass. The dashed lines correspond to the specific heat of the glass and liquid obtained by Yamamuro et al. [72].

the fast-cooled glass trace. The fastcooled glass is prepared from the liquid by passively cooling at ca. 500 K s^{-1}.

A rapid look at Figure 3.1, tells us that the whole devitrification process for VD toluene glasses depends on the deposition temperature, as clear differences can be seen in both the onset temperature and the area of the peak—the latter related to the excess of enthalpy. Whereas the FC glass exhibits both the lowest onset temperature and area under the peak, all the VD glasses exhibit higher onsets and peak overshoots.

The onset of the devitrification peak is indicative of the kinetic stability of the glass. This onset is calculated as the intersection between the extrapolated specific heat of the glass and the tangent line at the half maximum of the glass transition peak. More stable glasses are more deeply trapped in their potential energy landscape achieving larger relaxation times. Thus, the time needed for these molecules to be released from these locations is larger, which is translated either in major times for the devitrification in isothermal measurements near T_g or higher temperatures—higher required mobility—for the devitrification in temperature-ramping experiments. Since the glass transition is a kinetic phenomenon, the onset of the devitrification also depends strongly on the heating rates used or, generally, on the kinetics of the measurement.

Moreover, as we will see in the following chapter, the transformation mechanism by which the devitrification is taking place in some VD glasses is not homogenous. This

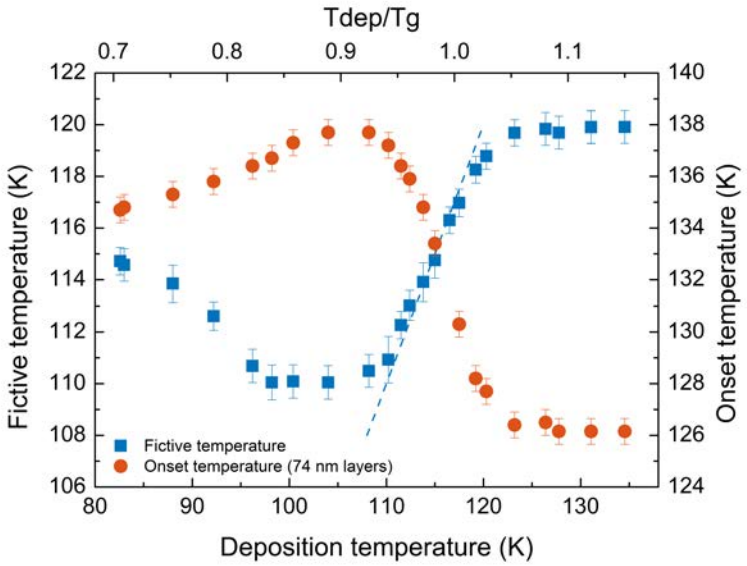

Figure 3.2: Limiting fictive temperature (blue squares, left-axis) and the onset of devitrification (red circles, right-axis) for toluene glasses as a function of the deposition temperature. The dashed line corresponds to the $T_f' = T_g$ curve. The T_f' values in the graph correspond to the average of films of different thicknesses (20 to 200 nm) since no evidence of size effects were observed when evaluating this parameter. The onset is evaluated only for 74 nm thick glasses to discard in this way the effect of the heterogeneous transformation mechanism on the normalisation of the data. The uncertainty for the T_{on} values corresponds to half the temperature step of the specific heat curves, 0.5 K in this case. The uncertainty of the T_f' corresponds to the square sum of the instrumental and statistical error.

affects the apparent onset of the glass transition in the specific heat representation—which equally weights the whole sample—leading to apparent size effects in the kinetic stability. The comparison of the specific heat curves between different stabilities is, therefore, done for a given heating rate and fixed thickness, to avoid mixing different effects in the onset of the devitrification. In Figure 3.1, the sample thickness is always 74 nm, with a dispersion in thicknesses of ± 4 nm. The onset of the devitrification as a function of deposition temperature is shown in Figure 3.2. As it was expected, the onset shows a maximum for glasses deposited around 0.89 – $0.91T_g$, indicating a maximum of kinetic stability for toluene glasses deposited in this temperature range. Above and below these temperatures, the kinetic stability decreases, although at different paces.

More information about the stability of our VD glasses can be obtained from the limiting fictive temperature (T_f'), a parameter that does not depend on the heating rates we use in our measurements and that is only dependent on the thermodynamic state at which the glass was trapped before the transformation. Specifically, in our case T_f' is defined as the intersection temperature between the glass and the supercooled liquid enthalpy curves. In particular, the enthalpy curve for the glass can be obtained by integrating the experimental specific heat curves, as shown in Figure 3.3a. In taking the

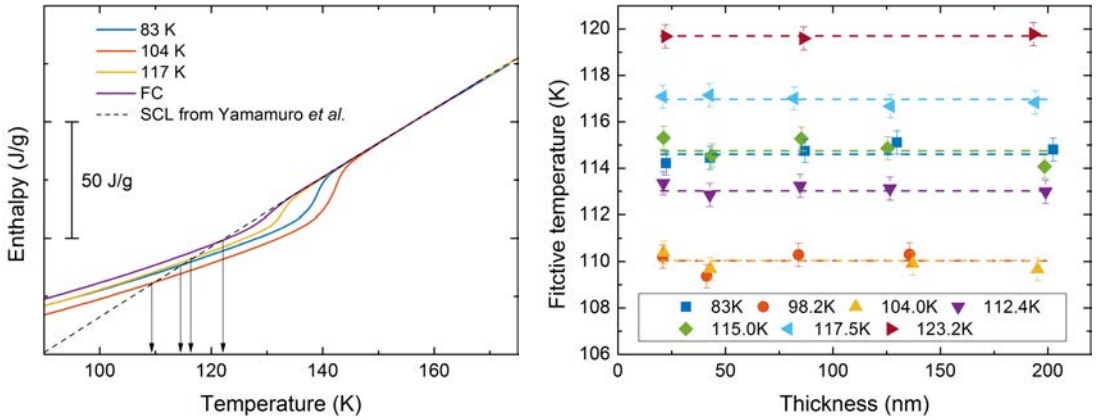

(a) Enthalpy versus temperature **(b)** T'_f versus thickness

Figure 3.3: (a) Limiting fictive temperature determination for ca. 130 nm thick layers of toluene deposited at different temperatures, as labelled in the legend. The FC stands for the fastcooled glass. The enthalpic curves for the different samples are obtained by integrating the specific heat with respect to the temperature. The dashed line corresponds to the extrapolated supercooled liquid (SCL) enthalpy using the specific heat data from Yamamuro et al. [72]. The arrows indicate how the limiting fictive temperature is determined for each curve. **(b)** The limiting fictive temperature versus thickness of toluene samples for different deposition temperatures, as indicated by the legend. The dashed lines correspond to the mean value.

SCL enthalpy curve as a reference, we are assuming that the liquid phase we obtain after the glass transition is always the same, independently on the previous thermal history of our glass. Contrary to the T_{on}, the T'_f does not depend on the transformation mechanism. T'_f does not depend either on the thickness of the films as can be seen in Figure 3.3b, at least for the deposition temperature range and thicknesses under study for toluene glasses.

In Figure 3.2, we represent also the limiting fictive temperature (red-circles, left-axis) together with the onset of devitrification (blue-squares, right-axis) as a function the deposition temperature for toluene glasses. There is a high coincidence between the maximum of kinetic and thermodynamic stability, which is evidenced by a minimum in T'_f, for the deposition temperature range of 100-108 K that corresponds to 0.85-0.92T_g. The high stability range at 100 – 108 K is in agreement with previously reported results from Ahrenberg et al. [35], where they measured with AC nanocalorimetry the onset temperature for vapour-deposited glasses of toluene at much lower heating rates of 10 K min^{-1}. The T'_f are slightly lower compared to the previously published values at GNaM [29]. This discrepancy is well-explained by the procedure they used to extract the heat capacity data of thick films, which underestimated the enthalpy involved in the transition leading to higher values of T'_f. See reference [30] for further details.

Another interesting feature that can be seen in Figure 3.2 is that glasses deposited between 110 K and 120 K have a limiting fictive temperature that coincides with their

deposition temperature. In a previous work from Dalal et al. [39], it was shown that a glass deposited at substrate temperatures between $\sim 0.89 T_g$ and T_g have the properties expected for the supercooled liquid at that temperature, what would indicate the equilibration to the supercooled liquid state during the deposition. In general, the lowest temperature of this equilibrium range depends on the deposition rate, i.e. for some molecules slower deposition rates yield a smaller low-temperature limit [69] since they have more time to equilibrate. However, there is still the limit of the laboratory time scales even for the surface equilibration process. On the other hand, the upper boundary of this temperature range is not necessarily the conventional T_g, but it is determined by the cooling rate imposed between the deposition temperature and the measurement temperature. It is possible to obtain glasses which are in equilibrium with the liquid above T_g if the cooling rate is fast enough. Consequently, above this upper-temperature limit, the stability of the resulting glass will become independent of the deposition temperature. In our case, glasses are grown in the range from 0.7 to $1.15 T_g$ (82 to 130 K) and passively cooled at a rate of ca. $500\,\mathrm{K\,s^{-1}}$. Cooling from a high temperature liquid at this rate results in a glass with a T_f' of ca. 120 K. Thus, if the deposition temperature is higher than 120 K, the resulting glass will always have, with this cooling rate, a T_f' of 120 K regardless of the deposition temperature, as can be seen in Figure 3.2.

3.2.2 TPD and α-NPD

A very similar study is now presented for two organic semiconductor glass-formers, from now on referred also as OSG. Now, thin layers between 20 and 200 nm are deposited at a rate of $0.21\,\mathrm{nm\,s^{-1}}$ for TPD and $0.16\,\mathrm{nm\,s^{-1}}$ for α-NPD. The explored substrate temperatures in this section are in the range of 0.6-$1.1 T_g$, being 333 K and 368 K the glass transition temperatures of TPD and α-NPD respectively.

Figures 3.4 for TPD and 3.5 for α-NPD show the calorimetric trace for 72 nm thick glasses of TPD and 95 nm thick glasses of α-NPD with thickness dispersion of 4 % and 7 %, respectively. Similarly as we have seen for toluene, both the onset and area of the peak clearly depend on T_{dep}. In both cases, the onset temperature is higher for glasses deposited in the range of 0.85-$0.9 T_g$. This increase in T_{on} is accompanied by a higher enthalpy overshoot, as described before for toluene films.

The calculation of T_f' for both TPD and α-NPD present some difficulties. The fast heating rates used in this study shift the glass transition to much higher temperatures and, consequently, the SCL specific heat has to be largely extrapolated to obtain the T_f'—around 100 K in the case of both OSG. To this drawback, we have to add the lack of specific heat data for these materials, both in the liquid and the glass region. Small

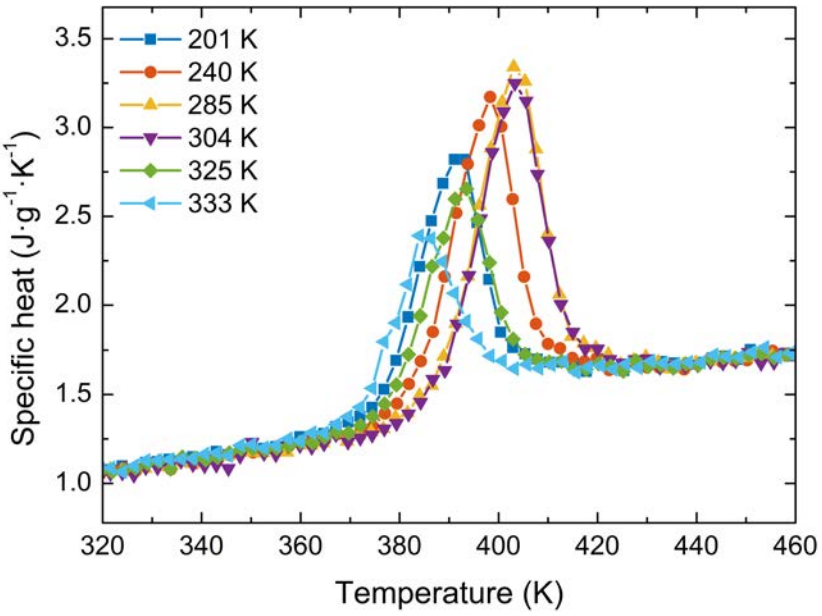

Figure 3.4: Specific heat curves of 72 nm thick film glasses of TPD deposited at different temperatures (indicated in the legend). The thickness dispersion within the samples is of ±4 %.

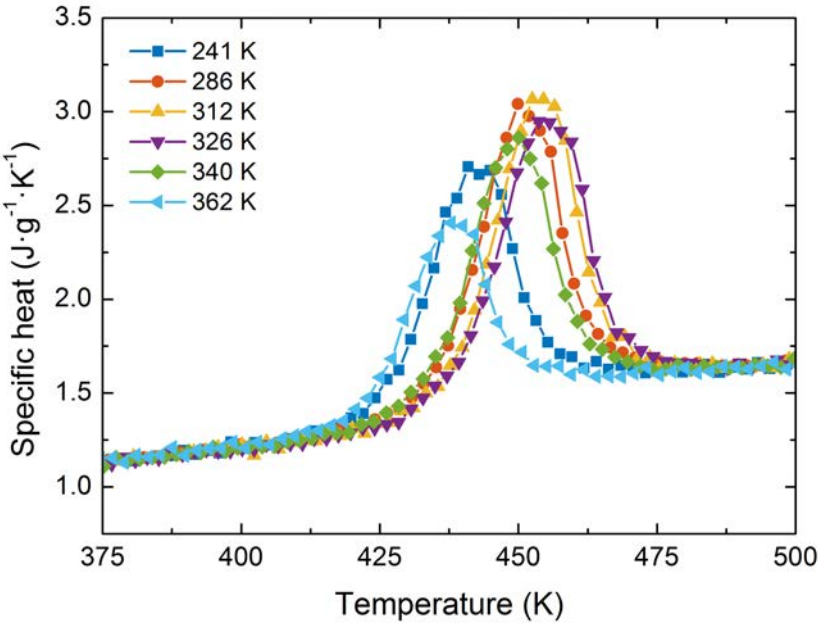

Figure 3.5: Specific heat curves of 95 nm thick α-NPD glasses deposited at different temperatures (indicated by the legend). The dispersion in thickness within the different samples is of ±7 %.

errors in the linear term of the specific heat of the SCL (quadratic in the enthalpy representation) can be largely magnified at the extrapolation. Consequently, it is not possible to give reliable absolute data of the fictive temperatures of our samples. Despite the lack of accuracy in the determination of the supercooled liquid enthalpy, it is possible

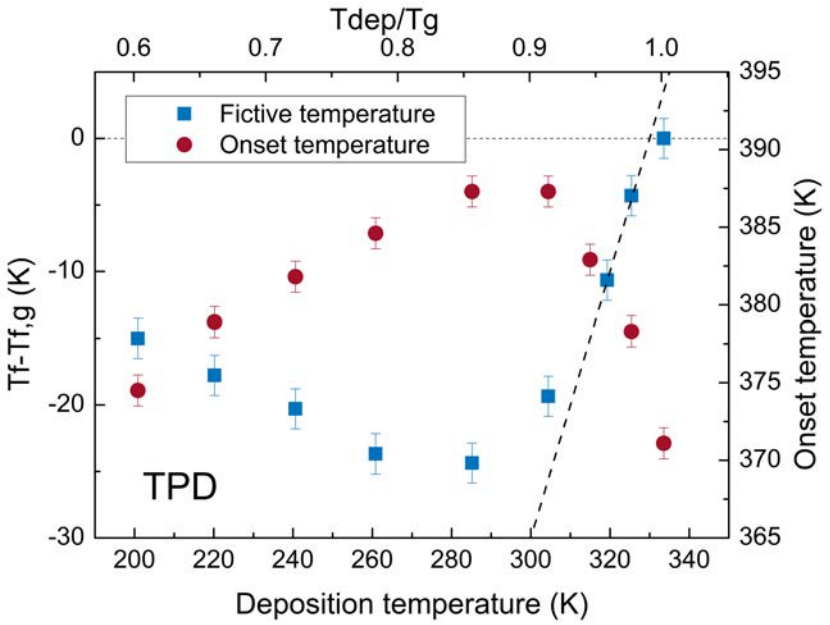

Figure 3.6: Limiting fictive temperature (blue squares, left-axis) and the onset of devitrification (red circles, right-axis) for TPD glasses as a function of the deposition temperature. The T'_f is expressed as the relative change with respect to the conventional glass, $T_{dep} = T_g$, plotted as a function of T_{dep}. The value at each T_{dep} is the mean T'_f of 20 to 200 nm thick layers, as it is size independent for this thickness and deposition temperature range. The dashed line correspond to a straight line with a slope of one. The uncertainty in T'_f corresponds to the square sum of statistical uncertainty (95 % of confidence interval) and the instrumental uncertainty.

to distinguish with precision and reproducibility the different thermodynamic stabilities since the error, if any, is systematic. Keeping this in mind, we can represent the difference $T'_f - T_{f,g}$ as a function of T_{dep}, where $T_{f,g}$ is the fictive temperature that we obtain for the glass deposited at T_g. In the case of toluene, reporting accurate values for the limiting fictive temperature is possible since the extrapolation needed is only about 30 to 40 K from the supercooled liquid region to the intersection with the T'_f at the glass region. Moreover, the liquid specific heat for toluene is well reported [72].

In Figure 3.6, for TPD, and in Figure 3.7, for α-NPD, we represent the fictive temperature change relative to a sample deposited at T_g, for which it is assumed that $T'_f = T_g$, and the onset temperature versus the deposition temperature. The dependence of the stability on T_{dep} is very similar to what we have seen for toluene. As we decrease the deposition temperature starting from T_g (or above), the stability of the evaporated samples increases until reaching a maximum in T_{on} (minimum in T'_f) around 285 K for TPD and 315 K for α-NPD. This maximum in the thermodynamic stability coincides now with a deposition temperature of $\sim$0.85T_g for both OSG. When the deposition temperature is further decreased, the stability of the evaporated samples starts to decrease again. Despite the determination in the T'_f lacks accuracy, we can plot a straight line with a slope of one—in analogy to what we have done for toluene—to represent the

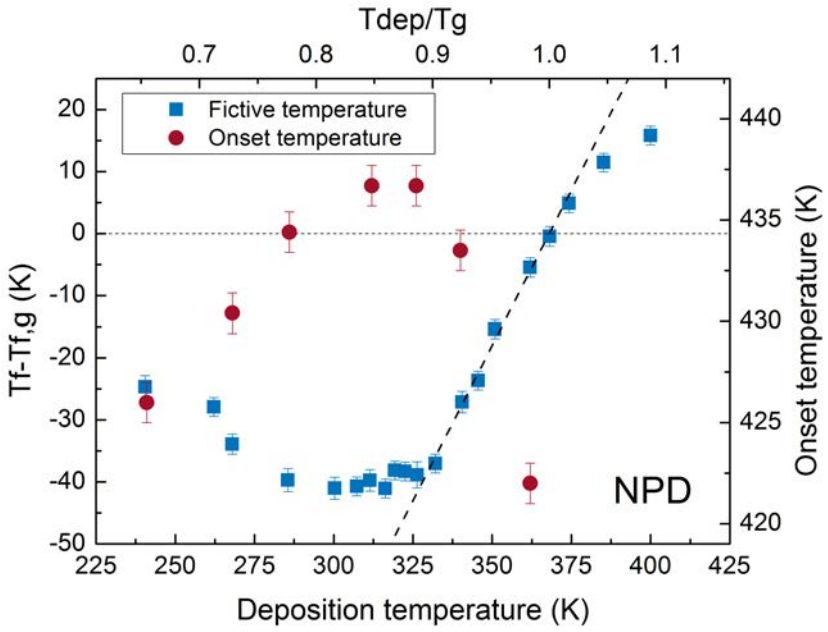

Figure 3.7: Limiting fictive temperature (blue squares, left-axis) and the onset of devitrification (red circles, right-axis) for α-NPD glasses as a function of the deposition temperature. The T_f' is expressed as the relative change with respect to the conventional glass, $T_{dep} = T_g$, plotted as a function of T_{dep}. The value at each T_{dep} is the mean T_f' of 20 to 200 nm thick layers, as it is size independent for this thickness and deposition temperature range. The dashed line corresponds to a straight line with a slope of one. The uncertainty in T_f' corresponds to the square sum of statistical uncertainty (95 % of confidence interval) and the instrumental uncertainty.

equilibrium SCL (dashed lines in Figures 3.6 and 3.7). We can see how the T_f' of glasses deposited above $0.85T_g$ follows reasonably well this line indicating the equilibration of these glasses to the SCL.

3.3 Correlation between stability and density

We have seen how three different molecular glass formers—toluene and the two organic semiconductor molecules—exhibit a similar behaviour when comparing the stability versus the deposition temperature, expressed in terms of the ratio T_{dep}/T_g. In all three cases, the stability of the evaporated glasses is maximum when evaporated in the temperature range of $0.8\text{-}0.90T_g$. In what seems a universal behaviour, many other molecular glass formers have also been reported to form ultrastable glasses when evaporated at the same temperature window. Within them, the first systems in which this behaviour was reported, TNB and the pharmaceutical drug indomethacin [10]. It has also been reported on other pharmaceutical drugs such as celecoxib [33], in other benzene derivatives such as ethylbenzene [29, 30, 43, 46] or methyl-m-toluate [38], and in the same organic semiconductors TPD and α-NPD [45].

The results shown in Figures 3.6 and 3.7 agree with the ones presented in Dalal et al. [45] and Walters et al. [40] for TPD and α-NPD. There, they report how these systems show a dependence of density on the substrate temperature. The parameter they use to characterise the glass stability is the density variation relative to the SCL. In Figures 3.8a and 3.8b we plot our limiting fictive temperature data together with density data of TPD [40] and α-NPD [45], respectively and with properly scaled axes. Both Figures show a good correlation between the $\Delta T_f'$ and the density variations. Regarding the α-NPD data, although there is a slight deviation at the lowest explored T_{dep} (the error bars from the reference are plotted in this case for the sake of comparison), the correlation is still high for the 0.7-1.0T_g range in the deposition temperatures. This good correlation between these two quantities was already reported by Rodríguez-Tinoco et al. for the model glass former indomethacin [54]. A resembling Figure for toluene is not shown since there is no density data covering all T_{dep} range found in the literature. Both the density and the limiting fictive temperatures measurements shown here are properties averaged over the whole sample. At the light of these results, one could say that glasses with the same T_f' (or density) deposited below and above the 0.85T_g are structurally equivalent. However, as we will see in Chapter 4, this equivalence does not hold true when looking at other glass properties. All we can say is that T_f' and density provide an equivalent way of characterising the thermal stability as a function of T_{dep}.

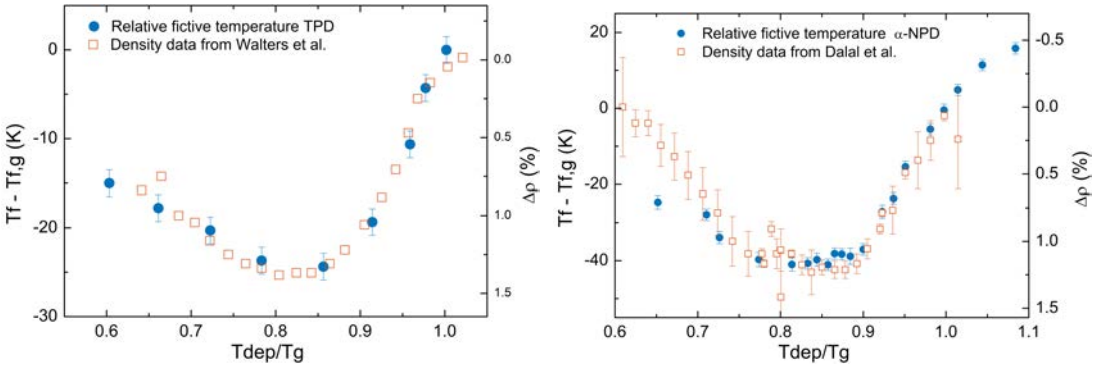

(a) TPD **(b)** α-NPD

Figure 3.8: Comparison between the limiting fictive temperature (left-axis) and density variation as a function of the deposition temperature for TPD and α-NPD glasses. Density data is taken from Wlaters et al. [40] for TPD and from Dalal et al. [45] for α-NPD

Toluene, TPD and α-NPD show the same behaviour with deposition temperature as many other molecular glass-formers, with a maximum of stability around the 0.85T_g. Below this temperature, the stability (and density) starts to decrease again. The most accepted view for the ultrastable glass formation is still the enhanced molecular mobility on the surface [28]. Molecules at the surface are much faster in sampling their configurational phase space than the molecules trapped in bulk—as it would happen in an ageing process—reaching lower-energy configurations even achieving the corresponding supercooled liquid equilibrium configuration. When the deposition temperature

is further decreased, even the surface equilibration times become larger than the lab timescales precluding the molecules the possibility to sample their best configurations in the potential energy landscape properly. Very recently, Ngai et al. [31] have related the stable glass formation to the enhanced surface mobility and the β-relaxation. Briefly, they state that the stable glass T_{dep} region falls in-between the standard T_g, where the α-relaxation time is 100-1000 s, and the secondary $T_{g,\beta}$, where the relaxation time of the β-relaxation is 100-1000 s too.

3.4 Summary

We have used fast scanning quasi-adiabatic nanocalorimetry to characterise the glass transition in toluene, TPD and α-NPD glasses obtained by physical vapour deposition at different substrate temperatures. When this temperature is set in the range of 0.80-0.90T_g, glasses with the highest stability can be obtained, compared to the conventional glasses prepared from the liquid.

We have seen how glasses grown above ca. 0.90T_g have a limiting fictive temperature that corresponds to their deposition temperature. This suggests that these glasses are in equilibrium with the liquid, in agreement with previous results in indomethacin from density measurements and nanocalorimetry. For TPD and α-NPD, a good correlation between the limiting fictive temperature—or thermodynamic stability—and the glass density has been found, in agreement with resembling results obtained for indomethacin.

Chapter 4

Heterogeneous transformation mechanism in vapour-deposited glasses

4.1 Introduction

Among outstanding properties of vapour-deposited thin film glasses, the heterogeneous transformation mechanism by which they overcome the devitrification process into the supercooled liquid state [34, 41, 42, 88] is, probably, the most remarkable. This mechanism contrasts with the homogeneous transformation observed in glasses prepared by quenching the liquid. It has been proposed that in ultrastable glasses the molecules are so tightly packed that the transformation begins where the mobility is higher, i.e. at surfaces and/or interfaces [27]. Experimentally, this phenomenon has been seen using a variety of techniques in several systems. For instance, secondary mass ion spectrometry (SIMS) [41, 42] has been used to trace the evolution and transformation into the supercooled liquid by following the evolution of deutered IMC multilayers. A propagating transformation front has also been measured using spectroscopic ellipsometry [40, 89] by modelling the optical response of vapour-deposited glasses of IMC and TPD through time during isothermal experiments. In AC-calorimetry for IMC [36], ethylbenzene and toluene [35], the propagating front has been inferred from the linear dependence of the transformation time with the thickness of the samples. Finally, in previous studies on IMC, we have inferred the growth front from the calorimetric trace of the devitrification using differential scanning calorimetry [34] and fast-scanning nanocalorimetry [34, 54] whereas Bhattacharya and Sadtchenko [53] identified the transformation front, in toluene also, using another fast-scanning calorimetry technique.

Previous studies on many of the mentioned glass-formers have shown that the transformation rate is mainly driven by the mobility of the adjacent new formed liquid

layer [34, 40, 41, 88]. Specifically, for many organic glasses it has been found that the transformation rate follows an empirical relation with τ_α, the α-relaxation time of the supercooled liquid [90]:

$$v_{gr} = C\tau_\alpha^{-\gamma} \tag{4.1}$$

where C depends on the deposition conditions [54] and is independent of temperature and $-\gamma$ defines the slope of the growth front velocity as a function of the relaxation time of the liquid in a log-log plot. Generally, in these molecular glass formers, the relaxation time of the liquid follows a VFT-type expression (equation 1.6). The relation expressed in 4.1 was initially found for vapour-deposited glasses of IMC and TNB using secondary ion mass spectrometry [41] in a limited temperature range around the corresponding T_g of the material. More recently, we have shown using fast-scanning nanocalorimetry on that the same relationship holds across a very wide temperature range, from T_g up to 75 K above T_g, corresponding to 12 orders of magnitude in relaxation time in the particular case of IMC [34].

One of the advantages of physical vapour deposition is the possibility to tailor the stability of the produced glass by tuning the deposition conditions. Several studies have already shown that not only highly stable glasses transform via a heterogeneous mechanism, but, in general, vapour-deposited glasses with lower stability also start the transformation process via a growth front [40, 54, 89]. For instance, Walters et al. [89] and Dalal et al. [89] measured, respectively, the front velocity of glasses of TPD and IMC with different stability by ellipsometry close to ambient temperature. Rodríguez-Tinoco et al. used fast-scanning nanocalorimetry to measure the growth front velocity of IMC glasses spanning a broad range of stabilities [54]. It was found that the velocity at which the front propagates in glasses of different stabilities, including the ultrastable glass, had the same temperature dependence. However, the absolute value of the growth front velocity depends on the stability of the glass. This result was in contrast with both RFOT and pinning models, which foresee a strong temperature dependence of the growth front velocity but a much smaller influence of the stability [66, 91], determined in our case by the deposition temperature.

As shown in the previous chapter, the thermodynamic stability of a glass is typically quantified using the limiting fictive temperature. Several studies have concluded, though, that this parameter does not univocally determine some properties of the glass [92]. In this context, we established in a previous work [54] that the growth front velocity of a transforming glass of IMC could not be determined considering only its limiting fictive temperature, but two different dependencies arose, depending on whether the glass was deposited above or below $0.85T_g$. According to previous studies [39, 93, 94], IMC vapour-deposited glasses exhibit certain molecular anisotropy that depends on the deposition conditions. From the correlation between growth front velocity and molecular anisotropy in IMC glassy films, it was inferred that the arrangement of the

molecules in the glass could also play a role in the transformation velocity. Yokoyama showed that molecular orientation in organic glasses is directly related to the shape of the molecules [95]; more planar or linear molecules tend to align parallel to the substrate at certain deposition conditions, while more bulky or compact molecules tend to have random orientation producing more isotropic glasses. Depending on the deposition temperature, molecules can even tend to align perpendicular to the substrate, as was shown for different organic molecules by Dalal and co-workers [45, 93]. In particular, the two organic semiconductors studied in this thesis—TPD and α-NPD—have been shown to exhibit a molecular orientation that depends on the deposition conditions [45].

In this chapter, we first present a method to identify the transformation mechanism governing the glass transition in vapour-deposited glasses. Secondly, we address the variables that apparently control the heterogeneous transformation mechanism of glasses prepared in a wide range of stabilities. For that purpose, we extract from the calorimetric trace corresponding to samples of toluene, TPD and α-NPD the growth front velocity and analyse it as a function of the different glass properties, such as thermal stability or molecular orientation.

4.2 Identification of the transformation mechanism

The specific heat curves seen in Figures 3.2, 3.6 and 3.7 are obtained by dividing the heat capacity curve by the total mass of the film, and thus equally weighting the contribution of the whole sample during the transformation. When using this type of normalisation—i.e. the specific heat—, samples transforming via a homogeneous bulk mechanism show a complete overlap regardless of their thickness, as in the case of the fast-cooled glass. On the other hand, if the glass transition is not a homogeneous process, mass normalisation yields curves with different onset temperatures. This is the case of our VD films with onset temperatures that shift depending on the thickness of the sample, as shown in the left-side panels of Figures 4.1, 4.2 and 4.3 for toluene, TPD and α-NPD respectively. We had previously observed this shift for indomethacin thin film glasses [34, 54], where this behaviour was shown to be related to the transformation mechanism [34].

An ad-hoc normalisation procedure of the heat capacity curves that considers the surface of the sample allows the identification of the transformation mechanism. This normalisation procedure consists in separating the different contributions of the experimental heat capacity:

$$C_p^{exp}(T) = (m_0 - m_l(T))c_p^g + m_l(T)c_p^l + \Delta h \frac{dm_l(T)}{dT} \tag{4.2}$$

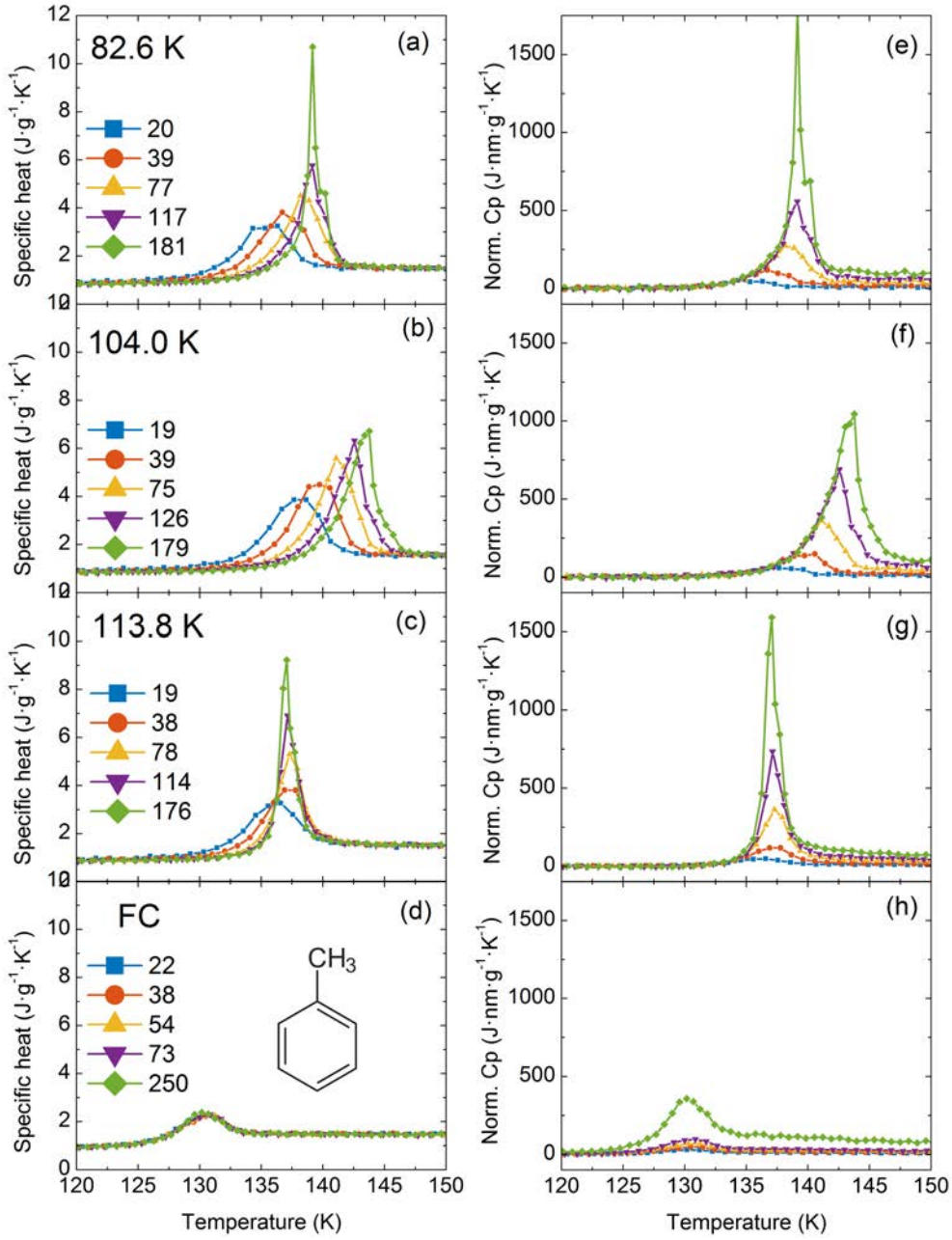

Figure 4.1: Left panels: specific heat curves for toluene films obtained at different deposition temperatures: **(a)** 82.6 K ($0.7T_g$), **(b)** 104.0 K ($0.89T_g$) and **(c)** 113.8 K ($0.97T_g$); and **(d)** after fast cooling the super-cooled liquid. Right panels: curves obtained by normalizing the same heat capacity data from the left panel using equation 4.3. The legend indicates the thickness of the films in nm.

where c_p^l and c_p^g refer respectively to the specific heat capacity of the liquid and the glass, Δh the enthalpy involved in the transformation, m_0 the total mass of the sample and m_l the mass that has transformed already to the liquid, which is a function of time and temperature and can be expressed as $m_l(T) = \rho_l(T)A\xi_l(T)$ where ρ is the density of the material, A is the surface and ξ_l is the film thickness that has already

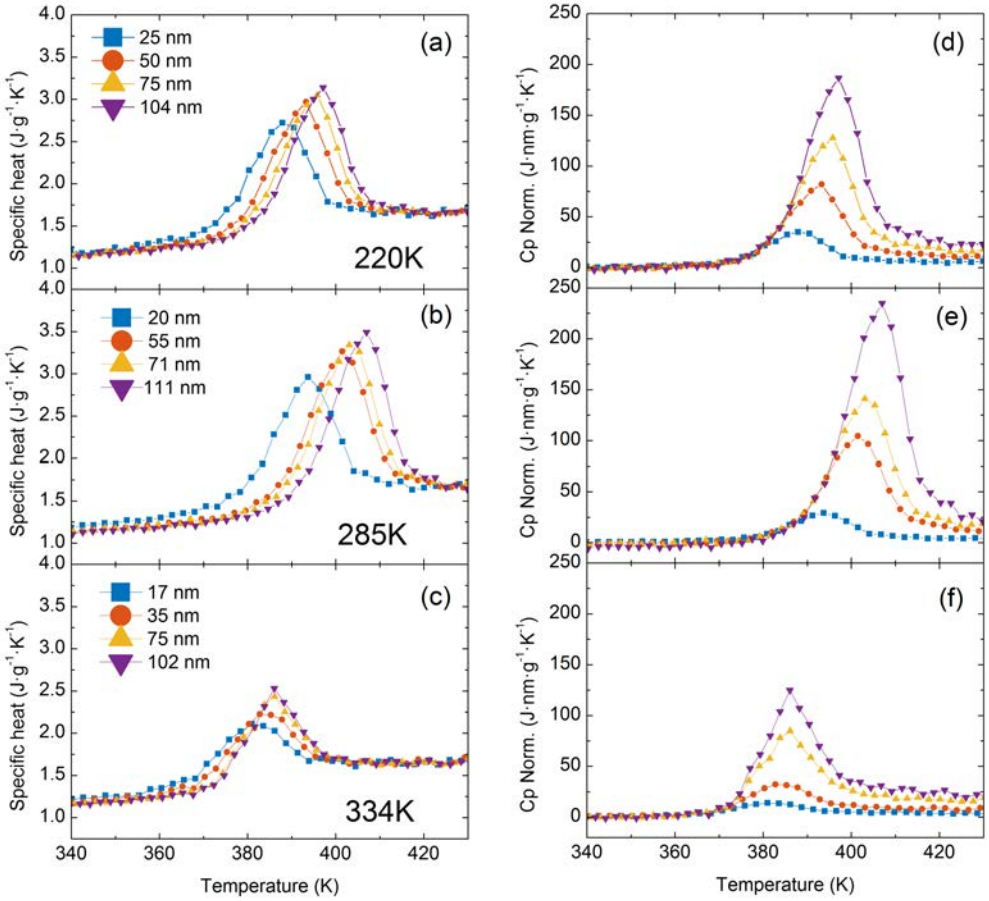

Figure 4.2: Left panels: specific heat curves for TPD films obtained at different deposition temperatures: **(a)** 220 K ($0.66T_g$), **(b)** 285 K ($0.86T_g$) and **(c)** 334K (T_g). Right panels: curves obtained by normalising the same heat capacity data from the left panel using equation 4.3. The legend indicates the thickness of the films.

transformed to liquid, assuming a situation where exclusively a transformation front is taking place. Expressing equation 4.2 in terms of film thickness and moving all the potential non-common parameters of the different samples, i.e. surface area and total thickness, to the left side of the equation we get:

$$c_p^{norm}(T) = \frac{C_p^{exp}(T)}{\rho A} - c_p^g \xi_0 = \xi_l(T)\left(c_p^l - c_p^g\right) + \Delta h \frac{d\xi_l(T)}{dT} \tag{4.3}$$

where ξ_0 is the total thickness of the sample and ξ_l the liquid transformed fraction. This accounts for the change in thickness from glass to liquid. The thicknesses are inferred from the mass (inferred from the c_p at the liquid phase) using the density, assumed constant, and the area, corresponding to the sensing area of the chip. The density values are reported in Section 2.1.6. The model proposed in equation 4.3 allows the identification of this heterogeneous mechanism because we have two distinct phases during the transformation: a fraction of the sample that has already been transformed to the supercooled liquid and a fraction that remains still a glass.

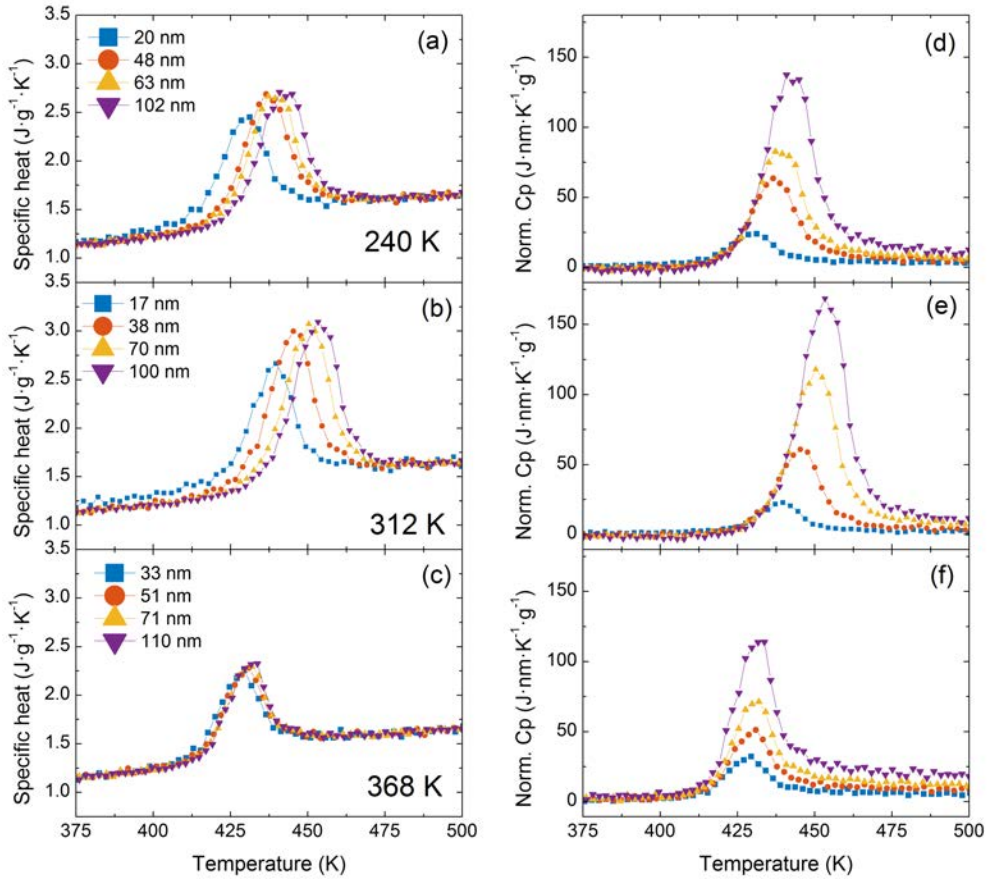

Figure 4.3: (Left panels) Specific heat curves for α-NPD films obtained at different deposition temperatures: (a) 240 K ($0.65T_g$), (b) 285 K ($0.85T_g$) and (c) 368 K (T_g). (Right panels) Curves obtained by normalising the same heat capacity data from the left panel using equation 4.3. The legend indicates the thickness of the films.

In the case of a heterogeneous transformation mechanism consisting of parallel fronts that advance at a constant temperature-dependent rate, i.e. independent of the thickness of the film, the onset of the normalised curves should collapse while this mechanism is dominating the transformation. If the sample is thick enough—the exact limit for "enough" will depend on the stability of the glass—, during the progression of the front the homogeneous transformation is triggered, and this normalisation procedure is no longer valid. Once the bulk transformation starts to be dominant, mass normalisation is again easier to interpret. In this latter case, in the specific heat representation, the curves would begin to collapse into a single one as we scan thicker and thicker samples.

Right panels in Figure 4.1 show the resulting curves for toluene after applying the normalisation presented in equation 4.3. For samples deposited at 104 K (Figure 4.1f), the onset of all the curves collapses into a single curve irrespectively of their thicknesses. On the other hand, when looking at the calorimetric trace of the samples deposited at 82.6 K and 113.8 K (Figures 4.1e and 4.1g respectively), we see that the onsets of the

normalised curves overlap only up to ca. 138 K and 133 K, respectively. Above that temperature, the bulk transformation is triggered, and the front normalization procedure starts to underestimate the transformed volume which, in the case of homogeneous bulk processes, depends on the total mass of the sample. It is worth noticing that the normalization procedure described by equation 4.3 does not provide any meaningful interpretation for the FC glass (see Figure 4.1h). In the specific heat representation, all the curves for the FC glasses collapse into a single one, indicative of a homogenous mechanism (see Figure 4.1d).

A similar analysis can be done with the organic semiconductor molecules. Figures 4.2 and 4.3 represent the specific heat (left panels) and the ad hoc normalised curves (right panels) for TPD and α-NPD, respectively. Like before, we show the calorimetric trace for glasses deposited at three different deposition temperatures for each material, the UG glass with a T_{dep} around $0.85T_g$, a lower stability glass the deposited around $0.65T_g$ (left-branch of Figure 3.6) and a glass deposited at T_g. Glasses deposited at T_g show an apparent shift in the onset of the transformation only for the thinnest samples, approximately up to 40 nm in both materials. For thicker films, the bulk is triggered, and the specific heat curves start to collapse since the transformation takes place homogeneously in the rest of the volume. On the other hand, glasses deposited at $0.65T_g$ and $0.85T_g$ (Figures 4.2a-b and 4.3a-b) show a clear onset shift with the thickness in the specific heat curves (left-panels) whereas the surface normalization produces the collapse of all curves to a common onset (right-panels).

We rationalise the collapse of the calorimetric trace using the normalisation presented in equation 4.3 (left panels of Figures 4.1, 4.2 and 4.3) with the existence of a parallel growth front mechanism. In the proposed model we have assumed a growth front velocity that does not depend on the sample's thickness. Under this assumption, the curves would only collapse when this parallel growth front is the only—or the dominating—transformation mechanism. As soon as the bulk transformation mechanism appears, the ad hoc normalisation does no longer yield a single onset of the transformation. We can define the crossover length ξ_{co} as the distance that the propagation front travels before the bulk transformation is triggered. This distance strongly depends not only on the stability of the glasses but also on the deposition temperature and is further investigated in Section 4.6 for the toluene system. This combined heterogeneous and homogeneous transformation mechanism has been observed experimentally for IMC [36], TNB [96] and methyl-m-toluate [38, 90] but has also been predicted by simulations based on facilitated Ising models [63, 64] and random pinning models [66].

Finally, it is worth noticing that, while we can identify that the glasses transform via a propagating growth front, we cannot distinguish between the existence of one (surface-initiated) or two fronts (surface and interface-initiated). Contrary to other techniques

where the growth front is directly traced—such as SIMS [41]—, in our case the front is inferred by comparing several samples with different thicknesses that exhibit a sufficiently dominant growth front mechanism that allows its detection. The detection of the existence of one or two growth fronts using nanocalorimetry can done by using capping layers to block the front and subsequently analyse the calorimetric trace. This strategy is further addressed in Chapter 5.

4.3 Front velocity calculation

The differential equation 4.3 can be solved for $\xi_l(T)$ using the experimental data. The derivative of $\xi_l(T)$ is, precisely, the transformation rate of the transition (see Figure 4.4a). While the dominating transformation mechanism is the surface-initiated front—as already indicated on the right side of equation 4.3—this rate can directly yield the growth front velocity by:

$$v_{gr}\left(T\right) = \beta\left(T\right)\frac{d\xi_l(T)}{dT} \tag{4.4}$$

where β is the instantaneous heating rate evaluated at each temperature.

The only parameter that must be imposed in solving equation 4.4 is the total excess enthalpy of the process. This parameter is obtained by imposing that the transformed liquid fraction goes from 0, at the glass region, to ξ_0, which is the total thickness of the sample fully transformed into the SCL. To obtain the front velocity, we must multiply it by the heating rate. The latter, due to the nature of the technique, is temperature dependent and can be readily obtained from the raw data. It is important to note that the growth front velocity is taken from the temperature range where all the curves—corresponding to different thicknesses and a given deposition temperature—collapse (Figure 4.4b). The velocity values for the common range are subsequently averaged among the different thicknesses.

The range in which the propagating front can be calculated is limited, therefore, by the amount of sample that transforms via this mechanism before the bulk is triggered. In that framework, once the homogeneous transformation starts, the curves do no longer collapse when using the ad hoc normalisation and the v_{gr} values cannot be obtained. We have to note that for both OSG the low accuracy of our specific heat data for both materials might lead, as happened with the limiting fictive temperature, to less accurate absolute values of the front velocity. It is important to remark that high precision is reached anyway with relative values.

Figure 4.5 shows the growth front velocity for the three thin-film glass-formers with thicknesses between 20 and 200 nm obtained at different deposition temperatures. Clearly, a change in the deposition temperature yields a glass with a different front

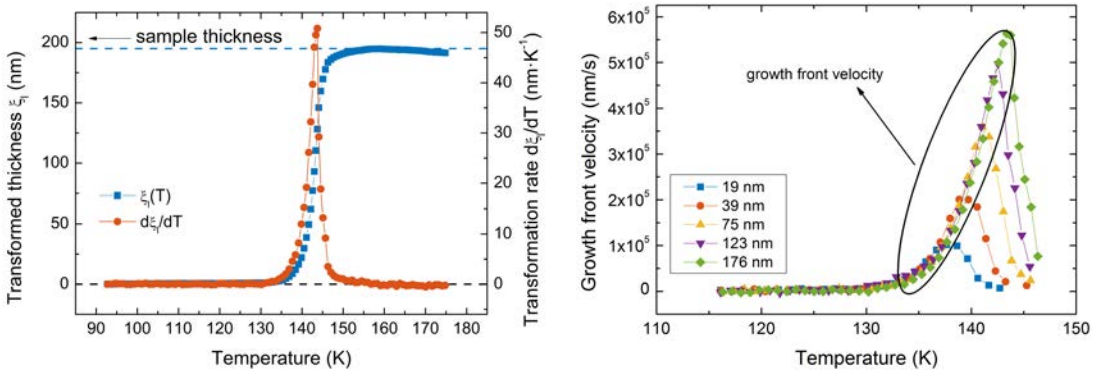

(a) Calorimetric signal deconvolution **(b)** v_{gr} determination

Figure 4.4: Determination of the growth front velocity. **(a)** Solution of the differential equation 4.3 (blue squares, left-axis) going from zero to the total thickness of the sample. The transformation rate is also represented (red circles, right axis). **(b)** Growth front velocity of an UG of toluene. The legend indicates the thickness of the sample. The highlighted region corresponds to the overlapping region from where the growth front velocity is inferred.

velocity. At the temperature range where the front is the dominating transformation mechanism, all three materials exhibit a linear relationship between the logarithm of the growth front velocity and the inverse of the temperature, irrespectively of the deposition temperature. The temperature range in which we are obtaining the growth front velocities is different for each material. For toluene, this range covers about 8 K—approximately from 132 K to 140 K, depending on the stability. In TPD we are covering at most 20 K in temperature, starting around $Tg + 37\,\mathrm{K}$ and in α-NPD, we are covering at most 26 K, starting around $Tg + 40\,\mathrm{K}$.

4.4 Effect of liquid mobility on the transformation rate

From the kinetic facilitation perspective [63], transformation fronts are expected to start where the mobility is higher and to facilitate the movement of the subsequent lower mobility regions. Following this reasoning, the higher the temperature, the higher the mobility of the molecules at the already transformed supercooled liquid layer and therefore, the faster the front.

Toluene is a well-characterised system and many properties of the glass and the supercooled liquid are easily found in the literature (specific heat [72], specific volumes [46] or relaxation time [97]). This allows us to further extend the analysis of the effect of the liquid mobility on the transformation front behaviour. With this purpose, we represent the front velocity as a function of the structural relaxation time of the liquid. For toluene, we use the relaxation time of the liquid derived by Hatase [97], which follows a VFT relationship with temperature, $\tau = \tau_0 \exp\left(DT_0/(T - T_0)\right)$, with $DT_0 = 434\,\mathrm{K}$, $T_0 = 104\,\mathrm{K}$ and $\tau_0 = 6.3 \times 10^{-13}\,\mathrm{s}$. Figure 4.6 shows a log-log plot representation of the

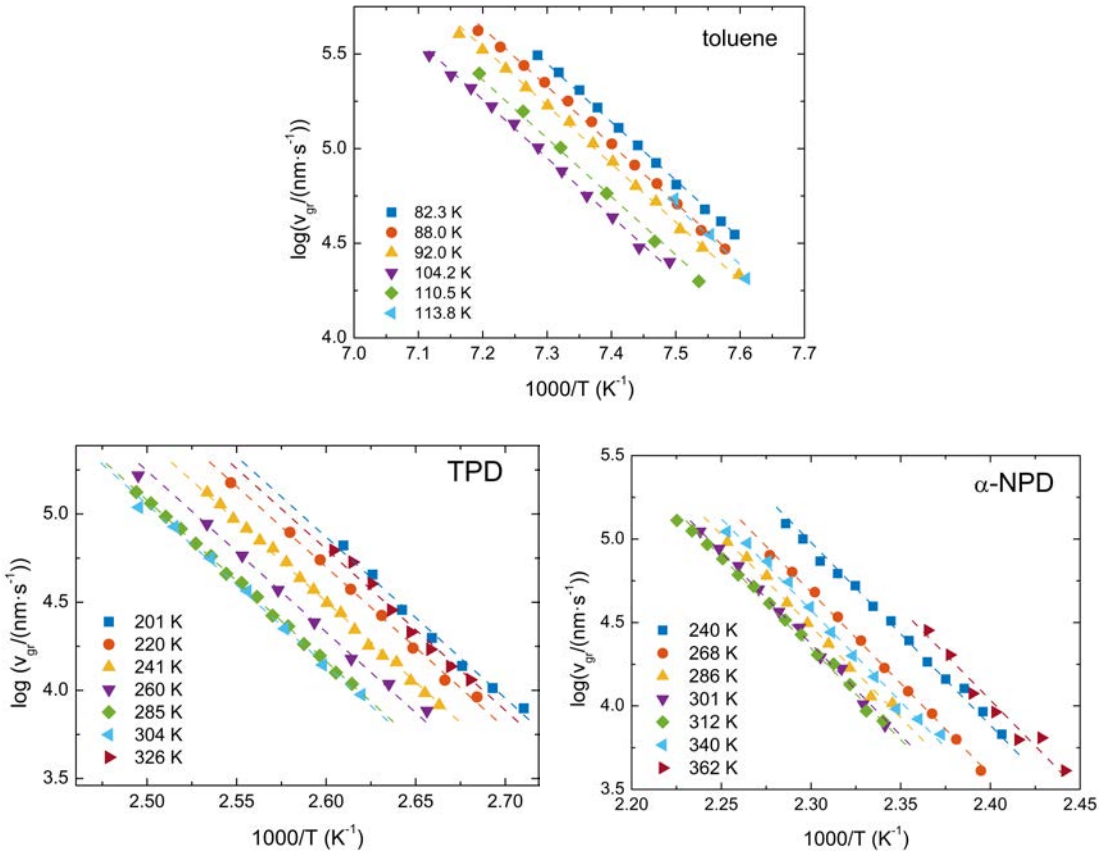

Figure 4.5: . The logarithm of the growth front velocities for toluene (top panel), TPD (bottom-left) and α-NPD (bottom-right) versus the reciprocal of the temperature. The lines are merely a guide to the eye that helps to visualise that the velocities show the same trend with respect to temperature (the lines are parallel) for all stabilities despite having different values. In all three cases, the more stable the sample, 0.85-0.89T_g, the slowest the transformation rate.

front velocity as a function of τ. We see that in this representation of the data, all the stabilities can be fitted by parallel straight lines, and, in agreement with equation 4.1, they all have a common slope of $\gamma = -0.92 \pm 0.06$ and a C value that depends on the deposition conditions.

The exponent γ is similar in different organic compounds [38, 90], indicating that the dependence of the growth front velocity on the liquid relaxation time is nearly independent of the molecular nature of the glass forming material. Typical values found in various systems are 0.85 for IMC [41], 0.71 for TNB [41] or 0.73 for TPD [40]. Toluene and ethylbenzene exhibit values of γ closer to one [35, 90]. Still, if the transformation front was fully controlled by the relaxation time of the liquid we would expect the exponent γ in equation 4.1 to be one. Smaller values of γ indicate a weaker dependence of v_{gr} with τ_α and can be attributed, following references [17, 41] to the spatially heterogeneous dynamics in the SCL. Nevertheless, the relationship shown in equation 4.1 has mainly been tested in a limited temperature range in annealing experiments

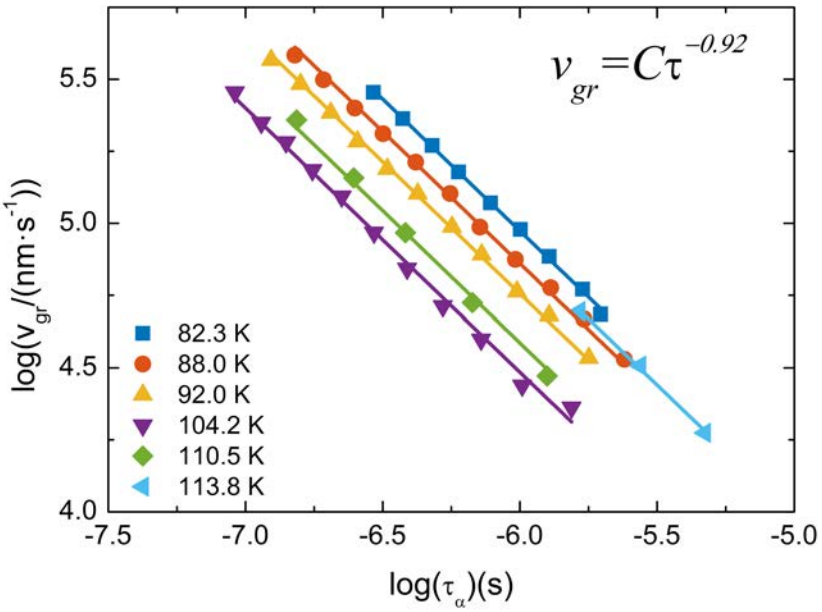

Figure 4.6: The logarithm of the growth front velocity corresponding to samples grown at the indicated deposition temperatures versus the logarithm of the relaxation time of the supercooled liquid, which has been calculated using the VFT equation with the values given by Hatase et al. [97]. The lines are fits of the data using the expression $v_{gr} = C\tau^{-\gamma}$, considering the exponent γ as a common fit parameter.

close to T_g [35, 40, 41, 69]. At this temperature range, the v_{gr} values are translated in transformation times of the order of seconds to hours, sufficient for the different direct techniques to track the transformation front. On the contrary, by using fast-scanning nanocalorimetry, the high heating rates imposed during the measurement of the heat capacity of the system permit to push the transition towards much higher temperature values, gaining access to the properties of the system in a temperature range unreachable with conventional techniques. Hence, it is possible to check if this relationship still holds for relaxation times orders of magnitude smaller than the ones available with annealing experiments, in which the direct evolution of the front is followed. In fact, recently, and using high-heating rates, we proved that this relation applies for ultrastable glasses of IMC in a broad T range covering from T_g to $T_g + 75\,\mathrm{K}$ [34]. Moreover, we were also able to prove this relationship for glasses with different stability [54].

To check if this relationship between growth front and relaxation time of the liquid holds for an extended range of temperatures also in the case of toluene, we incorporate to Figure 4.6 the data obtained by Ahrenberg et al. [35] using AC-nanocalorimetry for glasses of toluene. Their data correspond to their most stable glass, deposited at $2\,\mathrm{nm\,s^{-1}}$ and 105 K. Our samples, on the other hand, are prepared at $0.32\,\mathrm{nm\,s^{-1}}$. However, according to previous works, this change in deposition rate should not represent a major change in the stability of toluene thin film glasses [29, 35]. We therefore assume that the characteristics of their glass will lie in between the ones we deposited at 104.2 K and 110.4 K. We also plot in Figure 4.7 a representation of the expression 4.1 using γ =

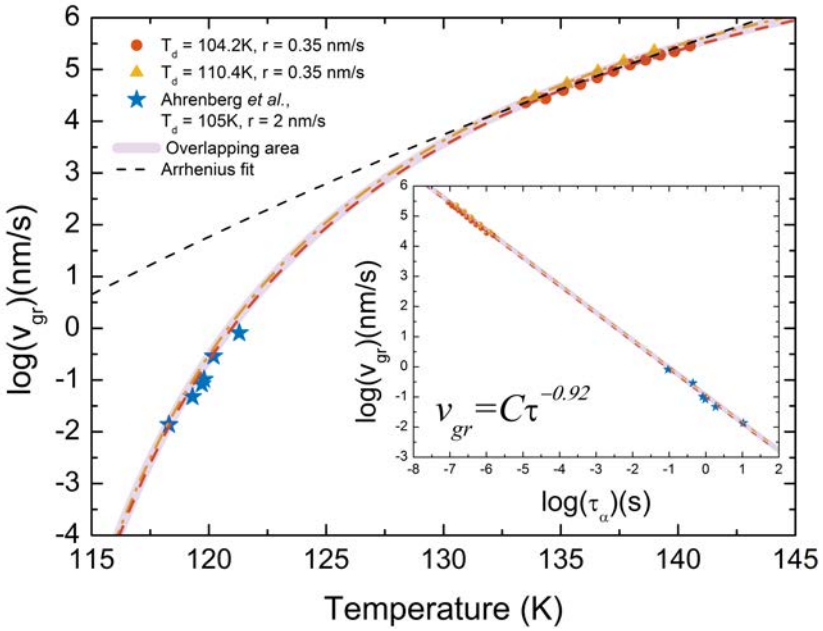

Figure 4.7: The logarithm of the front velocity as a function of temperature for toluene samples deposited at 104.2 and 110.4 K and at a deposition rate of 0.35 nm s^{-1}. Dashed red and yellow lines correspond to the fit of the data shown in panel figure 4.6 extended to lower temperatures. Star symbols correspond to data obtained by Ahrenberg et al. [35] using AC-calorimetry at low temperatures. Ahrenberg's films were grown at 2 nm s^{-1} and at a deposition temperature of 105 K. The continuous grey line is a representation of the expression $v_{gr} = C\tau^{-\gamma}$ using $\gamma = 0.92$ and a prefactor C that fits both our 104.2 and 110.4 K data and the 105 K data from Ahrenberg et al., using a line width of around $\pm 13\,\%$. The black dashed line corresponds to two independent Arrhenius fits for the high and low temperature data shown. The inset shows the same data but as a function of the relaxation time of the liquid.

0.92 and a prefactor C that fits both our 104.2 and 110.4 K data and the 105 K data from Ahrenberg et al. [35] within a tolerance of $\pm 13\,\%$. Considering this uncertainty, we can see a good match of our high-temperature data and Ahrenberg's low-temperature data, spanning the relationship between liquid relaxation time and front velocity up to $T_g + 25\,\mathrm{K}$, equivalent to eight orders of magnitude in relaxation time. We want to remark that an Arrhenius relation would not fit both the low and high-temperature data, as can be seen in Figure 4.7. There, we see how different activation energies would be necessary to fit the two sets of data.

Still, our technique cannot distinguish between the existence of one or two fronts, coming from the surface and the interface with the substrate, and thus, our growth rate values can differ up to a factor 2 when compared with those obtained by other techniques that can differentiate the evolution of single fronts [42]. Some novel strategies can be employed to infer the simultaneous existence of one or two fronts in temperature-ramping experiments, such as using a lower mobility materials as a capping layer, which will be shown in Chapter 5. However, this strategy was not straightforward applicable to the case of toluene analysed here.

Our lack of accurate specific heat data for TPD and α-NPD precludes us to perform a similar analysis on these two materials. However, in the case of TPD, Walters et al. [40] calculate the activation energy—fitting an Arrhenius equation—for the transformation front propagation rate which we can use to compare with the values we obtain. There, as in our case, the front velocity dependence on temperature seems independent of the deposition temperature. In their case, the average activation energy for their surface-initiated front is of (380 ± 20) kJ mol^{-1}. In a similar way, from our data in Figure 4.5 for TPD we can extract the activation energy:

$$E_a = -R \log e \, \frac{\partial \log v_{gr}}{\partial (1/T)} \tag{4.5}$$

where R is the universal gas constant. Thus, the average activation energy we obtain for our data is (176 ± 10) kJ mol^{-1}, which is the mean value of the slope obtained from independent linear fits of the different deposition temperatures.

Our activation energy value differs from the reported value in Ref. [40], about a factor of 2. However, again, we must consider that we are comparing the front velocity within two completely different temperature regimes. Transformation front velocity data by Walters et al. [40] is obtained through isothermal measurements at $T_g + 13\,\mathrm{K}$ at most. Our data is obtained at $T_g + 40\,\mathrm{K}$ and above. We can look in Figure 4.7 for toluene, to provide a better picture of this mismatch. We have seen that, in a wider temperature range, the growth front velocity does not follow an Arrhenius behaviour in the whole range. Instead, the growth front velocity behaviour follows a VFT-like behaviour mediated by the structural relaxation time τ_α of the liquid. In that scenario, different apparent activation energies are expected when looking at distinct temperature range. Particularly, the apparent activation energy at high temperatures is expected to be smaller than close to T_g, as seen from the slopes of the black dashed lines in Figure 4.7. Since structural relaxation time of TPD follows a VFT expression [40], our lower activation energy is consistent with a growth front velocity depending on the mobility of the SCL via the power relationship with τ_α of equation 4.1.

4.5 Effect of glass properties on the transformation rate

Using fast-scanning nanocalorimetry, we find that the dependence with temperature of the transformation front is the same irrespective of the stability of the samples. These results are in line with those of previous studies on indomethacin [54, 89] and on TPD [40]. This common dependence on temperature of the transformation front provides additional evidence of the dominating role of the mobility of the supercooled liquid layer on the velocity of the front. Still, glasses deposited at different temperatures transform at distinct pace as seen from Figures 4.8a and 4.8b for the OSG and in Figure

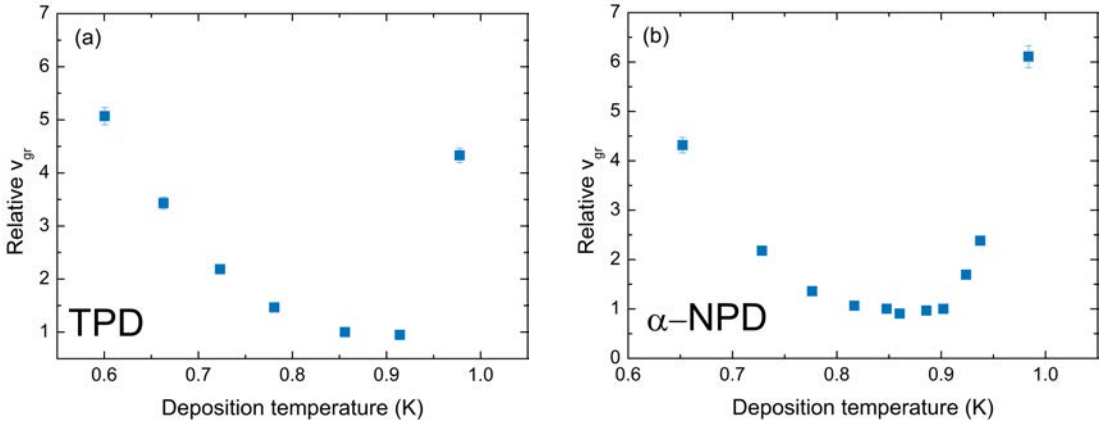

Figure 4.8: Growth front velocity (relative to the slowest value, the UG) as a function of the deposition temperature for **(a)** TPD and **(b)** α-NPD.

4.9a for toluene (right-axis, red diamonds), where the v_{gr} values have been expressed relative to the slowest velocity.

For instance, toluene glasses prepared at $T_{dep} = 82.3\,\mathrm{K} = 0.70T_g$ have a transformation front that advances 3 times faster than the glass prepared at $T_{dep} = 104.2\,\mathrm{K} = 0.89T_g$. In fact, the most thermally stable glass shows the slower transformation front. In a similar way, the TPD glasses prepared at $T_{dep} = 285\,\mathrm{K}$ and 304 K—corresponding to $0.86T_g$ and $0.91T_g$. Figure 4.9a exhibits the slowest transformation front, up to five to six times slower than the ones prepared at $T_{dep} = 201\,\mathrm{K}$ ($0.60T_g$). α-NPD behaves in the same way, with the most stable glasses presenting the lower front velocities (Figure 4.8b).

As we have seen in Chapter 3, the deposition temperature determines the stability of the PVD glasses, and a commonly used parameter to quantify this stability is the limiting fictive temperature. In Figure 4.9a and using a proper scaling factor, the limiting fictive temperature data has been superimposed (blue open squares, left-axis) to front velocity data. We can see a good agreement between both quantities. This agreement is better seen in Figure 4.9b, where the front velocity is represented versus the limiting fictive temperature, in this case, scaled as $(T_g - T_f)/T_g)$. The different symbols from Figure 4.9b indicate if the glasses have been grown at a deposition temperature above (squares) or below (triangles) $0.89T_g$ (UG). We can see that there is no significant difference in growth front velocity between depositing below and above $0.89T_g$ and that the transformation rate appears to be mostly determined by the thermodynamic stability of the glass.

These results contrast with what is observed for the organic semiconductors TPD and α-NPD, as can be seen in Figures 4.10a and 4.10b, where we directly plot the front versus the limiting fictive temperature, making a distinction (using different symbols) for glasses deposited above and below the maximum of thermal stability, at $0.85T_g$ in

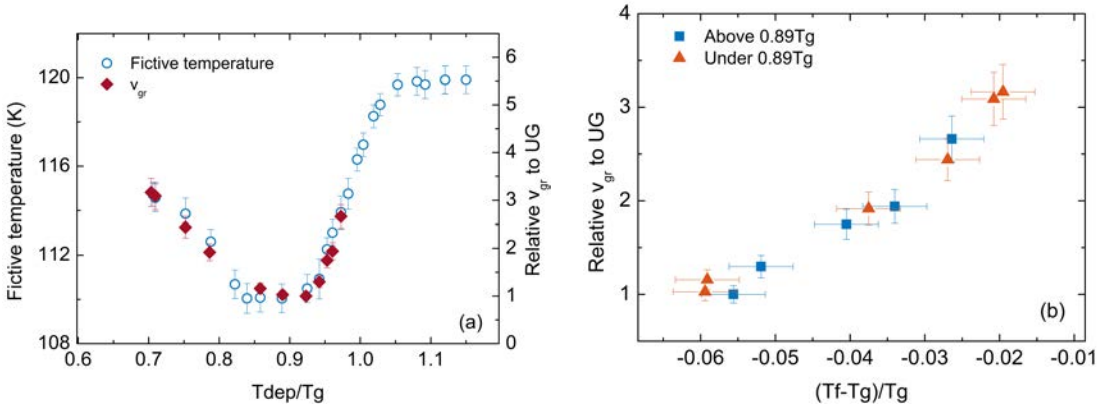

Figure 4.9: Relative growth front velocity versus T_{dep} and T'_f for toluene. **(a)** Limiting fictive temperature of thin film toluene glasses (left axis, squares) and growth front velocity expressed relative to the slowest value (corresponding to $T_{dep} = 0.92Tg$ =108 K, right axis, circles) as a function of deposition temperature. **(b)** Growth front velocity relative to the slowest value as a function of the increment of limiting fictive temperature with respect to $(T'_f - T_g)/T_g$. The different symbols indicate if the glasses have been grown at a deposition temperature above (squares) or below (triangles) $0.89T_g$.

this case. Now two differentiated branches clearly emerge. The growth front velocity decreases with the increase of stability, but at two distinct rates. In a previous study on indomethacin vapour-deposited glasses [54], we showed that for this organic molecule there was not a one-to-one relation between front velocity and limiting fictive temperature, similarly to what is reported here. There, we observed also how two branches emerged when considering the dependence between these two magnitudes for glasses deposited below and above the temperature producing the maximum stability (inset in Figure 4.10a). In fact, for equal limiting fictive temperature $287K \pm 0.5K$ the samples deposited below $0.85T_g$ present faster velocities, up to a factor 3.5 [54].

Dalal et al. [45] on indomethacin and Walters et al. [40] on TPD had already reported the lack of correlation between the growth front velocity and the density of the glass in the whole range of deposition temperatures. This lack of a one to one correlation can also be extrapolated to thermodynamic stability since, as we have seen in the previous chapter, density variation and limiting fictive temperature scale both in a similar manner with deposition temperature for the IMC, TPD and α-NPD systems.

The question that remains now is which other glass properties do influence the front velocity? We have already seen that glasses with equal thermodynamic stability—or density—can show differences up to a factor of several times the front velocity. In the aforementioned study on indomethacin glasses [54], we associated the emergence of the two branches to a different orientation of the molecules depending on the deposition temperature. This molecular orientation can be quantified through birefringence measurements, being birefringence the difference between the refraction indices

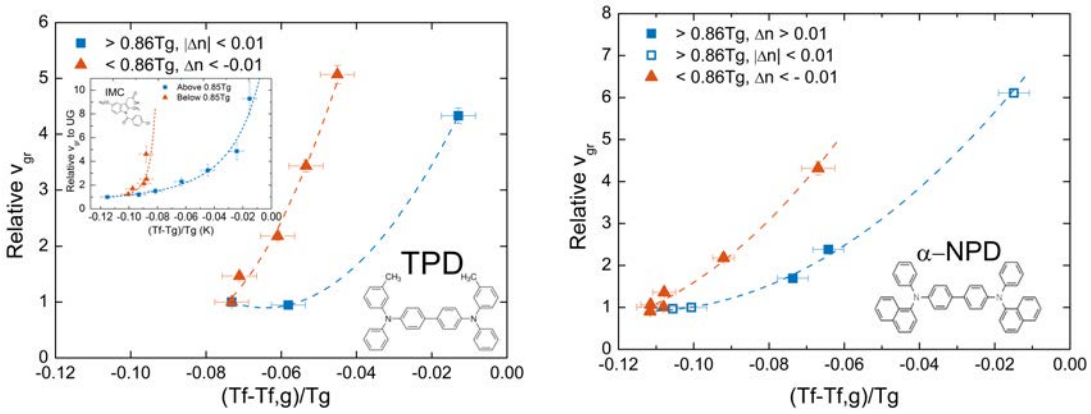

(a) TPD **(b)** α-NPD

Figure 4.10: Growth front velocity relative to the lowest velocity (the glass deposited at $0.86T_g$) is plotted as a function of $(T'_f - T'_{f,g})/T_g$ (where $T'_{f,g}$ is the fictive temperature for the glass deposited at T_g) for both OSG. The square points correspond to samples deposited below $0.86T_g$, whereas the circles correspond to samples deposited above $0.86T_g$. The symbol scheme is also used to distinguish between negative birefringence (orange circle), positive (open blue squares) and zero (blue filled squares) correlating our data with reported birefringence values from Dalal et al. [45]. The zero birefringence is considered when $|\Delta n| < 0.01$. Positive birefringence data, only distinguished for α-NPD. Inset: equivalent representation for indomethacin data, adapted from Rodríguez-Tinoco et al. [54]

$\Delta n = n_z - n_{xy}$, a direct consequence of molecular orientation and the anisotropic polarizability tensors from these molecules. In a similar study on TPD and α-NPD [45], the order parameter S_z—the average orientation of the long axis of the molecules to the surface normal—is also measured from dichroism measurements and shown to scale with birefringence (see Figure 4.11, reprinted from [45]). In this figure, three distinct three regions (sketched in Figure 4.12) depending on the values of these parameters can be distinguished:

(i) Negative birefringence and $-0.5 < S_z < 0$, associated with molecules with a certain degree of horizontal orientation. In Figure 4.11, negative birefringence values and S_z are reported for glasses deposited below ca. $0.90T_g$.

(ii) Zero birefringence and $S_z = 0$, corresponding to isotropic molecular orientation. Glasses deposited above $0.97T_g$ are isotropic.

(iii) Positive birefringence and $0 < S_z < 1$, associated with molecules that tend to orient vertically. Those glasses deposited between $0.90T_g$ and $0.97T_g$ show small positive values of birefringence and S_z.

To perform a similar analysis on TPD and α-NPD, our front velocity data is also represented in Figure 4.10a considering birefringence data from Figure 4.11 [45] on these two molecules. Although birefringence is a good indicator of the anisotropy of the

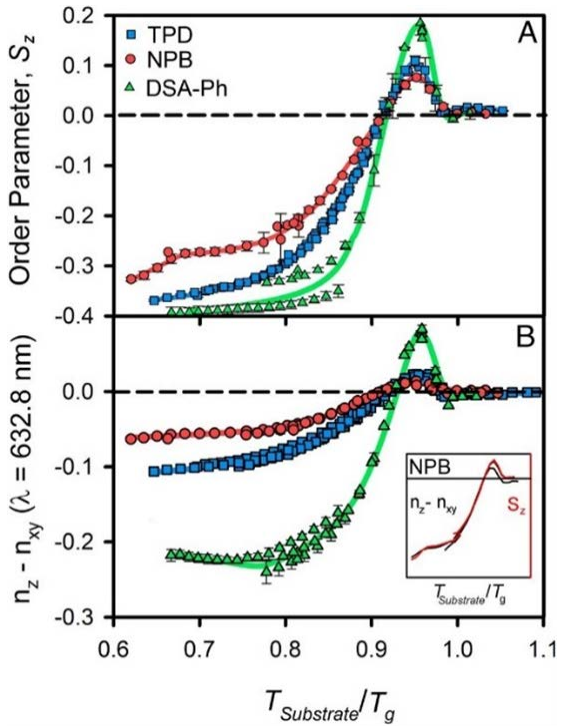

Figure 4.11: Order parameter (top) and birefringence (bottom) as a function of the deposition temperature for the three organic semiconductors TPD, α-NPD[1] and DSA-Ph. Reprinted from [45].

glasses, the order parameter is more suitable to quantify the absolute degree of orientation. Both organic semiconductors show a higher tendency to have the long axis lying parallel to the substrate, with values closer to total horizontal orientation $S_z = -0.5$, rather than perpendicular, with values far from total vertical orientation $S_z = 1$. This fact allows us to simplify the picture making only the distinction between horizontal and nearly isotropic molecular arrangement. When this discernment is done, the same $0.86T_g$ criteria can be used to differentiate the same two branches in Figure 4.10a for TPD between negative (triangles) and zero birefringences (squares). For α-NPD, data with small positive birefringence is distinguished (open squares) for the $>0.86T_g$ branch and the values fall in the same trend as the zero-birefringence data, in agreement with our assumption.

As we already suggested in [54], we can disentangle two factors that control the transformation dynamics: the molecular orientation and the fictive temperature. Higher fictive temperatures lead to higher transformation rates with the emergence of two clear branches for the same fictive temperature. The faster branch corresponds to strongly horizontal oriented samples, whereas the slower branch corresponds to nearly isotropic samples. In the lower branch, we find the nearly isotropic glasses which also present

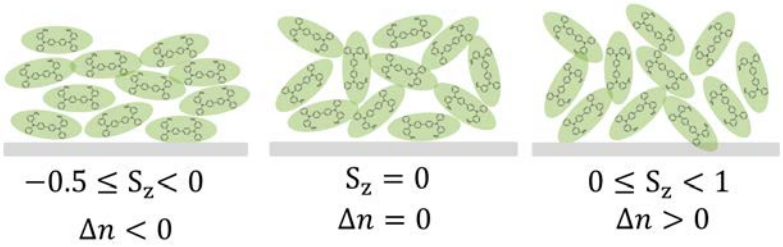

Figure 4.12: Schematic representation in 2D of three possible molecular arrangements (horizontal, isotropic, and vertical) and the parameters used in reference [45] to quantify it. S_z is the order parameter and Δn the birefringence.

clearly different transformation velocities. In the latter case, the fictive temperature—or density—dominates the growth front, with the less stable glasses—or less dense—being the ones exhibiting faster velocities. In the faster branch, this discrimination is not so clear, as lower deposition temperatures yield both less stable glasses and more horizontally oriented molecules.

Is this picture of non-isotropic molecular packing consistent with our observations in toluene? Although not symmetrical, the toluene molecule has indeed a much lower aspect ratio than TPD or α-NPD. If molecular orientation played a role in the velocity of the front, the absence or a small contribution of anisotropy would result in a transformation rate that would only depend on the stability of the glass, which is indeed what we can see in Figure 4.9b for toluene. WAXS measurements by Ishii et al. [98] on toluene glasses deposited at $0.89T_g$ show a small anisotropic peak, which they associate to the formation of particular dimers more energetically favourable. However, the presence of these dimers does not imply necessarily that toluene molecules tend to align with a preferred orientation when deposited at different temperatures. According to previous work from Yokoyama et al. [95], small or no preferred orientation should be expected from a small molecule such as toluene. If this was the case, and no other parameters apart from molecular orientation and thermodynamic stability—or density—would play a role in determining the front velocity, then we would see a perfect correlation between front velocity and limiting fictive temperature, as in toluene.

4.6 Crossover length in toluene glasses

Up to now, we have focused our attention on the heterogeneous front-like transformation. However, as we have seen, if the samples are thick enough, the homogeneous transformation is eventually activated and will start dominating the transformation for increasing thicknesses.

We can define the crossover length, ξ_{co} as the distance travelled by the front before the homogeneous mechanism dominates the transformation. This distance can be infered

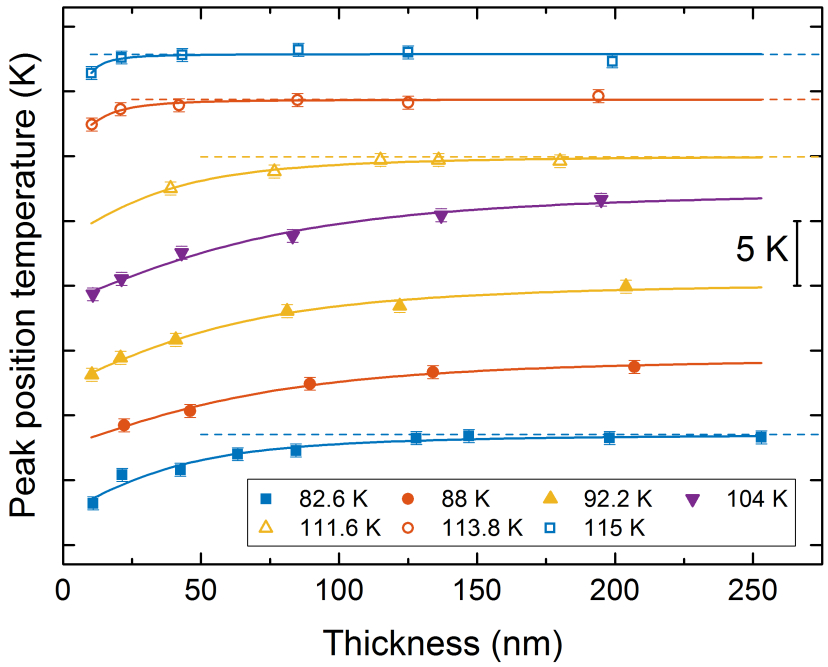

Figure 4.13: Position of the maximum of the glass transition peak as a function of the thickness of the film. The legend indicates the deposition temperature of the corresponding glasses. Samples with similar limiting fictive temperature have been plotted with the same type of symbol and colour. Void symbols correspond to glasses deposited above $0.89T_g$ and filled symbols to glasses obtained below $0.89T_g$. The curves are vertically shifted for clarity. Experimental data are fitted with an arbitrary function as a guide to the eye (continuous line). The dashed line provides an estimation of the position of the maximum of the glass transition peak once the homogeneous transformation mechanism dominates.

from the calorimetric specific heat curves. When the homogeneous transformation is the dominating mechanism, the glass transition simultaneously occurs in the remaining volume of the sample, and therefore, the transformed fraction is basically proportional to the total mass. In this way, if glasses are thicker than the crossover length, the mass normalised specific heat curves show a temperature value of the maximum of the glass transition peak that remains constant, independent of their thickness. A clear example of this tendency is found in Figures 4.1a and 4.1c. We can, therefore, infer the crossover length by representing the position of the maximum of the glass transition peak as a function of the thickness of the films. While there is a temperature shift of the peak position, the heterogeneous mechanism will still have a significant impact on the transformation. Figure 4.13 shows the position of the maximum of the glass transition peak as a function of the thickness of the films for toluene glasses grown at different deposition temperatures. The curves have been vertically shifted for clarity. To facilitate the interpretation of the results we have plotted the glasses with similar fictive temperature with the same symbol and colour. Data from glasses deposited above $0.89T_g$ are plotted using void symbols, and we have used filled symbols for glasses deposited below this temperature.

Irrespective of the deposition temperature the position of the glass transition peak shifts to higher temperatures as thickness increases and tends to stabilise at a certain thickness where bulk transformation sets in. As a guide to the eye, the different data sets from Figure 4.13 have been fitted with the same function. We can use the derivative of this function to provide a rough estimation of the crossover length. Considering the asymptotic nature of the function, we have defined the crossover length as the thickness at which the derivative of the function is equal to $0.002\,\mathrm{K\,nm^{-1}}$, i.e. when the change in the position of the glass transition peak is equal to a 0.2 %. Table 4.1 summarises the calculated values of crossover length together with the corresponding deposition and limiting fictive temperatures.

The first conclusion one can extract from the Figure 4.13 is that the crossover length depends strongly on the deposition temperature. Glasses deposited between 0.75 and $0.90T_g$, corresponding to the range of deposition temperatures for maximum stability [29, 30, 35] in toluene, achieve thicker crossover lengths. For higher and lower deposition temperatures, the homogeneous transformation mechanism starts at lower temperatures, dominating the transformation before the front has travelled a longer distance. In a previous study, Bhattacharya et al. found that stable toluene glasses transformed via a front mechanism up to thicknesses of around 2 µm [53]. With our technique, we are limited in film thickness, so it is not possible for us to determine the crossover length maximum for stable glasses.

T_{dep} [K]	82.6	88.0	92.2	104.0	110.8	111.6	112.6	113.8	115.0
T_{dep}/T_g	0.706	0.752	0.788	0.888	0.947	0.953	0.962	0.972	0.982
T'_f [K]	114.7	113.8	112.6	110.0	110.9	112.3	113.0	113.9	114.8
ξ_{co} [nm]	200 ±30	>200	>200	>200	200 ±30	200 ±30	115 ±30	77 ±30	53 ±20

Table 4.1: Limiting fictive temperature, T'_f, and cross-over length, ξ_{co}, for samples deposited at different substrate temperatures, T_{dep}. The cross-over length has been estimated as the thickness for which the variation of the position of the glass transition peak is only of 0.2 %. The uncertainty has been determined from propagation of the fitting function and the uncertainty in the fitting parameters. The uncertainty in deposition and limiting fictive temperature is ±0.5 K.

Although we do not see variations in the growth front velocity between glasses grown at different deposition temperatures but encoded with the same limiting fictive temperature, we do observe remarkable changes in their crossover lengths. The crossover length depends on the velocity of the front but also on the dynamics of the transformation mechanism in the remaining volume of glass [64, 66]. If the front velocity is univocally determined by T'_f, as our data in Figure 4.13 suggests, but the crossover length is not, then in the case of toluene the homogeneous transformation will not be determined by T'_f alone. In particular, glasses deposited at 115.0 K and 82.6 K having

$T'_f = (114.7 \pm 0.5)\,\mathrm{K}$, transform via a heterogeneous mechanism up to ca. 50 nm and 200 nm, respectively, while having similar front velocities. Since, as we have defined it, the crossover length represents the length that the front propagates before the bulk transformation dominates, the variation of crossover length can be related to a change in the onset temperature of the bulk glass. It is important to emphasise that the limiting fictive temperature provides information on the average stability of the glass and it has been previously shown that T'_f and density, both of them average magnitudes, show a good correlation [54] (see Figure 3.8).

The intriguing question is: why two glasses with comparable average stability may show different onset temperatures for the bulk transformation? In the ongoing debate about what happens to the relaxation time below T_g, there are some studies that reveal two equilibration time scenario [99, 100]. Cangialosi et al. [99] in a recent study about the enthalpy recovery in polymers aged at low temperatures for extended periods of time reported the existence of two relaxation mechanisms. According to these authors, the differences in the formation of the glass would be reflected in their devitrification behaviours. Extrapolating their results, we speculate that it may be the case that glasses deposited well below T_g are densified by a different mechanism compared with those deposited close to T_g, at the equilibrium line. This hypothesis could explain the different devitrification temperatures for glasses with the same limiting fictive temperature but deposited close or far from T_g. Data from Figure 4.13 can be further analysed using this new perspective. The dependence of fictive temperature with deposition temperature is clearly different on both sides of the minimum. While close to T_g the dependence is strong, a milder dependence can be observed at lower temperatures. Considering the divergence of relaxation times at temperatures close to T_0 ($T_0 = 104\,\mathrm{K}$ for toluene [97]), a much stronger dependence on the limiting fictive temperature should be expected for glasses deposited below $0.89T_g$, unless a different mechanism would dominate the formation of the glass. We are cautious since this interpretation seems to be in contrast with recent results from Zhang et al. [101], which show complete decoupling between surface and bulk dynamics. Enhanced surface mobility with respect to bulk appears to be the origin of the high stability of vapour-deposited glasses [27, 44]. Still, it is worth noting that a small difference of 2 K in the onset temperature would already produce the observed differences in crossover length for glasses with the same T'_f. A deeper understanding of the bulk transformation mechanism in toluene stable glasses as a function of the deposition temperature is needed to extract further conclusions.

4.7 Summary

We have seen how the first stages of the transformation of vapour-deposited glasses into the supercooled liquid state correspond to a heterogeneous mechanism, in particular, to a supercooled liquid parallel front that starts at the surface of the sample. The transformation mechanism can be readily identified by an appropriate analysis of the calorimetric trace of the devitrification. As has been demonstrated for other organic molecules, the propagation velocity of this transformation front is strongly dominated by the mobility of the supercooled liquid molecules. We have shown, specifically for toluene, how a linear relation holds between the logarithm of the front velocity and the logarithm of the relaxation time of the liquid for an extended temperature range, covering eight orders of magnitude in relaxation time.

While the most thermodynamically stable glasses present the slowest transformation rates, we have identified two different behaviours when trying to correlate the growth front velocity with the stability of the PVD glasses. For toluene, the front velocity correlates with the limiting fictive temperature and seems enough to determine the front velocity. However, in both organic semiconductors, the thermodynamic stability is not sufficient to explain the difference in the front velocities, leading to the appearance of two different relations between front velocity and limiting fictive temperature.

Molecular orientation could play a role in the way the molecules are incorporated in the liquid layer, as previous observations in vapour-deposited glasses of indomethacin have suggested. In this context, we can speculate that the differences observed between toluene and the two organic semiconductors are related to the different geometry of these molecules. While TPD and α-NPD present anisotropic molecular packing depending on the deposition temperature, the simplicity and low aspect ratio of the toluene molecule could preclude a strong molecular orientation in the films. In this way, only thermodynamic stability and equivalently density, would conditionate the transformation rate.

The stability however does not determine all the features observed for the glass transition in toluene glasses. Considerable differences in the crossover length can be seen for glasses with the same thermal stability but prepared at different deposition temperatures. Although this behaviour could be related to the existence of two distinct mechanisms of glass formation at temperatures close and far from T_g, a thorough analysis of the homogeneous (bulk) glass transition in a large deposition temperature range would be necessary to confirm or refute this hypothesis.

Chapter 5

Homogeneous transformation mechanism in vapour-deposited glasses

5.1 Introduction

We have seen how we can effectively produce highly stable glasses by vapour depositing them at the appropriate substrate temperature. Although the thermodynamic stability of an ultrastable glass cannot be significantly enhanced within experimental time scales, as it already has the properties of an equivalent hyper-aged glass [28], the kinetic stability of these glasses is dominated by the surface-initiated growth front mechanism they exhibit. For instance, a 20 nm thick layer of an ultrastable glass will take one-fifth less time to fully transform into supercooled liquid than a 100 nm thick layer at the same annealing temperature. Thus, the heterogeneous transformation can eventually dynamite the high stability achieved for these glasses. This represents the major limitation for the conceivable applications of the UG. The amount of time at a given temperature these glasses can endure before transforming to the supercooled liquid is what will, in the end, determine the practical applications they can be used for.

The transformation into the supercooled liquid of stable glasses is expected to begin at surfaces, where the mobility is higher. It can be free surfaces [26, 27], but also interfaces with a more mobile material, for instance, a layer of conventional glass [41]. Also, a slower propagating front starting at the interface with the substrate has been identified for TPD and IMC using spectroscopic ellipsometry during an isothermal annealing protocol [40, 89]. The transformation of stable glasses into the supercooled liquid can be elucidated in terms of the *kinetic facilitation* concept. That is, the idea that an immobile region can become mobile only if mobility is present in an adjacent region

[102]. Facilitated kinetic Ising models have already been successfully used to reproduce the behaviour of ultrastable glasses, more specifically, in predicting the constant velocity growth front [63, 64]. Hence, adopting the facilitated kinetics point of view, we can think of further manipulating the properties of the previously studied glasses. The basic idea is that if the highly-mobile surface layers are blocked—somehow—then the growth front transformation mechanism is suppressed. This methodology was already applied by Sepúlveda et al. [88], who capped the free surface of a stable glass of indomethacin with a higher T_g stable glass and was able to avoid in this way the formation of a growth front. By eliminating—apparently—the surface mobility, they increased the samples' kinetic stability by further delaying the transformation into the supercooled liquid.

An application field especially interested in increasing the thermal stability of vapour deposited amorphous thin films is the OLED industry. There, two or more thin organic layers in the range of tenths of nanometres thick are commonly used for building the electronic devices, all of them being generally in their glassy state. The glassy layers in OLED devices do not have any free surfaces, and therefore, their thermal stability will be determined by the layer with the lowest T_g material, among other factors [8, 103]. The layer with the lowest T_g will have either an interface capped by the electrode layer and the other by a higher T_g material or both interfaces covered with higher T_g materials, depending on the architecture of the device. Thus, it is of vital importance for this field to understand the effect of capping on the thermal stability of organic semiconductor glassy layers.

To carry out this study, we have chosen the organic semiconductor TPD, as it has been already characterised as a function of T_{dep} and has been shown to be a glass former with enhanced stability. To eliminate the surface mobility, we must choose a material with lower mobility, i.e. a material with a higher T_g. The chosen material is another organic semiconductor named TCTA, with its T_g at 424 K, 91 K above the glass transition temperature of TPD.

We characterise, as the first step, the thermal stability of TCTA as a function of deposition temperature since, when evaporated as a capping layer at a given deposition temperature, its glass properties could condition the capping properties of the film. Secondly, we will study the effect of positioning the capping layer at the top, or bottom, or on both sides of the glassy film under evaluation. In this way, we will explore the impact of this extra low-mobility layer on the transformation mechanism of the TPD glasses. Moreover, we will vary the deposition temperature of the TPD glasses to study the homogeneous transformation in glasses with different stability.

For this study, we use the experimental setup described in Section 2.1. Briefly, we use a UHV chamber equipped with two effusion cells, which allow creating multilayers of two organic materials without breaking the vacuum. Samples are deposited directly

onto the calorimeter membrane which is fed with a constant intensity to keep it at a given temperature. The TPD samples are grown at (0.08 ± 0.01) nm s-1 and TCTA samples at (0.07 ± 0.01) nm s-1. Once the corresponding multilayer is fully deposited, the nanocalorimetric temperature scan is performed as usual (see Chapter 2).

5.2 Stability of the TCTA

TCTA is an organic semiconductor molecule than yields a glass layer when evaporated below T_g. Figure 5.1 shows the nanocalorimetric trace for single TCTA layers deposited at different temperatures. The heat capacity curves have been normalised using equation 4.3 in order to account for the apparent onset shift due to the heterogeneous transformation mechanism, as explained in Section 4.2. The TCTA also exhibits a calorimetric trace typical of a propagating front transformation, inferred from the apparent onset shift that the calorimetric trace exhibits as a function of the sample's thickness (curves not shown). The onset of the devitrification, seen in the inset of Figure 5.1, is taken as the onset of the front and is analogous to comparing the onsets of samples with different thickness, as done previously in Chapter 3. Figure 5.1 reflects a similar behaviour to what we have seen for TPD, α-NPD and toluene as well as what have been reported for many other organic glass formers found in literature (see Section 1.2), i.e. a clear dependence of the stability on the deposition temperature, with a maximum of stability around $0.85T_g$. In this case, this maximum of both kinetic and thermodynamic stability corresponds to a substrate temperature around 360 K.

5.3 Capping configurations

Now, we want to study the impact that adding a TCTA layer in different configurations has on the devitrification of TPD thin films. Figure 5.2 shows the four configurations we analyse. First and for comparison purposes, we will prepare single layers of TPD (Figure 5.2a). The second step is to evaluate the effect of having one single TCTA layer either between substrate and TPD (Figure 5.2b) or capping the free surface exposed to the vacuum (Figure 5.2c). The final configuration is to deposit TCTA layers to cover both sides of the TPD film (Figure 5.2d).

The glass transition temperature of conventional TPD glasses is 27 K below the deposition temperature that yields the most stable form of TCTA. Therefore, we are limited to deposition temperatures located at the left branch of the inset from Figure 5.1. To maintain the experiment as simple as possible, we evaporate the capping layers of TCTA always at the same temperature—regardless of the deposition temperature of the TPD sample. For simplicity, this temperature is chosen to be 285 K, which corresponds to the

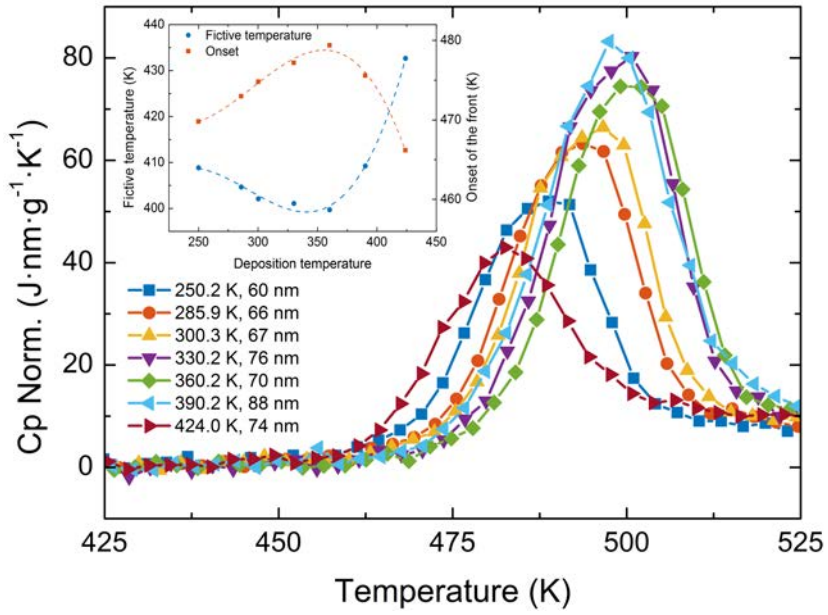

Figure 5.1: TCTA calorimetric trace for samples deposited at different temperatures (as indicated in the legend). Due to the dispersion in the thicknesses of the different samples, the heat capacity is normalised using equation 4.3. Inset: Shows the fictive temperature (blue circles, left axis) and onset temperature of the front (orange squares, right axis) as a function of deposition temperature. Lines are merely a guide-to-the-eye. Like many other organic glass-formers, it shows a maximum of stability around $0.85T_g$, corresponding to 360 K in this case.

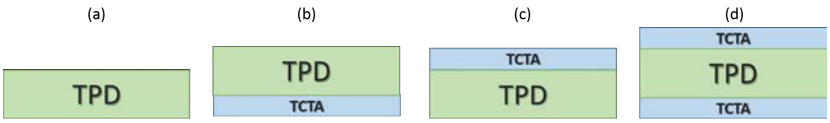

Figure 5.2: The four explored configurations using the organic semiconductor glass-former TCTA as a capping/substrate layer of TPD thin films.

UG of TPD and where TCTA is still relatively stable, as seen from Figure 5.1. Moreover, at such low temperature, the low mobility of TCTA will avoid any significant ageing.

Figure 5.3 shows the heat capacity scans corresponding to the four configurations presented in figure 5.2. TPD has been deposited at 285 K, in its most stable form. The thickness of each TCTA and TPD layers is the same in all cases, around (15 ± 5) nm and 35 nm respectively. We see two distinct scenarios: i) if a TCTA layer is capping the free surface of the TPD (Figure 5.3, up and down triangles), the onset of devitrification is shifted to much higher temperatures—about 35 K. ii) If the TCTA layer is placed between the substrate and the TPD, it results in a completely equivalent calorimetric trace as having a TPD layer deposited directly on the nanocalorimeter sensor (Figure 5.3, squares and circles respectively). This is a clear indication that in our TPD films, the devitrification process occurs only via a free surface-initiated front.

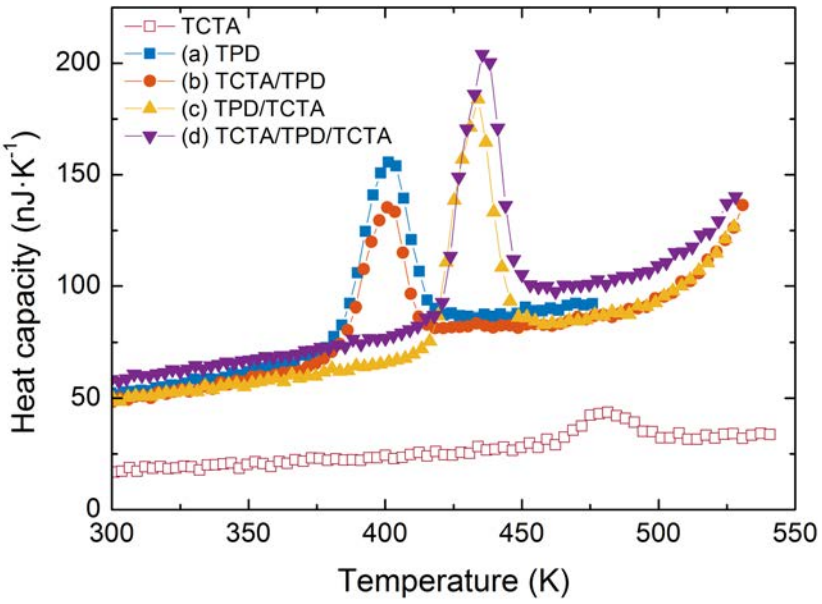

Figure 5.3: Heat capacity scans of the ultrastable glass of TPD for the different configurations presented in figure 5.2 as indicated in the legend. The thickness of the TCTA layers is of 17 nm. The thickness of the single TPD layer is 44 nm and of 34 nm for the TPD/TCTA, TCTA/TPD and TCTA/TPD/TCTA configurations.

We now look at the TCTA calorimetric trace. In the single TCTA scan, we see the devitrification around 460 K for a 15 nm thick layer (Figure 5.3, open squares). However, when TCTA is deposited in contact with a TPD layer, we do not see the calorimetric trace corresponding to its devitrification (Figure 5.3, triangles and circles). A better insight to this phenomenon can be found in Figure 5.4, where we plot the heat capacity of the TCTA/TPD/TCTA configuration for TPD samples deposited at $0.85T_g$ and at T_g together with the previous single scan of TCTA. The calorimetric trace of the sample deposited at T_g exhibits two well-defined transitions. The first one is the expected transition for TPD deposited at T_g, the second one corresponds to the devitrification of the TCTA occurring at much lower temperatures than the expected for a single TCTA layer, around 30 K below. Therefore, it seems likely that in the case of the capped ultrastable glass of TPD, both devitrifications—TPD and TCTA—are fully overlapped. That can also explain the slight differences in the onset and the area seen between the TCTA/TPD/TCTA configuration and the single top-capping layer. The double mass of TCTA transforming in the sandwich configuration with respect to the TPD layer overlapped with the glass transition of TPD. In fact, when looking at the curves from the configuration TCTA/TPD (Figure 5.3 circles), we can infer a small peak just after the devitrification of the TPD sample, around 430 K, which would correspond to the transformation the 15 nm TCTA layer.

The differences between the TCTA devitrification temperatures when arranged as a single layer or following a multilayer configuration with TPD can initially be explained from the kinetic facilitation point of view. A TCTA vapour deposited layer will start

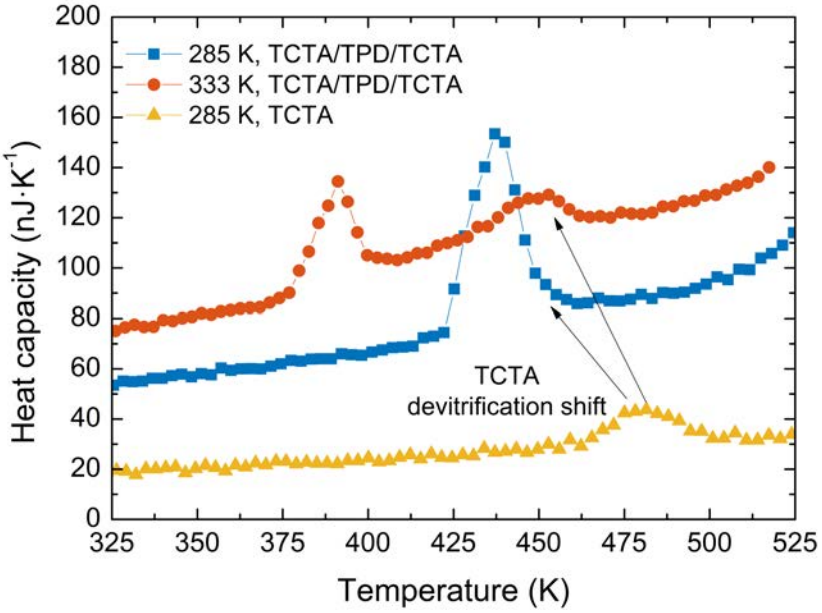

Figure 5.4: Heat capacity for capped TPD layers with the sandwich configuration deposited at T_g (circles) and $0.85T_g$ (squares) and for a single TCTA layer deposited at 285 K. The films' thicknesses are in all cases between 18 and 25 nm

.

transforming into supercooled liquid in the regions where the mobility is higher, that is, on the free surface of the TCTA single layer. However, when the TCTA layer is in contact with a TPD film, and the moment TPD devitrificates, the interface between TCTA and TPD becomes more mobile than TCTA's free surface at that temperature, inducing the transformation of the TCTA layer.

From a slightly different approach, the substantial decrease in the T_{on} of TCTA can also be rationalised in terms of interlayer diffusion. McEwan et al. [104] showed the mixing process of different glassy layers of organic semiconductor materials using neutron reflectometry measurements. They heated stacks of three organic layers with distinct glass transition temperatures and followed the diffusion profiles. They found out that a diffusion process started when the whole stack was heated to approximately 20 K above the lowest T_g material—having, therefore, the corresponding layer in the supercooled liquid state. In the case where the T_g's of the two materials forming the bilayer were significantly different ($\sim$55 K, in their case), the diffusion took place essentially from the high-T_g layer towards the adjacent supercooled liquid. On the other hand, the diffusion of the supercooled liquid to the higher-T_g materials—still a glass—was fundamentally zero [104]. The resulting intermixed layer exhibited a new T_g in between the original ones. Although their experiments were carried out under isothermal conditions, a similar rationalisation can be made for fast-scanning nanocalorimetry. Once our capped TPD sample has transformed into the supercooled liquid, TCTA molecules probably start to diffuse into the TPD layer. This process ends with the TCTA layer

intermixed with the newly formed layer, still glassy, with a depressed T_g with respect to TCTA. Despite diffusion processes in a heating ramp are slightly more complicated, this simple physical picture can explain the depressed T_g we observe for a TCTA layer in contact with a lower T_g material.

5.4 Transformation mechanisms in capped glasses

Although TPD layers do not show major differences in their devitrification process for the configurations TCTA/TPD/TCTA and TCTA/TPD/substrate, to reduce the number of factors controlling the devitrification we will continue our study with the full sandwich configuration. In this way, the TPD layers will have two identical interfaces as substrate and top layers.

Figure 5.3 shows how the devitrification of the TPD layer is delayed when the surface is capped, but the transformation mechanism of TPD under this configuration remains to be confirmed. As already mentioned when explaining how to analyse the specific heat curves of a glass transition, the transformation mechanism matters. If a homogeneous mechanism is governing the transformation into the supercooled liquid, samples with the same stability samples but with different thicknesses should exhibit a common onset—and single peak—in the specific heat curves. For that purpose, between three and four thicknesses of TPD layers (approximately 20, 40, 70 and 90 nm) have been evaporated at different substrate temperatures both as single layer and with the TCTA/TPD/TCTA sandwich geometry. The capping layers of TCTA are always evaporated at 285 K with thicknesses between 10 and 20 nm.

The contribution of the heat capacity of the TCTA glass is subtracted from each curve to simplify the analysis of the curves corresponding to different sample sizes. However, we must consider the following aspects: i) the mass from the TCTA layer must be inferred from the QCM reading since it is not possible to deconvolute the heat capacity signal from the TPD and TCTA layers separately. ii) The contribution of the TCTA layer cannot be subtracted in the whole temperature range of the calorimetric scan. This is because its devitrification occurs at different temperatures depending on whether it is in its single or multilayered configuration. Therefore, in the region after the transition, the TCTA contribution cannot be properly subtracted. iii) Consequently, the normalisation we are performing accounts neither for the area of the peak nor the specific heat in the liquid region. iv) Once the subtraction is performed, the mass of the TPD layer can be then inferred from the heat capacity in the glass region of the resulting curve, instead of using the supercooled liquid region as was used in previous measurements. This procedure yields thicknesses in agreement with the values measured by the QCM during the evaporation.

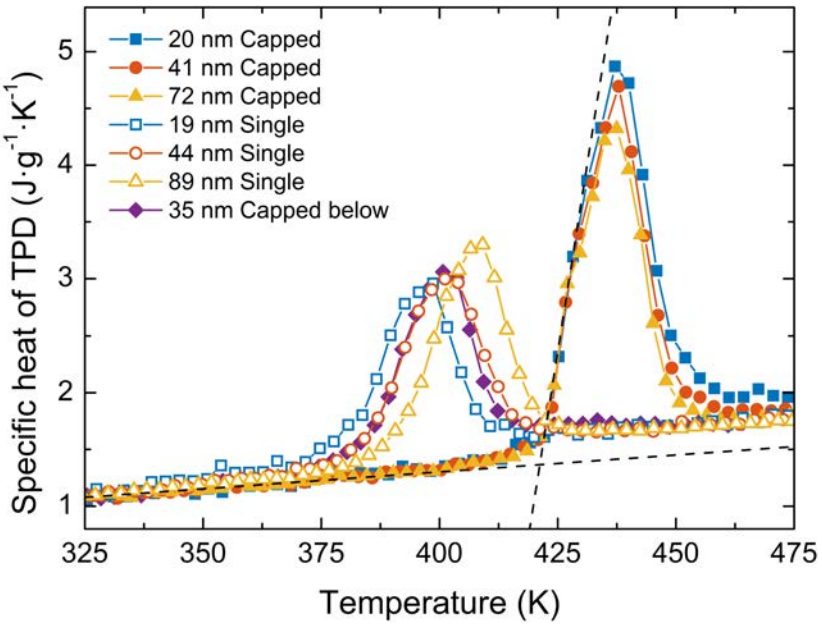

Figure 5.5: Calorimetric trace of ultrastable glasses of TPD deposited at 285 K for single (void symbols) and capped layers with configuration TCTA/TPD/TCTA (filled symbols). Different symbols indicate different TPD thicknesses, as labelled in the legend. The diamonds correspond to a TPD/TCTA bilayer configuration. The dashed black lines determine the onset of devitrification for the capped layers.

In Figure 5.5 we can see the specific heat trace for three different thicknesses of a TPD glass deposited at $0.85T_g$ for single and capped layers. While the single layers show the onset shift typical of heterogeneous transformations (void symbols), the onset and peak of the capped glass collapse regardless of the sample's thickness, indicative of a homogeneous transformation. The small variations in the area of the peak are an artefact produced by the different TPD/TCTA mass ratios that each sample has and that the normalisation is not considering. Equivalent results are obtained for TPD deposited at three more temperatures. The corresponding specific heat curves are shown in Figures 5.6a, 5.6b and 5.6c for deposition temperatures of 220 K, 250 K and 325 K respectively. These results corroborate that the transformation is taking place via a homogeneous mechanism not only in the case of the ultrastable glass but also for less stable glasses. From the kinetic facilitation point of view, we are, in fact, preventing the front by arresting the higher mobility region. Previous work from Sepúlveda et al. [88] showed that the propagating transformation front of ultrastable IMC glasses could be impeded with a capping layer of a higher T_g material, TNB in their case. There, they used deuterated IMC layers to follow the concentration profile during an annealing at $T_g + 11\,\mathrm{K}$. Although their capped samples eventually transformed into the SCL, this was accomplished at much longer times than the samples with a free surface. In our case instead, we use temperature-ramping experiments to prove that the growth front can be blocked and the glass transition delayed. For TPD, we see how not only the UG can be capped but also less stable glasses. In the light of these results with the

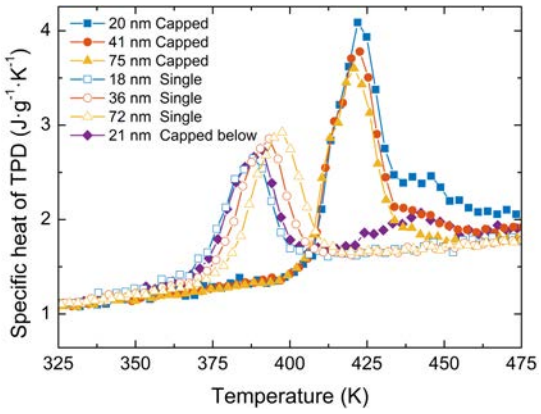

(a) $T_{dep} = 220\,\mathrm{K}$

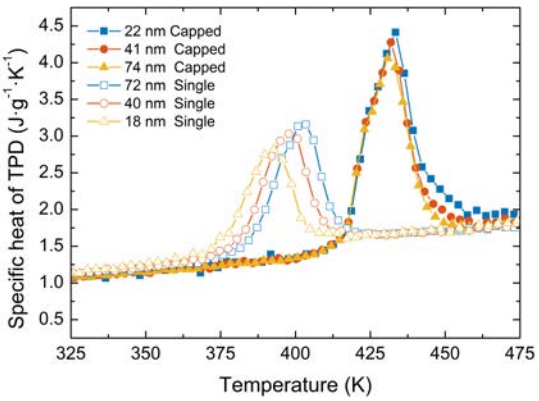

(b) $T_{dep} = 250\,\mathrm{K}$

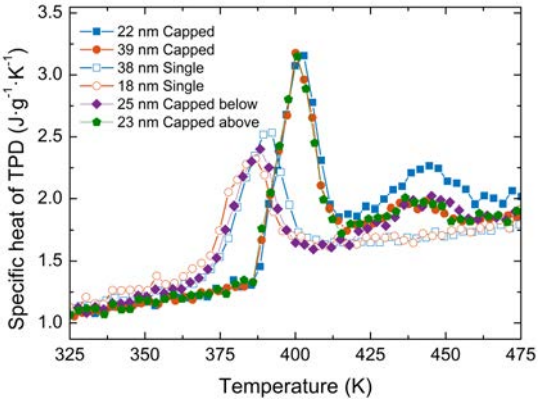

(c) $T_{dep} = 325\,\mathrm{K}$

Figure 5.6: Calorimetric trace of VD glasses of TPD deposited at three different T_{dep} for single (void symbols) and capped layers with configuration TCTA/TPD/TCTA (filled symbols). Different symbols indicate different TPD thicknesses, as labelled in the legends. The diamonds correspond to a TPD/TCTA bilayer configuration and pentagons to the TCTA/TPD configuration.

system TPD/TCTA together with the ones provided by Sepúlveda et al. [88] for the system IMC/TNB, the capping strategy to preclude the front transformation could be generalised to other glass-forming materials. Moreover, it provides us the opportunity to study the homogeneous transformation of very thin films.

Before continuing let's briefly have a look at the sample that has only TCTA acting as a substrate (Figure 5.5, diamond symbols). As we have previously anticipated for the UG, we ruled out the possibility of having two growth fronts—one starting at the free surface and one starting at the interface sample/substrate. Having a UG of TPD on top of a TCTA layer produces the same calorimetric trace as having a UG of TPD sample directly on the nanocalorimeter's substrate, Figure 5.5 (diamonds). In principle, we could not directly rule out the possibility of having two fronts for higher or lower deposition temperatures. As seen in the previous chapter, the growth front velocity of TPD glasses deposited below $0.85T_g$ can be up to 5 times faster than the

equivalent glasses deposited above $0.85T_g$. Without being able to distinguish between one or two fronts, a fraction of this velocity increment could be attributed to a second front initiated at the interface. However, Figure 5.6a shows—for a glass deposited below $0.85T_g$—a TPD layer on a TCTA substrate (purple diamonds) which completely overlaps with the single TPD layer of equivalent thickness (20 nm). Figure 5.6a shows—for a glass deposited above $0.85T_g$—the equivalent configuration with the same result. These results are entirely equivalent to the ones anticipated for the UG. Therefore, we can infer that only a surface-initiated front is responsible for the heterogeneous transformation mechanism of the non-capped TPD samples.

The single surface-initiated front we have inferred here for the transformation of stable glasses of TPD contrasts with the results obtained by Walters et al. [40]. There, they use spectroscopic ellipsometry and a multilayer optical model to trace the evolution of the isothermal transformation into the supercooled liquid of TPD stable glasses. Their data is best fitted using a two-front model, a surface and a substrate-induced front. However, our data is obtained in a much higher temperature range, about $T_g + 40\,\mathrm{K}$ and above, compared to their isothermal measurements at $T_g + 13\,\mathrm{K}$ at most. Their substrate-induced front exhibits slower velocities than the surface front. A first possible explanation might be that our substrate (aluminium) is more efficient in supressing the substrate induced front compared to theirs. Another reasonable explanation might be that, at our high-temperature range, the surface-initiated front completely dominates the transformation. Using SIMS, Sepúlveda et al. [41] did not find either evidence of a secondary front starting at the substrate on IMC and TNB glasses, although they sometimes see a front starting at the (deuterated)-IMC/IMC interface. Komino et al. [105] also used ellipsometry to investigate the transformation mechanism of organic semiconductors molecules. Their best fit of the experimental data is provided by a combined model of a surface-initiated front and a homogeneous transformation. Although this latter combined model was not tested by Walters et al. [40] it could provide another plausible explanation to their double-front best fit.

5.5 Kinetic stability of a capped glass

By capping the TPD layers, we are delaying the onset of devitrification and thus, enhancing the kinetic stability of these glasses. Figure 5.7 shows the specific heat trace for samples deposited at seven different T_{dep} for single layers of TPD (lower panel) and capped layers with the TCTA/TPD/TCTA geometry (upper panel). In the case of the single layers, the heterogeneous mechanism is the limiting factor for increasing the kinetic stability. For instance, the difference in the onset of devitrification for single layers (Figure 5.7, lower panel) between the sample deposited at T_g (red right-pointing triangles) and the UG (purple down-pointing triangles) is around 13 K, for ca. 40 nm

thick layers. Of course, this is an apparent onset due to the heterogeneous transformation mechanism and the specific heat representation of the data. This difference can become larger when comparing samples with different thicknesses. On the contrary, when capped, the onset difference between the same two samples is expanded up to 44 K. The onset of the $T_{dep} = T_g$ sample is practically the same in both cases—indicating a small crossover length of a few nanometres. The much larger shift in the UG is indicative of a much higher crossover length of probably few hundreds of nanometres. Glasses with stabilities in between the ultrastable and the conventional glass show intermediate onset shifts, showing again that the crossover length is a deposition temperature dependent variable.

From Figure 5.7, it is worth noticing that the devitrification of the TCTA can also be seen—better discerned for the less stable samples. When visible, the glass transition of TCTA seems to take place in all cases at the same temperature, clearly overlapping with the transition of the UG of TPD.

In Chapter 3, we have seen how the growth front velocity does not scale with the limiting fictive temperature—leading to the appearance of the two branches when representing the $v_{gr}(T'_f)$ plot (Figure 4.10a). There, the kinetics (growth front) and the thermodynamics (T'_f) were not completely correlated, and we invoked other glass properties to explain that behaviour, such as the molecular orientation. Now that we can gain access to the bulk devitrification onset, we examine the correlation between the kinetics and thermodynamics again, i.e. T_{on} and T'_f. Figure 5.8 shows the onset of the bulk (left axis) and the limiting fictive temperature (right-axis) versus the deposition temperature. The T'_f data used has been taken from Figure 3.6, since we cannot use the capped curves to extract this value. With properly scaled axes, we see an agreement between both quantities within an estimated error of ± 3 K. The only T_{dep} that seems to fall out of the trend slightly is the glass deposited at 200 K. Ramos et al. have measured the bulk calorimetric devitrification trace of VD glasses of ethylbenzene [56] and ethylcyclohexane [106] with DSC at very low heating rates. They report differences in the width of the devitrification overshoots for same T'_f glasses but deposited above and below the T_{dep} giving the maximum stability. They see that glasses deposited below this temperature show broader peaks than the ones deposited above the UG T_{dep}. When analysing their results it is also possible to conclude that glasses with the same T'_f present small differences in the devitrification temperature (about 1–2 K). Unfortunately, these features fall within our uncertainty and cannot be resolved with our technique.

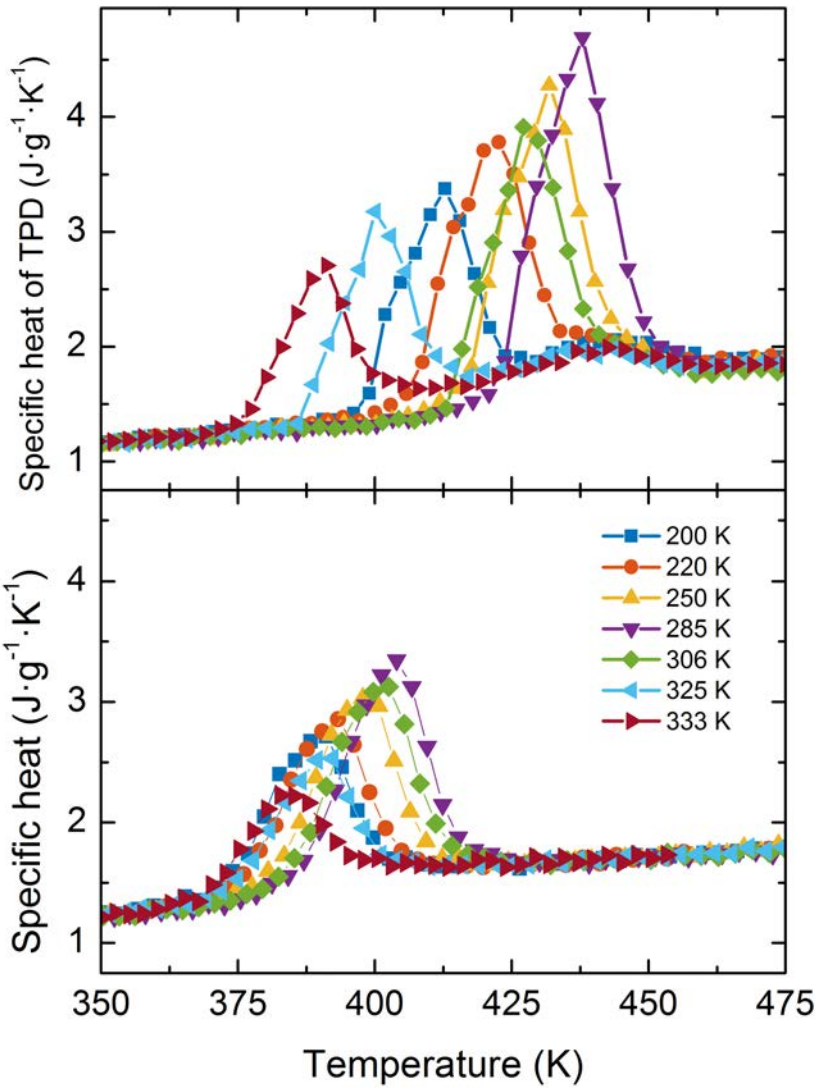

Figure 5.7: Calorimetric trace for capped (upper panel) and single (lower panel) TPD samples deposited at different temperatures. The calorimetric trace of the top panel is normalised to the TPD mass, before the subtraction of the TCTA glass contribution to the heat capacity. The deposition temperature is indicated in the lower legend (colour and symbol scheme valid for both graphs). The TPD thicknesses in the TCTA/TPD/TCTA geometry are 45 nm with a total dispersion between samples of ±13 % (upper panel). The thickness of the single TPD layers is 42 nm with a total dispersion of ±16 %.

5.6 Proving the isothermal kinetic stability

We have seen how by capping the stable glass of TPD—and the less stable—the surface-initiated growth front can be suppressed. The higher T_g layer with lower mobility on top of the TPD delays the onset of devitrification in a heating scan. However, in organic electronics applications such as OLEDs, the proper performance of these devices will ultimately be limited by the maximum temperature they can stand before the deterioration, leading basically to significant drops in their performance [103]. Hence,

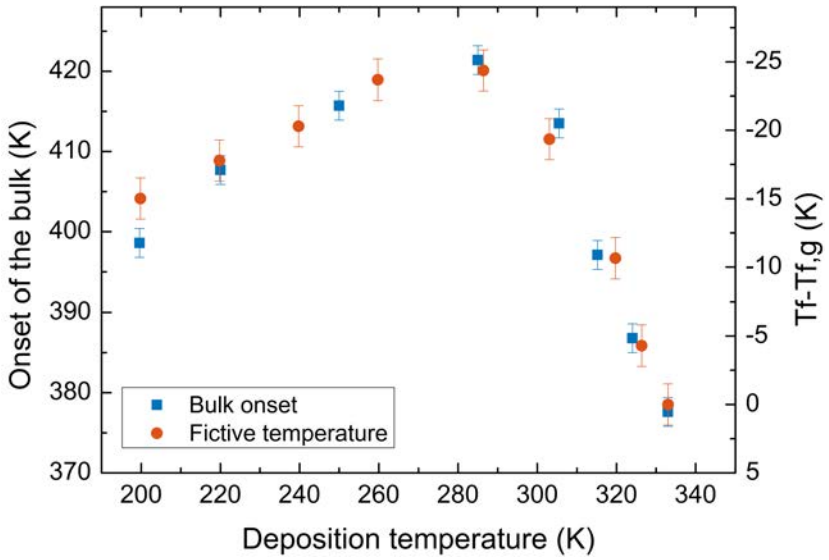

Figure 5.8: The onset of the bulk (blue squares, left-axis) and limiting fictive temperature (red circle, right-axis) as a function of the deposition temperature for capped TPD samples. The axes are appropriately scaled to superimpose both data sets. A good correlation is seen, except for the $T_{dep} = 200\,\mathrm{K}$, where the difference is slightly off the trend. The T_f' data is taken from figure 3.6.

isothermal stability—i.e. how much time takes the glass to rejuvenate completely—will provide more practical information on the hindrance of the devitrification in capped ultrastable glasses.

In this section, we present some preliminary results on the annealing of capped layers of UG of TPD. This is meant to be the seed of a new and more complete study on the homogeneous transformation mechanism in VD glasses. Figure 5.9 shows the calorimetric trace of 40 nm capped layers deposited at 285 K (the UG) and annealed at 347 K ($T_g + 14\,\mathrm{K}$) for four different annealing times. After the annealing, the glasses are passively cooled (ca. $500\,\mathrm{K\,s^{-1}}$) to the reference temperature (250 K) before performing the calorimetric scan. For completeness, the pristine non-annealed UG and a FC capped glass are also included. The FC was created by heating a freshly prepared UG sample up to $T_g + 40\,\mathrm{K}$ for some seconds and passively cooling to the reference temperature.

Annealing the UG glass during 10 and 46 minutes at 347 K shifts the onset of devitrification of the bulk to lower temperatures, hence, decreasing the kinetic stability. For the 90-minutes annealing, the onset is still decreasing and a second small peak around 375 K starts to appear. This second peak coincides with the fast-cooled glass of TPD. Finally, in the 180-minutes annealed sample, the area of the FC increases while it becomes difficult to distinguish between the TCTA peak and the possible original TPD rejuvenated peak. Assuming this last sample is in the final stages of its rejuvenation, we can estimate a total time for a nearly complete transformation of the capped glass

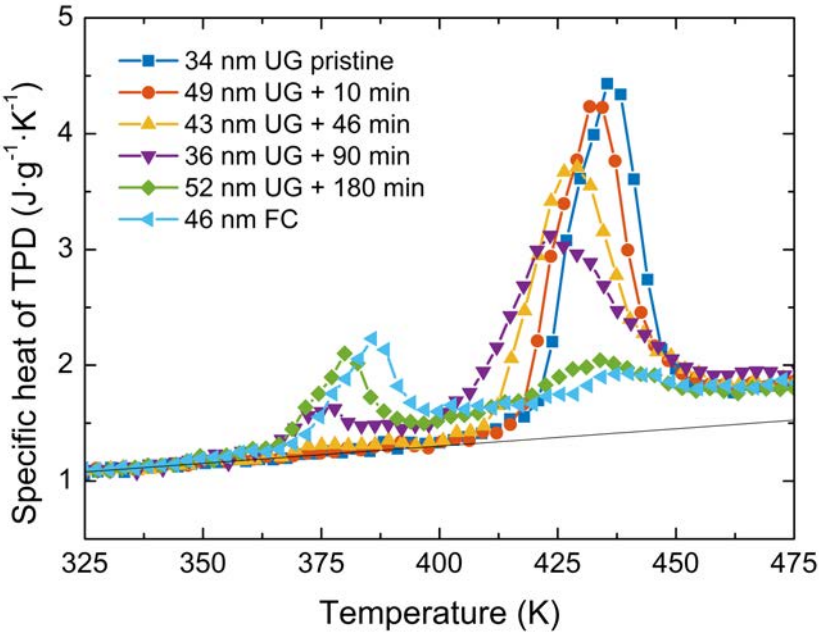

Figure 5.9: Capped ultrastable glasses of TPD annealed for different times at 347 K (T_g + 14 K). The legend indicates the thickness of the TPD layer together with the annealing time. FC stands for the fast-cooled glass, obtained after an already scanned sample. The black line corresponds to the specific heat of the TPD glass.

somewhere between 5400 s and 10 800 s. This is only meant to be a first approximation. A more thorough study with more annealing times, annealing temperatures and thicknesses must but carried out to fully characterise the isothermal rejuvenation.

To compare the time that would need a single sample of ultrastable TPD glass to transform into the liquid completely, we must use the growth front velocity at $T_g + 14$ K. We do not have access to this temperature regime with the fast-scanning nanocalorimetry technique. Walters et al. [40] use ellipsometry and an annealing protocol to provide the transformation front velocities of TPD glasses up to $T_g + 15$ K. At 347 K, they found a velocity of around 0.2 nm s^{-1} for the surface initiated front. Hence, a non-capped TPD sample of 40 nm would take of the order of 200 s to fully transform into the supercooled liquid via this heterogeneous mechanism. We can estimate, therefore, an increase in the isothermal kinetic stability of a factor 25-50, in time units, for a 40 nm stable sample of TPD. These results are consistent with the data obtained by Sepúlveda et al. [88], where they showed how the transformation front of IMC ultrastable glasses was effectively suppressed by capping it with a higher T_g material, TNB in that case. They demonstrated how the kinetic stability of a capped glass is substantially enhanced, with the interface TNB/IMC completely arrested. However, their glass eventually transformed at the interfaces between the stable glasses of indomethacin and the partially deuterated indomethacin they used to follow the transformation with SIMS. They argue that the kinetic stability might be further enhanced up to a factor of 50 for a 20 nm stable IMC glass without these artificial interfaces used for their measurements, as we are

showing here.

We have discussed the enhancement of the isothermal stability in terms of the rejuvenation of the primary peak, following its shift to lower temperatures with time. The shift of the whole primary peak is indicative of rejuvenation that is taking place cooperatively throughout the entire glass. However, the gradual appearance over time of the second peak corresponding to the FC glass is indicative of two differentiated regions. A first one, where a fraction of the glass is homogeneously rejuvenating and a second one that has completely transformed into the supercooled liquid. The latter region yields, after the fast cooling to the low-temperature transition, the first devitrification peak. Having two distinct regions during the annealing protocol is consistent with the thermodynamic picture where the transformation into the SCL—or melting—occurs via a 'nucleation and growth' from the higher mobility regions (liquid) to the lower mobility regions (glass), as conceived by random first order transition theory [17]. However, a note of caution is due here, as having these two distinct regions is also compatible with a slower growth front starting at one or both interfaces with TCTA which would indicate that the surface mobility is not completely suppressed by the TCTA but highly reduced instead. In fact, this double-peak feature was also observed by Sepúlveda et. al [107] in ultrastable glasses of toluene. However, in that case it was clearly a front mechanism since they used non-capped films. Further experiments are needed to explore these possibilities.

5.7 Summary

We have taken a step forward towards enhancing our understanding of the transformation mechanisms of stable glasses by gaining access to the bulk devitrification into the SCL. By capping the stable glasses of TPD with a higher T_g material we have effectively eliminated the growth front. Using four different multilayer configurations, we have inferred that our single samples of TPD transform through a surface-initiated front, which contrasts with the substrate-initiated front found by other authors. We have seen how the onset of the devitrification can be delayed up to 40 K by capping the free surface of an ultrastable glass, while without capping, this delay was limited to $\approx$20 K and thickness-dependent due to the appearance of a transformation front. We have found an excellent correlation between the onset of the bulk and the fictive temperature for glasses deposited in the 0.6-1.0T_g range. These results provide further support to the kinetic facilitation picture in which these highly packed glasses start transforming where the mobility is higher.

In a typical OLED device, the active organic layers are capped either by the electrodes or by another organic layer, so it is of vital importance to understand the effect of capping on the stability of a glass. We have shown here how the isothermal stability

can be enhanced by a 25 to 50 factor if the glass is capped with a higher T_g glass-former. In that sense, this reinforces the idea of employing stable glasses to design organic electronic devices—OLEDs, for instance—with enhanced temperature stability and operational lifetime. However, this last statement remains yet to be thoroughly addressed.

Chapter 6

Thermal conductivity on vapour-deposited glasses

6.1 Introduction

In Chapter 1, we have briefly detailed how organic—and inorganic—glasses are essential for a broad range of scientific and technological processes [13]. Particularly, their application into organic semiconductors stands out as a suitable candidate for a new generation of electronics due to their inherent flexibility, potential low fabrication cost and large area fabrication [7, 108]. Their utilisation in organic electronics applications ranges from organic light-emitting devices [108] (OLEDs), organic field-effect transistors [109], organic solar cells [110] or even thermoelectric generators[111]. Among the different routes for preparing the active layers of these devices, physical vapour deposition stands out as a prominent technique for small molecule organic semiconductors [7], which proves also a suitable tool to tailor the properties of the evaporated amorphous layers. We have already seen how properties such as thermodynamic and kinetic stability [10, 29, 45, 112] or higher densities [39, 40, 44, 46] can be effectively enhanced on different organic molecules when evaporating at substrate temperatures of 0.80-0.90T_g. Moreover, the orientation of the molecules also depends on the deposition temperature as seen with birefringence [39] and dichroism [45] measurements. However, to date, only a few studies are addressing the thermal conductivity of glassy thin films of small organic semiconductors molecules [113, 114], and none of them have focused on the role that molecular anisotropy or other glass features such as density variations, play on this property. However, several studies are addressing the thermal conductivity in organic semiconductor crystals [115–117].

Most of the works in organic electronics are focused on the electronic transport properties since this is a key parameter for the employment of these materials in optoelectronic devices. Nonetheless, thermal transport and thermal management in organic devices are becoming increasingly important, in particular for scaled-up large area applications and for the integration of these devices in complex arrays and systems.

Generally, the thermal conductivity in amorphous organic semiconductors is much lower than in traditional inorganic semiconductors [113, 118, 119], with typical values below $1\,W\,m^{-1}\,K^{-1}$. For the sake of comparison, silicon substrates used in microelectronics applications have a thermal conductivity of $150\,W\,m^{-1}\,K^{-1}$and stainless steel of $16\,W\,m^{-1}\,K^{-1}$ [120]. For instance, during its normal operation, OLED devices suffer thermal stress and degradation [121]. Luminance and lifetime also decrease when operated at high temperatures [103]. Localized Joule heating effects can highly reduce brightness homogeneity and it can be worsened as temperature increases with operation time [122]. Chung et al. showed how the lifetime of an OLED could be effectively enhanced by decreasing the peak temperature with efficient heat dissipation using, in their case, different substrates [123]. Although the heat capacities and the conductivity of active layers from these devices are rather small, evaluating the details of the heat generation and dissipation are required to fully understand the impact on their performance. Furthermore, recent studies are starting to pay attention also to organic semiconductors due to their potential for thermoelectric applications [124, 125]. Their semiconductor nature and the low thermal conductivities make them potential candidates to improve the thermoelectric figure-of-merit ZT. We note most of the previous studies in this direction have been reported for polymer-based devices and very few on small molecule organic semiconductors. Therefore, either for thermal management of organic devices or for thermoelectric applications, a key parameter that must be known is the thermal conductivity. Even more interesting than assessing its value, is the possibility of modifying it. Wang et al. reported the feasibility of tailoring the thermal conductivity of a novel organic semiconductor used in transistor devices with Ag nanoparticles [126], for which they measured the out-of-plane thermal conductivity.

The main difficulty towards a comprehensive analysis of the thermal conductivity arises from the lack of appropriate techniques to measure the in-plane thermal transport properties in thin films. Previous measurements on polymers or polymer nanofibers were conducted on suspended structures [127, 128] which directly provide the in-plane thermal conductance. This methodology, frequently used for inorganic nanowires of low thermal conductance, requires lengthy or sophisticated approaches to precisely place the sample bridging the heater/sensor platforms and it is not directly applicable to the kind of organic thin films of interest in this work. We have recently shown that a modification of the 3ω–Völklein technique [83, 84] can be used to monitor in real-time the growth of organic layers and to measure their in-plane thermal conductance ($k_{||}$) [129]. The high sensitivity of the technique and its versatility makes it an ideal tool to explore the in-plane thermal transport characteristics of organic thin films.

In this chapter, we use the modification of the 3ω–Völklein technique explained in Section 2.4 to measure, in situ, the thermal conductance of films of organic glass-formers

during and after its growth. We first use the high sensitivity of the technique to monitor in real-time the first stages of thin film growth of the hole transport materials TPD and α-NPD. The influence of the deposition temperature on the percolation threshold is also addressed. The in-plane thermal conductivity data is complemented with out-of-plane thermal conductivity ($k_\perp$) measurements using the standard 3ω technique, briefly described in Section 2.4.5. We investigate the impact that the deposition temperature impinges on the thermal conductivity of TPD and α-NPD films. The deposition temperature has a direct bearing on density, thermal and kinetic stability and molecular orientation, among other properties. Hence, we discuss the effect that all these properties have in the measured thermal conductivities.

6.2 Monitoring thermal conductivity during the film growth

Having the 3ω–Völklein sensors inside the UHV evaporation chamber allows not only to measure in situ the thermal conductivity of the deposited layer but also to monitor its evolution during the growth of the layer. To obtain the V_{3w} amplitude, we use a time window equal to 3 current periods, which is translated into a time resolution of 3 s for a current waveform of 1 Hz during the growth of the layer. To achieve sub-nm resolution during the growth of the layers, we must use very low deposition rates. We start by monitoring the thermal conductance of TPD layers while growing them at a rate of 0.02 nm s^{-1} for two different T_{dep}, (267 $\pm$ 2) K and (304 $\pm$ 2) K . The temperature uncertainty is due to the oscillation produced by the current wave. We also measure the growth of an α-NPD layer deposited at (296 $\pm$ 1) K at a rate of 0.015 nm s^{-1}. In this case, we use the same current wave amplitude but a frequency of 0.5 Hz, which is translated in a time window of 6 s for each measurement.

Figures 6.1a and 6.1b show the evolution of the conductance (G) versus thickness for the two TPD layers deposited at 267 K ($0.80T_g$) and 304 K ($0.91T_g$), respectively. In the inset of Figure 6.1a, the electrical conductance is represented versus the thickness of a TPD layer during its growth on top of a nitride membrane. Figure 6.2a shows the growth of α-NPD film deposited at 297 K ($0.81T_g$) whereas Figure 6.2b shows again an α-NPD film grown at the same temperature but deposited on top of a pre-existing continuous α-NPD layer.

We have identified four distinct regions during the growth of the OSG layers for the first three samples. Region I is characterised by an exponential drop of the conductance of the membrane in the first three cases. In region II, the decrease is slowed down to a minimum until it reaches region III, where the G starts to increase monotonically. Between region III and IV, there is a change into a linear regime of G versus thickness. As explained below, we can identify these regions with the growth modes of a film on a substrate: the first initial drop in region I corresponds to nucleation and island

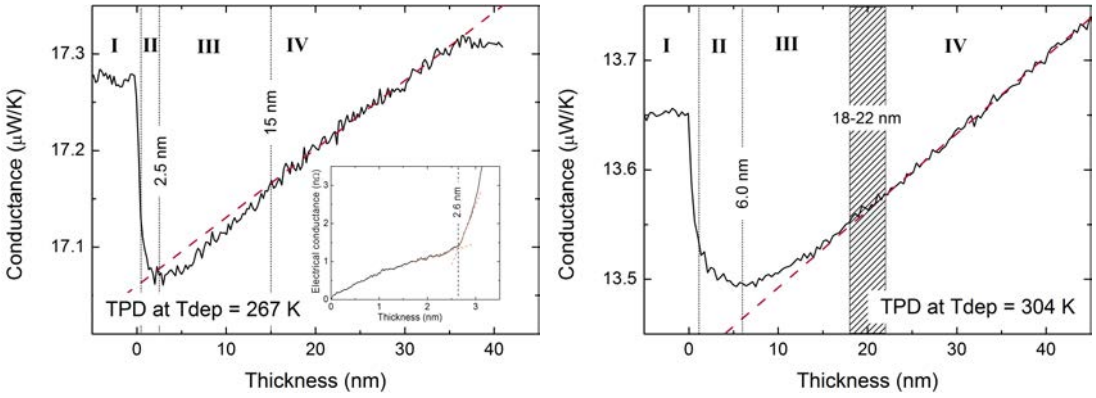

(a) Layer grown at $T_{dep} = (267 \pm 2)$ K, $0.80T_g$

(b) Layer grown at $T_{dep} = (304 \pm 2)$ K, $0.91T_g$.

Figure 6.1: Thermal conductance versus film thickness during the deposition of a TPD layer. The layers are deposited at $0.02\,\mathrm{nm\,s^{-1}}$. The vertical lines separate the different growth regions. Region I, between zero nanometers and the first line, correspond to nucleation and isolated island growth; region II to island growth and subsequent coalescence; region III marks the percolation across the surface until region IV is reached, where the vertical growth of a continuous layer starts. The inset of the Figure 6.1a shows the evolution of the electrical conductance during the growth of an equivalent TPD film.

growth, in region II the islands grow until they start to coalesce; region III marks the onset of the percolation until the full surface is covered at the onset of region IV, where the film starts the vertical and continuous growth. Amorphous organic layers grow following a 3D Volmer-Weber mechanism with isolated islands in the early growth stages on top of a silicon nitride substrate. This is further supported by Figure 6.3 which shows the presence of isolated islands for a 2.6 nm (nominal thickness) film of TPD grown at $0.80T_g$ (AFM image) whereas the 14.3 nm film is already continuous (SEM image). The morphological study of the vapour deposited samples was carried out ex situ and in different evaporation runs. This adds some uncertainty to the onsets of the different growth modes in our samples. Moreover, Zhang et al. [130] showed how surface diffusion in TPD was greatly enhanced compared to the bulk, using precisely the morphological changes in their surfaces to infer its value, even at room temperature. This prevents us from providing a thorough analysis of the topology evolution of our thin layers using either ex situ AFM or SEM.

6.2.1 Interpretation of the growth regions

The first fast initial drop in thermal conductance seen in region I of Figures 6.1a, 6.1b and 6.2a can be attributed to the nucleation and formation of the first islands on the top of the nitride membrane. To interpret the evolution of the thermal conductance with the organic film thickness we must first comment on the intrinsic thermal conductivity of the nitride membrane. The disordered nature of the membrane is consistent with the

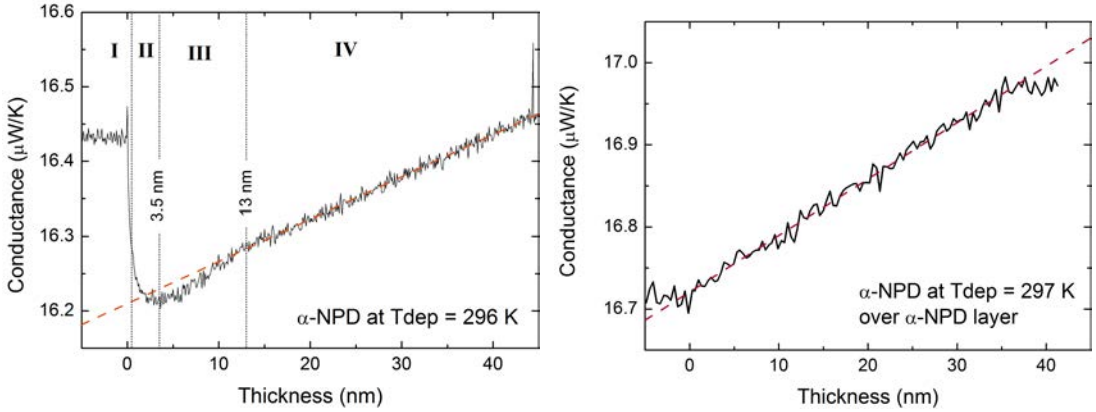

(a) Layer grown on top of the SiN_x at $T_{dep} = (296 \pm 1)$ K, $0.80T_g$

(b) Layer grown on top of a pre-existing α-NPD continuous layer at at $T_{dep} = (297 \pm 2)$ K, $0.81T_g$.

Figure 6.2: Thermal conductance versus film thickness during the deposition of a α-NPD layers at a rate of 0.015 nm s^{-1}. The distinct and marked regions in Figure 6.2a are the same explained in Figure's 6.1 caption. Figure 6.2b shows only a single growth region equivalent to IV.

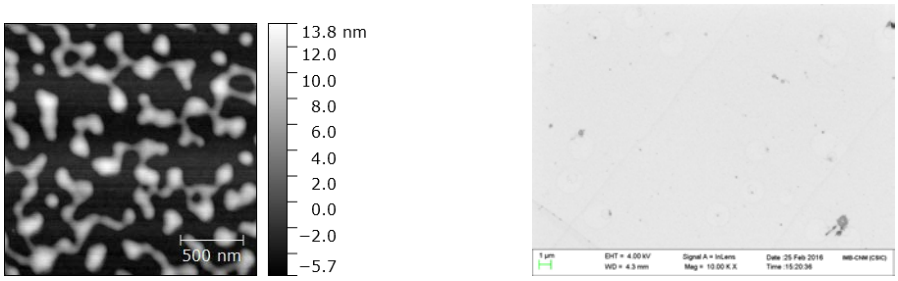

(a) AFM image of a 2.6 nm thick TPD layer.

(b) SEM image of a 14.3 nm

Figure 6.3: AFM and SEM images of discontinuous and continuous TPD layers. AFM was used to discriminate the material from the substrate in the discontinuous film.

low value of its thermal conductivity, i.e. 2.25 W m^{-1} K^{-1} at room T. The theory of the minimum thermal conductivity [131] in which lattice vibrations with mean free paths half of the interatomic distance—termed *diffusons*—are responsible for heat transfer does not provide a complete understanding of thermal transfer in many disordered solids [132]. Recently, it has been shown that longer-wavelength vibrations—the so-called *propagons*—also carry part of the heat in disordered materials [132]. Due to their non-localized nature, propagons, embedded with larger mean free paths, are more sensitive to surface variations than diffusons, which are more localised excitations, diffusons. We attribute the initial decrease of thermal conductance to scattering of propagons with the organic islands. We tentatively describe this process in terms of a change in the specularity of the surface that results in an enhancement of the interface scattering. This is supported by the fact that the sample deposited on top of a

pre-existing layer of the same material (Figure 6.2b) does not show any drop in conductance since there is no mismatch at the interface organic-organic and the new layer is expected to grow as a continuous film from the first stages.

Next, in region II, the thermal conductance starts to slow down until it stops. Here, the islands begin to coalesce and additional paths for the heat transfer are created, partially compensating the interface scattering. The inset of Figure 6.1a demonstrates that the minimum in thermal conductivity coincides with the percolation threshold, for the TPD sample deposited at 267 K. This measurement was carried out independently but under identical conditions as for the TPD sample shown in Figure 6.1a. The sharp increase in the electrical conductivity observed at 2.6 nm indicates that the percolation starts at this thickness range, providing a continuous conductive path between both electrodes. In region II, while percolation increases, new channels across the surface are created which provide further heat flow paths that compensate the contribution of the interfacial scattering. This rise in G lasts until a new linear regime is reached, which we identify with the growth of a continuous layer, marking the beginning of region IV. Therefore, this latter region corresponds to the vertical growth of a continuous film with a constant slope—pointed out by the broken line— imposed by the thermal conductivity of the material.

Contrary to what we have just seen, in Figure 6.2b for the α-NPD sample grown on top an α-NPD film, there are no differentiated regions. The film starts growing in a linear regime from the very beginning since we are not creating any new interface between the two layers.

6.2.2 Interpretation of the growth behaviour as a function of T_{dep}

TPD has been evaporated at two different deposition temperatures. We can compare in this way the growth dynamics of the two T_{dep}/T_g ratios explored. TPD samples deposited at $0.80T_g$ and $0.91T_g$ are both stable glasses, and according to Walters et al. [40], the difference in density is roughly about 0.3 %. The initial drop of the thermal conductance is relatively similar for both samples, a maximum drop of 1.23 % and 1.17 % for the $0.80T_g$ (Figure 6.1a) and $0.91T_g$ (Figure 6.1b), respectively (the α-NPD sample deposited at $0.8T_g$ exhibits also a similar drop of 1.34 %, Figure 6.2a). However, a remarkable difference can appreciated between Figures 6.1a and 6.1b, for TPD, in the percolation threshold, marked by the separation lines between region I and II. For the sample grown at 267 K percolation starts around 2.5–3.0 nm whereas the sample grown at 304 K has this threshold around 6 nm. It is also possible to identify that the thickness at which the films become continuous also differs, being around 15 nm for the 267 K sample and between 18–22 nm for the 304 K . Although the latter is not so clearly resolved from the data since the onset of the change in the slope between both

regions is subtle. Notwithstanding, the different growth dynamics is unmistakably identified by the different behaviour in region III. In the sample grown at 267 K, the thermal conductance in the percolation region increases faster than the vertical growth from region IV. In contrast, the sample deposited at 304 K exhibits a smaller slope in region III.

We can now rationalise these findings qualitatively in terms of surface diffusivity. Assuming that surface tension changes only slightly in this temperature range, variations in surface mobility with substrate temperature could be at the origin of the observed behaviour. According to Zhang and co-workers [130] surface mobility in TPD is of Arrhenius-type with values of $D_s = 7 \times 10^{-18}\,\mathrm{m^2\,s^{-1}}$ at 304 K and $8 \times 10^{-19}\,\mathrm{m^2\,s^{-1}}$ at 296 K. Extrapolating to 267 K leads to $D_s = 4 \times 10^{-23}\,\mathrm{m^2\,s^{-1}}$. With those values and using $x \approx (4Dt)^{1/2}$ as the mean distance molecules diffuse during time t, it is possible to roughly infer if island formation is driven by diffusion-limited aggregation or by attachment-limited aggregation mechanisms. As growth rate was $0.02\,\mathrm{nm\,s^{-1}}$ the residence time of surface molecules before being buried by new molecules impinging from the vapour is of the order of 25 s for a 1 nm layer. Therefore, at $T_{dep} = 304$ K, $x \approx$ 26 nm while at $T_{dep} = 267$ K , $x \approx 0.06$ nm. Within this assumption, the layer at 267 K will be composed of many, but small, islands, while growth at 304 K will result in less, but larger islands. This is compatible with the results of Figure 6.2a which shows that films grown at 267 K achieve the onset of percolation and a continuous film at smaller thicknesses compared to the sample grown at higher T. Although we do not have two temperatures for the sake of comparison for the α-NPD, the sample grown at $0.80T_g$ behaves similarly to the equivalent TPD sample, i.e. drop of thermal conductance upon island formation, percolation threshold thickness at around 3.5 nm and continuous film at 13 nm. Our threshold for continuous films is in agreement with recent work from [130]. In their work, they obtained uniform layers at thicknesses above 20 nm, although their films were deposited at a higher temperature of 330 K ($0.99T_g$). A complete analysis of these growth mechanisms is out of the scope of this work, but it seems clear that the 3ω–Völklein technique opens a new avenue to unravel the physics of film growth of vapour-deposited glasses.

6.3 Thermal conductivity dependence on deposition temperature

We focus now our attention on the dependence of the thermal conductivities for continuous films of TPD and α-NPD over a wide range of deposition temperatures, from 220 K to 333 K and 368 K, respectively. For these measurements, we do not require the low deposition rates we needed to follow the early stages of the growing films. Hence,

we use faster rates of $(0.21 \pm 0.02)\,\mathrm{nm\,s^{-1}}$ and $(0.10 \pm 0.02)\,\mathrm{nm\,s^{-1}}$ for TPD and α-NPD, respectively—similar to the rates used for the heat capacity characterisation.

Our aim is to compare the thermal conductivity of samples grown at different temperatures but measured at equal conditions. We start measuring the conductance of TPD films using two different approaches at each deposition temperature. In the first one, we carry out single conductance measurements on 340 nm thick layers evaporated directly on the clean surface of the membrane. As explained in Section 2.4.3, the in-plane conductivity $k_{\parallel}$ can be obtained from the slope of the linear regime (region IV) using equation 2.24. Although the dependence of k with temperature is weak in organic amorphous systems [74], we must compare values measured at the same temperature—precluding us to use the slope of equation 2.24 to extract the conductivity. So, after each deposition at a certain T_{dep}, the sample is set back to a reference temperature, T_{ref}, where all the conductivity measurements are performed. The conductance at T_{ref} is obtained from the difference in the measured conductance before, and after the deposition of the film, that is

$$G_{film} = G_{total} - G_{SiN_x} \tag{6.1}$$

Once the thermal conductance is measured, we can make use of equation 2.20 to get the thermal conductivity considering the thickness of the film and length of the sensor's strip. The amplitude of the current waveform injected to the sensor is chosen accordingly to produce a $\Delta T = 4$ K at a frequency of 1 Hz. While the reference temperature is set to 295 K, the effective temperature is (297 ± 1) K, due to the thermal oscillations produced by the current wave across the sensing area. After each deposition, the sensor is cleaned outside the UHV chamber using acetone and ethanol, and prepared for the subsequent evaporation. The thermal conductivity values obtained using this procedure are shown in Figure 6.5 (labelled as *single-layer*) as a function of T_{dep}. This method is time-consuming as it requires opening and closing the UHV chamber for each measurement. Moreover, the sensor must be manipulated between measurements for the manual cleaning and the wiring to the socket with the consequent membrane weakening or possible structural damage.

In the second approach, the thermal conductance of samples prepared at several deposition temperatures is measured in a single run at a reference temperature of 296 K. Without breaking the vacuum, 150 nm thick layers are grown on top of each other at different T_{dep} while the conductance measurements are performed in-between depositions. Figure 6.4 represents a scheme of the followed protocol. The deposition temperature in two consecutive samples is deliberately alternated between temperatures above and below T_{ref}. In such a way, the effects of conceivable instrumental drifts when evaluating k are randomised. For instance, we start measuring the conductance of the bare SiN_x membrane to get the initial conductance at the reference

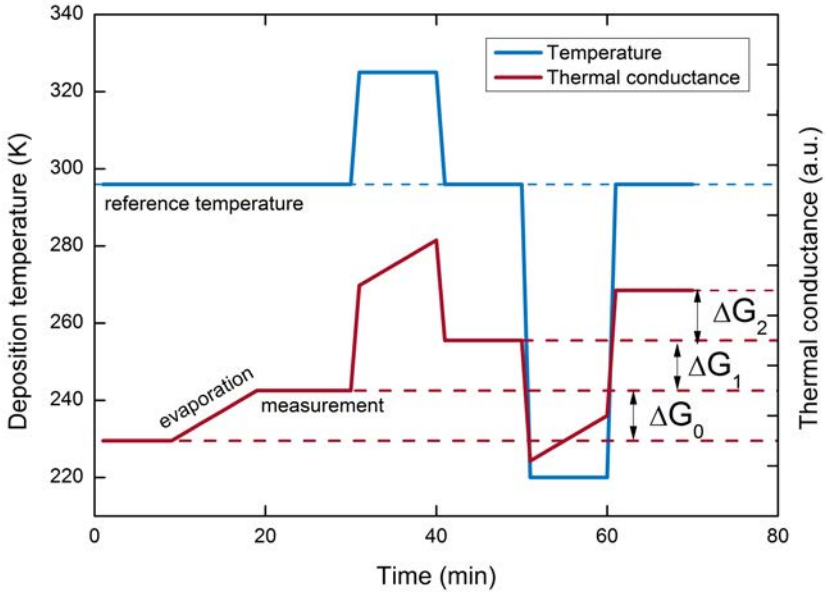

Figure 6.4: Temperature scheme followed (blue-line) to measure the thermal conductance of multiple layers evaporated at different substrate temperatures. The conductance of each layer (red-line) is obtained as the differential increment between two consecutive evaporations, always at a reference temperature of 295 K, as indicated in equation 6.2.

temperature. Then, we evaporate a 150 nm layer at this same temperature, and the conductance starts growing until the layer is finished. The conductance of the layer is obtained again as the differential measurement, following the expression 6.1. We then increase the substrate temperature and so does the conductance because of the temperature. We evaporate a layer of the same thickness at this new temperature, and G increases linearly. Once deposited, the temperature is set back to T_{ref}, and the new G is measured again. Therefore, the layer conductance is obtained as the differential increment before and after each deposition, following the straightforward expression:

$$G_{film,i} = G_{total,i} - G_{total,i-1} \tag{6.2}$$

where i corresponds to each step.

The scheme is then repeated for another set of deposition temperatures. For this type of measurement, we use a frequency of 0.5 Hz for the current waveform, instead of the 1 Hz used in the previous approach. As explained in Section 2.4.3, lowering the frequency increases the accuracy of the measurements as well as it decreases the $G_{2\omega}$ dependence on other properties of the sample. This allows us to measure thicker samples without compromising the accuracy of the conductance. For instance, if we go back to Figure 2.14, we can see how for a frequency of 0.5 Hz, the $G_{2\omega}$ is less than 1 % away from the real conductance. In this second approach, the amplitude of the current wave is also reduced, producing, in this case, a ΔT = 2.25 K. Finally, when

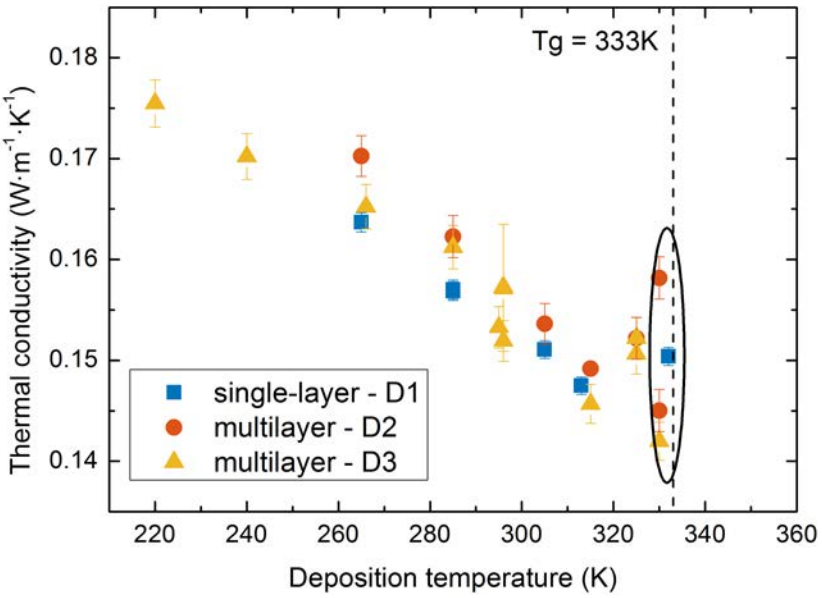

Figure 6.5: Measured thermal conductivity of TPD glasses as a function of T_{dep} and measured at (296 ± 1) K. The two different procedures are labelled as *single-layer* measurements and *multilayer* measurements. Hence, each blue-square value is obtained from independent evaporations of 340 nm thick layers, cleaning the sensor after each sample deposition. Circle and triangle points are obtained following the continuous method, in which a multilayer is deposited, and the conductivity measured differentially between 150 nm thick layers. Three independent devices (D1, D2, D3) have been used for the determination of G. The error bars are calculated from uncertainty in the thickness determination from profilometry.

using this approach, we are assuming that the glass layers are not affected by a possible rejuvenation or ageing when depositing the different layers. As long as the T_{dep} is kept below T_g and the deposition times short compared to the vast timescales required for rejuvenation, this effect is hindered. The results obtained using this procedure are shown in Figure 6.5, labelled as *multilayer*, together with the results obtained using the other approach. In all cases, the use of different devices is labelled as sensor Di (where i stands for the device number).

From Figure 6.5 it is clearly seen that the two approaches are in reasonable agreement. As commented in Section 2.4, the sensitivity of this technique is remarkably high, about $\Delta G/G \simeq 10^{-3}$ in conductance. However, the final accuracy of the thermal conductivity is not limited by the conductance measurement itself but from the uncertainty in the amount of mass sensed. The uncertainty in the initial calibration using profilometry is of ±2 nm, represented by the error bars in Figure 6.5 using the corresponding error propagation. However, other factors such as the reproducibility in the reading of the QCM or the use of different devices might contribute to the small dispersion. Using 95 % confidence interval for the standard error for T_{dep} with more than one point we can estimate an upper limit of the statistical error in thermal conductivity of $\pm 0.004\,\mathrm{W\,m^{-1}\,K^{-1}}$.

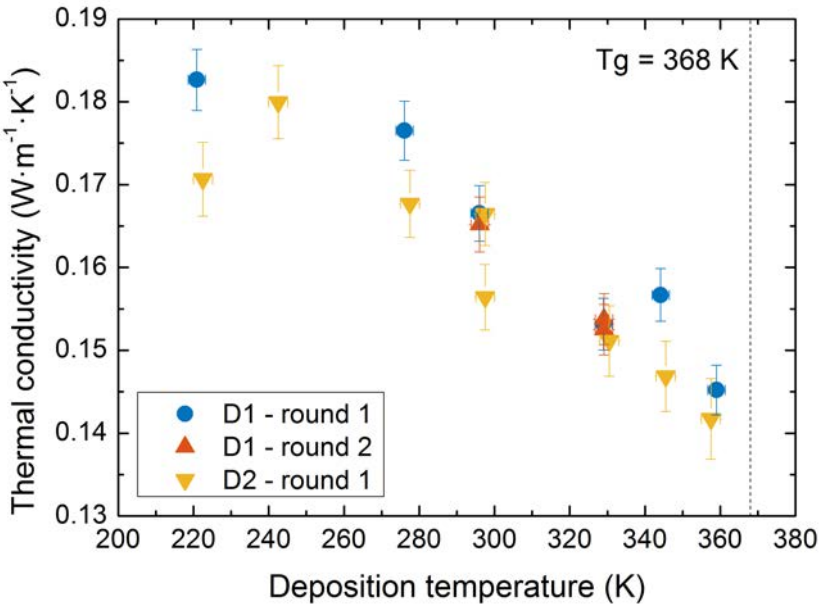

Figure 6.6: Thermal conductivity measured of α-NPD glasses as a function of T_{dep} and measured at (296 $\pm$ 1) K Circle and triangle points are obtained following the multilayer measurements, in which a multilayer is deposited, and the conductivity measured differentially between 150 nm thick layers. In this case, the same device (labelled D1) is used in two independent depositions.

The values for the thermal conductivity obtained at different deposition temperatures range from 0.175 W m^{-1} K^{-1} to 0.145 W m^{-1} K^{-1}. Such low values are an indication of the amorphous character of the layers. What is immediately seen in Figure 6.5 is the k dependence on the T_{dep}. There is a clear trend to higher values of k for the lower deposition temperatures. The lowest conductivity is obtained at a deposition temperature of 315 K, after which the conductivity slightly increases when the substrate is set to 325 K. Unfortunately, we are not able to reproduce k values for deposition temperatures close to the glass transition of TPD. Several samples evaporated at substrate temperatures between 325 K and 340 K do not show reproducible results (some even falling out of the graph window range). For temperatures below 325 K, the measurements at different temperatures and using the two different procedures are reproducible with an uncertainty of at most $\pm$0.004 W m^{-1} K^{-1}, as previously mentioned.

Figure 6.6 shows the results obtained for α-NPD using uniquely the second approach. In this case, we used the same device to perform two series of "multilayerv" experiments. The third set corresponds to the utilization of a new sensor device. An analogous behaviour to the k dependence on T_{dep} is found for α-NPD. The thermal conductivity increases from 0.142 W m^{-1} K^{-1} at $T_{dep} = 359$ K to 0.183 W m^{-1} K^{-1} at $T_{dep} = 221$ K. This variation corresponds to an increase in k between 20 % and 28 % when the data scattering is considered.

Regarding the lack of reproducibility close to T_g, we attribute it to the geometry of the

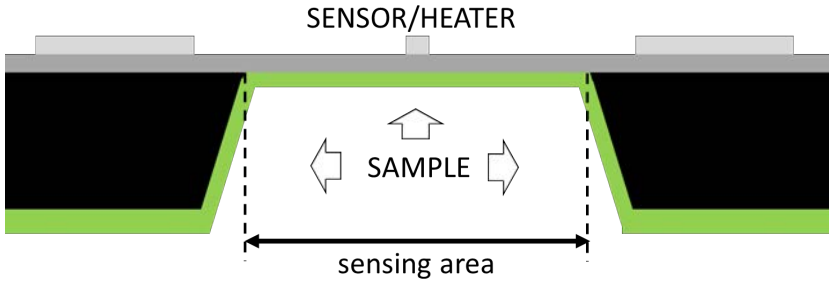

Figure 6.7: Side view of the 3ω–Völklein sensor with a deposited sample sketched in green (not to scale).

sensor and the uncertainty in the amount of mass sensed. The sensor is used without a mask to delimit the evaporation just to the sensing area (Figure 6.7), so some dewetting can occur at the edges of the membrane and the silicon frame, possibly causing some material aggregation because of surface tensions. This mechanism effect would be especially enhanced when the molecular mobility is high enough—i.e. closer to T_g. In this situation, the thermal conductance measurement can be performed as usual although the uncertainty in the amount of mass sensed leads to low accuracies and reproducibilities of the values at this region.

6.3.1 Origin of the dependence of in-plane thermal conductivity on T_{dep}

The most remarkable finding in Figures 6.5 and 6.6 is the patent dependence of the in-plane thermal conductivity on the deposition temperature. These results are in line with those of several previous studies showing how the properties of VD organic glasses can be tailored by tuning the deposition conditions such as the substrate temperature or the evaporation rate.

As already seen and thoroughly demonstrated in the previous chapters, the highest density and the highest thermal and kinetic stabilities are achieved for samples deposited around $0.85T_g$. For instance, TPD has been shown to have a maximum in stability and density around 285 K, while above and below this temperature both the density and the stability decrease (Figure 3.6). However, the behaviour of k with respect T_{dep} does not resemble those of the properties above mentioned. In Figure 6.8 we represent the TPD density (open circles, left-axis) dependence on T_{dep} from Walters et al. [40] together with our average value of k at each T_{dep} for TPD (squares, right-axis). Density data is represented as the relative variation with respect to the glass deposited at T_g. Our k data is also represented as the relative variation compared to the sample deposited at 325 K —the closest temperature to T_g with reproducible results. The temperature range between $0.80–0.85T_g$—highest density—does not show any evidence of having an inflexion point in the conductivity trend. Instead, the conductivity, shows a

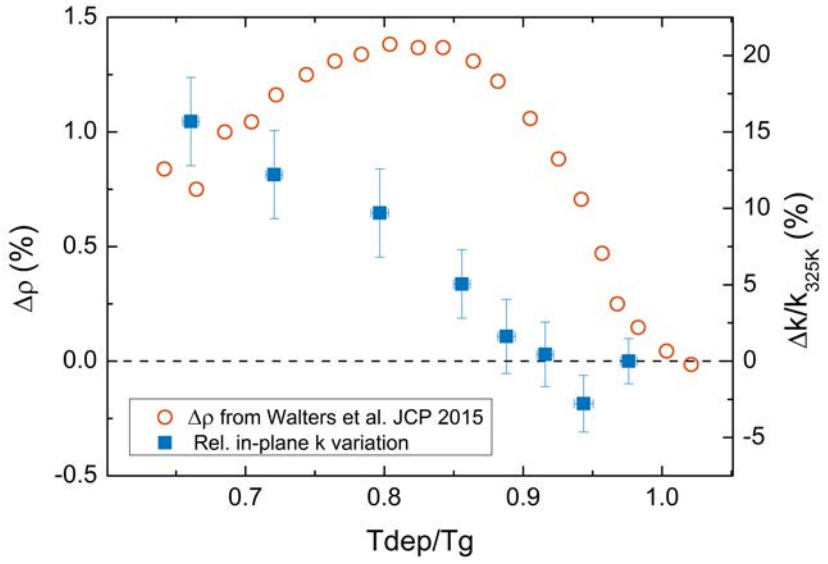

Figure 6.8: In red circles, left-axis, the density variation of TPD glasses with respect to the glass deposited at T_g, taken from Walters et al. [40]. In blue squares, right-axis, the relative variation of the thermal conductivity with respect to the sample deposited at 325 K. The $k_{\parallel}$ data is the average of the multiple measurements shown in Figure 6.5, the error bars represent the 95 % confidence interval of the mean value.

minimum at 315 K and a later increase at 325 K. In fact, the two T_{dep} with the highest ($0.66T_g$) and lowest ($0.95T_g$) thermal conductivity, only differ in density about a 0.3 %. It is also worth noticing that to calculate k one must divide by the geometric factor and by the thickness of the sample (see equation 2.20). This thickness is obtained from the QCM reading—held at room temperature—which does not account for the different densities that different T_{dep}'s impinge to the deposited samples. However, density variations are at most of 1.5 % relative to the SCL in both OSG [40, 45]. These values are below the uncertainty, so they cannot account for the conductivity variations on T_{dep}. In conclusion, although the density could be a good candidate to explain the observed differences in thermal conductivity, the lack of correlation between those quantities indicates that there is some other factor accounting for the thermal conductivity variation over T_{dep}.

To understand the origin of such behaviour, we must look at other properties of VD glasses. Works from Yokoyama et al. [133] and Dalal et al. [45] showed how different organic semiconductor molecules exhibit distinct degrees of orientation depending on the molecular aspect ratio and the deposition conditions. In Chapter 4 we have already discussed how the molecular arrangement could play a role in the way in which molecules are incorporated into the supercooled liquid propagating front during the transformation of a glassy layer. In the work from Dalal et al. [45] they perform dichroism and birefringence measurements on TPD and α-NPD—together with another OSG—and propose the molecular orientation to strongly depend on the ratio T_{dep}/T_g. Their data evidenced that the lower the temperature, the higher the tendency towards horizontal

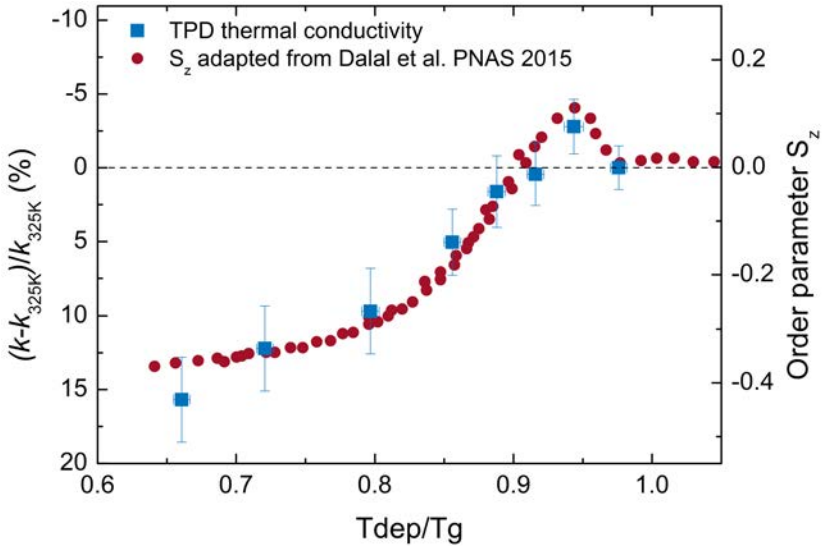

Figure 6.9: In blue squares, left-axis, the relative variation of the TPD thermal conductivity concerning the sample deposited at 325 K (notice the inverted y-axis). In red triangles, right-axis, the order parameter S_z for TPD taken from Dalal et al. [45]

orientation, reaching a plateau at low temperatures. Figure 6.9 shows the relative variation in thermal conductivity (blue squares, left-axis) normalised to the 325 K value of 0.152 W m^{-1} K^{-1}—which coincides both with the highest temperature with reproducible results and the temperature at which the sample is already isotropic. In the right axis and red triangles, the order parameter S_z from reference [45] is plotted with a common x-axis. The order parameter S_z is a measure of the average orientation of the long axis of the molecules relative to the surface normal. A value of −0.5 indicates all the molecules lying parallel in the plane of the substrate; zero indicates random orientation and a value of one indicates a perfect vertical alignment. The correlation between this parameter and the thermal conductivity variation is remarkably good, as seen in Figure 6.9 for TPD. When the molecules are more horizontally oriented, the in-plane thermal conductivity is higher. From Figure 6.9, it is worth noticing that even the small peak at 315 K ($0.95T_g$)—indicating a slight tendency to vertical orientation—is also reproduced in the thermal conductivity, showing its lowest value for the in-plane conductivity and proving the high sensitivity of the technique. Figure 6.10 represents the equivalent representation of Figure 6.9 but for α-NPD this time. Although the data from Figure 6.10 show more uncertainty, we see how the same argument is still valid also for this molecule, which reinforces the role that molecular orientation plays in the thermal conductivity.

6.3.2 Out-of-plane thermal conductivity measurements

Our results suggest that heat transport in the parallel direction is favoured when molecules have the propensity to lie with the long molecular axis (along with the

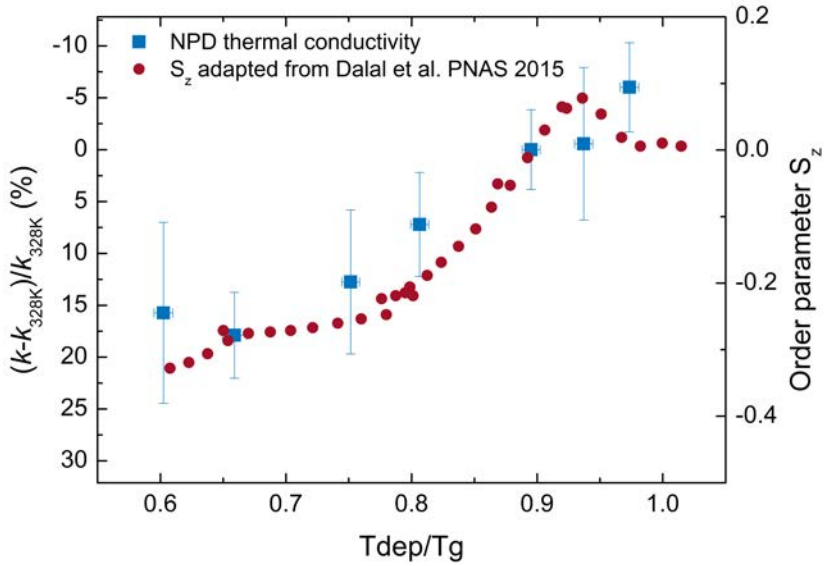

Figure 6.10: In blue squares, left-axis, the relative variation of the α-NPD thermal conductivity concerning the sample deposited at 325 K (notice the inverted y-axis). In red triangles, right-axis, the order parameter S_z for α-NPD taken from Dalal et al. [45]

N-N axis, see Figure 2.5b) parallel to the surface. On the contrary, the resistance to in-plane thermal transport is higher when molecules are isotropically oriented or even have a slight tendency to align in the out-of-plane direction. At first glimpse, this is somewhat surprising given the small size of the molecular unit and the disorder inherent to the glass. To confirm the existence of thermal anisotropy we carried out out-of-plane thermal conductivity ($k_\perp$) measurements with the 3ω technique for thin films (see Section 2.4.5 for further details) on two TPD samples: one grown at $T_{dep} =$ 220 K with the molecules preferentially aligned parallel to the substrate and another at $T_{dep} = 304$ K with isotropic orientation. As the $k_\perp$ measurement required an ex situ preparation, the sample deposited at $T_{dep} = 304$ K ($0.91T_g$) was chosen as the isotropic representation—instead of sample deposited closer to T_g—because of its higher thermal stability. An out-of-plane thermal conductivity of $(0.18 \pm 0.02)\,\mathrm{W\,m^{-1}\,K^{-1}}$ was obtained for the anisotropic sample and a value of $(0.23 \pm 0.02)\,\mathrm{W\,m^{-1}\,K^{-1}}$ for the isotropic one.

The value for the $k_\perp$ for $T_{dep} = 304$ K is in agreement with the value found in literature. Kim et al. [113] obtained a value of $0.24\,\mathrm{W\,m^{-1}\,K^{-1}}$ for the out-of-plane thermal conductivity of TPD films deposited at room temperature. Although the room temperature value is not specified in their work, it will be presumably close to the 304 K sample prepared here. However, the absolute values obtained for $k_\parallel$ and $k_\perp$ (both our and literature values) are not in agreement. The discrepancy in the accuracy of the values is expected to come from the $k_\perp$ measurements. These values are affected by two factors that differ from the in-plane measurements. First, in this geometry, there

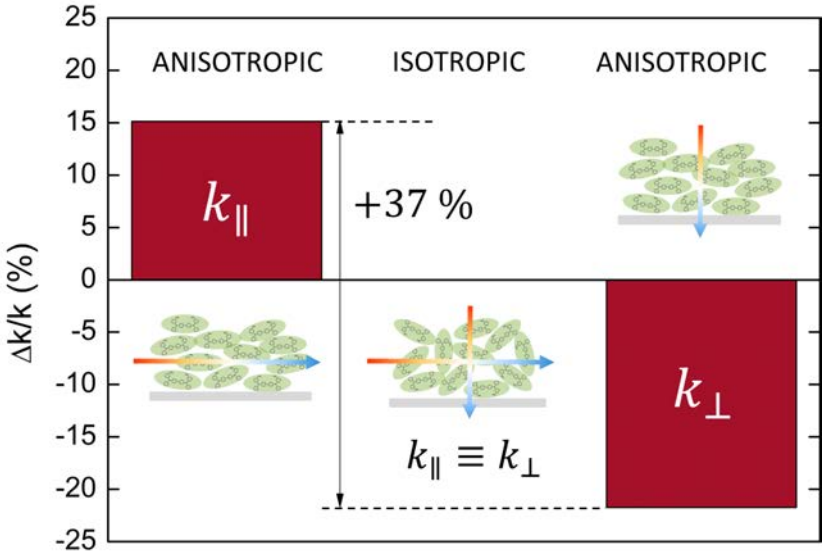

Figure 6.11: Schematics representation showing the relative variation of thermal conductivity (in-plane and out-of-plane) for the anisotropic sample at $T_{dep} = 220$ K. For the sake of comparison, we have assumed that $k_{\perp}$ and $k_{\parallel}$ are the same in the isotropic sample ($T_{dep} = 304$ K) and we have used this values as a reference for the anisotropic sample.

are several interface thermal resistances between the layers which can affect the accuracy of the values obtained. From the sample measurements, we have the interface electrode/organic and organic/SiN_x whereas from the reference measurement there is also the interface electrode/SiN_x. Secondly, the $k_{\perp}$ is obtained from the approximation of the one-dimensionality of the heat propagation. That propagation holds true as long as the half-width of the strip is much larger than the thickness of the film covered $w >> t_{film}$. The validity of this approximation for these measurements is commented in Section 2.4.5. None the less, it is interesting to note that these potential shortcomings that limit the accuracy of the absolute value of $k_{\perp}$ do not affect the relative variation of the 3ω measurements carried out on the two samples grown at a different T_{dep}. In both measurements, the mentioned two factors equally impact the accuracy of the measured thermal conductivity. Therefore, it is safe to assume that the isotropic sample ($T_{dep} = 304$ K) should have equal parallel and perpendicular conductivities. We can estimate, therefore, the relative values of the in-plane and out-of-plane conductivities with respect to the isotropic one.

The results are summarised in Figure 6.11. The $k_{\perp}$ of the sample grown at 220 K is ca. 22 % lower than the one measured for the isotropic one. This result agrees with the previous in-plane measurements (Figure 6.5) and the influence of the molecular packing anisotropy since thermal transport in the perpendicular direction is low when molecules lie roughly parallel to the substrate, i.e. when $k_{\parallel}$ is maximal. The maximum thermal anisotropy ratio in our samples, i.e. the difference between in-plane and through-plane conductivity measured for the anisotropic sample $T_{dep} = 220$ K is ≈37 %

(Figure 6.11).

6.3.3 Physical picture

We are not aware of any study addressing thermal conductivity of small organic glass-formers as a function of its degree of molecular orientation. Still, these results agree with those of previous studies in polymer science. In fact, recent work [134] has shown that amorphous polymers with very low thermal conductivities (0.1-0.5 $\mathrm{W\,m^{-1}\,K^{-1}}$) can be tuned into high thermal conductors ($\approx$100 $\mathrm{W\,m^{-1}\,K^{-1}}$) if the polymer chain is straight and aligned along the nanofiber axis. Other works have shown how, in the chain direction, amorphous polymers exhibit increased thermal conductivity compared to bulk polymers [127, 135]. From molecular dynamics simulations, thermal transport through covalent bonds (intra-molecular) has been shown to dominate the effective thermal conductivity over the Van der Waals bonds (inter-molecular) [135]. Using the same approach in our slightly oriented small organic glass-formers, the in-plane thermal transport is enhanced when molecules are settled parallel to the substrate—slightly increasing the mean free path of the atomic vibrations. Using a simplified picture, the thermal conductivity can be approximated from kinetic theory by the expression (for the lattice contribution) [74]

$$k = \frac{1}{3}\sum_{\lambda}\int v_g(\omega)l(\omega)C(\omega)d\omega \tag{6.3}$$

where v_g is the group velocity of the heat carriers, and corresponds to the sound velocity in amorphous solids, l is the mean free path of heat carriers (the atomic spacing) and C the heat capacity, all three frequency dependent. The sum over λ considers all the phononic branches. The specific heat varies at most a 4 % between the most stable glass and the conventional glass [35, 36]. The specific heat is lower for glasses deposited around $0.85T_g$, following the same trend as the density or stability. Therefore, in equation 6.3, the C cannot account for the thermal conductivity behaviour we see. Due to the covalent bonds along the backbone of the molecules both the mean free path and the sound velocity may be enhanced in this direction [135]. In fact, previous studies on indomethacin PVD glasses have precisely shown how the longitudinal sound velocity also depends on T_{dep} [39, 136]. For the IMC system, the sound velocity had a maximum at $\sim 0.75T_g$ in contrast to the maximum in density achieved at the well-known $0.85T_g$. The deposition temperature range between 0.70–0.82T_g showed equal or higher velocities than the maximum density glass. In polymers, the relation between fibre orientation and sound velocity has been known for years and used to quantify the degree of orientation [137]. These results corroborate the idea of being the molecular arrangement the dominating factor controlling the thermal transport rather than the small density variations expected between these deposition temperatures.

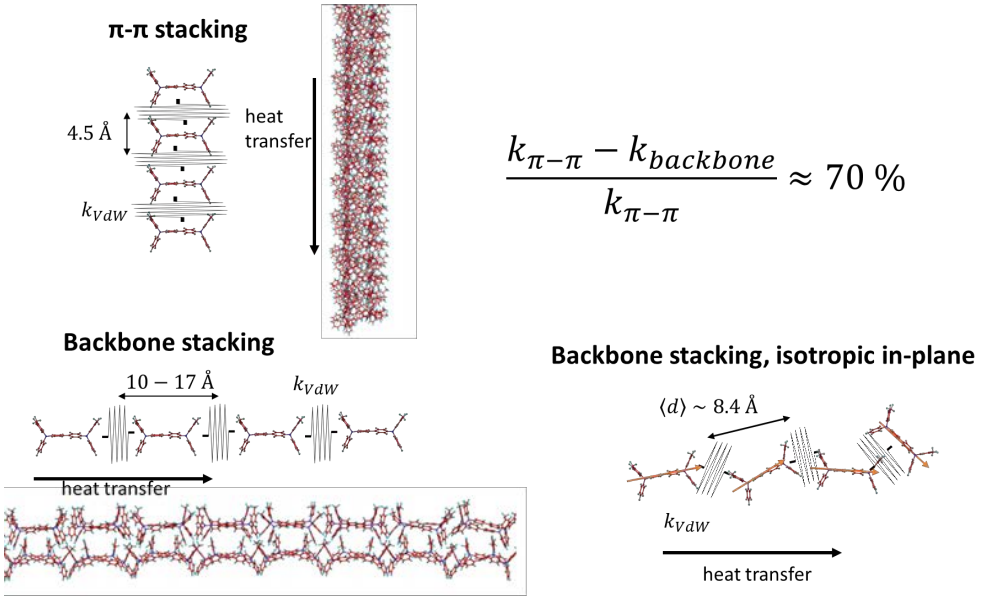

Figure 6.12: On the left, the sketch of two different molecular packings simulated, along with the backbone of the molecule and along the π-π stacking. On the right, a sketch of a simplistic model where the interaction energies between each molecule are sketched as thermal resistances (inverse of thermal conductivity).

To gain a more fundamental understanding of this effect we simulated two different quasi-1D-like structures[1]: one formed by a linear chain of TPD molecules stacked along their backbone and another chain with the molecules piled perpendicular to their backbone, in a π-π stacking, as shown in Figure 6.12. The thermal conductivity along the backbone stacking results 70 % higher than the thermal conductivity along the perpendicular direction. We can rationalise the result obtained for the 1D-structures—and eventually extend it to the 3D glasses—by introducing the concept of interface thermal resistance (ITR) that corresponds somehow to the coupling between neighbouring molecules or to the hopping barriers of lattice vibrations between molecules that are joined through weak Van der Waals interactions. An effective thermal conductivity of the stack geometry in Figure 6.12, considering a length L, can be written as the inverse sum of the thermal conductivity—or, simply, the sum of the interface thermal resistances—of each Van der Waals interaction

$$k_{\perp,e} = \left(\frac{N}{k_{VdW}}\right)^{-1} = \frac{d_\perp k_{VdW}}{L} \tag{6.4}$$

where N is the number of molecules that is rewritten as $N = L/d_\perp$ where $d_\perp$ is the

[1]These simulations based on molecular dynamics are part of an ongoing collaboration with the group of Luciano Colombo from the University of Cagliari (Italy) and performed by Riccardo Dettori. The TPD molecule is modelled according to the CVFF [138] force field (which uses complete force field developed for small molecules), where cross-coupling terms between the various bonded terms provide an accurate description of intra-molecular interactions. The non-bonded interactions are in turn described by a superposition of a Lennard-Jones potential (addressed to describe the Van der Waals contribution) and a Coulomb term.

intermolecular distance in this stacking configuration. Similarly, the effective thermal conductivity in the backbone direction can be written as

$$k_{\parallel,e} = \left(\frac{N}{k_{VdW}}\right)^{-1} = \frac{d_{\parallel} k_{VdW}}{L} \tag{6.5}$$

where the only different parameter is now the intermolecular distance, which corresponds now to the backbone molecular distance, i.e. roughly the molecule's length. The values of the intermolecular distances in TPD glasses grown at different substrate temperatures were previously investigated by Gujral et al. [52] using X-ray diffraction. The average intermolecular distance along the perpendicular (here, $k_{\perp}$) direction when molecules are grown at low T (molecules oriented parallel to the surface) is 4.5 Å, while the mean intermolecular distance in the in-plane (here, $k_{\parallel}$) direction is 8.4 Å. We can calculate the relative difference between both conductivities, which reads

$$\frac{k_{\parallel} - k_{\perp}}{k_{\perp}} = \left(\frac{d_{\parallel}}{d_{\perp}} - 1\right) \approx 87\,\% \tag{6.6}$$

In this simple model we have assumed that the effective thermal resistance is equal in both stacking schemes. From the molecular dynamics simulations it possible to extract a force constant K—equivalent to an effective spring—associated to the intermolecular coupling in the $\pi - \pi$ and the backbone stackings. The ratio between the force constant of the backbone stacking to the $\pi - \pi$ stacking from simulations is 2.6-fold. Thermal conductivity is proportional to the phonon group velocity which, in turn, scales as $v_g \propto \sqrt{K}$. Therefore, a stiffer spring would yield also higher thermal conductivity. This argument favours again the increased thermal conductivity along the backbone stacking.

This simplified model suggests, in agreement with what has been already seen in polymers, that increasing the length of the molecule would be an efficient way to increase the thermal anisotropy ratio. Of course, this simulations and model offer only a highly simplified picture of our system. Our samples are amorphous showing only a certain horizontal alignment along the z-direction and no anisotropy in the xy plane—as the backbone configuration would suggest. This would, of course, lower the anisotropy factor that we have estimated from the simulations and the highly simplified model.

6.4 Summary

We have presented a highly sensitive and versatile method to measure the in-plane thermal conductance of thin films during its growth—hence, in situ and in real-time. The high sensitivity together with the possibility to achieve low evaporation rates has allowed us to distinguish the different growth stages of amorphous organic films. The

first drop in conductance in the early stages is caused by the nucleation and isolated island growth, which affect the interfacial phonon scattering of the SiN_x membrane. This initial drop is afterwards compensated by the coalescence and the percolation along the surface, which increases the conductance again. Once a continuous layer is formed, the thermal conductivity shows a linear dependence with thickness, indicating a vertical growth of the films. New and more thorough studies in this direction are planned since we foresee a potential use of this methodology to provide valuable data at the earlier stages and on the mechanism of the film growth of organic glass-formers deposited at different temperatures.

We have measured, for the first time, the in-plane thermal conductivity as a function of the deposition temperatures for two organic semiconductor glass-formers, TPD and α-NPD. A clear dependence of k on the substrate temperature has emerged in agreement with many other glass properties from several small molecule glass formers that can be tuned with the deposition temperature. In this case, the lower the deposition temperatures, the higher the thermal conductivity, achieving an increase of 20 % between the lowest and highest values obtained.

We have seen that the higher densities that stable glasses exhibit cannot account for the thermal conductivity increase as T_{dep} is decreased. Instead, we have correlated k with the molecular orientation using the order parameter found in the literature for the same molecules. The correlation is surprisingly high, reproducing even the slight tendency to the vertical molecular alignment that these glasses show between $0.91T_g$ and $0.98T_g$. Additional measurements on TPD samples in the out-of-plane direction of one anisotropic and one isotropic sample have allowed us to evaluate the thermal conductivity anisotropy, obtaining a value of $\sim$37 %. One of the most significant findings to extract from this study is that thermal conductivity is highly dependent on the molecular orientation, something that had already been shown for polymers but not yet for small organic molecules, such as the two studied systems. This strategy could be employed in future developments to implement small-molecule thin films for its use in thermoelectric-based applications.

Chapter 7

Ultrastable organic-light emitting diodes

The work we are presenting in this chapter is part of a collaboration with the group of Prof. Dr Sebastian Reineke from the Dresden Integrated Center for Applied Physics and Photonic Materials (IAPP) and Institute for Applied Physics at the Technische Universität Dresden. Part of the presented measurements were performed by Paul-Anton Will (RGB OLED characterisation and PL lifetime measurements) and Christian Hänisch (optical modelling to obtain the anisotropy factor). Dr. Simone Lenk took part in conceiving the sample architecture and processing scheme. This chapter will be structured as follows. First, an introduction to the state-of-the-art of organic light-emitting diodes (OLEDs) is provided. Although the results will be analysed in terms of vapour deposited glasses and "glass science", some OLED background is needed to follow the discussion. For that purpose, a more theoretical introduction with some of the basic concepts of organic semiconductors and OLEDs is given to offer the reader the adequate theoretical framework. Then, the studied OLED device is presented and its performance evaluated as a function of the deposition temperature of the conforming organic layers. The link between the device's performance and the ultrastable glass properties is subsequently addressed. The reader will find also that, exceptionally, the temperatures are given in this chapter in Celsius degrees instead of Kelvin.

7.1 Introduction

The technology behind semiconductor light-emitting diodes, also called LEDs, has been known already for decades and it has become omnipresent in our daily life. Nowadays, we are facing the appearance of a whole new family of electronics, which has been possible thanks to the development and better understanding of the so-called organic semiconductors. The works on electroluminescence of thin organic films of low-molecular weight molecules and conducting polymers—back at the end of the 1980s—triggered a new field of research. Thanks to the efforts of both the academic

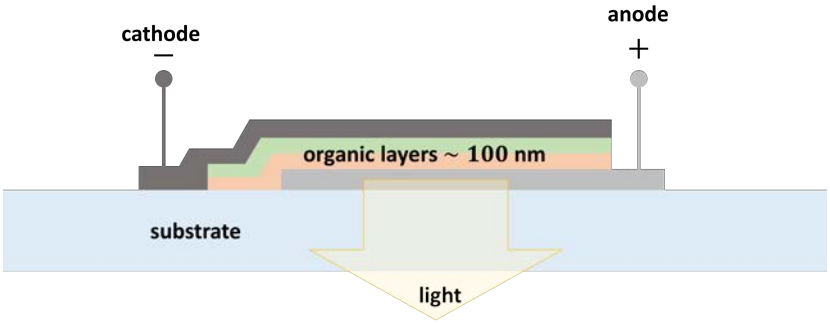

Figure 7.1: Sketch of the side view of a bottom-emitting (through the substrate) of an OLED device, with the different layers and electrodes indicated. Reprinted from [139].

and industrial research laboratories, organic light-emitting diode (OLED) devices have progressed rapidly and are no longer a lab curiosity but rather a present and mature technology that allows for high-performance displays and extremely customizable area light sources to be used in signalling and solid-state lighting.

As the name itself already points out and, contrary to the conventional LEDs, all the functional materials of OLED devices are organic semiconductor compounds. Due to the inherent crystallinity required for the inorganic semiconductors, LEDs are nearly perfect point-like sources with a forward-direction light emission. On the other hand, OLEDs are ultra-thin and area-emitting light sources (about $\sim$100 nm thick typically, see Figure 7.1) and offer wider viewing angles, a richer colour-space and a whole new range of design possibilities. They presumably can be prepared over large areas, processed on flexible surfaces and offer the possibility to be made transparent or semi-transparent. Briefly, the working principle consist of injecting charge carriers through the electrodes when a voltage is applied. These carriers met at the organic/organic interface, and they recombine emitting light. The emitted light in this interface has to be outcoupled[1] to be useful. A more detailed description of its working principle is provided in Section 7.2.4.

Although promising for several applications, there are still some challenges that OLEDs must overcome. One is the long-term stability of state-of-the-art OLEDs, which constantly defines the range of possible applications. Currently, the specifications for mobile displays and TVs are reached. The longevity of OLEDs correlates inversely to the operating brightness which preclude their use for high brightness applications ($>$1000 cd m^{-2}) and, therefore, still not compatible with such LEDs made of inorganic materials as they lack sufficient stability [140–142]. Another challenge, although closely related to the previous one, is the efficiency of these devices. Efficiency optimisation of OLEDs has been and is still approached from various angles, which can be grouped

[1] To let the light escape from an optical confining cavity.

in two: material development of emitters and other functional materials and the exploration of advanced optics concepts for improved light outcoupling efficiency. The former is currently led by the investigation of thermally activated delayed fluorescence (TADF) as a novel excitonic concept to realise 100 % of exciton harvesting [143]. The latter research facet to achieve higher light outcoupling makes use of stack layer optimisation to minimise the coupling of emission to loss modes [144], microstructures to control the light scattering [145], advanced optical elements as outermost interfaces to air [144, 146] or orientation of the emitter's transition dipole moment [147–149]. To date, a global solution for a successful optical concept has not been found, as it heavily depends on the given OLED architecture as an input parameter, its potential to be scaled up and the additional cost it brings to the systematic production.

Remarkably, when it comes to improvement, the growth of the organic layers used in OLEDs has widely been unaddressed [108]. Typically, OLEDs based on small molecules are prepared using physical vapour deposition, which results in amorphous layers. A typical OLED device can have from two to several thin organic functional glassy layers. All the layers are usually deposited at room temperature regardless the T_g of each material evaporated. The possibility of using PVD and the idea of ultrastable glasses to optimise the properties according to the role of the layer in an OLED device opens a whole new research strategy to improve the devices' performance. This concept joins the current previously mentioned strategies—material development and advance optical concepts—to overcome the limitations of these devices' efficiency.

While the impact of the deposition temperature of the layers on the performance of OLED stacks has generally gone unnoticed in the OLED community, some recent studies have analysed how T_{dep} affects molecular alignment in single layers of organic semiconductors, as we have already pointed out in Chapter 4 and 6. Recent works from Yokoyama et al. [150] and Dalal et al. [45] report how the molecular orientation of linear-shaped molecules can be effectively tuned from horizontal orientation—when deposited at lower temperatures—to a complete randomisation when increasing the deposition temperature close to T_g. The horizontal orientation of the emitting molecules in an OLED device is preferred since more of the internally emitted light can be outcoupled (see Section 7.2.5). The former work also reports how a higher horizontal degree of orientation of the molecules increases charge mobility due to a higher $\pi - \pi$ orbital overlap. A more recent study by Mu et al. [151] addressed the effect of the deposition temperature on the performance of a highly-simplified OLED based on CBP/CBP:Ir(ppy)$_3$:TPBi. However, in this study the best performance devices were grown at temperatures above the glass transition temperature of the emission and hole-transport layers, i.e. in their supercooled liquid state, precluding a proper correlation between the properties of the organic layers and the variation of the external quantum

efficiency. On the other hand, it should be pointed out that a frequent practice for solution processed OLEDs is performing a thermal annealing after the preparation of the emissive layers, a procedure that has been previously shown to be effective in enhancing the performance of polymer OLEDs [152]. However, vapour-deposition at temperatures around $0.85T_g$ has demonstrated to be much more efficient than annealing in accessing low energy positions in the potential energy landscape and consequently, achieveing glasses with enhanced stability and higher density [10].

In this work, we focus on the influence of ultrastable glass formation on two key OLED performance indicators being the external quantum efficiency (EQE) and the operational stability. First, and before presenting the OLED device and the results, we start by introducing some notions for organic semiconductors[2] and organic light-emitting diodes. Here, we describe only the most basic and well-established concepts of OLED science and technology that are necessary to build the framework in which the results are later discussed.

7.2 Organic semiconductors and OLEDs

The building blocks of organic semiconductors can be distinguished in two major groups: low-molecular weight materials and polymers. The most important and practical difference between these two types of materials lies—for this work—in the way in which they are processed as thin films. Whereas small molecules are prepared by PVD methods (generally vacuum evaporation), the conjugated polymers can only be processed from solution (e.g. spin coating or printing techniques). It is important to note that when small molecules are vapour deposited, they yield amorphous layers which are—of course—the main reason for this study of OLEDs from the "glass physics" point of view. What all the organic semiconductors have in common is the origin of their "semiconductor" nature, which differs strongly from the inorganic's.

7.2.1 Molecular orbitals

All the organic semiconductors have in common the conjugated π-electron systems, generally provided by the phenyl rings. A free carbon has an electronic structure of $1s^2 2s^2 2p^2$. However, when this C atom is bound to other atoms, this configuration might not be necessarily its optimal configuration. For instance, in benzene (Figure 7.2) the single carbon orbitals suffer the so-called hybridisation when the $2s$ and two of the $2p$ orbitals mix forming the new sp^2 orbitals, distributed in the xy plane with an angle of 120° between them. The remaining p_z is orthogonal to that plane. The overlap of

[2] We will focus only on the most relevant features for organic light-emitting diodes, despite being a field that goes beyond this particular application (organic solar cells, organic transistors,...)

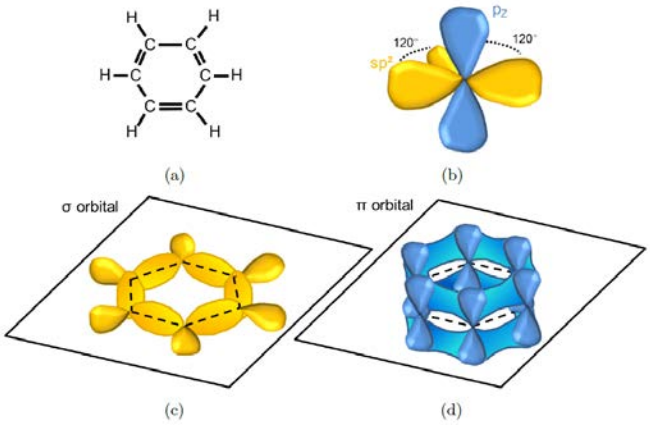

Figure 7.2: Molecular orbitals formation. **(a)** Benzene chemical structure. **(b)** The sp^2 hybridisation for a single C atom. **(c)** The σ-orbital in the xy plane. **(d)** The π-orbital with its delocalized electrons along the molecule. Reprinted from [139].

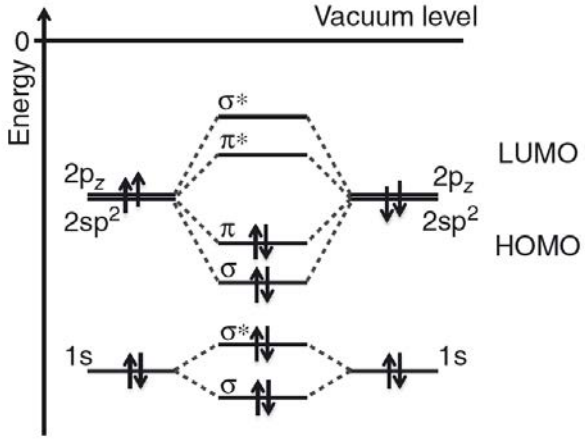

Figure 7.3: Simple energy diagram illustrating the formation of the $\sigma - \sigma^*$ and $\pi - \pi^*$ orbitals in the case of only two C atoms involved. Reprinted from [153].

the sp^2-orbitals produces the strong and directional σ-bonds that give rise to the ring-shaped structure of benzene (Figure 7.2). The remaining p_z orbitals form a delocalized electron cloud named π-bonds.

Molecular orbitals can be thought as a linear combination of atomic orbitals. The linear combination of two carbon atom orbitals can be written as the sum of the two electron wavefunctions or as the subtraction of them, which can also be considered regarding the constructive and destructive interferences. In the former case, the charge density (through the probability density function) between the atomic nuclei is increased and, thus, a bonding orbital is formed. In the latter case, the electron cloud does not screen the nuclei (carbon atoms) attraction, leading to the so-called anti-bonding orbital. The energy splitting between these orbitals strongly depends on the amount of overlap in their wavefunction (exchange integral), which leads to a higher splitting between the

σ (bonding) and σ^* (anti-bonding) states than between the π and π^* states. This energy splitting is further illustrated in Figure 7.3 for the interaction of two carbon atoms. In this scenario, the *highest occupied molecular orbital* (HOMO) is a π-orbital. The following higher orbital is, therefore, the π^* and is empty. This orbital is the so-called *lowest unoccupied molecular orbital* (LUMO). These delocalized $\pi - \pi^*$ orbitals are the mainly responsible ones for the electrical and optical properties of the organic semiconductor molecules. On the other hand, the stronger and directional covalent σ bonds are the ones conferring most of the chemical properties to the molecule [153].

The energy gap between the HOMO and the LUMO is typically between 1.5 and 3.0 eV, which leads to the absorption of light in the visible spectrum. This gap can be controlled by the conjugation degree of the molecules. In that sense, chemistry offers a broad range of possibilities to synthesise different organic semiconductors with the desired optoelectronic properties. These molecules are usually a group of phenyl rings, some 5 or 6-membered rings with some heteroatom—neither carbon nor hydrogen—such as nitrogen or sulphur together with alternated single and double bonds. The function that a molecule will have on a device depends strongly on the HOMO/LUMO gap for the emission and absorption properties and the energy of these orbitals with respect to the work function of the electrode material.

When using these organic semiconductors in OLEDs[3], it is generally difficult to obtain a molecule that is efficient at the same time in emitting light, transporting electrons or transporting holes. In that sense, molecules are typically selected to accomplish its best convenient and specific function in an OLED device . For instance, molecules with a high quantum yield of luminescence are chosen as emitters, molecules that easily give away electrons are used as hole transport layers (HTL) and molecules that easily accept electrons are used as electron transport layers (ETL).

7.2.2 Optical properties

Electrons and holes have a spin of $s = 1/2$. The total spin of an atomic/molecular state is given basically for all the unpaired electrons in the orbitals since the filled orbitals do not contribute to the total spin. An excited state with one electron in the π^*-orbital and one electron in the π-orbital can have a $S = 0$ with anti-parallel electron spins (singlet) or $S = 1$ with both spins parallel (triplet). With the rules of quantum mechanics (also considering the z-component of the spin, M_s) we know that, in a two-particle system, there are four possible eigenstates; the singlet and the triplet, which can take three possible values for the M_s component (1, 0 and -1).

[3]Other devices based on organic semiconductors can be fabricated, such as organic solar cells, organic field-effect transistors or even organic lasers. Here we just focus on the specific application of these materials in organic light-emitting diodes.

When an organic molecule is excited, either optically or electrically, an exciton—a pair of electron-hole bounded by Coulomb interaction—is formed. These excitons can end up either in a singlet or triplet state. Statistically, a ratio of 3:1 of triplets to singlets states are formed during an electric excitation. On the other hand, since the ground state is a singlet and due to the spin conservation rules, only transitions from singlet states to the ground state are allowed. That means that transitions from the triplet states to the ground are forbidden. However, these kind of transitions are experimentally observed, a process referred as *phosphorescence* in distinction to the singlet to singlet transition known as *fluorescence*. This is because "forbidden" is used in the quantum-mechanical sense, i.e. the probability of phosphorescence to happen is, generally, orders of magnitude lower than fluorescence which, in practice, means that the lifetime of phosphorescence is much longer. The ratio of optically excited singlet/triplet states in organic materials can be as high as 10^9-10^{10} to 1 [154].

A mechanism that weakens the spin selection rules and, therefore, allows an efficient phosphorescence is the spin-orbit coupling, which induces a mixing of the singlet and triplet states. Since it is the total angular momentum (orbital plus spin) what must be conserved, this mechanism can flip the spin of the electron at expenses of also changing the orbital momentum. However, the spin-orbit coupling is minimal in low atomic mass elements and cannot provide an efficient radiative relaxation from the triplet to the singlet state that must, instead, relax to nonradiative processes (vibrational mainly) [153]. An OLED device based only on fluorescence would be rather inefficient since only 25 % of the excitons would be allowed to decay radiatively because the emission would only take place from the singlet state, as sketched in Figure 7.4. For few years already, this limitation has been overcome by the incorporation of phosphorescent emitters to the organic matrix at low-concentrations [155] to avoid the so-called triplet-triplet annihilation[4]. These materials consist of organometallic complexes with a heavy metal atom in their core (e.g. platinum or iridium) enhancing the spin-orbit coupling, which implies that these molecules can effectively emit from the triplet state (phosphorescence). Moreover, the intersystem crossing (ISC) rate—transitions with a change of spin involved—between the singlet and the triplet is also increased. That means that the fraction of the singlets created by electrical excitation is converted to triplets before they radiatively decay. In such a way, the phosphorescent OLEDs have a total internal electroluminescent efficiency of 100 %, instead of the 25 % of fluorescence-based OLEDs. Figure 7.4 sums up the different and most important radiative and nonradiative transitions within an excited molecule. Notice that an additional splitting of the main levels is also drawn, which corresponds to the vibrational states, typically exhibiting a factor of 10 lower energy differences.

[4]The interaction of two triplet excitons that can lead to the annihilation of the these and that must be avoided.

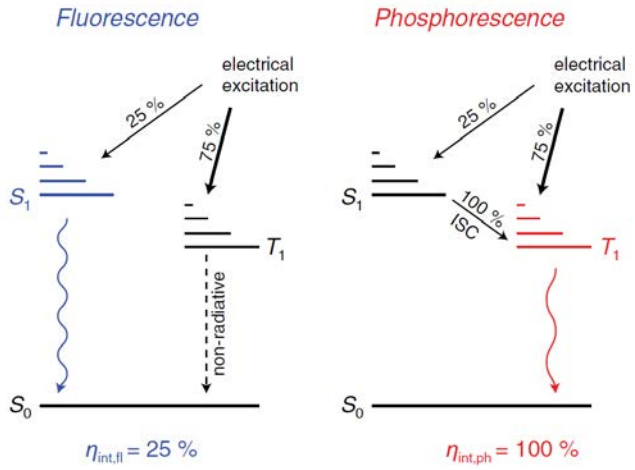

Figure 7.4: Fluorescence versus phosphorescence. Scheme of the relaxation processes taking place under electrical excitation. The shorter lines represent the vibrational levels. In phosphorescence, the singlet excitons are transferred to the triplet state due to an efficient intersystem crossing rate. Figure reprinted from [108].

Finally, it is important to notice also that OLED devices are practically transparent to the emitted wavelength coming out either because of an electrical or optical excitation. The fact of not reabsorbing their own emitted light is a great advantage compared to the inorganic LEDs. This is the so-called Stokes shift and can be well explained by the Frank-Condon principle, where the fast-relaxation of the vibrational states within an electronic state is invoked.

7.2.3 Charge carrier transport

When a molecule is charged with an extra electron, the molecule will be negatively charged, and the additional electron will occupy the LUMO. If an electron is missing, the molecules will be positively charged, and a hole will occupy the HOMO. The HOMO and the LUMO can be thought as the equivalent valence and conduction bands from the inorganic semiconductors. In a first approximation, we can express the current through a material as the product of charge carrier density n and drift velocity v which, according to the Drude model, is given by the mobility (μ) and the electrical field E, that reads:

$$j = env = en\mu E \tag{7.1}$$

where e is the elementary charge. It should be noticed that the mobility is not an intrinsic property and strongly depends on the preparation conditions, material's purity, the morphology of the substrate or the same electric field. It also depends on the temperature, charge density and or the direction (anisotropic) [154].

A significant difference between the organic and inorganic LEDs—and semiconductors in general—is the nature of the charge carrier transport. The well-established band transport is invoked to explain the charge transport mechanism in inorganic semiconductors. However, in amorphous organic semiconductors, the electrons and holes are strongly localised in the π orbitals of the molecule. Since no or small coupling of these orbitals is present, the band-like transport is precluded in this case. Instead, the current takes place due to a series of hopping events of the charge carriers between neighbouring molecules. The mobilities achieved by this transport mechanism are much lower than for inorganic materials, in the range of 10^{-6} to $10^{-2}\,\mathrm{cm^2\,V^{-1}\,s^{-1}}$ [156] compared for instance to the $1400\,\mathrm{cm^2\,V^{-1}\,s^{-1}}$ or $1\,\mathrm{cm^2\,V^{-1}\,s^{-1}}$ of crystalline and amorphous silicon. The hopping events are thermally activated: the mobility in organic semiconductors increases with temperature in stark contrast with the loss of mobility in inorganic semiconductors due to the phonon scattering.

Another significant difference is the charge carrier density n, which scales as $n \propto \exp\left(-E_g/k_BT\right)$ where the E_g is the gap energy. Traditional inorganic semiconductors have low band gaps, e.g. 1.1 eV for Si, what makes possible to create intrinsic free charges from thermal excitation. In the organics, the found gaps lie between 2 and 3 eV, values that hinder the creation of thermal excitations at room temperature for any practical purposes. In contrast, the conductivity in organic semiconductors—strictly more insulators than semiconductors—is generally extrinsic and is the result of doping, photo-generation of carriers (like in solar cells) or the injection of carriers from the contacts. The latter is the one governing the device operation of the OLEDs used in this work, since we will be using intrinsic material layers.

7.2.4 Working principle of OLEDs

Organic light-emitting diodes, as well as inorganic LED, are based on electroluminescence, i.e. the luminescence caused by the injection and flow of charges across a material. Figure 7.5 describes the basic working principle of a simple two organic layer OLED device, similar to the one addressed in this work. In this case, we have an electron transport layer and a hole transport layer. Charge carriers are injected into the device when a voltage V is applied; electrons are injected from the cathode to the LUMO of the ETL whereas holes are injected from the cathode to the HOMO of the HTL. These charges accumulate at the interface of the organic layers forming an exciton that eventually relaxes by emitting a photon. The electrode materials must be chosen accordingly to their work function since they have to provide enough charge carriers to the HOMO and LUMO of the corresponding layer—less critical if the transport layers are doped. The cathode is generally a reflective metallic element, such as aluminium, whereas the anode is usually indium-doped tin oxide (ITO). The latter is

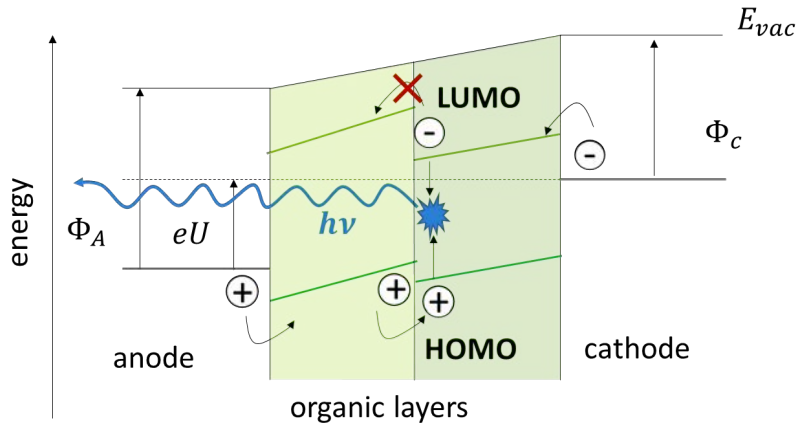

Figure 7.5: OLED device working principle. The electroluminescence is achieved when a voltage is applied across the electrodes allowing the injection of holes and electrons to the HOMO and LUMO levels of the respective organic layers. Those form an exciton that recombines radiatively.

the most commonly used anode material for OLEDs since it is conductive and transparent at the same time. Therefore, the produced light of the OLED is outcoupled through the transparent ITO anode. Due to its semiconductor nature, OLED devices exhibit current-voltage curves with diode-like characteristics.

As mentioned before, current OLEDs have normally incorporated phosphorescent emitters so they can emit efficiently from the triplet state. In practice and in short, this is achieved by introducing an emission layer (EML) between the ETL and HTL. This layer consists of a matrix material (can be the same material as the electron or hole transport layers) doped with a small concentration (generally less than 10 wt%) of an organometallic complex and is usually about few nanometres thick. Current OLED devices can be far more complex than the one depicted in Figure 7.5. They can have doped HTL/ETL layers, additional functional layers such as hole and electron blocking layers, multiple emission layers for white OLEDs, among other functional layers [7].

7.2.5 Light outcoupling

It is of fundamental importance to assess which fraction of all the photons produced inside an OLED (generated in the emission layer) can escape to the air. Figure 7.6 shows a scheme of the side view of an OLED including the glass substrate. In this case, the emission takes place through the substrate—meaning that the transparent anode is the first deposited layer. This device geometry is called bottom-emitting (like the ones prepared in this work). The different refractive indices of the layers are indicated in Figure 7.6. The organic functional layers are not distinguished since they exhibit very similar refractive indices, which can change from 1.7 to 2.1 depending on the wavelength.

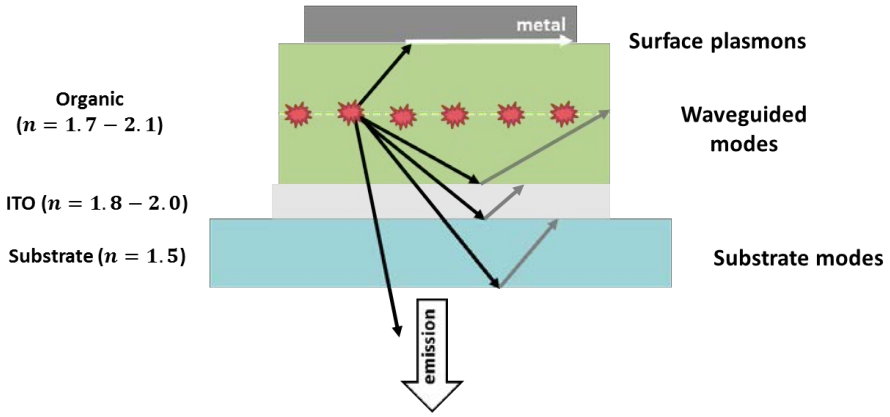

Figure 7.6: OLED light outcoupling. Sketch of the different light losses mechanism that can occur within an OLED device. Total internal reflection will be produced for emission at higher angles than the critical angle.

From all the generated photons in the emission layer, only a small fraction will be outcoupled to the air. Total internal reflections at the organic/ITO and ITO/substrates will trap most of the light in the device in the so-called organic or waveguided modes as well as in substrate modes. Furthermore, the emitting molecules can couple to the conductive cathode as surface plasmons, providing an additional loss mechanism.

A way to quantify the overall efficiency of an OLED is the external quantum efficiency (EQE) which measures the ratio between the outcoupled photons to the input charges. This parameter can be split into four terms [157]:

$$EQE \equiv \eta_{EQE} = \gamma\, \eta_{S/T}\, \eta_{rad,eff}\, \eta_{out} \tag{7.2}$$

The first factor γ is the electrical efficiency, which accounts for the injected charge carriers that do not contribute to exciton formation. The second factor $\eta_{S/T}$ quantifies the fraction of excitons that are allowed to decay radiatively due to the quantum-mechanics spin selection rules and is one for phosphorescent emitters, as we have previously seen [158]. $\eta_{rad,eff}$ expresses the effective radiative quantum efficiency of the emitter material that describes the capability of the emitter to recombine radiatively from the emitting state (here triplet state). It accounts for possible enhancements of the radiative transition rate induced by the optical cavity [157]. Ultimately, η_{out} denotes the outcoupling factor, which depends mainly on the optical environment and the orientation of the emitter. As a rough approximation and using geometrical optics it can be shown that most of the generated light, about 80 %, will get trapped inside the device [157]. Therefore, the outcoupling efficiency will limit the device efficiency to ∼20 % which is, in reasonable agreement with the state-of-the-art OLED efficiencies, that can reach 20–30 %in EQE [157].

The outcoupling efficiency also exhibits a strong dependence on the ETL thickness. The electron transport layer sets the distance between the EML and the reflective cathode

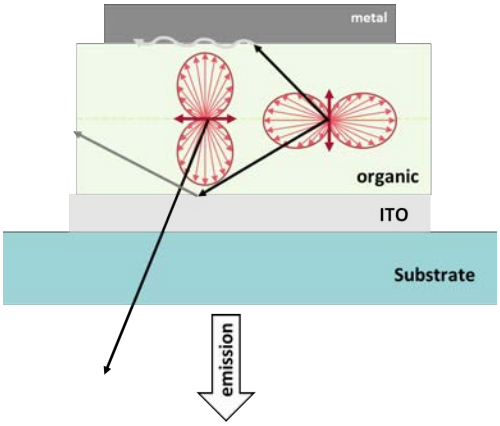

Figure 7.7: Effect of the orientation of transition dipoles. Sketch of the effect of the orientation of the dipoles as a function of its orientation. The direction of the transition dipole is marked by the dark-red thicker arrow, whereas the length of light-red arrow indicates the direction and strength of the emitted radiation.

which, in the end, determines the resonant conditions inside the OLED cavity because of the interferences—constructive and destructive—of the light waves. For that reason, optical simulations are performed to determine the optimal thicknesses of the functional layers. The OLEDs are built in their first (as in this work) or second optical maximum.

7.2.6 Orientation of the emitting dipoles

The orientation of the transition dipoles (where the emission takes place) strongly influences the outcoupling efficiency. In an OLED device, a horizontal dipole orientation of the emitting molecules is preferred. There are two main reasons for that. In Figure 7.7 we can see how vertical dipoles emit light preferentially at higher angles with respect to the substrate normal, which will suffer total internal reflections and will be coupled to waveguide modes. On the other hand, horizontal dipoles emit light preferentially at lower angles with respect to the substrate normal allowing, therefore, more light can be directly outcoupled. Additionally, vertical dipoles only emit p-polarized light whereas horizontal dipoles have the contribution of both p-polarized and s-polarized light. Only the p-polarized modes can couple to surface plasmons modes; therefore, horizontal orientation is preferred, so more s-polarized modes contribute to the light outcoupling [157].

As we have seen in the previous chapter, physical vapour deposition can be used to tune the orientation of the molecules by changing the deposition temperature. This strategy could offer new possibilities to enhance the outcoupling efficiency of OLED devices.

7.3 Experimental

In this section, both the preparation and characterisation of the OLED devices studied in this work is explained. It is important to note that the devices were prepared and characterized at the IAPP in Dresden. We provide here a description of the fabrication process and of the specific techniques used to characterize the device. The samples were prepared in a highly-standardised evaporation tool at the IAPP which ensures the proper reproducibility of the devices.

7.3.1 Sample preparation

Glass substrates (Corning Eagle XG, Thin Films devices, Inc.) with a thickness of 1.1 mm and with 90 nm of pre-deposited ITO as a transparent bottom electrode followed a standard cleaning procedure (including rinsing with NMP, ethanol and deionised water as well as treatment with UV ozone). The ITO is patterned in a such a structure that will allow the creation of four independent pixels in each one of the 25×25 mm^2 substrates. Figure 7.8 shows an image of a final OLED were the four pixels can be seen.

All the subsequent layers were deposited in a single vacuum chamber evaporation tool (Kurt J. LESKER & Co.) at a base pressure of 10^{-7} mbar. In a single evaporation run, a 150×150 mm^2 wafer, patterned with the 25×25 mm^2 ITO-contacts, is used, allowing to obtain up to 36 OLED devices with four (identical) pixels each one. The use of different wedge tools makes possible to individually address each column/row, obtaining different samples in a single run. The substrate rotates during the evaporation to ensure a homogeneous layer thickness. The structuring of the different evaporated layers is achieved using shadow masks.

The thickness and deposition rates were monitored using a quartz crystal microbalance. The evaporation tool has up to 12 organic sources plus three other metal sources. This tool allows to evaporate the whole device structure in a single run and perform co-evaporation for the mixed layers. First, a 0.5 nm thin layer of MoO_3 was evaporated on top of the ITO to facilitate the injection of the holes into the cathode. The electrode is followed by the two organic layers TCTA and TPBi, as hole transport and electron transport layers, respectively (see Section 2.1.6 for full names). The emission layer (EML) was formed by doping the first part of the ETL layer with the respective phosphorescent dopant (later described). Additionally, four different phosphorescent emitters were tested, with the remaining stack architecture kept identical. For all emitters, the layer thicknesses of HTL and ETL were optimised using a thin film optics simulation tool [159], which also considered the transition dipole moment orientation. Different samples were prepared by changing only the substrate temperature during

Figure 7.8: Photographs of the prepared OLED devices. In the left picture (device off), the four pixels can be seen. In the right, the central to pixels have been turned on.

the evaporation of the EML and ETL layers for each of the mentioned devices to study the effect of the TPBi layer's properties on the device performance. Finally, a bilayer cathode consisting of 0.5 nm of LiF/ aluminium was deposited on top of the organic layers. The overlap between the ITO contact and the aluminium cathode defines the active area of each pixel which is, in our case, of 6.49 mm^2.

The OLEDs are highly sensitive to air and moisture. For that reason, a glove box under a nitrogen atmosphere is directly coupled to the evaporation chamber where, immediately after fabrication, all OLEDs are encapsulated with glass lids with a small cavity to prevent the direct contact. Once finished, the glass wafer is cut to obtain the 36 individual samples.

In the first studied device, referred from now on as G0, the precise structure was as follows: ITO (90 nm) / MoO_3 (0.5 nm) / TCTA (64 nm) / TPBi:$Ir(ppy)_2(acac)$ 8 wt% (10 nm) / TPBi (60 nm) / LiF (0.5 nm) / Al (100 nm), where $Ir(ppy)_2(acac)$ [5] is a green phosphorescent emitter dopant. After depositing the HTL layer, the temperature of the whole substrate was radiatively heated and set to the highest temperature studied, 90 °C, where the EML and ETL were evaporated to a limited area (a column of six samples) using the wedge tool. After reaching the next temperature (another column) by passively cooling the whole substrate, the EML and ETL were evaporated again into another predefined region. This procedure was repeated six times (one for each column) at the nominal temperatures of 90 °C, 80 °C, 70 °C, 60 °C, 50 °C and room temperature (ca. 30 °C). A previously performed calibration determined the real substrate temperature. Once room temperature is reached, the cathode layers were evaporated at once for all the samples.

The other set of three different devices was prepared using the same structure and changing only the emitter—i.e. using same electrode scheme and with the HTL and ETL thicknesses optimised for each emitter spectra. All three devices were prepared in

[5] Full name: bis(2-phenylpyridine) (acetylacetonate)iridium(III)

a single run by using shadow masks. The structure of these three devices summarised by Table 7.1 and will be referred as device R1 for the red emitter $Ir(MDQ)_2(acac)$[6], device G1 for the new green emitter $Ir(ppy)_3$[7] and device B1 for the blue emitter FIrpic[8].

device	Hole transport layer TCTA	Emission layer TPBi:emitter	Electron transport layer TPBi
G0	64 nm	10 nm $Ir(ppy)_2(acac)$ 8 wt%	60 nm
R1	90 nm	10 nm $Ir(MDQ)_2(acac)$ 10 wt%	70 nm
G1	64 nm	10 nm $Ir(ppy)_3$ 10 wt%	60 nm
B1	40 nm	10 nm FIrpic 10 wt%	35 nm

Table 7.1: Device architecture of all the devices studied in this chapter. The thickness of the electrode and injection layers are the same in all cases and reported in the text.

Based on the results obtained from the G0 device, for each one of the three devices, R1, G1 and B1, two deposition temperatures for the EML and ETL layers were explored: room temperature and 66 °C using the aforementioned procedure.

7.3.2 OLED characterization

The basic OLED characterisation is based mainly on three quantities: current density, voltage and luminance—or, equivalently, brightness. While the former two do not need any clarification, the luminance requires a brief introduction. The radiance of a light source is a measure of the radiant power (Φ_r), per unit of solid angle and unit of projected area:

$$L_r = \frac{d^2\Phi_r}{d\Omega dA_{source}\cos\vartheta} \qquad \left[\mathrm{W\,sr^{-1}\,m^{-2}}\right] \tag{7.3}$$

which is a so-called radiometric quantity. However, organic LED, as well as other light-emitting sources, are generally characterised by photometric quantities. Contrary to radiometry, photometry considers the human eye sensitivity to the light and weights the different wavelengths according to it. In analogy to the radiometric radiant power (units Watts), the equivalent photometric quantity is defined as luminous flux Φ_{ph} (units Lumen or lm). Both quantities are related by

$$\frac{d\Phi_r}{d\lambda} = K_m V(\lambda)\frac{d\Phi_{ph}}{d\lambda} \tag{7.4}$$

[6]Full name: Bis(2-methyldibenzo[f,h]quinoxaline)(acetylacetonate)iridium(III)
[7]Full name: Tris[2-phenylpyridine]iridium(III)
[8]Full name: Bis[2-(4,6-difluorophenyl)pyridinato-C2,N](picolinato)iridium(III)

Where $K_m = 638\,\mathrm{lm\,W^{-1}}$ is a conversion constant resulting from historical considerations and $V(\lambda)$ is the weighing function which considers the human eye's sensitivity to the different wavelengths. The equivalent magnitude to the radiance, the luminance (or brightness), can be defined now as

$$L_r = \frac{d^2\Phi_{ph}}{d\Omega dA_{source}\cos\vartheta} \qquad \left[\mathrm{cd\,m^{-2}}\right] \tag{7.5}$$

Which is expressed in the SI units for the luminous intensity, the candela (cd).

Luminance, describing the brightness of a light source, is a significant quantity for the lighting industry and technology. Typical brightness values for displays are found between 100 and 500 cd m^{-2}. Depending on the lighting applications the brightness requirements can vary from 200 to 10 000 cd/m^2. Above 10 000 cd m^{-2} the human eye glares, and it cannot adapt anymore to this brightness.

Current-voltage characteristics

Current-voltage characteristics (I–V) were measured using a Keithley 2400 sourcemeter unit while the luminance was recorded simultaneously with a fast Si-photodiode. For luminance calibration, the spectral radiance in the forward direction was taken by a calibrated Instrument Systems GmbH CAS 140 CT spectrometer at approximately 1000 cd/m^2.

Efficiencies

OLEDs can be characterised by three essential efficiencies: the current efficiency, the luminous efficacy (LE) and the external quantum efficiency (EQE). Here we will only describe the latter two. In Section 7.2.5 we have already defined the external quantum efficiency as the ratio of outcoupled photons to injected charges, which can be calculated from measurements as

$$\eta_{EQE} = \frac{n_\gamma}{n_e} = \frac{2\pi e}{Ihc}\iint \lambda I_e(\vartheta,\lambda)\sin\vartheta d\lambda d\vartheta \qquad [\%] \tag{7.6}$$

Where the spectral radiant intensity I_e has already been integrated over the azimuthal angle due to the symmetry (as sketched in Figure 7.9).

The luminous efficacy describes the ratio between the emitted luminous flux (output optical power) to the input electrical power (it considers also the voltage), which reads

$$\eta_{LE} = \frac{\Phi_{ph}}{P} = \frac{\Phi_{ph}}{VI} = \frac{2\pi K_m}{VI}\iint V(\lambda)I_e\left(\vartheta,\lambda\right)\sin\vartheta d\lambda d\vartheta \qquad \left[\mathrm{lm\,W^{-1}}\right] \tag{7.7}$$

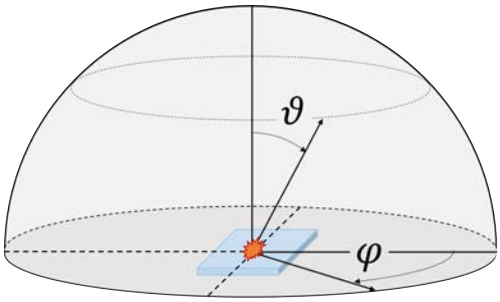

Figure 7.9: The geometry of the OLED allows only the emission through the forward hemisphere since the backwards emission is blocked by the metallic electrode. The polar coordinates are used to calculate the total EQE and LE using the integrating sphere setup. The azimuthal angle is given already integrated in equations 7.6 and 7.7.

Since it is a photometric quantity, it includes the aforementioned weighting function for the human eye.

Both integral terms in equation 7.6 and 7.7 can be obtained at a constant current using an integrating sphere. In such system, the spectral emission in all directions (into the forward half space due to the OLED geometry, see Figure 7.9) of an OLED is captured, which allows obtaining the integral term experimentally. Therefore, the EQE and LE are measured at only one current value, corresponding approximately to 1000 cd m^{-2}. To these values for the whole j range we proceed as follows:

(i) Our OLED does not exhibit any colour shift at different currents (same spectra) and is planar. Therefore, we assume that the spectral radiant intensity (over all angles) is constant for all currents.

(ii) The EQE and LE curves as a function of the current are obtained from the luminance (defined for forward direction) of the previous j–V–L characterisation and assuming a lambertian emitter [9], i.e. ($I_e = I_e^0 \cos\vartheta$).

(iii) The measurement at the integrating sphere allows correcting the EQE for the non-lambertian characteristics of the OLED. The scale factor obtained from the two EQE values (from the lambertian assumption and integrating-sphere measurement) at 1000 cd m^{-2} is applied to the whole current range.

In this work, an integrating sphere (LMS-100 Labsphere Inc.) with a calibrated spectrometer (CDS-600, Labsphere Inc) was used. For each deposition temperature, the data from two to four identically prepared devices, having four distinct pixels each, were averaged. The error bars correspond to the standard deviation with 95 % confidence interval corrected by the t-student factor for a small number of samples.

[9] Which states that the radiant intensity directly observed from the emission area is proportional to $\cos\vartheta$, where ϑ is the angle between the surface normal and the direction of the incident light.

Lifetime measurements

The mechanisms and reactions involved in an OLED degradation are several and, despite lots of research focusing in that issue, it is still difficult to disentangle all the possible causes [8]. This degradation is manifested through a continuous loss of device efficiency, typically seen both as a luminance decrease and voltage increase. The higher the luminance (or current density), the lower the lifetime of the device.

The OLED's lifetime is defined as the time at which the forward luminance drops to a certain value, typically for a decrease of a 50 % of its initial value. In this work, the device lifetime was measured for all devices at different current densities and are reported as the LT_{70} lifetime, which is defined as the time at which the brightness of the OLEDs drops to the 70 % of the initial value.

7.4 Results

7.4.1 OLED stack

For our study, we have chosen a simple but yet highly efficient OLED stack by Meyer et al. [160] (see Figure 7.10). This stack matches several requirements, which are crucial for our investigations. First of all, it consists merely of two organic layers, which reduces the complexity of the OLED. The hole transport material is based on TCTA whereas TPBi serves both as emitter matrix for the emission layer and the electron transport layer. Both materials have their $0.85T_g$ quantity above room temperature in a technically feasible range with T_g = 151 °C and T_g = 122 °C, for TCTA and TPBi respectively (see Table 2.1, in Kelvin). Furthermore, the T_g of the first evaporated material (TCTA) is higher than the one of the matrix material under investigation, which is important to minimise any influence caused by possible TCTA morphology changes. The fabricated OLEDs can be divided into two groups: firstly, a full temperature sweep (30 °C – 90 °C) is performed with the green (G0) phosphorescent emitter $Ir(ppy)_2(acac)$. Secondly, two distinct temperatures (31 °C, 66 °C) are used during the deposition of the three additional commonly used emitters $Ir(MDQ)_2(acac)$ for red (R1), $Ir(ppy)_3$ for green (G1), and FIrpic for blue (B1), where the higher temperature, 66 °C, is selected based on the optimal deposition temperature for TPBi. Furthermore, we prepared photoluminescence samples with $Ir(ppy)_2(acac)$ as emitter embedded in TPBi at deposition temperatures of 30 °C – 100 °C for the determination of the transition dipole moment orientation to analyse how any configurational changes affect the outcoupling efficiency. Finally, a detailed thermal characterisation using in situ nanocalorimetry technique of the matrix TPBi is performed at deposition temperatures ranging from −20 °C to 120 °C.

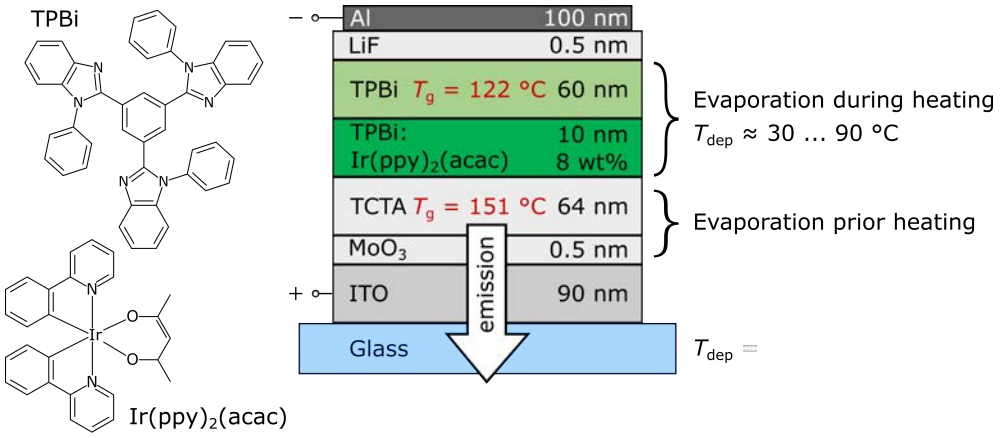

Figure 7.10: Schematic device structure of the studied device. As a first study, and single OLED run was prepared using the green emitter $Ir(ppy)_2(acac)$ (8 wt%) and evaporating the EML and ETL layers at six different substrate temperatures. The rest of the layers were deposited at room temperature. A second run, explained later in the text, consisted in using the same stack but with three different emitters and just two substrate temperatures for each emitter.

7.4.2 Devices' performance

Figure 7.11a shows the j–V–L characteristics and the electroluminescence (inset) spectra of the G0 devices for three (out of six) of the explored deposition temperatures for the TPBi layers. While the j–V data is very similar for all deposition temperatures, the device fabricated at 69 °C shows the highest luminance output (see also the inset of Figure 7.11a). Figure 7.11b shows the EQE for the same three devices as a function of the luminance. The complete device performance dependence on the deposition temperature is summarised in Figure 7.12, showing the EQE (red-squares, left-axis) and the luminous efficacy (LE) (blue-circles, right-axis) at a luminance of 100 cd m^{-2} as a function of the deposition temperature. A maximum EQE of 24.0 % and a LE of 86 lm W^{-1} is achieved for the device deposited at 69 °C. This gives significant relative improvements with respect to the room temperature device of +24 % and +37 % for the EQE and LE[10], respectively. The tendency is similar for both quantities, they increase over substrate temperature up to a maximum around 69 °C, and then it starts to decrease again. The last studied temperature of 90 °C is still giving a better performance in terms of efficiencies than the reference sample at room temperature. The green highlighted region in Figure 7.12 corresponds to the range 0.84–0.9T_g, being T_g the glass transition of TPBi expressed in Kelvin.

The results concerning the performance of the devices R1, G1 and B1 are summarized in Figure 7.13a, b, c with the EQE curves versus luminance for two substrate temperatures: the reference at room temperature of 31 °C and at 66 °C, close to the temperature

[10]Note that the relative changes in EQE and LE are given with the explicit sign "+" to distinguish from the EQE values, which are given also as a percentage.

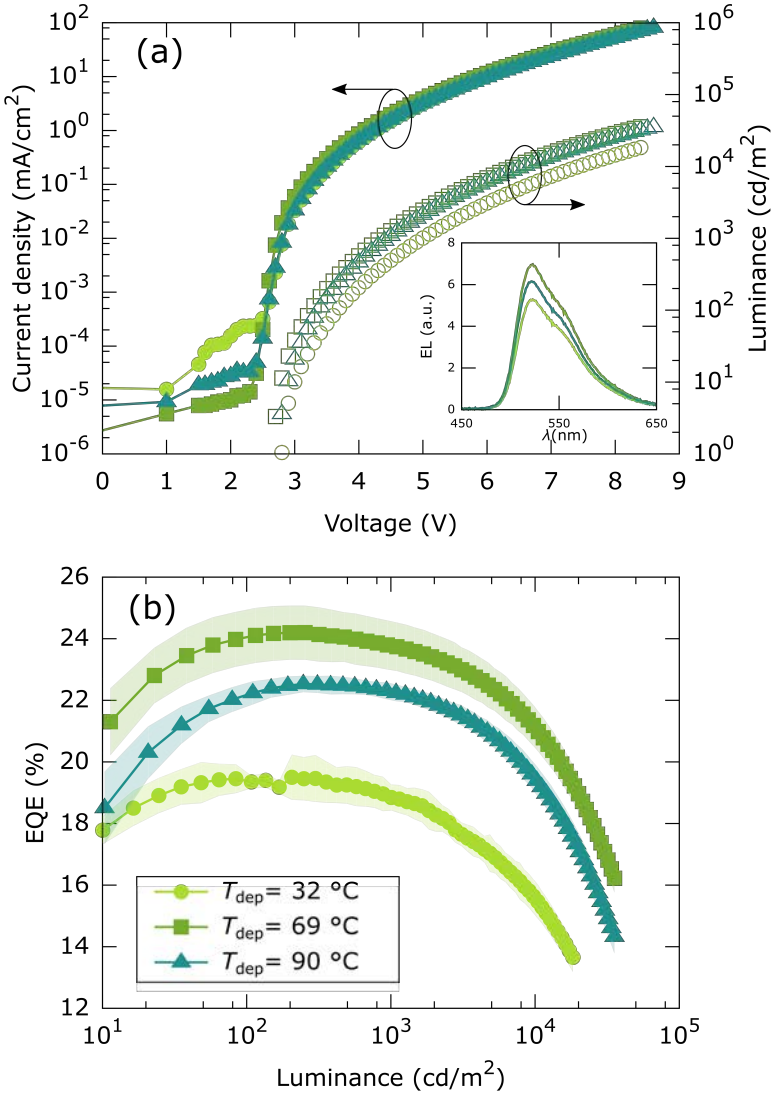

Figure 7.11: Optoelectronic characterisation of device G0. **(a)** j–V and L–V characteristics of the G0 devices prepared at three different substrate temperatures: 32 °C (room temperature), 69 °C and 90 °C, the other three temperatures are not shown for clarity. Each curve is the mean of 2-6 pixels. **(b)** External quantum efficiency characteristics for the same three different temperatures over luminance for the G0 devices. The shadowed area represents the errobars, which are the standard deviation at the 95 % confidence interval and weighted with the t-student factor for small samples sizes (between two to six pixel for each temperature).

with the best performance for the G0 device. The electroluminescence spectra obtained in an integrating sphere are shown for a current density of 15.4 mA cm^{-2} and same integration time in Figure 7.13d, e, f. In all three devices, there is a significant enhancement between the reference device prepared at room temperature and the device with

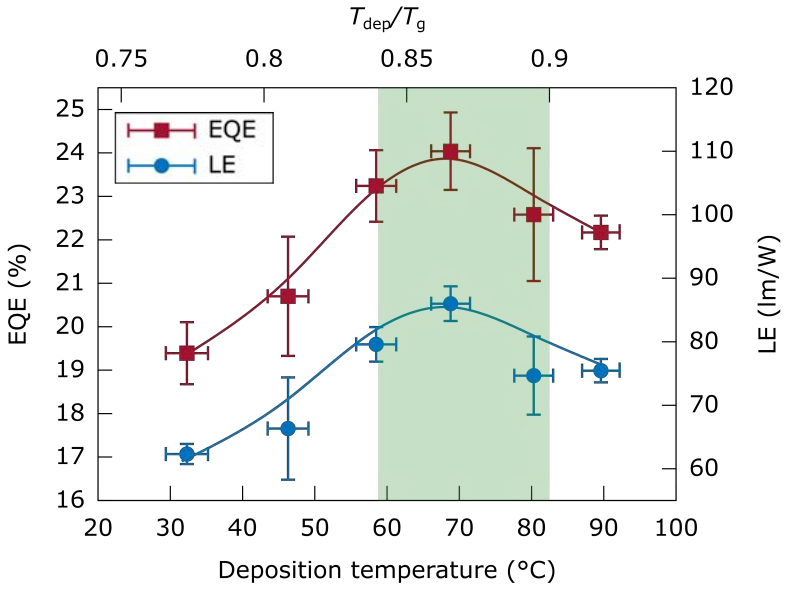

Figure 7.12: Devices performance versus deposition temperature. External quantum efficiency (EQE) (red, left-axis) and luminous efficacy (LE) (blue, right-axis) at 100 cd m^{-2} as a function of the deposition temperature. The errorbars are the standard deviation at the 95 % confidence interval and weighted with the t-student factor for small samples sizes (between 2 and 6 samples for each temperature). Lines are a guide-to-the-eyes.

the ETL and EML deposited at 66 °C. The EQE enhancements over the respective reference OLEDs at 100 cd m^{-2} are +14.5 % for the red R1 devices, +21.7 % for the green G1 devices, and +165 % for the blue B1 devices. All devices fabricated at 66 °C show an increased phosphorescence lifetime of 1.16 to 1.36 µs (+17 % increase) for R1, 0.87 to 1.00 µs (+15 %) for G1, and 1.07 to 1.38 µs (+29 %) for B1, as obtained from photoluminescence spectroscopy of the complete OLEDs (see Figure 7.13g, h, i). The j–V–L curves of all devices R1, G1, and B1 can be found in the Appendix A.

7.4.3 Lifetime

Figure 7.14 shows an example of lifetime curves for luminance (left-axis) and voltage (right-axis). Figure 7.15 summarises the device lifetimes LT_{70} (i.e. time to reach 70 % of initial luminance) for the green devices G0, G1 and the red device R1 at various current densities. For G0 at 5 and 10 mA cm^{-2}, we find in average the highest LT_{70} at a substrate temperature of 59 °C ($0.84T_g$). This is an enhancement compared to room temperature of +41 % (7.98 h versus 5.65 h) and +11 % (2.63 h versus 2.36 h), respectively. Similarly, for G1 and R1, the LT_{70} peaks for all investigated current densities at 66 °C. Even at 30 mA cm^{-2} an enhancement of +14 % is found for G1 (0.49 h versus 0.43 h) and +58 % for R1 (2.72 h versus 1.72 h). Similar to the correlation of the device efficiency values, the different maxima in device lifetimes are coinciding with the substrate temperature

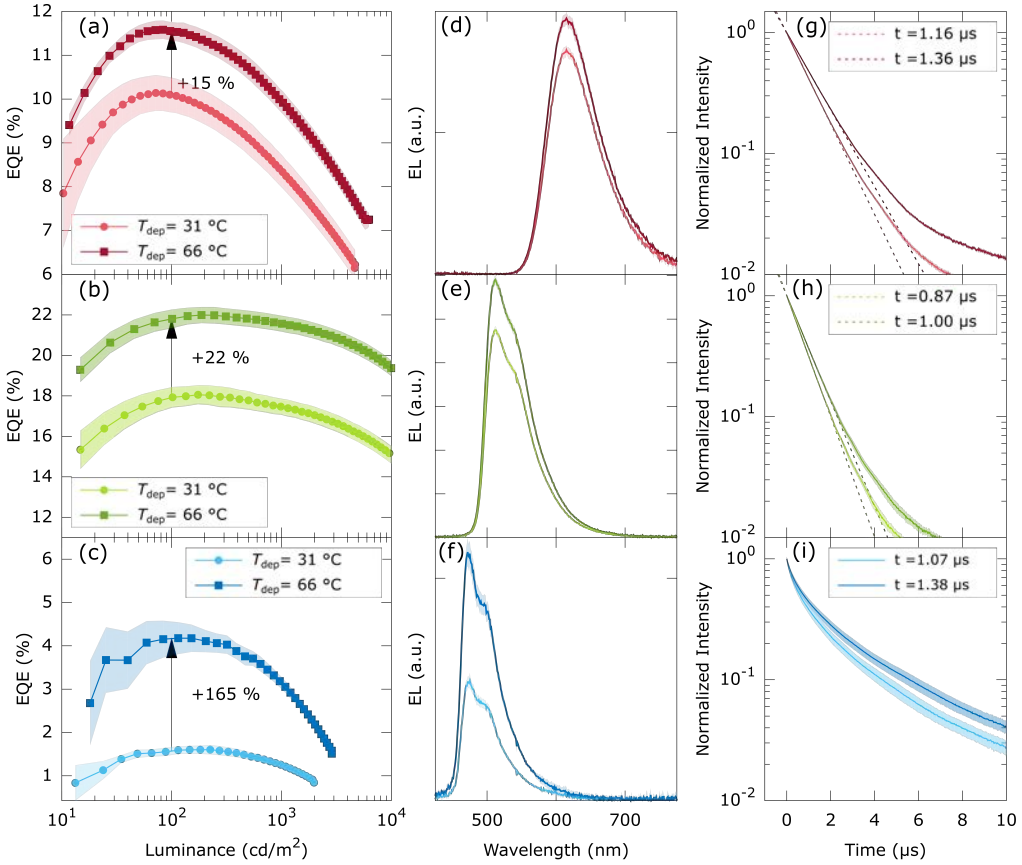

Figure 7.13: Performance characteristics for different phosphorescent emitters and different deposition temperatures. External quantum efficiency **(a-c)**, electroluminescence **(d-f)** and photoluminescence lifetime **(g-i)** for the devices R1, G1 and B1, which only differ in the emitter respect to the G0 stack. (a), (d) and (c) OLED with the red emitter ($Ir(MDQ)_2(acac)$). (b), (e) and (h) OLED with a second green emitter $Ir(ppy)_3$ and (c), (f) and (i) OLED with the blue emitter (FIrpic). For each different emitter two deposition temperatures were studied; room temperature (31 °C) and 66 °C. The arrow with the label indicates the EQE improvement respect the RT devices at a luminance of 100 cd m^{-2} in all three cases.

range for the formation of ultrastable glasses. The lifetime of the blue device series B1 was not evaluated because the emitter FIrpic has only a very short intrinsic stability not allowing for a sound analysis [142]. A summary of the devices' performance (EQE and LT_{70}) is given in Table 7.2.

7.5 Discussion

As seen in Figure 7.12 and Figure 7.14, the deposition temperature at which the ETL and EML layers are evaporated has a clear impact on the device's performance (for both efficiency and lifetime). For instance, looking at the EQE as a benchmark efficiency, it can be enhanced from 19.4 % to 24.0 % between the room temperature and the 69 °C G0 devices. When trying to understand the origin of this improvement, we

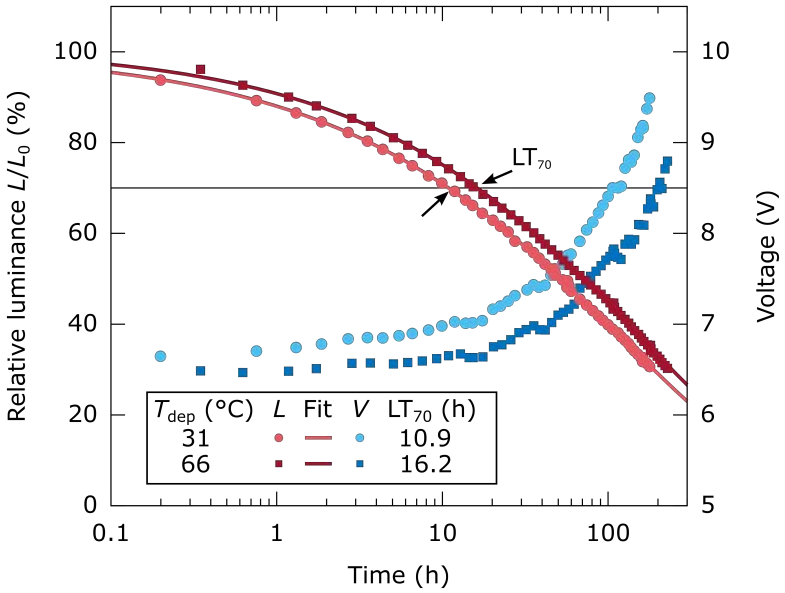

Figure 7.14: Example of OLED R1 lifetime and voltage over ageing time. Decreased luminance and increase voltage for a constant current density of 10 mA cm^{-2} for the R1 devices evaporated at 30 °C (a) and 65 °C (b), respectively. The LT_{70} is enhanced by 54 %.

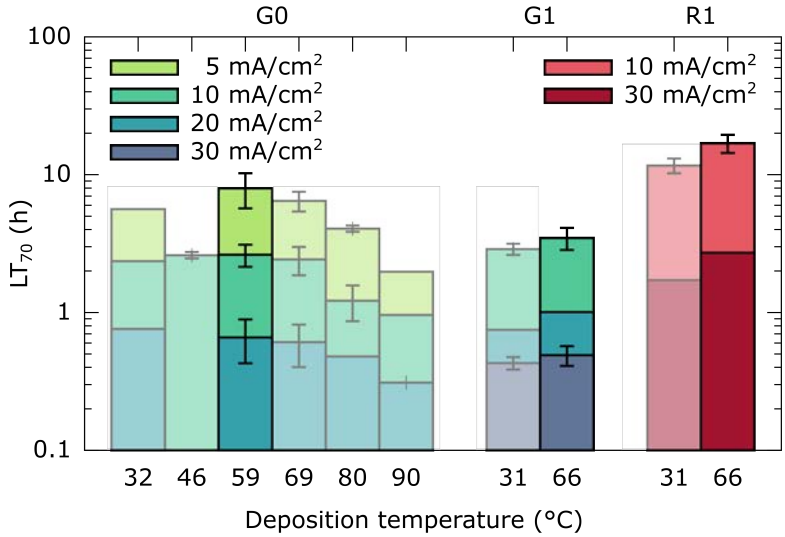

Figure 7.15: Device lifetimes at different current densities as a function of the deposition temperature. The lifetime LT_{70} is defined as the time it takes for the initial luminance to drop to 70 %. Lower current densities j lead to higher lifetimes, e.g. the bars with lower j are mostly hidden by bars with higher j. For G0, G1 and R1 we find enhanced LT_{70} for all current densities at the temperature close to $0.85T_g$ (solid bars), except for 30 mA cm^{-2} for G0. Device B1 could not be measured because of the very unstable blue emitter FIrpic. The errorbars account for identical measurements setup (e.g. j, T_{dep}) of devices. If no errorbar is given, the measurement is unique.

	T_{dep}	G0	R1	G1	B1
EQE (%)	RT	19.4 ± 0.7	10.1 ± 0.4	17.9 ± 0.5	1.6 ± 0.1
	$0.85T_g$	24.0 ± 0.9	11.6 ± 0.2	21.8 ± 0.5	4.2 ± 0.4
LT_{70} (h)	RT	2.36	11.70	2.89	–
	$0.85T_g$	2.63	16.94	3.48	–

Table 7.2: . External quantum efficiencies (EQEs) and lifetimes (LT_{70}). The EQEs are obtained at 100 cd m^{-2}, the lifetime values at 10 mA cm^{-2}. RT (room temperature) refers to the evaporation chamber standard temperature, which is close to 30 °C. The $0.85T_g$ criteria refers to the temperature closest to the optimal growth condition of the TPBi layers.

have to consider all possible sources of influence on the device efficiency. Following equation 7.2, the EQE can be factorized into four main influencing parameters: the electrical efficiency (γ), the spin formation factor ($\eta_{S/T}$), the effective radiative efficiency ($\eta_{rad,eff}$) and the outcoupling efficiency (η_{out}). In the following, these parameters are discussed one by one with respect to the observed EQE enhancement. Only the spin formation factor $\eta_{S/T}$ does not need discussion, as it can be considered unity for all phosphorescent emitters used [161].

7.5.1 Geometry and emitter orientation

Beginning with η_{out}, it is known that the thickness of an OLED has direct and significant influence on the EQE [162]. In the present configuration, the thickness of the ETL sets the crucial distance between the EML and the opaque reflective electrode, determining, thus, the amount of light that can be outcoupled due to the cavity resonances inside the device [159]. Here multiple samples are created in a single run to assure comparability between the different samples that could be scrutinized in a sequential fabrication scheme. A minor thickness gradient might be the result of devices being located at different positions on the 150×150 mm^2 glass wafer. The comparison of different OLEDs with nominally identical stack sequence on this wafer did not yield any noticeable difference. Still, based on tool calibration test, thickness deviations of ± 10 % at most can occur across the substrate. In addition, the mentioned density changes of the evaporated materials can alter the layer thickness, although the optical thickness is expected to be constant. To evaluate the impact of any thickness change, we performed optical simulations with an ETL thickness of 60 nm with generous deviations of ± 20 %. These variations yield relative EQE changes smaller than 5 %, which are much lower than the experimental EQE enhancements obtained. Therefore, it can be assumed that possible differences in the ETL layer thickness, if any, play a minimal role in the EQE improvement. It should be pointed out that these arguments cannot be generalized to all OLED concepts. While they are reasonable for bottom-emitting OLEDs that form

a weak optical cavity [11], top-emitting or cavity enhanced designs will be much more sensitive to thickness changes [163].

Another major parameter that strongly affects the light outcoupling is the transition dipole moment orientation of the emissive molecules within an OLED stack [147]. Most of the light gets trapped in substrate, waveguided and plasmonic modes (see Section 7.2.5) when the emissive dipoles are oriented vertically to the substrate plane. On the contrary, horizontally oriented dipoles can couple most of the emitted light to the outside of the device. Yokoyama et al. [150] and Dalal et al. [45] showed how the molecular orientation of different organic semiconductor molecules could be tuned solely by changing the deposition temperature. In all cases, and as a general trend, the lower the substrate temperature, the more horizontally oriented are the molecules. Although the substrate temperature might influence the orientation of both the matrix and the emitter, only the orientation of the emitter influences η_{out}. The anisotropy coefficient a, which corresponds to the ratio between the number of vertically oriented dipoles to the total number of dipoles [149], is commonly used to quantify the effect of emitter orientation. For our G0 device, with the matrix-emitter system TBPi:Ir(ppy)$_2$(acac), a value of $a = 0.27$ is found in literature when deposited at room temperature [164]. The use of other deposition temperatures have not been reported[12].

To better evaluate this possible effect in our devices, we measure the transition dipole moment orientation of 50 nm thick TPBi:Ir(ppy)$_2$(acac) layers evaporated at substrate temperatures T_{dep} ranging from 28 °C–99 °C according to the method of Frischeisen et al. [165] (see Appendix A). In agreement to literature [164], Figure 7.16 shows a preferentially horizontal alignment of the emitting dipoles from room temperature up to 59 °C, with $a = 0.30$ (blue points). However, surpassing 59 °C the dipole orientation becomes less horizontal and finally even reaches a slightly vertical alignment at 99 °C with $a = 0.35$ (0.33 corresponds to isotropic orientation), which is an expected result when considering the similar behaviour seen in other organic molecules [45]. The inset shows angular dependent p-polarized PL intensity at the peak wavelength of 526 nm indicating increasing contributions of the vertical dipoles with increasing temperature, as seen from the high-angle contribution. Optical simulations reveal that this leads to an absolute drop of the outcoupling efficiency of 2 % (red points) for the transition from room temperature to 99 °C. This anticipated fact should produce the contrary effect seen in our devices; the higher temperature OLED should give, if any, less amount of outcoupled light if only the orientation was considered. Thus, there must be some

[11] The light that is confined in a cavity with some mirror-like arrangements will reflect multiple times producing standing waves at the resonant frequencies. The emitter placed in an OLED stack is, therefore, influenced by this cavity

[12] It is interesting to point out that in this latter study by Mayr et al. [164], the orientation of the emitter is well-correlated with the glass transition temperature of the several hosts tested: the higher the glass transition of the host—lower mobility at RT—the higher the degree of horizontal orientation of the emitter. They control the orientation using higher-T_g host materials instead of changing the substrate temperature.

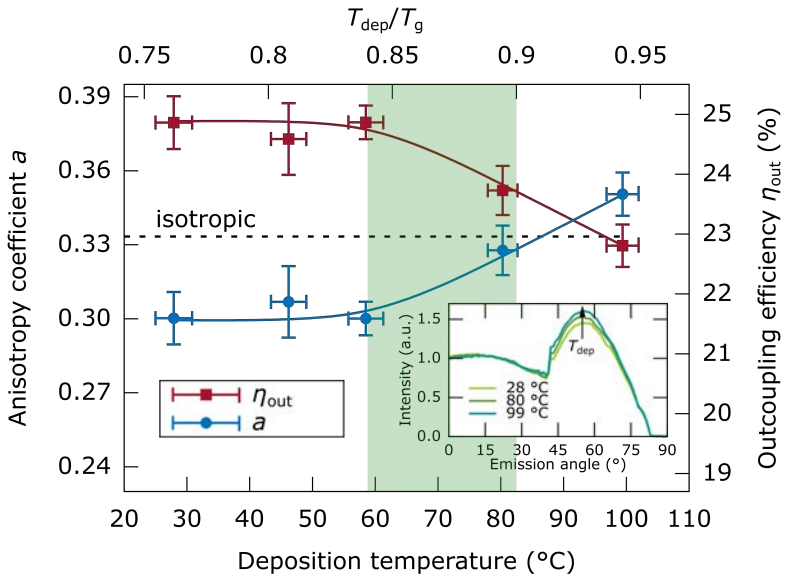

Figure 7.16: Anisotropy coefficient and outcoupling efficiency for different deposition temperatures. The anisotropy coefficient was determined by angle dependent PL measurements (inset) of the p-polarized light from a 50 nm thick layers of TPBi:Ir(ppy)$_2$(acac) 8 wt%. Based on optical thin film simulations of dipole emitters in stratified layers, the outcoupling efficiency is calculated. Both quantities stay constant until $0.84T_g$. Reaching the substrate temperature of 99 °C the anisotropy coefficient is increased from 0.30 to 0.35 changing from preferentially horizontal aligned transition dipole moments to more vertical alignment. This leads to a absolute drop in outcoupling efficiency of approximately 2 %.

other property producing the enhancement of the OLED performance and even further compensating the decreased outcoupling factor due to the dipole orientation.

7.5.2 Ultrastability of the TPBi matrix

Having ruled out the outcoupling factor in equation 7.2 as the cause of the performance enhancement, γ and $\eta_{rad,eff}$ remain as possible origins. The materials, as well as the layer and heating sequence chosen, allow to exclusively study the effects that the variation of the deposition temperature has on the host and ETL material TPBi. Besides possible changes in the molecular orientation, it has been shown that more stable and dense amorphous layers can be obtained if the substrate temperature is set around the 85 % of the corresponding material's T_g (see Section 1.2). Using fast-scanning quasi-adiabatic nanocalorimetry it is possible to measure the specific heat of TPBi layers deposited at different temperatures. Looking at the devitrification peak in the specific heat curves (see Figure A.2), it is possible to extract valuable data regarding the glass stability of a given material. Figure 7.17 shows the limiting fictive temperature and the onset temperature as a function of the deposition temperature of TPBi. These quantities indicate a maximum in both stabilities around the highlighted region of 0.84 – 0.9 T_g.

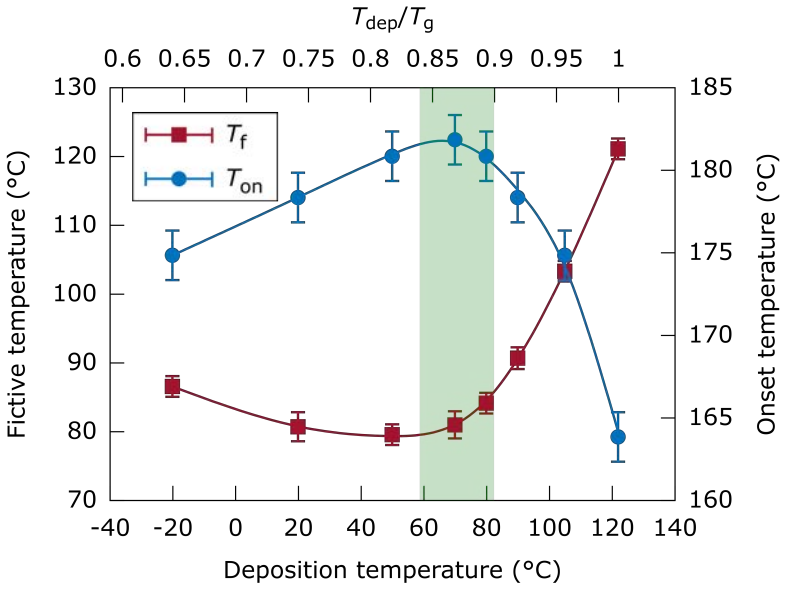

Figure 7.17: Thermal characterization as a function of the deposition temperature of TPBi layers. The fictive temperature (red, left-axis) as a thermal stability parameter and the onset of the glass transition (blue, right-axis) as a kinetic stability parameter of 60 to 80 nm films of TPBi as a function of the substrate temperature. These parameters are extracted from the heat capacity curves performed using quasi-adiabatic fast-scanning calorimetry, see Figure A.2 in Appendix A.

Although the T_f' shows a minimum plateau over a wide range between the 20 °C and 70 °C, the kinetic stability shows a clear maximum around 60–70 °C, which coincides with the typical highly stable glass formation range. These results prove that TPBi is part of the extensive family of organic molecular glass-formers that can be prepared into their ultrastable glass form when deposited at the optimal T_{dep}. Although we do not have a direct measure of density changes for TPBi, increased densities have been observed for similar OLED materials before [45].

While the absolute changes of the layer density are typically in the range of 1–2 % [45], such subtle difference will likely influence the excitonic properties significantly, as all couplings and transfer processes come with nanoscale sensitivity [166]. The TPBi layer is the host for the for the green emitter in the G0 devices, in which the 8 wt% doping of $Ir(ppy)_2(acac)$ is assumed not to influence the glassy matrix properties decisively. To test the hypothesis that the changes in stability and molecular packing of the TPBi cause the enhanced efficiencies, the same device architecture is used with three additional phosphorescent emitters ($Ir(MDQ)_2(acac)$, $Ir(ppy)_3$, and FIrpic). Figure 7.13 shows how the EQE is enhanced when the temperature is set to 66 °C for the devices R1, G1 and B1, using the red, the green and the blue emitter respectively. These results further support the idea that the host (TPBi) properties are the ones affecting the device performance.

The radiative efficiency can be written as the ratio between the radiative decay rate in the optical cavity (Γ_r^*) to the total exciton decay rates [159], which reads

$$\eta_{rad,eff} = \frac{\Gamma_r^*}{\Gamma_r^* + \Gamma_{nr}} = \Gamma_r^* \tau_{rad,eff} \tag{7.8}$$

where the Γ_{nr} are the nonradiative decay rates. The inverse of the sum of the total exciton decay rates is defined as the effective lifetime and can be measured by the photoluminescence (PL) decay times (see Appendix A). Looking at the increased $\tau_{rad,eff}$ (i.e. excited state lifetimes of the emitters in the OLED micro cavity) of +15 % (G1), +17 % (R1) and +29 % (B1) in Figure 7.13g,h,i, with the assumption that the radiative rate stays constant [159], one can relate the transient time enhancement directly to an improved radiative efficiency due to reduced nonradiative rates. The EQE increase can be fully correlated to the changes observed for the excited state lifetime $\tau_{rad,eff}$. This reduction could be rationalized in terms of a possible reduction or suppression of the β-relaxation—molecule vibrations within a cage formed by its neighbors—in the ultrastable glass of TPBi, which could slow down the nonradiative phonon-mediated monomolecular thermal relaxation processes [159]. Similar observations of reduced nonradiative recombination rates have been observed in polymer-based systems that were prepared in a very rigid form that led to a higher packing density compared to a conventionally fabricated reference sample [167, 168]. Currently, in vapour-deposited small molecules, a suppression of the β-relaxation has been reported for ultrastable glasses of toluene, n-propanol and 2-picoline by Yu et al. [50] and etoricoxib by Rodríguez-Tinoco et al. [51] but, while caution must be applied at the limited data available, it may be a general feature of ultrastable glasses.

However, while the increase of radiative efficiency for the device B1 is significantly larger with (+29 %), it fails to explain the massive enhancement of the device efficiency (+165 %). In this particular case, host and emitter are energetically in resonance at about 2.6 eV (see Figure A.3) with respect to their triplet (T1) levels, where a delayed emitter population has been shown [142]. Increased packing would greatly enhance triplet migration in the film and by that the efficiency. Unfortunately, the transient measurements do not allow to investigate this delayed effect in more detail.

The remaining parameter of equation 7.2 determining the OLED EQE is γ. Referring to the heating sequence during device processing, a change in transport properties can only be expected for the TPBi based layers, because the TCTA hole transport layers undergo identical treatment for all devices. While both j–V characteristics (Figure 7.11a and A.1) and EQE vs luminance data (Figure 7.12 and 7.13a, b, c) for the different devices look very similar, changes in the mobility may induce subtle changes in the electron and hole concentration and distribution, which could be a cause for efficiency modulations. Such carrier transport related changes however do not influence the

radiative efficiency $\eta_{rad,eff}$. Hence, with the good agreement of EQE and $\eta_{rad,eff}$ for devices G1 and R1, an altered electrical efficiency can be considered, at first glance, a minor effect. On the contrary, transport changes seem to cause most of the EQE enhancement for the FIrpic based devices B1. Here, it is possible that the resonant triplet energy character of the TPBi:FIrpic EML as mentioned above is more sensitive to a re-distribution of the charge carrier and recombination profiles [169].

7.5.3 Other temperature-OLED devices

In reviewing the literature, we only found the work by Mu et al. [151] that addressed the electroluminescent dependence of a simplified OLED on the deposition temperature of the devices. In their work, they use the simplified stack CBP/CBP:Ir(ppy)$_3$/TPBi prepared under different deposition temperatures (the whole device). While they report a significant EQE improvement, it is worth noting that their RT reference device only reached 10.6 % EQE and the best thermally treated OLED 17.9 %, where the latter is about as efficient as the reference in this study (see Table7.2, device G1). Surprisingly, the temperature at which the maximum EQE is reached coincides ours. This effect is attributed by Mu et al. [151] partly to the impact that the deposition temperature has on the surface roughness of the CBP/CBP:Ir(ppy)$_3$ and partly to an enhancement of the electron and hole mobility of their respective transport layers. However, some crucial differences should be pointed out. First, the choice of CBP as HTL and EML with its poor glass formation ability, the T_g is barely reported in literature due to its difficulty to create a CBP glass from the supercooled liquid since it normally crystallises. Secondly, in that work, their best performance is given for the device prepared 7 °C above the T_g of the CBP, so that it would be a supercooled liquid. This full combination makes harder to decorrelate the impact of each layer properties on device performance.

In another study, performed by Burns et al. [152], the properties of the emissive layer are addressed in terms of the glass transition. They use a polymer-based OLED prepared by spin coating to study the effect that thermal annealing at different temperatures has in the device performance. Thermally annealed devices show enhanced performance (EQE and current efficiencies) compared to the as-prepared sample. Their best performance is achieved for the device annealed below the T_g of the emissive layer, whereas a decreasing trend in the performance is seen with increasing the annealing temperature. Although a clear explanation for the enhancement of the performance of the as-prepared device and the annealed below T_g is not provided in their study, we can reason it in terms of physical ageing and a reduction of the β-relaxation too [167].

7.5.4 Lifetime improvement

Besides the EQE, the lifetime of the devices prepared at $\sim 0.85T_g$ is also improved (see Figure 7.14 and Table 7.2). In general, it is a tough and laborious task to investigate the degradation of OLEDs and correlate these findings to the nanoscopic level of the molecular building blocks [8]. Here, if only a change of the deposition parameters for EML and ETL (composed mostly of TPBi) lead to a similar correlation with the $0.85T_g$ criteria to form an ultrastable glass, i.e. LT_{70} peaks at these deposition temperatures, it can be deduced that the molecular conformation at the nanoscale favours a more durable device operation. A clear correlation between the glass density and the photostability—which measures the resistance of the material to light irradiation—has been recently established by Qiu et al. [170]. They prepare samples of DO37 (Dispersive Orange 37) glass by physical vapour deposition at different substrates temperatures and find that glasses prepared at $0.88T_g$ have, besides higher kinetic stability and higher density, higher photostability. They argue that higher density glasses have also higher intermolecular barriers for the molecular rearrangement, which prevent the cis-to-trans photoisomerization causing the loss of photostability in their DO37 glasses. Notwithstanding that some works have reported isomerization reaction of Ir-based emitters due to the device aging or to thermal heating needed for the vacuum-deposition process [171], it is still unknown the contribution that isomers—if any—have on the device efficiency or degradation [8] mechanism. A qualitative argument for the enhanced stability is like the one used above for increased radiative efficiency. The rigidity of the films formed as ultrastable glasses is likely to suppress coupling to generally accessible decomposition routes present in OLEDs.

7.6 Summary

In summary, this study shows that the performance of state-of-the-art organic light-emitting diodes can be significantly enhanced by optimizing the growth condition of the organic layers. We have prepared a highly simplified OLED device and tested its performance upon the deposition temperature of its EML and ETL layer, consisting of TPBi. The maximum performance for both the external quantum efficiency and the luminous efficacy, is achieved when the deposition temperature is ca. the $0.85T_g$ of the TPBi layer, in agreement with the maximum thermal stability.

We have proved that the orientation of the emitter cannot explain this improvement since it should produce a decrease in the efficiency if solely this factor was considered. We have the same device structure to check for three other emitters, exhibiting all of them efficiency enhancements at the $\sim 0.85T_g$. We have measured the phosphorescence lifetime in these devices to assess the radiative efficiency of the emission layer. The

results have shown that the enhancements in devices' EQE can be well-correlated to an increased radiative efficiency which, in turn, exhibit an excellent correlation with the thermal stability of the TPBi layer. We rationalize these findings with a likely decrease of the β-relaxation in the TPBi ultrastable matrix which would decrease the nonradiative decay processes.

A good correlation has also been found for the improvement of the OLED's lifetime and the $\sim 0.85 T_g$ deposition temperature. A better packing and rigidity of the matrix is also thought to preclude some of the degradation routes of the emitters and, therefore, increasing the operational lifetime.

Chapter 8

Conclusions

The main goal of this work was to deepen into the understanding of the glass transition phenomenon through organic vapour-deposited glasses. For that, we have explored and characterised several facets of vapour-deposited glasses of different molecular glass-formers, addressing both fundamental aspects as well as their possible application in organic light-emitting diode technology. As materials, we have first chosen toluene, a model glass-former which ultrastability had been previously established. The other materials used are organic semiconductor molecules widely employed in the organic electronics field.

An extensive part of the results presented in this work has been obtained using quasi-adiabatic fast-scanning nanocalorimetry. Various key features make nanocalorimetry a prominent technique to assess several aspects of organic vapour-deposited glasses. First, it allows measuring in situ the as deposited samples with the possibility to clean the devices just after the measurement of each sample. Second, the high heating rates push the devitrification process to much higher temperature ranges where other—more conventional—techniques do not have access. Third, the sensitivity of the technique allows sensing the heat capacity of very low masses, as in the case of nanometric films.

Glasses of toluene, TPD, α-NPD, TCTA and TPBi have been deposited using physical vapour deposition in a broad range of deposition temperatures at low growth rates of $\approx$0.2 nm s^{-1}. The deposition temperature has been shown to play a significant role in setting the kinetic and thermodynamic stability of glasses of all the studied materials. Glasses prepared at deposition temperatures around 0.85-0.89T_g exhibit the maximum stability. Glasses prepared above this maximum exhibit a limiting fictive temperature equal to the deposition temperature, which would indicate equilibration between glassy and liquid states. Specifically, for toluene, TPD and α-NPD, we have seen that the thermodynamic stability is independent of the thickness of the sample for the deposition temperatures and thickness range addressed. These results are in agreement with previous findings corresponding to other molecular glass-forming systems.

We have seen how vapour-deposited glasses transform into the supercooled liquid via a propagating growth front depending on their T_{dep}, in stark contrast to conventional glasses prepared from the liquid. The transformation mechanism has been inferred from the calorimetric trace of the devitrification using an ad hoc normalisation procedure. As has been demonstrated for other organic molecules, in toluene, the propagation velocity of this transformation front is firmly dominated by the mobility of the supercooled liquid molecules. A linear relation holds between the logarithm of the front velocity and the logarithm of the relaxation time of the liquid for an extended temperature range, covering eight orders of magnitude. For TPD, different activation energies are obtained at low and high temperature when considering an Arrhenius dependence, which is consistent the observed relation between front velocity and the mobility of the supercooled liquid layer.

As seen for toluene, TPD and α-NPD, the most thermodynamically stable glasses present the slowest transformation rates and higher crossover lengths. In the case of toluene, the stability of the glass and the mobility of the liquid seems enough to determine the growth front velocity. On the other hand, in both organic semiconductor glass-formers, the stability does not univocally determine the front velocity and the orientation of the molecules—which also depends on the T_{dep}—is proposed to be also one of the factors governing the assimilation of the molecules from the glass into the supercooled liquid front. Our study suggests a prominent relation between molecular geometry, and therefore anisotropy of the produced glass, and transformation velocity. In that scenario, the one-to-one relationship between growth front velocity and stability of toluene would suggest a much lower degree, if any, of molecular orientation. It would be interesting to reproduce similar studies of growth front velocity on well-known isotropic systems.

Together with the front velocity, we have also seen how the extend into which the heterogenous mechanism dominates strongly depends on the T_{dep}. In glasses deposited close to T_g , the bulk transformation rapidly dominates within the very first nanometers of front transformation. Surprisingly, the $v_{gr} - T'_f$ good correlation in toluene system is not reproduced for the crossover length. We have seen up to a 4-fold change in the crossover length of glasses with the same thermal stability but prepared at different deposition temperatures. A possible explanation for this behaviour could be the existence of two distinct mechanisms of glass formation at temperatures close and far from T_g . A thorough analysis of the homogeneous (bulk) glass transition in an extensive deposition temperature range would be necessary to confirm or refute this hypothesis in the toluene system. On the other hand, the crossover length of TPD and a-NPD glasses of same T'_f but deposited at different T_{dep}—above and below T_g—is expected to be distinct since they already present significantly different growth front velocities.

To gain access to the bulk transformation, we have capped TPD layers with a higher-T_g

material—TCTA—and have measured its devitrification also using nanocalorimetry. The growth transformation front of TPD films is effectively suppressed when the high mobility interface is capped, and then the glass transition occurs via a bulk mechanism. These results agree with previous results on the IMC/TNB system and the kinetic facilitation framework. We have successfully capped glasses from a wide range of stabilities. By testing different multilayer configurations, we have been able to infer that there is only one growth front mechanism starting from the free surface and none in the organic/substrate interface, regardless the stability of the glass.

The suppression (or significant delay) of the high-mobility layer improves the isothermal stability of ultrastable glasses. Further experiments, though, are required to fully explore the mechanisms behind the rejuvenation of the ultrastable—and also less stable—glasses. Capped organic layers conform the core of OLEDs, where the improved isothermal stability could play a role in determining the maximum working temperature.

We have used the newly implemented 3ω–Völklein method in GNaM to measure—in situ—the thermal conductivity in organic vapour-deposited glasses. First, we have used this technique to monitor the growth of a film from the very first stages. The sensitivity of the technique has allowed us to identify different growth regimes of the film before becoming continuous. We have started to explored the possibility to use this strategy to obtain valuable information on the different growth mechanisms of vapour-deposited glasses at various T_{dep}.

Secondly, we have shown that the in-plane thermal conductivity of TPD and α-NPD vapour-deposited can be controlled by the deposition temperature and that it correlates well with the reported anisotropy data. Using the well-established 3ω, we have been able to establish a thermal anisotropy ratio of $\approx$37 % for TPD between in-plane and out-of-plane thermal conductivities. Complementary molecular dynamics simulations have shown how the thermal conductivity is favoured along the direction of the backbone of the TPD molecule and, with a simplified model, how this can explain the anisotropy in thermal conductivity even in such small molecule systems. The thermal transport anisotropy is at odds with electronic transport that favours propagation along the perpendicular direction to the long axis of the molecule provided there is sufficient π-π interaction. This strategy could be employed in future developments to implement small molecule thin films for its use in thermoelectric-based applications.

We have prepared a proof-of-concept OLED device to test the impact of highly stable glasses in a real state-of-the-art applicaton. We have demonstrated that a significant enhancement of the efficiency and lifetime of a simplified OLED stack correlates with the increased stability and better packing of the electron and host transport layers when deposited at temperatures in the vicinity of $0.85T_g$. At this same deposition temperature, an increase of the emitter's excited state lifetime is also observed. We

have rationalised this improvement with a decrease of the nonradiative recombination rates due to a better packed and more rigid environment. Regarding the lifetime of the devices, the rigidity of the matrix is also likely to suppress or slow down the accessible decomposition routes present in OLED devices. While the orientation of the emitter has been completely ruled out as a possible factor influencing the efficiency, other factors, such as the charge transport properties are not readily discarded to play also a minor role. Further work needs to be done to understand better and quantify the contribution of the several factors implied in a device performance.

We anticipate that our findings can be generalised to any OLED, leading to improvements in both efficiency and lifetime, especially because they can be directly correlated to a very fundamental material's property such as the glass transition temperature. Therefore, the present study provides an additional approach to existing strategies—material development and advanced optical solutions—for efficiency optimisation.

Finally, we would like to remark the significance that the findings from this study provide both in the fundamental understanding of vapour-deposited glasses and their potential applications for state-of-the-art technologies.

Appendix A

Supplementary information

In this appendix, we briefly describe two of the techniques that have been used in Chapter 7 to quantify the photoluminescence lifetime of the emission layer of the R1, G1 and B1 devices and the orientation of the emitter for the device G0 as a function of the deposition temperature. These measurements are framed in the context of the ongoing collaboration with the group of Prof. Dr Sebastian Reineke from the IAPP. The time-resolved experiments were carried out by Paul-Anton Will. The angular resolved photoluminescence spectra were measured by the author whereas the modelling and the development of the fitting algorithm to extract the anisotropy value were carried out by Christian Hänisch. Moreover, we include some supplementary figures that have been left out of the main text for clarity purposed.

A.1 Time-resolved photoluminescence

For measuring the time-resolved photoluminescence, the OLEDs R1, G1, B1 were excited with a pulsed nitrogen laser (MNL 202-C/ATM 200, Lasertechnik Berlin) with an operational wavelength of 337.1 nm. A mask was used to ensure excitation to be only in the active area of the devices. The emitted light is focused and recorded with a Si amplified photodetector (PDA100A-EC, Thorlabs). Various long pass filters are used to exclude the laser and fluorescence from the signal.

A.2 Orientation of the emitter measurements

The anisotropy coefficient as a measure of the emitter molecules' transition dipole moments is extracted from angular resolved photoluminescence spectra following the method of Frischeisen et al. [165]. We use a 50 nm thick encapsulated single layer of TPBi:Ir(ppy)$_2$(acac) evaporated on a 1.1 mm thick Eagle XG glass (Corning) substrate which is attached to a 4 cm glass half-cylinder prism via index matching oil. The organic film is excited optically by a 405 nm laser diode (STAR405F10, Roithner Lasertechnik).

The emitted light is detected by a USB4000 spectrometer from OceanOptics. To balance the vertical and horizontal contributions of the transition dipole emission only the p-polarized light is measured by inserting a Glan-Taylor polarizer (PGT-5010, Casix). Furthermore, the excitation light is filtered out using a 435 nm edge filter. The sample and the excitation source are placed on a rotary stage which allows an automated angle by angle emission measurement resulting in the so called spectral radiant intensity (SRI). Finally, a fitting algorithm based on the optical model described in reference [159] is used to approximate the experimental SRI numerically and to obtain the anisotropy coefficient as a fitting parameter. In this optical simulation, the EML is represented by six infinitely thin active layers which are homogeneously distributed over the total EML thickness and separated by five passive layers with the same optical constants. The overall thickness serves as a second fitting parameter to regard for production caused thickness variations between the samples.

A.3 Supplementary figures

Here we present the exluded figures from Chapter 7. Figure A.1 shows the j–V–L characteristics of the R1, G1 and B1 devices for the two explored deposition temperatures for the TPBi layers. While the j–V data is very similar for both deposition temperatures in all cases, the device fabricated at 66 °C shows the highest luminance output.

Figure A.2 shows the specific heat obtained using quasi-adiabatic fast-scanning nanocalorimetry of TPBi layers deposited at several temperatures with thicknesses ranges between 60 and 80 nm. We see how the onset temperature of the transformation is higher for the sample deposited at $T_{dep} = 70\,^{\circ}\mathrm{C} = 0.87 T_g$.

Figure A.3 is a sketch reporting the values of the HOMO and LUMO levels for the different materials used in Chapter 7. The energy of the triplet levels is also reported.

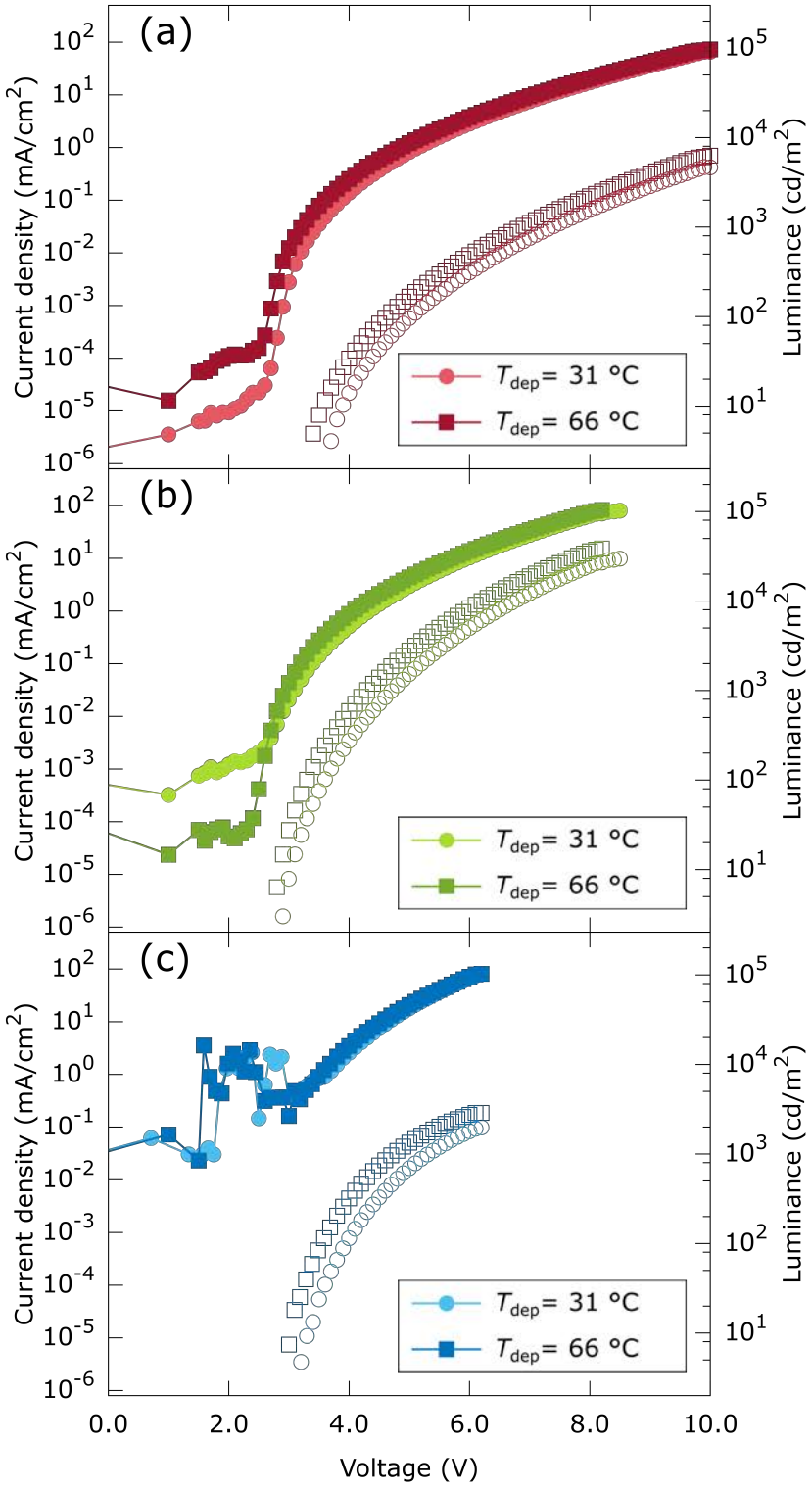

Figure A.1: Optoelectronic characterization of devices R1, G1 and B1. The j-V and L-V characteristics of the OLED devices R1 **(a)**, G1 **(b)** and B1 **(c)** are shown, which only differ from the G0 devices in the emitter used. For each different emitter two deposition temperatures were studied; room temperature (31 °C) and 66 °C.

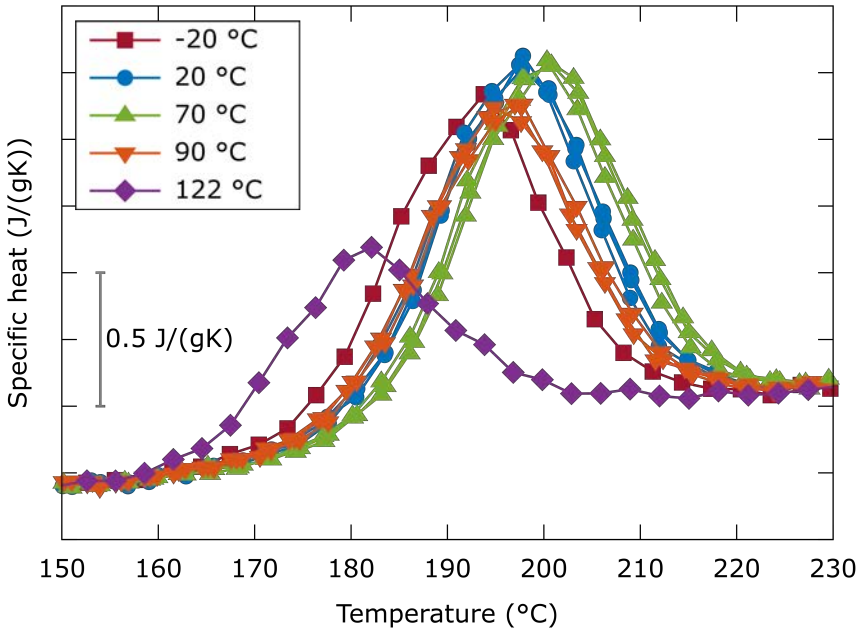

Figure A.2: Calorimetric trace of TPBi layers deposited at different temperatures. Specific heat capacity trace during a heating scan of TPBi layers (between 60 and 80 nm) deposited at different temperatures, as indicated in the legend. Multiple curves for the same temperature represent different samples. The heat capacity is obtained using quasi-adiabatic fast-scanning nanocalorimetry which uses high heating rates.

Figure A.3: Top: HOMO and LUMO values for the materials used in Chapter 7. Bottom: Triplet energy levels of used materials. The energy of the emitters (coloured) is the energy of their emission peak. The values for the TCTA and TPBi are determined at low-temperature. Figure adapted from [172].

References

[1] Pablo G. Debenedetti and Frank H. Stillinger. "Supercooled liquids and the glass transition". In: *Nature* 410.6825 (Mar. 2001), pp. 259–267. DOI: 10.1038/35065704. arXiv: 9911023v1 [arXiv:cond-mat].

[2] A. L. Greer. "Metallic Glasses". In: *Science* 267.5206 (Mar. 1995), pp. 1947–1953. DOI: 10.1126/science.267.5206.1947.

[3] Ian L. Pegg. "Turning nuclear waste into glass". In: *Physics Today* 68.2 (Feb. 2015), pp. 33–39. DOI: 10.1063/PT.3.2687.

[4] Gregory M. Fahy et al. "Physical and biological aspects of renal vitrification". In: *Organogenesis* 5.3 (July 2009), pp. 167–175. DOI: 10.4161/org.5.3.9974.

[5] John W. Delano. "Pristine lunar glasses: Criteria, data, and implications". In: *Journal of Geophysical Research: Solid Earth* 91.B4 (Mar. 1986), pp. 201–213. DOI: 10.1029/JB091iB04p0D201.

[6] Bruno C. Hancock and George Zografi. "Characteristics and Significance of the Amorphous State in Pharmaceutical Systems". In: *Journal of Pharmaceutical Sciences* 86.1 (Jan. 1997), pp. 1–12. DOI: 10.1021/js9601896.

[7] Bernard Geffroy, Philippe le Roy, and Christophe Prat. "Organic light-emitting diode (OLED) technology: materials, devices and display technologies". In: *Polymer International* 55.6 (June 2006), pp. 572–582. DOI: 10.1002/pi.1974.

[8] Sebastian Scholz et al. "Degradation Mechanisms and Reactions in Organic Light-Emitting Devices". In: *Chemical Reviews* 115.16 (Aug. 2015), pp. 8449–8503. DOI: 10.1021/cr400704v.

[9] Salvatore Torquato. "Glass transition: hard knock for thermodynamics". In: *Nature* 405.6786 (June 2000), pp. 521–523. DOI: 10.1038/35014711.

[10] S. F. Swallen et al. "Organic Glasses with Exceptional Thermodynamic and Kinetic Stability". In: *Science* 315.5810 (Jan. 2007), pp. 353–356. DOI: 10.1126/science.1135795.

[11] Andrea Cavagna. "Supercooled liquids for pedestrians". In: *Physics Reports* 476.4-6 (June 2009), pp. 51–124. DOI: 10.1016/j.physrep.2009.03.003.

[12] C. M. Roland. "Characteristic relaxation times and their invariance to thermodynamic conditions". In: *Soft Matter* 4.12 (Nov. 2008), p. 2316. DOI: 10.1039/b804794d.

[13] CA Austen Angell. "Formation of Glasses from Liquids and Biopolymers". In: *Science* 267.5206 (Mar. 1995), pp. 1924–1935. DOI: 10.1126/science.267.5206.1924.

[14] Mark D. Ediger. "Spatially heterogeneous dynamics in supercooled liquids". In: *Annual review of physical chemistry* 51.1 (Oct. 2000), pp. 99–128. DOI: 10.1146/annurev.physchem.51.1.99. arXiv: 0066-426X.

[15] E. Vidal Russell and N. E. Israeloff. "No Title". In: *Nature* 408.6813 (Dec. 2000), pp. 695–698. DOI: 10.1038/35047037.

[16] Donna Perera and Peter Harrowell. "Consequences of kinetic inhomogeneities in glasses". In: *Physical Review E* 54.2 (Aug. 1996), pp. 1652–1662. DOI: 10.1103/PhysRevE.54.1652.

[17] Peter G Wolynes. "Spatiotemporal structures in aging and rejuvenating glasses". In: *Proceedings of the National Academy of Sciences of the United States of America* 106.5 (Feb. 2009), pp. 1353–8. DOI: 10.1073/pnas.0812418106.

[18] Marcus T. Cicerone and Mark D. Ediger. "Enhanced translation of probe molecules in supercooled o-terphenyl: Signature of spatially heterogeneous dynamics?" In: *The Journal of Chemical Physics* 104.18 (May 1996), pp. 7210–7218. DOI: 10.1063/1.471433.

[19] AP Sokolov et al. "Dynamics of strong and fragile glass formers: Differences and correlation with low-temperature properties". In: *Physical review letters* 71.13 (1993), pp. 1–4.

[20] Gregory B. McKenna. "Physical Aging in Glasses and Composites". In: *Long-Term Durability of Polymeric Matrix Composites*. Ed. by Kishore V. Pochiraju, Gyaneshwar P. Tandon, and Gregory A. Schoeppner. Vol. 44. 8. Boston, MA: Springer US, Nov. 2012, pp. 237–309. DOI: 10.1007/978-1-4419-9308-3_7. arXiv: 1011.1669.

[21] Cornelius T. Moynihan et al. "Dependence of the Fictive Temperature of Glass on Cooling Rate". In: *Journal of the American Ceramic Society* 59.1-2 (Jan. 1976), pp. 12–16. DOI: 10.1111/j.1151-2916.1976.tb09376.x.

[22] M. G. Abiad, M. T. Carvajal, and O. H. Campanella. "A Review on Methods and Theories to Describe the Glass Transition Phenomenon: Applications in Food and Pharmaceutical Products". In: *Food Engineering Reviews* 1.2 (Dec. 2009), pp. 105–132. DOI: 10.1007/s12393-009-9009-1.

[23] Hideaki Hikawa, Masaharu Oguni, and Hiroshi Suga. "Construction of an adiabatic calorimeter for a vapor-deposited sample and thermal characterization of amorphous butyronitrile". In: *Journal of Non-Crystalline Solids* 101.1 (1988), pp. 90–100. DOI: 10.1016/0022-3093(88)90373-0.

[24] K Takeda, O Yamamuro, and Hiroshi Suga. "Calorimetric study on structural relaxation of 1-pentene in vapor deposited and liquid-quenched glassy states". In: *The Journal of Physical Chemistry* 99 (1995), pp. 1602–1607.

[25] Christopher J Ellison and John M Torkelson. "The distribution of glass-transition temperatures in nanoscopically confined glass formers". In: *Nature Materials* 2.10 (Sept. 2003), pp. 695–700. DOI: 10.1038/nmat980.

[26] C. R. Daley et al. "Comparing surface and bulk flow of a molecular glass former". In: *Soft Matter* 8.7 (2012), p. 2206. DOI: 10.1039/c2sm06826e.

[27] L. Zhu et al. "Surface Self-Diffusion of an Organic Glass". In: *Physical Review Letters* 106.25 (June 2011), p. 256103. DOI: 10.1103/PhysRevLett.106.256103.

[28] Kenneth L. Kearns, S. F. Swallen, and Mark D. Ediger. "Hiking down the energy landscape: Progress toward the Kauzmann temperature via vapor deposition". In: *The Journal of Physical Chemistry B* 112.16 (Apr. 2008), pp. 4934–4942. DOI: 10.1021/jp7113384.

[29] Edgar Leon-Gutierrez et al. "Stability of thin film glasses of toluene and ethylbenzene formed by vapor deposition: an in situ nanocalorimetric study". In: *Phys. Chem. Chem. Phys.* 12.44 (Nov. 2010), pp. 14693–14698. DOI: 10.1039/C0CP00208A.

[30] Edgar Leon-Gutierrez et al. "Correction: Stability of thin film glasses of toluene and ethylbenzene formed by vapor deposition: an in situ nanocalorimetric study". In: *Phys. Chem. Chem. Phys.* 18.11 (2016), pp. 8244–8245. DOI: 10.1039/C6CP90023B.

[31] K. L. Ngai, Li-Min Wang, and Hai-Bin Yu. "Relating Ultrastable Glass Formation to Enhanced Surface Diffusion via the Johari-Goldstein β-Relaxation in Molecular Glasses". In: *The Journal of Physical Chemistry Letters* 8.12 (June 2017), pp. 2739–2744. DOI: 10.1021/acs.jpclett.7b01192.

[32] Zahra Fakhraai. "The Role of Surface-Mediated Equilibration in the Formation of Stable Glasses". 8th International Discussion Meeting on Relaxations in Complex Systems. 2017.

[33] Cristian Rodríguez-Tinoco et al. "Highly stable glasses of celecoxib: Influence on thermo-kinetic properties, microstructure and response towards crystal growth". In: *Journal of Non-Crystalline Solids* 0 (Aug. 2014), pp. –. DOI: 10.1016/j.jnoncrysol.2014.07.031.

[34] Cristian Rodríguez-Tinoco et al. "Evaluation of Growth Front Velocity in Ultrastable Glasses of Indomethacin over a Wide Temperature Interval". In: *The Journal of Physical Chemistry B* 118.36 (Sept. 2014), pp. 10795–10801. DOI: 10.1021/jp506782d.

[35] Mathias Ahrenberg et al. "In situ investigation of vapor-deposited glasses of toluene and ethylbenzene via alternating current chip-nanocalorimetry". In: *The Journal of Chemical Physics* 138.2 (Jan. 2013), p. 024501. DOI: 10.1063/1.4773354.

[36] Kenneth L. Kearns et al. "Observation of low heat capacities for vapor-deposited glasses of indomethacin as determined by AC nanocalorimetry". In: *The Journal of Chemical Physics* 133.1 (July 2010), p. 014702. DOI: 10.1063/1.3442416.

[37] Z Chen et al. "Dynamics of glass-forming liquids. XVI. Observation of ultrastable glass transformation via dielectric spectroscopy". In: *The Journal of Chemical Physics* 138.12 (Mar. 2013), 12A519. DOI: 10.1063/1.4771695.

[38] A. Sepúlveda et al. "Role of Fragility in the Formation of Highly Stable Organic Glasses". In: *Physical Review Letters* 113.4 (July 2014), p. 045901. DOI: 10.1103/PhysRevLett.113.045901.

[39] Shakeel S. Dalal, Zahra Fakhraai, and Mark D. Ediger. "High-Throughput Ellipsometric Characterization of Vapor-Deposited Indomethacin Glasses". In: *The Journal of Physical Chemistry B* 117.49 (Dec. 2013), pp. 15415–15425. DOI: 10.1021/jp405005n.

[40] Diane M. Walters, Ranko Richert, and Mark D. Ediger. "Thermal stability of vapor-deposited stable glasses of an organic semiconductor". In: *The Journal of Chemical Physics* 142.13 (Apr. 2015), p. 134504. DOI: 10.1063/1.4916649.

[41] A. Sepúlveda et al. "Stable glasses of indomethacin and α,α,β-tris-naphthylbenzene transform into ordinary supercooled liquids". In: *The Journal of Chemical Physics* 137.20 (Nov. 2012), p. 204508. DOI: 10.1063/1.4768168.

[42] Stephen F. Swallen et al. "Stable Glass Transformation to Supercooled Liquid via Surface-Initiated Growth Front". In: *Physical Review Letters* 102.6 (Feb. 2009), p. 065503. DOI: 10.1103/PhysRevLett.102.065503.

[43] R. Scott Smith, R. Alan May, and Bruce D. Kay. "Probing Toluene and Ethylbenzene Stable Glass Formation Using Inert Gas Permeation". In: *The Journal of Physical Chemistry Letters* 6.18 (Sept. 2015), pp. 3639–3644. DOI: 10.1021/acs.jpclett.5b01611.

[44] Shakeel S. Dalal et al. "Density and birefringence of a highly stable α,α,β-trisnaphthylbenzene glass". In: *The Journal of chemical physics* 136.20 (May 2012), p. 204501. DOI: 10.1063/1.4719532.

[45] Shakeel S. Dalal et al. "Tunable molecular orientation and elevated thermal stability of vapor-deposited organic semiconductors". In: *Proceedings of the National Academy of Sciences* 112.14 (Apr. 2015), pp. 4227–4232. DOI: 10.1073/pnas.1421042112.

[46] Kikujiro Ishii et al. "Behavior of glass and supercooled liquid Alkylbenzenes vapor-deposited on cold substrates: Toward the understanding of the curious light scattering observed in some supercooled liquid states". In: *Bulletin of the Chemical Society of Japan* 82.10 (2009), pp. 1240–1247. DOI: 10.1246/bcsj.82.1240.

[47] Kenneth L. Kearns et al. "High Modulus Organic Glasses Prepared by Physical Vapor Deposition". In: *Advanced Materials* 22.1 (Jan. 2010), pp. 39–42. DOI: 10.1002/adma.200901673.

[48] Jessica M. Torres et al. "Substrate Temperature to Control Moduli and Water Uptake in Thin Films of Vapor Deposited N,N '-Di(1-naphthyl)-N,N '-diphenyl-(1,1'-biphenyl)-4,4'-diamine (NPD)". In: *The Journal of Physical Chemistry B* 119.35 (2015), pp. 11928–11934. DOI: 10.1021/acs.jpcb.5b05814.

[49] Kevin J Dawson et al. "Highly stable indomethacin glasses resist uptake of water vapor". In: *The journal of physical chemistry. B* 113.8 (Feb. 2009), pp. 2422–7. DOI: 10.1021/jp808838t.

[50] H. B. Yu et al. "Suppression of β Relaxation in Vapor-Deposited Ultrastable Glasses". In: *Physical review letters* 115.18 (Oct. 2015), p. 185501. DOI: 10.1103/PhysRevLett.115.185501.

[51] Cristian Rodríguez-Tinoco et al. "Secondary relaxation in ultrastable etoricoxib: evidence of correlation with structural relaxation". In: *to be determined* (2017). Forthcoming.

[52] Ankit Gujral et al. "Structural Characterization of Vapor-Deposited Glasses of an Organic Hole Transport Material with X-ray Scattering". In: *Chemistry of Materials* 27.9 (May 2015), pp. 3341–3348. DOI: 10.1021/acs.chemmater.5b00583.

[53] Deepanjan Bhattacharya and Vlad Sadtchenko. "Enthalpy and high temperature relaxation kinetics of stable vapor-deposited glasses of toluene". In: *The Journal of Chemical Physics* 141.9 (Sept. 2014), p. 094502. DOI: 10.1063/1.4893716.

[54] Cristian Rodríguez-Tinoco et al. "Transformation kinetics of vapor-deposited thin film organic glasses: the role of stability and molecular packing anisotropy". In: *Phys. Chem. Chem. Phys.* 17.46 (Dec. 2015), pp. 31195–31201. DOI: 10.1039/C5CP04692K. arXiv: arXiv:1011.1669v3.

[55] Tomás Pérez-Castañeda et al. "Suppression of tunneling two-level systems in ultrastable glasses of indomethacin". In: *Proceedings of the National Academy of Sciences of the United States of America* (July 2014), pp. 1–6. DOI: 10.1073/pnas.1405545111.

[56] Sergio Luis L M Ramos et al. "Character of Devitrification, Viewed from Enthalpic Paths, of the Vapor-Deposited Ethylbenzene Glasses". In: *The Journal of Physical Chemistry B* 115.49 (Dec. 2011), pp. 14327–14332. DOI: 10.1021/jp203612s.

[57] Lei Zhu and Lian Yu. "Generality of forming stable organic glasses by vapor deposition". In: *Chemical Physics Letters* 499.1-3 (Oct. 2010), pp. 62–65. DOI: 10.1016/j.cplett.2010.09.010.

[58] Katherine R. Whitaker et al. “Highly Stable Glasses of cis -Decalin and cis / trans -Decalin Mixtures”. In: *The Journal of Physical Chemistry B* 117.42 (Oct. 2013), pp. 12724–12733. DOI: 10.1021/jp400960g.

[59] Katherine R. Whitaker et al. “Kinetic stability and heat capacity of vapor-deposited glasses of o -terphenyl”. In: *The Journal of Chemical Physics* 143.8 (Aug. 2015), p. 084511. DOI: 10.1063/1.4929511.

[60] Y. Z. Chua et al. “Glass transition and stable glass formation of tetrachloromethane”. In: *The Journal of Chemical Physics* 144.24 (June 2016), p. 244503. DOI: 10.1063/1.4954665.

[61] Hai-Bin Yu, Yuansu Luo, and Konrad Samwer. “Ultrastable Metallic Glass”. In: *Advanced Materials* 25.41 (Nov. 2013), pp. 5904–5908. DOI: 10.1002/adma.201302700.

[62] Heedong Yoon et al. “An Ultrastable Polymeric Glass: Amorphous Fluoropolymer with Extreme Fictive Temperature Reduction by Vacuum Pyrolysis”. In: *Macromolecules* 50.11 (June 2017), pp. 4562–4574. DOI: 10.1021/acs.macromol.7b00623.

[63] Sébastien Léonard and Peter Harrowell. “Macroscopic facilitation of glassy relaxation kinetics: Ultrastable glass films with frontlike thermal response”. In: *The Journal of chemical physics* 133.24 (Dec. 2010), p. 244502. DOI: 10.1063/1.3511721.

[64] Ricardo Gutiérrez and Juan P Garrahan. “Front propagation versus bulk relaxation in the annealing dynamics of a kinetically constrained model of ultrastable glasses”. In: *Journal of Statistical Mechanics: Theory and Experiment* 2016.7 (July 2016), p. 074005. DOI: 10.1088/1742-5468/2016/07/074005. arXiv: 1604.03495.

[65] Sadanand Singh, Mark D. Ediger, and JJ de Pablo. “Ultrastable glasses from in silico vapour deposition”. In: *Nature materials* 12.2 (Feb. 2013), pp. 139–44. DOI: 10.1038/nmat3521.

[66] Glen M Hocky, Ludovic Berthier, and David R Reichman. “Equilibrium ultrastable glasses produced by random pinning”. In: *The Journal of chemical physics* 141.22 (Dec. 2014), p. 224503. DOI: 10.1063/1.4903200.

[67] Ludovic Berthier et al. “Equilibrium Sampling of Hard Spheres up to the Jamming Density and beyond”. In: *Physical Review Letters* 116.23 (June 2016), p. 238002. DOI: 10.1103/PhysRevLett.116.238002. arXiv: 1511.06182.

[68] C. Austen Angell. “Fragile Glass Formers: Evidence for a New Paradigm, and a New Relation to Strong Liquids”. In: *Structural Glasses and Supercooled Liquids: Theory, Experiment, and Applications*. Hoboken, NJ, USA: John Wiley & Sons, Inc., Mar. 2012, pp. 237–278. DOI: 10.1002/9781118202470.ch7.

[69] Y. Z. Chua et al. “How much time is needed to form a kinetically stable glass? AC calorimetric study of vapor-deposited glasses of ethylcyclohexane”. In: *The*

Journal of Chemical Physics 142.5 (Feb. 2015), p. 054506. DOI: 10.1063/1.4906806.

[70] Donald M. Mattox. "Introduction". In: *Handbook of Physical Vapor Deposition (PVD) Processing*. Elsevier, 2010, pp. 1–24. DOI: 10.1016/B978-0-8155-2037-5.00001-0.

[71] Donald M. Mattox. "The "Good" Vacuum (Low Pressure) Processing Environment". In: *Handbook of Physical Vapor Deposition (PVD) Processing*. Elsevier, 2010, pp. 73–145. DOI: 10.1016/B978-0-8155-2037-5.00003-4.

[72] Osamu Yamamuro et al. "Calorimetric Study of Glassy and Liquid Toluene and Ethylbenzene: Thermodynamic Approach to Spatial Heterogeneity in Glass-Forming Molecular Liquids". In: *The Journal of Physical Chemistry B* 102.9 (Feb. 1998), pp. 1605–1609. DOI: 10.1021/jp973439v.

[73] Hai-Feng Xiang et al. "Method for measurement of the density of thin films of small organic molecules". In: *The Review of scientific instruments* 78.3 (2007), p. 034104. DOI: 10.1063/1.2712932.

[74] Terry M. Tritt. *Thermal conductivity : theory, properties, and applications*. Kluwer Academic/Plenum Publishers, 2004, p. 290.

[75] M.Yu. Efremov et al. "Thin-film differential scanning nanocalorimetry: heat capacity analysis". In: *Thermochimica Acta* 412.1-2 (Mar. 2004), pp. 13–23. DOI: 10.1016/j.tca.2003.08.019.

[76] Aitor Fernandez Lopeandia et al. "Heat transfer in symmetric U-shaped microreactors for thin film calorimetry". In: *Journal of Micromechanics and Microengineering* 16.5 (May 2006), pp. 965–971. DOI: 10.1088/0960-1317/16/5/013.

[77] J. Rodríguez-Viejo and A. F. Lopeandía. "Quasi-adiabatic, Membrane-Based, Highly Sensitive Fast Scanning Nanocalorimetry". In: *Fast Scanning Calorimetry*. Cham: Springer International Publishing, 2016, pp. 105–149. DOI: 10.1007/978-3-319-31329-0_3.

[78] Manel Molina-Ruiz. "Nanocalorimetric studies of size effects in magnetic oxides and formation kinetics in silicides". PhD thesis. Universitat Autònoma de Barcelona, 2014.

[79] Aitor Fernandez Lopeandia. "Development of Membrane-based Calorimeters to Measure Phase Transitions at the Nanoscale". PhD thesis. Universitat Autònoma de Barcelona, 2007, p. 205.

[80] David G. Cahill. "Thermal conductivity measurement from 30 to 750 K: The 3ω method". In: *Review of Scientific Instruments* 61.2 (Feb. 1990), pp. 802–808. DOI: 10.1063/1.1141498. arXiv: arXiv:1011.1669v3.

[81] David G. Cahill, M. Katiyar, and J. R. Abelson. "Thermal conductivity of a-Si:H thin films". In: *Physical Review B* 50.9 (Sept. 1994), pp. 6077–6081. DOI: 10.1103/PhysRevB.50.6077.

[82] Tao Tong and Arun Majumdar. "Reexamining the 3-omega technique for thin film thermal characterization". In: *Review of Scientific Instruments*. Vol. 77. 10. American Institute of Physics, Oct. 2006, p. 104902. DOI: 10.1063/1.2349601.

[83] F. Volklein and T. Starz. "Thermal conductivity of thin films-experimental methods and theoretical interpretation". In: *XVI ICT '97. Proceedings ICT'97. 16th International Conference on Thermoelectrics (Cat. No.97TH8291)*. IEEE, 1997, pp. 711–718. DOI: 10.1109/ICT.1997.667630.

[84] A. Sikora et al. "Highly sensitive thermal conductivity measurements of suspended membranes (SiN and diamond) using a 3ω-Völklein method". In: *Review of Scientific Instruments* 83.5 (May 2012), p. 054902. DOI: 10.1063/1.4704086. arXiv: 1201.4034.

[85] Pablo Ferrando Villalba. "Thermal characterization of Si-based nanostructures". PhD thesis. Universitat Autònoma de Barcelona, 2016.

[86] A. Sikora et al. "Erratum: "Highly sensitive thermal conductivity measurements of suspended membranes (SiN and diamond) using a 3ω-Völklein method" [Rev. Sci. Instrum. 83, 054902 (2012)]". In: *Review of Scientific Instruments* 84.2 (Feb. 2013), p. 029901. DOI: 10.1063/1.4793652.

[87] Kikujiro Ishii et al. "Excess Volume of Vapor-Deposited Molecular Glass and Its Change Due to Structural Relaxation: Studies of Light Interference in Film Samples". In: *The Journal of Physical Chemistry B* 107.3 (Jan. 2003), pp. 876–881. DOI: 10.1021/jp0260604.

[88] A. Sepúlveda, S. F. Swallen, and Mark D. Ediger. "Manipulating the properties of stable organic glasses using kinetic facilitation". In: *The Journal of Chemical Physics* 138.12 (Mar. 2013), 12A517. DOI: 10.1063/1.4772594.

[89] Shakeel S. Dalal and Mark D. Ediger. "Influence of substrate temperature on the transformation front velocities that determine thermal stability of vapor-deposited glasses". In: *The journal of physical chemistry. B* 119.9 (Mar. 2015), pp. 3875–82. DOI: 10.1021/jp512905a.

[90] M. Tylinski et al. "Vapor-deposited glasses of methyl- m -toluate: How uniform is stable glass transformation?" In: *The Journal of Chemical Physics* 143.24 (Dec. 2015), p. 244509. DOI: 10.1063/1.4938420.

[91] Apiwat Wisitsorasak and Peter G. Wolynes. "Fluctuating mobility generation and transport in glasses". In: *Physical Review E* 88.2 (Aug. 2013), p. 022308. DOI: 10.1103/PhysRevE.88.022308.

[92] H. N. Ritland. "Limitations of the Fictive Temperature Concept". In: *Journal of the American Ceramic Society* 39.12 (Dec. 1956), pp. 403–406. DOI: 10.1111/j.1151-2916.1956.tb15613.x.

[93] Shakeel S. Dalal and Mark D. Ediger. "Molecular Orientation in Stable Glasses of Indomethacin". In: *The Journal of Physical Chemistry Letters* 3 (2012), pp. 1229–1233. DOI: 10.1021/jz3003266.

[94] Kevin J. Dawson et al. "Anisotropic Structure and Transformation Kinetics of Vapor-Deposited Indomethacin Glasses". In: *The Journal of Physical Chemistry B* 115.3 (Jan. 2011), pp. 455–463. DOI: 10.1021/jp1092916.

[95] Daisuke Yokoyama. "Molecular orientation in small-molecule organic light-emitting diodes". In: *Journal of Materials Chemistry* 21 (2011), p. 19187. DOI: 10.1039/c1jm13417e.

[96] Katherine R. Whitaker et al. "Vapor-deposited α,α,β-tris-naphthylbenzene glasses with low heat capacity and high kinetic stability". In: *The Journal of Chemical Physics* 137.15 (Oct. 2012), p. 154502. DOI: 10.1063/1.4758807.

[97] Minoru Hatase et al. "Discovery of homogeneous-nucleation-based crystallization in simple glass-forming liquid of toluene below its glass-transition temperature". In: *Journal of Non-Crystalline Solids* 307-310 (2002), pp. 257–263. DOI: 10.1016/S0022-3093(02)01473-4.

[98] Kikujiro Ishii and Hideyuki Nakayama. "Structural relaxation of vapor-deposited molecular glasses and supercooled liquids". In: *Phys. Chem. Chem. Phys.* 16.24 (2014), pp. 12073–12092. DOI: 10.1039/C4CP00458B.

[99] Daniele Cangialosi et al. "Direct Evidence of Two Equilibration Mechanisms in Glassy Polymers". In: *Physical Review Letters* 111.9 (Aug. 2013), p. 095701. DOI: 10.1103/PhysRevLett.111.095701.

[100] Daniele Cangialosi. "Dynamics and thermodynamics of polymer glasses". In: *Journal of Physics: Condensed Matter* 26.15 (Apr. 2014), p. 153101. DOI: 10.1088/0953-8984/26/15/153101.

[101] Yue Zhang and Zahra Fakhraai. "Invariant Fast Diffusion on the Surfaces of Ultrastable and Aged Molecular Glasses". In: *Physical Review Letters* 118.6 (Feb. 2017), p. 066101. DOI: 10.1103/PhysRevLett.118.066101.

[102] Scott Butler and Peter Harrowell. "The origin of glassy dynamics in the 2D facilitated kinetic Ising model". In: *The Journal of Chemical Physics* 95.6 (Sept. 1991), p. 4454. DOI: 10.1063/1.461768.

[103] X. Zhou et al. "Real-Time Observation of Temperature Rise and Thermal Breakdown Processes in Organic LEDs Using an IR Imaging and Analysis System". In: *Advanced Materials* 12.4 (Feb. 2000), pp. 265–269. DOI: 10.1002/(SICI)1521-4095(200002)12:4<265::AID-ADMA265>3.0.CO;2-L.

[104] Jake A Mcewan et al. "Dependence of Organic Interlayer Diffusion on Glass-Transition Temperature in OLEDs". In: (2017). DOI: 10.1021/acsami.7b01450.

[105] Takeshi Komino et al. "Real-Time Measurement of Molecular Orientational Randomization Dynamics during Annealing Treatments by In-Situ Ellipsometry". In: *The Journal of Physical Chemistry C* 116.21 (May 2012), pp. 11584–11588. DOI: 10.1021/jp302158k.

[106] Sergio Luis L. M. Ramos, Atsuko. K. Chigira, and Masaharu Oguni. "Devitrification Properties of Vapor-Deposited Ethylcyclohexane Glasses and Interpretation of the Molecular Mechanism for Formation of Vapor-Deposited Glasses". In: *The Journal of Physical Chemistry B* 119.10 (Mar. 2015), pp. 4076–4083. DOI: 10.1021/jp5109174.

[107] A. Sepúlveda et al. "Anomalous Transformation of Vapor-Deposited Highly Stable Glasses of Toluene into Mixed Glassy States by Annealing Above T g". In: *The Journal of Physical Chemistry Letters* 3.7 (Apr. 2012), pp. 919–923. DOI: 10.1021/jz201681v.

[108] Sebastian Reineke et al. "White organic light-emitting diodes: Status and perspective". In: *Reviews of Modern Physics* 85.3 (July 2013), pp. 1245–1293. DOI: 10.1103/RevModPhys.85.1245. arXiv: 1302.3435.

[109] Hagen Klauk. "Organic thin-film transistors". In: *Chemical Society Reviews* 39.7 (June 2010), p. 2643. DOI: 10.1039/b909902f.

[110] Weiran Cao and Jiangeng Xue. "Recent progress in organic photovoltaics: device architecture and optical design". en. In: *Energy & Environmental Science* 7.7 (June 2014), pp. 2123–2144. DOI: 10.1039/c4ee00260a.

[111] Jinji Luo et al. "Enhancement of the thermoelectric properties of PEDOT:PSS thin films by post-treatment". In: *Journal of Materials Chemistry A* 1.26 (June 2013), p. 7576. DOI: 10.1039/c3ta11209h.

[112] Kenneth L. Kearns et al. "Influence of substrate temperature on the stability of glasses prepared by vapor deposition". In: *The Journal of Chemical Physics* 127.15 (Oct. 2007), p. 154702. DOI: 10.1063/1.2789438.

[113] Namsu Kim et al. "Thermal transport properties of thin films of small molecule organic semiconductors". In: *Applied Physics Letters* 87.24 (Dec. 2005), p. 241908. DOI: 10.1063/1.2140478.

[114] Nianduan Lu et al. "A unified description of thermal transport performance in disordered organic semiconductors". In: *Organic Electronics* 41 (Feb. 2017), pp. 294–300. DOI: 10.1016/j.orgel.2016.11.019.

[115] J. W. Brill et al. "Frequency-dependent photothermal measurement of transverse thermal diffusivity of organic semiconductors". In: *Journal of Applied Physics* 118.23 (Dec. 2015), p. 235501. DOI: 10.1063/1.4937565. arXiv: 1508.03300.

[116] Jillian Epstein et al. "Temperature Dependent Thermal Conductivity and Thermal Interface Resistance of Pentacene Thin Films with Varying Morphology". In: *ACS Applied Materials and Interfaces* 8.29 (2016), pp. 19168–19174. DOI: 10.1021/acsami.6b06338.

[117] Y. Okada et al. "Low-temperature thermal conductivity of bulk and film-like rubrene single crystals". In: *Physical Review B - Condensed Matter and Materials Physics* 83.11 (Mar. 2011), p. 113305. DOI: 10.1103/PhysRevB.83.113305.

[118] John C. Duda et al. "Thermal transport in organic semiconducting polymers". In: *Applied Physics Letters* 102.25 (June 2013), p. 251912. DOI: 10.1063/1.4812234.

[119] Xiaojia Wang et al. "Ultralow thermal conductivity of fullerene derivatives". In: *Physical Review B - Condensed Matter and Materials Physics* 88.7 (2013), pp. 1–7. DOI: 10.1103/PhysRevB.88.075310.

[120] C. Y. Ho, R. W. Powell, and P. E. Liley. "Thermal Conductivity of the Elements". In: *Journal of Physical and Chemical Reference Data* 1.2 (Apr. 1972), pp. 279–421. DOI: 10.1063/1.3253100.

[121] J. R. Sheats et al. "Organic Electroluminescent Devices". In: *Science* 273.5277 (Aug. 1996), pp. 884–888. DOI: 10.1126/science.273.5277.884.

[122] C. Gärditz et al. "Impact of Joule heating on the brightness homogeneity of organic light emitting devices". In: *Applied Physics Letters* 90.10 (Mar. 2007), p. 103506. DOI: 10.1063/1.2711708.

[123] Seungjun Chung et al. "Substrate thermal conductivity effect on heat dissipation and lifetime improvement of organic light-emitting diodes". In: *Applied Physics Letters* 94.25 (June 2009), p. 253302. DOI: 10.1063/1.3154557.

[124] Olga Bubnova et al. "Optimization of the thermoelectric figure of merit in the conducting polymer poly(3,4-ethylenedioxythiophene)". In: *Nature materials* 10.6 (2011), pp. 429–433. DOI: Doi10.1038/Nmat3012.

[125] Qian Zhang et al. "Organic Thermoelectric Materials: Emerging Green Energy Materials Converting Heat to Electricity Directly and Efficiently". In: *Advanced Materials* 26.40 (Oct. 2014), pp. 6829–6851. DOI: 10.1002/adma.201305371.

[126] Xinyu Wang et al. "Modifying the thermal conductivity of small molecule organic semiconductor thin films with metal nanoparticles". In: *Scientific Reports* 5.1 (Dec. 2015), p. 16095. DOI: 10.1038/srep16095.

[127] Virendra Singh et al. "High thermal conductivity of chain-oriented amorphous polythiophene". In: *Nature Nanotechnology* 9.5 (Mar. 2014), pp. 384–390. DOI: 10.1038/nnano.2014.44.

[128] Annie Weathers et al. "Significant electronic thermal transport in the conducting polymer poly(3,4-ethylenedioxythiophene)". In: *Advanced Materials* 27.12 (Mar. 2015), pp. 2101–2106. DOI: 10.1002/adma.201404738.

[129] Pablo Ferrando-Villalba et al. "Growth monitoring with sub-monolayer sensitivity via real time thermal conductance measurements". In: *Scientific reports* (2017), Submitted.

[130] Yue Zhang et al. "Using tobacco mosaic virus to probe enhanced surface diffusion of molecular glasses". In: *Soft Matter* 12.44 (2016), pp. 9115–9120. DOI: 10.1039/C6SM01566B.

[131] David G Cahill and R O Pohl. "Thermal conductivity of amorphous solids above the plateau". In: *Physical Review B* 35.8 (Mar. 1987), pp. 4067–4073. DOI: 10.1103/PhysRevB.35.4067. arXiv: arXiv:1011.1669v3.

[132] Philip B. Allen et al. "Diffusons, locons and propagons: Character of atomic vibrations in amorphous Si". In: *Philosophical Magazine Part B* 79.11-12 (1999), pp. 1715–1731. DOI: 10.1080/13642819908223054. eprint: http://dx.doi.org/10.1080/13642819908223054.

[133] Daisuke Yokoyama and Chihaya Adachi. "In situ real-time spectroscopic ellipsometry measurement for the investigation of molecular orientation in organic amorphous multilayer structures". In: *Journal of Applied Physics* 107.12 (June 2010), p. 123512. DOI: 10.1063/1.3432568.

[134] Sheng Shen et al. "Polyethylene nanofibres with very high thermal conductivities". In: *Nature Nanotechnology* 5.4 (Apr. 2010), pp. 251–255. DOI: 10.1038/nnano.2010.27.

[135] Shrayesh N. Patel and Michael L. Chabinyc. "Anisotropies and the thermoelectric properties of semiconducting polymers". In: *Journal of Applied Polymer Science* 134.3 (Jan. 2017). DOI: 10.1002/app.44403.

[136] Eva Arianna Aurelia Pogna et al. "Probing equilibrium glass flow up to exapoise viscosities". In: *Proceedings of the National Academy of Sciences* 112.8 (Feb. 2015), pp. 2331–2336. DOI: 10.1073/pnas.1423435112.

[137] W. W. Moseley. "The measurement of molecular orientation in fibers by acoustic methods". In: *Journal of Applied Polymer Science* 3.9 (May 1960), pp. 266–276. DOI: 10.1002/app.1960.070030902.

[138] Pnina Dauber-Osguthorpe et al. "Structure and energetics of ligand binding to proteins: Escherichia coli dihydrofolate reductase-trimethoprim, a drug-receptor system". In: *Proteins: Structure, Function, and Bioinformatics* 4.1 (Jan. 1988), pp. 31–47. DOI: 10.1002/prot.340040106.

[139] Simone Hofmann. "Exciton Dynamics in White Organic Light-Emitting Diodes comprising Triplet Harvesting". PhD thesis. Technische Universität Dresden, Dec. 2012.

[140] Jaesang Lee et al. "Hot excited state management for long-lived blue phosphorescent organic light-emitting diodes". en. In: *Nature Communications* 8.5 (May 2017), p. 15566. DOI: 10.1038/ncomms15566.

[141] Jaesang Lee et al. "Deep blue phosphorescent organic light-emitting diodes with very high brightness and efficiency". en. In: *Nature Materials* 15.1 (Oct. 2015), pp. 92–98. DOI: 10.1038/nmat4446.

[142] Sebastian Reineke et al. "White organic light-emitting diodes with fluorescent tube efficiency". en. In: *Nature* 459.7244 (May 2009), pp. 234–238. DOI: 10.1038/nature08003.

[143] Hiroki Uoyama et al. "Highly efficient organic light-emitting diodes from delayed fluorescence". en. In: *Nature* 492.7428 (Dec. 2012), pp. 234–238. DOI: 10.1038/nature11687.

[144] Malte C. Gather and Sebastian Reineke. "Recent advances in light outcoupling from white organic light-emitting diodes". In: *J. Photon. Energy* 5.1 (2015), p. 057607. DOI: 10.1117/1.JPE.5.

[145] Benjamin J. Matterson et al. "Increased efficiency and controlled light output from a microstructured light-emitting diode". en. In: *Advanced Materials* 13.2 (Jan. 2001), pp. 123–127. DOI: 10.1002/1521-4095(200101)13:2<123::AID-ADMA123>3.0.CO;2-D.

[146] Yang Doo Kim et al. "Recent advances in functional structures for light extraction of organic light-emitting diodes". en. In: *Japanese Journal of Applied Physics* 56.6S1 (June 2017), 06GA04. DOI: 10.7567/JJAP.56.06GA04.

[147] Jörg Frischeisen et al. "Increased light outcoupling efficiency in dye-doped small molecule organic light-emitting diodes with horizontally oriented emitters". In: *Organic Electronics: physics, materials, applications* 12.5 (May 2011), pp. 809–817. DOI: 10.1016/j.orgel.2011.02.005.

[148] Michael Flämmich et al. "Oriented phosphorescent emitters boost OLED efficiency". In: *Organic Electronics: physics, materials, applications* 12.10 (2011), pp. 1663–1668. DOI: 10.1016/j.orgel.2011.06.011.

[149] Philipp Liehm et al. "Comparing the emissive dipole orientation of two similar phosphorescent green emitter molecules in highly efficient organic light-emitting diodes". In: *Applied Physics Letters* 101.25 (2012). DOI: 10.1063/1.4773188.

[150] Daisuke Yokoyama et al. "Orientation control of linear-shaped molecules in vacuum-deposited organic amorphous films and its effect on carrier mobilities". In: *Advanced Functional Materials* 20.3 (2010), pp. 386–391. DOI: 10.1002/adfm.200901684.

[151] Haichuan Mu et al. "Electroluminescence dependence of the simplified green light organic light emitting diodes on in situ thermal treatment". In: *Applied Surface Science* 357 (Dec. 2015), pp. 2241–2247. DOI: 10.1016/j.apsusc.2015.09.217.

[152] Samantha Burns et al. "Effect of thermal annealing Super Yellow emissive layer on efficiency of OLEDs". In: *Scientific Reports* 7 (Jan. 2017), p. 40805. DOI: 10.1038/srep40805.

[153] Anna Koehler and Heinz Baessler. "The Electronic Structure of Organic Semiconductors". In: *Electronic Processes in Organic Semiconductors*. Weinheim, Germany: Wiley-VCH Verlag GmbH & Co. KGaA, Mar. 2015, pp. 1–86. DOI: 10.1002/9783527685172.ch1.

[154] W. Brutting. *Physics of Organic Semiconductors*. Ed. by Wolfgang Brütting. Weinheim, FRG: Wiley-VCH Verlag GmbH & Co. KGaA, May 2005, p. 536. DOI: 10.1002/3527606637.

[155] M. A. Baldo et al. "Highly efficient phosphorescent emission from organic electroluminescent devices". In: *Nature* 395.September (Sept. 1998), pp. 151–154. DOI: 10.1038/25954. arXiv: arXiv:1011.1669v3.

[156] Wolfgang Brütting, Stefan Berleb, and Anton G. Mückl. "Device physics of organic light-emitting diodes based on molecular materials". In: *Organic Electronics* 2.1 (2001), pp. 1–36. DOI: 10.1016/S1566-1199(01)00009-X.

[157] Wolfgang Brütting et al. "Device efficiency of organic light-emitting diodes: Progress by improved light outcoupling". In: *physica status solidi (a)* 210.1 (Jan. 2013), pp. 44–65. DOI: 10.1002/pssa.201228320.

[158] M. Segal et al. "Excitonic singlet-triplet ratios in molecular and polymeric organic materials". In: *Physical Review B* 68.7 (Aug. 2003), p. 075211. DOI: 10.1103/PhysRevB.68.075211.

[159] Mauro Furno et al. "Efficiency and rate of spontaneous emission in organic electroluminescent devices". In: *Physical Review B - Condensed Matter and Materials Physics* 85.11 (2012), pp. 1–21. DOI: 10.1103/PhysRevB.85.115205.

[160] J Meyer et al. "Highly efficient simplified organic light emitting diodes". In: *Applied Physics Letters* 91.11 (Sept. 2007), p. 113506. DOI: 10.1063/1.2784176.

[161] Sebastian Reineke and Marc A. Baldo. *Recent progress in the understanding of exciton dynamics within phosphorescent OLEDs*. Dec. 2012. DOI: 10.1002/pssa.201228292. arXiv: /cactus.nci.nih.gov/download/nci/ [http:].

[162] Rico Meerheim et al. "Quantification of energy loss mechanisms in organic light-emitting diodes". In: *Applied Physics Letters* 97.25 (2010), pp. 2010–2012. DOI: 10.1063/1.3527936.

[163] Simone Hofmann et al. "Top-emitting organic light-emitting diodes: Influence of cavity design". In: *Applied Physics Letters* 97.25 (Dec. 2010), p. 253308. DOI: 10.1063/1.3530447.

[164] Christian Mayr and Wolfgang Brütting. "Control of Molecular Dye Orientation in Organic Luminescent Films by the Glass Transition Temperature of the Host Material". In: *Chemistry of Materials* 27.8 (Apr. 2015), pp. 2759–2762. DOI: 10.1021/acs.chemmater.5b00062.

[165] Jörg Frischeisen et al. "Determination of molecular dipole orientation in doped fluorescent organic thin films by photoluminescence measurements". In: *Applied Physics Letters* 96.7 (2010), pp. 10–13. DOI: 10.1063/1.3309705.

[166] Martin Pope and Charles E. Swenberg. *Electronic Processes in Organic Crystals*. New York: Oxford University Press, 1982.

[167] Dongwook Lee et al. "Room temperature phosphorescence of metal-free organic materials in amorphous polymer matrices". In: *Journal of the American Chemical Society* 135.16 (Apr. 2013), pp. 6325–6329. DOI: 10.1021/ja401769g.

[168] Sebastian Reineke and Marc A. Baldo. "Room temperature triplet state spectroscopy of organic semiconductors". en. In: *Scientific Reports* 4.1 (Jan. 2015), p. 3797. DOI: 10.1038/srep03797.

[169] Nicholas C. Erickson and Russell J. Holmes. "Investigating the role of emissive layer architecture on the exciton recombination zone in organic light-emitting devices". en. In: *Advanced Functional Materials* 23.41 (Nov. 2013), pp. 5190–5198. DOI: 10.1002/adfm.201300101.

[170] Yue Qiu et al. "Photostability Can Be Significantly Modulated by Molecular Packing in Glasses". In: *Journal of the American Chemical Society* 138.35 (Sept. 2016), pp. 11282–11289. DOI: 10.1021/jacs.6b06372.

[171] Etienne Baranoff et al. "Sublimation Not an Innocent Technique: A Case of Bis-Cyclometalated Iridium Emitter for OLED". In: *Inorganic Chemistry* 47.15 (Aug. 2008), pp. 6575–6577. DOI: 10.1021/ic800747t.

[172] Sebastian. Reineke. "Controlling Excitons : Concepts for Phosphorescent Organic LEDs at High Brightness Sebastian Reineke". PhD thesis. Technische Universität Dresden, 2009.

[173] Joan Ràfols-Ribé et al. "Evidence of thermal transport anisotropy in stable glasses of vapour deposited organic molecules". In: *Submitted* (2017).

[174] Joan Ràfols-Ribé et al. "High-performance organic light-emitting diodes comprising ultrastable glass layers". In: *Submitted* (2017).

[175] Joan Ràfols-Ribé et al. "The role of thermodynamic stability in the characteristics of the devitrification front of vapour-deposited glasses of toluene". In: *Phys. Chem. Chem. Phys.* 19 (Apr. 2017), pp. 11089–11097. DOI: 10.1039/C7CP00741H.

[176] Cristian Rodríguez-Tinoco et al. "Relaxation dynamics of glasses along a wide stability and temperature range". In: *Scientific Reports* 6 (Oct. 2016), pp. 35607 –. DOI: 10.1038/srep35607.

List of publications

- Joan Ràfols-Ribé, Riccardo Dettori, Pablo Ferrando-Villalba, Marta Gonzalez-Silveira, Aitor F. Lopeandía, Luciano Colombo, and Javier Rodríguez-Viejo. "Evidence of thermal transport anisotropy in stable glasses of vapour deposited organic molecules". In: *Submitted* (2017)
- Joan Ràfols-Ribé, Paul-Anton Will, Christian Hänisch, Marta Gonzalez-Silveira, Simone Lenk, Javier Rodríguez-Viejo, and Sebastian Reineke. "High-performance organic light-emitting diodes comprising ultrastable glass layers". In: *Submitted* (2017)
- Pablo Ferrando-Villalba, Daisuke Takegami, Libertad Abad, Joan Ràfols-Ribé, Gemma Garcia, Javier Rodríguez-Viejo, and Aitor F. Lopeandía. "Growth monitoring with sub-monolayer sensitivity via real time thermal conductance measurements". In: *Scientific reports* (2017), Submitted
- Joan Ràfols-Ribé, Marta González-Silveira, Cristian Rodríguez-Tinoco, and Javier Rodríguez-Viejo. "The role of thermodynamic stability in the characteristics of the devitrification front of vapour-deposited glasses of toluene". In: *Phys. Chem. Chem. Phys.* 19 (Apr. 2017), pp. 11089–11097. DOI: 10.1039/C7CP00741H
- Cristian Rodríguez-Tinoco, Joan Ràfols-Ribé, Marta González-Silveira, and Javier Rodriguez-Viejo. "Relaxation dynamics of glasses along a wide stability and temperature range". In: *Scientific Reports* 6 (Oct. 2016), pp. 35607 –. DOI: 10.1038/srep35607
- Cristian Rodríguez-Tinoco, Marta Gonzalez-Silveira, Joan Ràfols-Ribé, Aitor F. Lopeandía, and Javier Rodríguez-Viejo. "Transformation kinetics of vapor-deposited thin film organic glasses: the role of stability and molecular packing anisotropy". In: *Phys. Chem. Chem. Phys.* 17.46 (Dec. 2015), pp. 31195–31201. DOI: 10.1039/C5CP04692K. arXiv: arXiv:1011.1669v3
- Cristian Rodríguez-Tinoco, Marta Gonzalez-Silveira, Joan Ràfols-Ribé, Gemma Garcia, and Javier Rodíguez-Viejo. "Highly stable glasses of celecoxib: Influence on thermo-kinetic properties, microstructure and response towards crystal growth". In: *Journal of Non-Crystalline Solids* 0 (Aug. 2014), pp. –. DOI: 10.1016/j.jnoncrysol.2014.07.031

- Cristian Rodríguez-Tinoco, Marta Gonzalez-Silveira, Joan Ràfols-Ribé, Aitor F. Lopeandía, Maria Teresa Clavaguera-Mora, and Javier Rodríguez-Viejo. "Evaluation of Growth Front Velocity in Ultrastable Glasses of Indomethacin over a Wide Temperature Interval". In: *The Journal of Physical Chemistry B* 118.36 (Sept. 2014), pp. 10795–10801. DOI: 10.1021/jp506782d